AN ABSTRACT OF THE DISSERTATION OF

Peter B. Kreider for the degree of Doctor of Philosophy in Chemical Engineering presented on September 11, 2015.

Title: *Applications of Nonthermal Microplasmas in Chemical Reaction Engineering*

Abstract approved: _____

Alexandre F.T. Yokochi

Nonthermal plasmas generate high concentrations of excited species that can simultaneously exist at high energy and far from thermodynamic equilibrium, making them useful tools in chemistry and engineering. Microplasmas, roughly defined as plasmas that are generated within sub-millimeter dimensions, provide enhanced stability, improved excited species density, increased nonequilibrium properties, higher electron temperature, and better energy efficiency along with reduced onset voltages compared to traditional nonthermal plasmas, making them promising candidates for novel chemical processing pathways. This work summarizes current knowledge regarding the advantages gained by generating nonthermal microplasmas in constricted spaces, on reduced timescales, and with engineered electrodes. Those insights are then used in the experimental evaluation of DC microplasma reaction systems in methane processing and the oxidation of model refractory sulfur compounds in fuel-like media.

The reaction environment generated by nonthermal plasmas is well suited for the activation of non-spontaneous gas phase reactions. Here, a microreactor capable of generating low power atmospheric pressure glow discharges is used in methane processing. The reactor effectively performs oxidative methane coupling to C2 and C3 hydrocarbons with methane conversions up to 50% and selectivity to C2/C3 products greater than 90%, achieving one pass yields that surpass state-of-the-art catalysis.

The generation of DC nonthermal plasmas in fuel-like media for the oxidative desulfurization of dibenzothiphene has also been investigated. At discharge gaps around 250 microns, plasmas can be initiated with DC potentials above 6 kV for short periods of time before carbon bridges are formed that short the reactor. These simple DC discharges show little promise for continuous flow desulfurization processes. However, in flat plate reaction systems with silver epoxy electrode surfaces with discharge gaps less than 50 microns, electrically driven reactions can occur at much less than 1,000 volts. These discharges warrant further investigation and characterization in future works, and could be promising systems for the oxidative desulfurization of diesel fuel.

Complementary to experimental investigations, COMSOL multiphysics models have been developed to provide insight into the kinetics of gas phase plasmachemical reactions, as well as the electric field of point-to-plane microplasma reactor designs. The kinetic models of the oxidative coupling of methane are preliminary, however, the current simulations produce the same compounds as the experimental system with realistic kinetic parameters. These models provide an excellent platform for more complicated kinetic modeling. Increasing the number of modeled plasmachemical reaction pathways will likely allow the model to converge on experimental data and be used in predictive analysis of the constructed microplasma reactor in the oxidative coupling of methane.

# Applications of Nonthermal Microplasmas in Chemical Reaction Engineering

by

Peter B. Kreider

A DISSERTATION

Submitted to

Oregon State University

in partial fulfillment of

the requirements for the

degree of

Doctor of Philosophy

Presented September 11, 2015

Commencement June 2016

Doctor of Philosophy dissertation of Peter B. Kreider presented on September 11, 2015

APPROVED:

---

Major Professor, representing Chemical Engineering

---

Head of the School of Chemical, Biological, and Environmental Engineering

---

Dean of the Graduate School

I understand that my dissertation will become part of the permanent collection of Oregon State University libraries. My signature below authorizes release of my dissertation to any reader upon request.

---

Peter B. Kreider, Author

# ACKNOWLEDGEMENTS

Graduate school has been a great experience for me. Many people in my life deserve my gratitude for their support, guidance, and companionship. So first and foremost, thank you to the multitude that will go unnamed here, for all that you did for me and continue to do for those around you.

I'd like to acknowledge the ACS Petroleum Research Fund (ACS-PRF #52025-ND9), the National Science Foundation (NSF-CBET 1134249), and the Oregon Nanoscience and Microtechnologies Institute (ONAMI) for financial support throughout this project.

Thank you to my adviser, Alex Yokochi. I'm forever grateful for your guidance and support through grad school. You've always trusted in me and my abilities, even in the times that you probably shouldn't have, and that confidence in me has instilled a confidence of my own. Thank you for all of the opportunities you've provided, and for the opportunities your support has and will continue to unlock. I'd also like to thank my co-adviser, Chih-Hung Chang. I truly appreciate the time I spent working with you and your lab group. Your patience and understanding allowed me to complete graduate school in the way that best suited me, and for that, I am grateful. To all of the members of the Yokochi and Chang Labs who've helped in ways great and small: thank you.

To Ki-Joong Kim: Thank you for being such a great friend and mentor. I owe much of my success in graduate school to you. We really do make a great team!

No graduate school experience is complete without friends to share, laugh, and commiserate with. These people comprise a collection of graduate school peers and people who I've had the good fortune of meeting in Corvallis. Matt Coblyn, Mike Knapp, Justen Dill, Matt Ryder, Kegan Sims, Alex Sims, Carson Dunlap, Malachi Bunn. You have all become true friends.

Finally, I'd like to thank my parents, Rea and Sharon, for their unwavering support in all that I do. They always see the best in me and have shown nothing but positive encouragement at all times. I continually strive to meet the example they have set for me, and I feel proud to be their son. To my sister, Natalie: Thank you for always making me feel smarter and more accomplished than I am, and for simply being you. I love you all.

# TABLE OF CONTENTS

Page

# TABLE OF CONTENTS (CONTINUED)

Page

# TABLE OF CONTENTS (CONTINUED)

# TABLE OF CONTENTS (CONTINUED)

# TABLE OF CONTENTS (CONTINUED)

# LIST OF FIGURES

Figure Page

# LIST OF FIGURES (Continued)

Figure Page

# LIST OF FIGURES (Continued)

Figure Page

# LIST OF FIGURES (Continued)

Figure Page

# LIST OF FIGURES (Continued)

Figure Page

# LIST OF FIGURES (Continued)

Figure Page

# LIST OF FIGURES (Continued)

Figure Page

# LIST OF FIGURES (Continued)

Figure Page

# LIST OF FIGURES (Continued)

Figure Page

# LIST OF TABLES

Table Page

# Introduction

This work examines how non-thermal plasmas generated through electrical discharge may be used to drive chemical reactions in microscale reactors. The use of microplasmas in volumetric chemical processing is still a relatively unexplored field. There have been several studies using microplasma reactors for chemical conversion, but they rarely focus on how plasma operating parameters and specific microplasma properties affect chemical conversion, selectivity, and energy efficiency in driving chemical reactions. Beyond the stability and efficiency advantages of microdischarges, there exists the potential to adjust reactivity and selectivity of desired chemical reactions along with microplasma properties.

In order to evaluate the feasibility of this process, two model reactions have been chosen as representative systems for the liquid and gas phases. Investigating the performance of the non-thermal plasma microreactor in the model chemical reactions will allow for general conclusions to be drawn about the systems performance and will allow for preliminary mathematical modeling. The two model reactions are summarized briefly below:

(1) The partial oxidation of methane to methanol. Liquid methanol can be stored easily at standard temperatures and pressures and is much more accessible in processing pathways in chemical synthesis. However, methanol is historically difficult to directly synthesize from methane. As a result, the work herein will also involve investigating more easily attainable methane conversion products such C2 hydrocarbons through methane coupling.

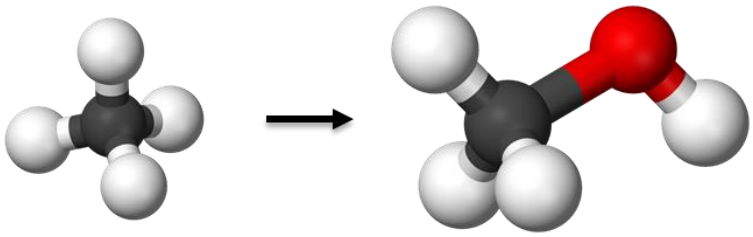

Figure 1: Partial oxidation of methane to methanol.

(2) The oxidation of dibenzothiophene (DBT) to dibenzothiophene sulfoxide (DBTO) and dibenzothiophene sulfone ($DBTO_2$) in fuel-like media. Dibenzothiophene is a refractory sulfur compound in desulfurization processes related to the oil and gas industry. Efficient oxidation to the sulfone and sulfoxide form allows for advanced separation techniques to be employed in sulfur removal from products like diesel fuel.

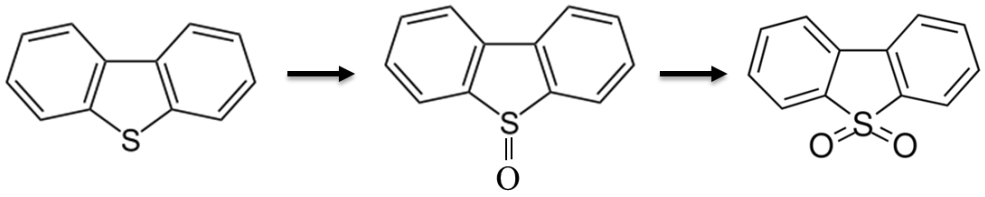


Figure 2: Oxidation pathway of dibenzothiophene to dibenzothiophene sulfoxide and dibenzothiophene sulfone.

These model reactions are of industrial interest and should effectively represent the initial feasibility of this process in both liquid and gas phases. Preliminary work in our labs has demonstrated that the corona discharge activated oxidation of sulfur compounds in fuel-like media takes place, and the technical literature suggests that electrical discharge activation of the partial oxidation of methane also occurs. The development of an efficient corona discharge activated microchannel reactor could lead to both an efficient approach to diesel desulfurization through advanced oxidation and a method to constructively use stranded methane that is currently too expensive to recover. Additionally, this novel approach to the general activation of chemical reactions through electrically generated plasmas in microreactors could open new processing options for various applications.

# Research Plan

The primary objective of this work is to acquire fundamental insights on the use of non-thermal plasmas generated by electrical corona discharge through fluids to drive chemical reactions. The generation of non-thermal plasmas at the microscale should enable stable discharge modes that operate at low power and facilitate modeling efforts. Two model reactions have been chosen for this project: the oxidation of thiophenic molecules dissolved in organic fuel-like media by dissolved atmospheric oxygen and the partial

oxidation of methane. The entire research plan can be summarized concisely in four main objectives.

**1. The construction and characterization of an experimental corona discharge activated reactor.**

The investigation of corona discharge activation of reactions in a microreactor requires the construction of a microscale device that can reproducibly generate a stable, non-thermal plasma. The constructed device must be able to withstand the pressure required to force gas and fluid flow through a microsized channel and it must also allow for the conduction of electricity, but only through the desired pathway and not into parts of the device that are not associated with the reaction zone. The formation of corona discharge requires highly non-uniform electric fields of adequate strength, and the fabricated reactor must enable this phenomena. As a result, the device fabrication objective will necessarily include experimentation with reactor geometry and electrode design. Ideally, the device should be as simple as possible in order to facilitate modeling efforts, minimize manufacturing costs, and simplify experimental work and data analysis.

**2. Experimental evaluation of the corona discharge reactor performance in the partial oxidation of methane.**

After a device that can reliably create a microscale corona discharge has been constructed, the next objective is to collect data to characterize device performance. This will include data that demonstrates effectiveness in performing the model reactions (i.e. conversion, yield, and selectivity), but also data that will allow for insights into detailed device performance and modeling of the reaction kinetics (e.g. effect of residence time, discharge current, etc.). In partial oxidation, the formation of methanol is the ultimate goal, however other reactions of interest include the formation of organic oxygenates and longer chain hydrocarbons via methane coupling.

**3. Experimental evaluation of the corona discharge reactor performance in the oxidation of refractory sulfur compounds in fuel-like media.**

The corona discharge activated oxidation of refractory sulfur compounds in decane has been demonstrated in our lab previously, but without detailed investigation into the characteristics of the electrical discharge or the specific reaction mechanism. The

characteristics of the electrical discharge in decane will be investigated in order to achieve a more complete understanding of the oxidation of dibenzothiophene in fuel-like media.

**4. Development of an explanatory/predictive model of the constructed reactor's performance.**

A predictive model based on the kinetic reaction parameters will be created using a COMSOL Multiphysics with the data collected in objectives and 3 and 4. The model will take into account all relevant aspects of the physical system, including fluid flow, reactor dimensions, concentrations of reactive species, and transport phenomena including diffusion and convection. After the model is constructed, it will be used to extract the true kinetics of reactions rather than the apparent kinetics of the reactor.

# Background Information and Motivation

## Microreactors

Microreaction systems offer several fundamental advantages in chemical processing.[1] Microscale reaction environments allow for strong gradients with respect to temperature, concentration, pressure, and reactive species. This enables rapid heat and mass transfer within the system, which allows for new processing regimes that are especially beneficial for reactions involving fast reaction times and/or unstable intermediates. The fast heat and mass transport capabilities of microreaction systems are further enhanced by their intrinsically large surface to volume ratios. As a result, these systems are characterized by fast changes in temperature and concentration and efficient heat and energy management. The small volumes usually allow for defined flow characteristics. Most flows, especially in the liquid phase, are laminar in nature at the microscale. Microreactors also exhibit narrow residence time distributions and uniform mass transport kinetics. This allows for increased reliability in simulations and theoretical predictions.

In addition, microreaction systems are typically associated with waste reduction, and increased safety. Their small size allows for rapid parametric testing, which leads to fast process optimization. Increases in scale of production can be achieved by numbering up, with no changes in system performance. The tiny systems allow for distributed processing.

## Methane Partial Oxidation

Natural gas is a valuable fuel, as it burns cleanly and is effective for both electricity production and as a source of heat. Natural gas production in remote areas is uneconomical largely because of the cost of transportation. Methane, the predominant component of natural gas, requires a pipeline in order for transportation in the gas phase to be possible. In addition, many oil and gas wells end up flaring an appreciable amount of natural gas simply because efficient capture and utilization of that gas is prohibitively expensive or technically challenging. Collectively, the gas in remote areas that is not extracted along with gas that must be flared is often referred to stranded gas. The most

common alternative to pipeline transport of natural gas is liquefaction and subsequent transportation as liquid natural gas (LNG). Unfortunately, this method is also expensive as it requires liquid nitrogen refrigeration as methane boils around -164 °C.[2] The most attractive alternative to these methods is the chemical conversion of methane to other products, which are either more valuable or easier to store and transport. For instance, methanol, a liquid at standard temperatures and pressures, could easily be stored in tanks at almost any site, including those associated with stranded gas, for later collection and transport. Alternatively, methane could be converted to higher hydrocarbons via methane coupling or to organic oxygenates, which are more valuable and provide more incentive to recover the products from remote locations.

The partial oxidation of methane has been of particular research interest since the early 1900s.[2] The partial oxidation of methane can create many different organic oxygenates, most notably methanol, and has been and continues to be of significant interest due to the widespread use of organic oxygenates in chemical synthesis. Methanol is of particular interest because it is a valuable feedstock in the synthesis of many industrially relevant chemicals, such as formaldehyde and dimethyl ether. Methanol retains most of desirable properties of methane, with the added benefits of being a stable liquid at standard conditions and enhanced reactivity in chemical synthesis. Approximately 85% of methanol produced is used in the chemical industry as a feedstock or as a solvent in chemical synthesis.[3] Methanol also holds promise as an additive in fuels or as a standalone fuel in cars and other vehicles and can also be consumed in fuel cells at premium efficiency. However, while the partial oxidation of methane is typically thought of as a partial combustion in that the typical products considered are CO and $H_2$, as shown in figure 3A, methane can be chemically converted to a wide range of products. Figure 3B shows some possible conversion routes for methane.

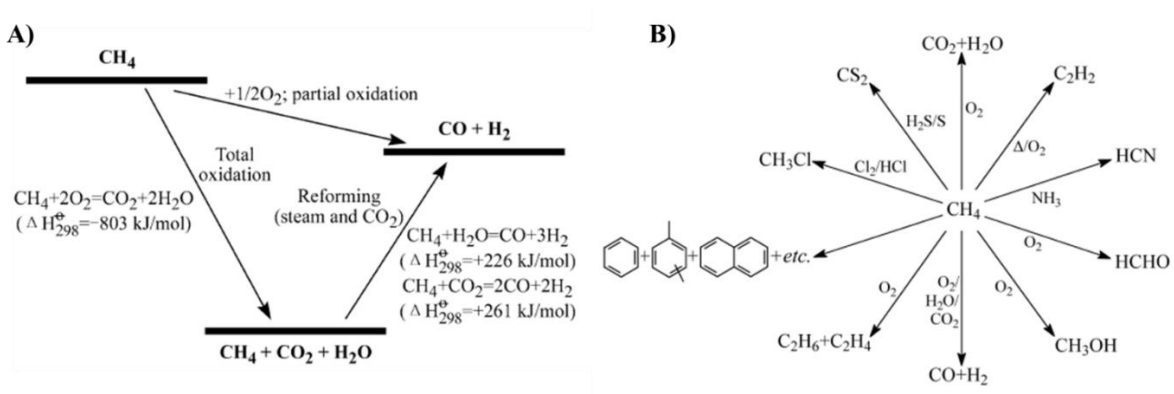


Figure 3: A) Methane partial oxidation to syngas. B) Possible methane conversion pathways. (© Journal of Natural Gas Chemistry 2004)[4]

Many researchers have investigated the potential of plasmachemical activation of the methane C-H bond. These efforts have focused on dielectric barrier discharge (DBD)[3, 5-8], corona discharge[5, 9-12], the combination of a plasma and traditional catalysis[13-16], and occasionally other plasma sources such as gliding arcs or microwaves[17, 18]. Largely, these efforts have been unsuccessful due to either low chemical conversion of methane, low selectivity towards methanol and other oxygenates, or a combination of both. The difficulty in methane partial oxidation arises mostly as a result of the properties of methane. The H-$CH_3$ bond is 440 kJ/mol and is difficult to activate in chemical reaction pathways.[2] Methane is also a symmetric molecule, so it has no dipole moments to aid in chemical activation or attack. Once an oxygen is added to the system, the H-$CH_2OH$ weakens to 393 kJ/mol and the molecule becomes polar.[2] This change in bond strength and polarity leads to easy activation once the oxidation of methane has begun, resulting in deep oxidation of methane. As a consequence, it is difficult to activate the methane oxidation pathway without simultaneously enabling the formation of deep oxidation products, CO and $CO_2$. There are two traditional methods for methane partial oxidation. The first is the simple, homogenous gas phase reaction at elevated temperature (300-500 °C). Historically, these methods have demonstrated poor reproducibility and a very narrow operating range before complete oxidation becomes dominant. In these "homogenous" reactions, the reactor wall has a significant impact on product selectivities, suggesting at least a combination of homogenous and inhomogeneous reaction pathways. The second method is thermo-catalytic processing. There have been

many studies on the subject, using a variety of different simple and supported catalyst materials including $MoO_3$, $Fe_2O_3(MoO_3)_3$, $MoO_3/SiO_2$, $V_2O_5$, Mo-V-Cr-Bi-$O_x/SiO_2$, and others, summarized well by Zhang et al.[2] The studies using catalytic partial oxidation also have difficulty with poor reproducibility. More exotic, less traditional methods for methane partial oxidation have been explored as well, and include liquid phase homogenous catalysis, supercritical fluid extraction,[2] laser stimulated surface reactions (LSSR),[2] and the use of $N_2O$ as an oxidant.[2]

## Desulfurization

Sulfur compounds are undesirable in refining processes because they contribute to the deactivation of catalysts used in downstream processing and upgrading of hydrocarbons. In liquid products, they contribute to the formation of deposits which can plug the filters of the fuel-handling system of engines. Sulfur compounds in fuel oils also cause corrosion to certain parts of internal combustion engines and refineries, due in large part to the formation of the oxyacids of sulfur. Sulfur content in combustible fuels results in the formation of $SO_2$ and other sulfur containing emissions that play a large part in the formation of acid rain and other pollution. Residual sulfur compounds contained in fuel products are problematic for refining processes, emission control, and the general fuel quality for direct combustion. Therefore, desulfurization of fuel (both liquid and gaseous) is extremely important in the petroleum-processing industry.

Reduced sulfur content diesel is also beneficial in regards to its use in vehicles. Less sulfur leads to lower $SO_2$ and sulfate particulate emission.[19] In addition, reduced sulfur content allows for more advanced handling of other pollutants ($NO_X$, particulates) and also allows for more fuel efficient engine designs to be actively used.[19] In general, the benefits associated with reduced sulfur content are tiered, with more desirable conditions associated with ever decreasing sulfur content. Sulfur levels at or below 150 ppm reduce sulfur emissions and makes catalytic converters more effective as fouling is significantly reduced.[19] Decreasing to approximately 50 ppm S allows for more advanced control strategies such as particulate sulfur filters and selective catalytic reduction.[19] At sulfur concentrations at 15 ppm and lower, NOx control over 90% is achievable, particulate

filters can approach 100% effectiveness, and extremely efficient engine designs that are incompatible with more traditional emission control systems can be used.[19]

Hydrodesulfurization (HDS) is the removal of sulfur compounds during petroleum and natural gas processing using industrial catalysts and large amounts of hydrogen gas. HDS requires intense operational conditions including high $H_2$ pressure, elevated temperatures, severe space velocities, and high maintenance investment.[20] Substantial hydrogen consumption is required in the petrochemical refining, due in large part to the hydrogenation of olefins and aromatics that occurs as a result of reaching required fuel specifications. This hydrorefining process is efficient in the removal of thiols and aliphatic disulfides but not as effective in processing thiophenes, which are aromatic sulfur-containing hydrocarbon heterocycles. For this reason, aromatic thiophenes, especially alkylated dibenzothiophenes, are refractory for HDS and often referred to as refractory sulfur compounds. Substances like dibenzothiophene, 4-methyldibenzothiophene and 4,6 dimethyldibenzothiophene are the challenge molecules for the removal of sulfur pollutants. Most HDS processes use supported metal catalysts, most commonly molybdenum disulfide but also others transition metal mixtures such as CoMo, NiMo, W, and NiW. The catalytic HDS process is widely used in industry and has been heavily researched in the last few decades.[20-24]

An interesting alternative technology to hydrodesulfurization (HDS) is the oxidative desulfurization process (ODS), also called oxidesulfurization, in which refractory sulfur compounds are oxidized to their respective sulfones or sulfoxides. These sulfones and sulfoxides are slightly more polar than their unoxidized counterparts, allowing for liquid extraction or solid absorption separation.

# Literature Review: Nonthermal Plasmas in Reaction Engineering

Most research in plasma chemistry for reaction engineering has focused on several select areas, including reactions involving the transformation of methane and other hydrocarbons[3, 5-18, 25], VOC destruction and the removal of hazardous compounds[26-41], ammonia synthesis and nitrogen fixation[42-52], nanoparticle and other material synthesis[53-61], and carbon dioxide reduction and water splitting.[62-71] Atmospheric pressure plasmas have many other uses not covered in detail here, including gas cleaning, gas sensing, surface cleaning, surface etching, surface activation, powder treatments, surface coatings (oxides, polymers, carbon), material machining, and as photon sources and detectors.[72-75] There has also been a great deal of research done on plasmas generated above, in, and in contact with condensed phases for chemical treatment and wastewater treatment applications.[76, 77]

## Methane and Hydrocarbon reactions

Efforts investigating the nonthermal plasmachemical activation of methane and other simple hydrocarbons have focused on dielectric barrier discharge (DBD)[3, 5-8, 25], corona discharge[5, 9-12], the combination of a plasma and traditional catalysis[13-16], and other plasma sources such as gliding arcs or microwaves.[17, 18] The use of nonthermal plasmas limits soot formation in hydrocarbon processing, allowing for higher theoretical energy efficiency in nonthermal plasmas than in thermal plasmas.[78] These research efforts are summarized in the following sections.

### *Methane Reactions in Dielectric barrier Discharge*

The dielectric barrier discharge has garnered much attention because it is simple to form and easy to control. DBD reactions with pure methane seem to promote methane coupling and further coupling reactions to higher hydrocarbons.[25] Larkin et al. have studied the effectiveness of using an axial flow dielectric barrier discharge (DBD) as a catalytic reactor analog; that is, using plasma generated via DBD in place of traditional catalysis.[7, 8] Using a $CH_4$:$O_2$ ratio of 3:1, along with the presence of either CO or $CO_2$,

they investigated the conversion and selectivity of the gaseous and liquid products. Their results suggest that CO and $CO_2$ do not affect the selectivities of the liquid products (formate, formic acid, and formaldehyde) and that CO and $CO_2$ are not viable oxygen sources in the partial oxidation of methane. $CH_4$ with only CO or $CO_2$ promotes methane coupling to $C_2$ hydrocarbons with significant amounts of $H_2$ gas also produced. Their later work reveals that changes in the reduced electric field strength in the DBD can shift the products of reaction from $C_2$ hydrocarbons at lower field strengths (18 V/cm/torr) to organic oxygenates at high reduced electric field strength (30 V/cm/torr). This change in reduced E-field was accomplished by decreasing the discharge gap from 12 to 4 mm. They also suggest that cooled reactor walls allow for the condensation of liquid products and increase the yield of organic oxygenates. The investigation of using multi-phase flow in a DBD reactor can effectively remove liquid products from the reaction zone and provide cooling of reactor walls to enhance the production of oxygenates.[79] Zhang et al. demonstrated the formation of methanol in axial flow DBD using mixtures of methane in air and in pure $O_2$.[3] In both mixtures, products such as CO, $CO_2$, $H_2O$, and small amounts of $C_2H_4$, $C_2H_6$, $C_3H_8$, and $C_2H_5OH$ were created along with the target product $CH_3OH$. Okumoto et al. also explored general methane reactivity in partial oxidation plasma systems and found similar products to Zhang et al, with methanol and formaldehyde products at low specific energy inputs.[80] A review of direct methane conversion to methanol in DBD has been completed by Indarto.[6] According to their review, several researchers suggest the $CH_4$:$O_2$ ratio lies somewhere around 4:1 for maximum methanol yield, while others claim that varying the feed gas ratios only limit the formation of CO and $CO_2$ and do not directly affect methanol yield. Residence times less than 2.5 seconds favor methanol formation, as methanol is further oxidized if allowed to remain in the reaction zone for longer periods of time. It is suggested that no methanol formation will be seen below an electric field strength of 21.3 kV/cm, which is equivalent to 28 V/cm/torr at atmospheric pressure. $CO_2$ as an oxidant produces very little methanol, and $CH_4$/$H_2O$ mixtures can synthesize methanol, but only around a yield of 1% or less. Yang investigated DBD in discharge gaps varying from 2-8 mm.[5] The main products in pure methane feed flows were ethane and propane, along with some ethylene and acetylene,

with total dehydrogenation of methane at higher input power. Wang et al. investigated combined steam and carbon dioxide reforming of methane in DBD and found effective conversion to hydrogen with both $CH_4$ and $CO_2$ conversion improving with steam present in the system.[81]

### *METHANE REACTIONS IN CORONA DISCHARGE*

The corona discharge has also been studied in the plasmachemical treatment of methane. The oxidative of methane with AC and DC corona discharges has been studied by Liu et al.[9] Using a point to plane reactor geometry with axial flow in a 7mm tube, the authors studied the effect of applied electrical frequency, oxygen partial pressure, flow rate/residence time, input voltage, and corona polarity. The positive DC corona polarity creates slightly more $C_2$ products than the negative DC, while the AC corona performs better methane coupling than its DC counterparts. Large amounts of ethylene and CO were observed in the reactor effluent. Supat et al. examined the possibility of combined steam reforming and partial oxidation of methane in a point-to-plane axial flow AC corona discharge with a 7 mm discharge gap.[10] Using flows of varying $CH_4$, $O_2$, and $H_2O$ content, they discovered that coupling to form $C_2$ hydrocarbons is favorable with less $O_2$, while oxygenates are more favorable with more $O_2$. The presence of water greatly enhanced methane conversion in an $O_2$ lean system and thus reduced the energy required per molecule of methane converted. The authors also looked at synthesis gas production from the partial oxidation of methane in air in the same system.[12] In addition to confirming that less oxygen content reduces methane conversion, they also saw that a larger discharge gap and larger gas flow rates also decrease methane conversion. The major products were CO, $C_2H_6$, and $C_2H_4$ with small amounts of $H_2$. Yang investigated the AC corona discharge in gaps around 2 mm and was able to form $H_2$ and acetylene with higher conversion and yield at higher power and lower flow rates.[5] Li et al. explored the possibility of carbon dioxide reforming methane in a DC corona discharge using an axial flow arrangement in a 13.2 mm diameter tube with a discharge gap of 10 mm.[11, 82, 83] The predominant products were $CO_2$, CO, $H_2$, $C_2H_2$, $C_2H_4$, $C_2H_6$, $H_2O$, and trace amounts of $C_3$-$C_6$ hydrocarbons, benzene, and toluene. The ratio of $H_2$/CO in the products depends strongly on the initial feed gas ratios and conversion of $CH_4$ and $CO_2$

are higher in positive polarity DC coronas. The authors observe the formation of coke on the cathode during the reaction and suggest that the likely mechanism of coke formation is methane decomposition. Corona discharge methane processing for COx free hydrogen, with C2 hydrocarbons as the co-products.[84]

### *Other Methane Reactions*

Both the plasmachemical partial oxidation of methane and plasmachemical methane reforming have been widely studied, and a large variety of methods to achieve this goal have been explored. While not all of these methods can be discussed here, some pertinent to this discussion are the use of gliding arc discharge and microwave generated plasmas. The gliding arc discharge starts to cross the boundary between non-thermal and thermal plasmas, and in general seem to have characteristics of both thermal and nonthermal plasmas. These gliding arc plasmas have demonstrated significant methane conversion to $H_2$, CO, $CO_2$, and $H_2O$.[18] Microwave generated plasmas have also been studied and mostly produce $C_2$ hydrocarbons, CO, $CO_2$, and small amounts of methanol in certain configurations.[17]

### *Hydrocarbon and Alcohol Reactions in Plasmacatalytic Systems*

Other works have investigated combined catalytic and plasmachemical reactions. The combination of traditional catalysis and plasmachemical methods has shown significant potential in chemical processing. There are two main approaches to the combined processing: (1) the use of a plasma to first excite and activate species before a catalyst is used to selectively produce desired products or (2) traditional catalysis followed by plasmachemical conversion to remove unwanted compounds and further synthesize desired products. Liu et al. investigated methane conversion to higher hydrocarbons using corona discharge over metal oxide catalysts.[14] The group tested various metal oxide and zeolite catalysts and demonstrated that their use significantly increase conversion to $C_2$ hydrocarbons when used in plasma activated gas flows. Further studies using various catalysts designed specifically for the formation of methanol from methane have also been done. A work by Indarto et al. shows that yttria-stabilized zirconia (YSZ) doped with Ni metal outperforms other common catalyst materials, such as $Al_2O_3$, $TiO_2$, and

$SiO_2$ in methanol selectivity after plasmachemical activation.[15] Synergistic catalytic interaction between non-thermal plasma species and nickel is suggested as a route to improve methanol yields.[85] A similar work by Indarto explores the same reaction system with a different catalyst, Cu-Zn-Al, and achieved similar conversion and slightly higher selectivity towards methanol.[86] Chen et al. also investigated the combination of DBD and traditional catalysis, but they studied CuO additions to $Fe_2O_3$ and had moderate success in increasing methanol selectivity.[16] Sobacchi et al. explored the conversion of longer carbon chains such as iso-octane to hydrogen via partial oxidation in a combined catalyst and plasma system.[13] They showed that pulsed corona plasma processing increases hydrogen yield when used before or after thermal catalytic processing, and that no hydrogen is produced with plasma alone. A summary of methane oxidation catalysts and their performance can be found in a work by Khirsariya and Mewada.[87]

Plasma systems and plasma catalytic systems have also been explored for use in alcohol reforming for hydrogen production. In a review, Du et al. thoroughly covers the different plasma and plasma catalytic configurations that can facilitate alcohol reformation.[88] Both nonthermal and thermal plasmas exhibited a broad range of reforming efficiencies, where plasma-generated radicals and ions behave in ways similar to catalysts, participating in chain reactions and promoting or accelerating reaction pathways.[88] Nonthermal plasmas can generate active species that promote chemical transformation, and traditional catalysis can promote further transformation and enhance chemical selectivity in the activated system.

## Destruction of VOCs and Hazardous Compounds

Nonthermal plasmas have been used extensively in the destruction of pollutants, VOCs, and other hazardous materials. The high energy environments created in the non-equilibrium plasma can be extremely effective at oxidation and physical destruction of these compounds, with studies often reporting removal efficiencies greater than 90% in residence times on the order of or less than one second. The nonthermal plasma destruction and oxidation of VOCs, pollutants, and other contaminants is an extremely wide reaching research area, due in part to the large number of compounds of interest.

Several research efforts have been focused on using plasma processes for NO and $SO_2$ removal from exhaust and flue gases.[26-28] The studies of nonthermal plasmas for gas cleaning applications have been largely successful, especially with respect to NO removal. The reaction mechanisms are relatively well-understood compared to other chemical species in non-thermal plasmas. The oxidation of benzene has shown simple conversion of around 30% to oxidized products, mainly phenols, in dielectric barrier discharge.[29] The addition of MS10X packing leads to more complex products, such as ethers, aldehydes, esters, and napthalenes. While DBD has shown favorable comparison to other discharge types in the destruction of benzene[30], studies using needle-to-plane corona discharge have also achieved significant conversion.[31] DBD has also shown promise in the removal of ammonia, isopropanol, and acetaldehyde.[32-34] The use of surface discharges has demonstrated 90% to 99% removal efficiencies for NOx, toluene, acetone, isopropyl alcohol, trichloroethylene, and CFC-113.[28, 35] Studies utilizing pulsed corona discharge have been effective at oxidizing propane, propene, and isopropyl alcohol, toluene, ethylene, methylene chloride, and dichlorodifluromethane, methanol, acetone, dimethyl sulfide, alpha-pinene, and sulfur hexafluoride.[36-40] The atmospheric pressure plasma jet (APPJ) is a combination of thermal and nonthermal plasma processing, and has been shown to be effective at decontamination in general. In one particular work, an APPJ system was able to efficiently destroy a variety of biological and chemical warefare agents, including anthrax, yellowfever and E. Coli bacteria, viruses, biotoxins, mustard gas, sarin gas, and phosgene gas.[41]

## Ammonia Synthesis and Nitrogen Fixation

Nitrogen fixation using electrically generated plasmas has been around since 1903, with the inception of the Birkeland–Eyde process and the beginning of the ammonia based fertilizer industry. The Birkeland–Eyde process, which uses thermal arcs to fix nitrogen, is not particularly energy efficient and was gradually replaced by the Haber process. Much more recently, the possibility of using nonthermal plasmas to more efficiently fix nitrogen has been receiving attention.

The synthesis of ammonia from $N_2$ and $H_2$ in DBD reactors has achieved yields around 1.25% in a discharge gap of 35 mm.[42] Other studies using nonthermal plasma reactors

have shown enhanced ammonia production when using catalysts, such as Fe, Mo, MgO.[43-45] Ammonia is only produced when both $N_2$ and $H_2$ are exposed to the plasma.[44] $NH_3$ has also been successfully synthesized in microwave and radio frequency plasmas.[46-48] These works also looked at the effect of electrode material on ammonia synthesis yields. They found an approximate linear relationship between the work function of the metal electrode and production of ammonia, with higher work functions (Pt) being the most effective electrode material in ammonia synthesis.[46] In a later work, the same research group showed increased conversion of nitrogen to ammonia by changing materials of construction of condensing wall surfaces.[47]

Simple plasmachemical nitrogen fixation in combinations of $N_2$ and $O_2$ is also of significant interest. Positive corona discharge for nitrogen fixation has been investigated in laboratory and field studies.[49] A high relative humidity can produce $NO_x$ more efficiently than dry air, and the positive polarity corona slightly outperforms the negative polarity. It is suggested that $N_2O$ dissociates to NO in corona discharge. Mass spectroscopic studies of corona discharge in air at atmospheric pressure shows that water is the dominant charge carrier, except at extremely low concentrations, and that water forms hydrated charged species with both O and N.[50] Other works have shown that increasing oxygen content increases the formation of $NO_x$ in a pulsed corona reactor.[51] A review on combined plasma/catalytic systems for ammonia synthesis with a special focus on nitrogen-fixation has also been completed.[52]

## Nanoparticle and Materials Synthesis

Nonthermal plasma techniques have also proven useful in the synthesis of nanoparticles and nanomaterials. For example, traditional thermal plasmas have long been used to synthesize carbon based nanoparticles such as carbon black or carbon nanotubes. Recently, nonthermal plasma processing has demonstrated the ability to produce a broad range of carbon nanomaterials, including furnace-type and acetylene-type carbon black in addition to nanoparticles with novel morphology.[53] In general, nonthermal plasmas seem to have beneficial properties for nanomaterial synthesis.[54-56]

The synthesis and preparation of catalysts is another field in which nonthermal plasma technologies have applications. Ultrafine catalyst particles and supported catalytic

materials show improved properties and benefit from efficient preparation utilizing plasma technologies.[57, 58] Plasma enhanced synthesis of catalysts can help improve distribution of active catalytic material on supports, reduce energy consumption required during preparation, shorten preparation time, and improve catalyst properties such as turnover frequencies, selectivity, and catalyst lifetime.[57]

Nonthermal plasma synthesis environments have specific properties beneficial for the production of semiconductor nanomaterials.[59] The highly reactive environments provide rapid synthesis times while the particles themselves tend be unipolar in charge, which reduces agglomeration and particle interactions with reactor walls. The plasma synthetic methods tend to selectively heat particles to high temperatures, which is especially beneficial for materials like semiconductors that have high crystallization temperatures. Amorphous silicon, p and n doped silicon, germanium, gallium nitride, indium phosphide, and silicon-germanium alloys have all been successfully synthesized via nonthermal plasma processes.[59, 60] These nanocrystals have applications in nanoelectronics, thermoelectric materials, photovoltaics, and light-emitting devices. Radascsi et al. have shown that nonthermal plasma reactions can produce organic nanomaterials with higher quality crystalline properties.[61] Their work focused on plasma assisted crystallization of the explosive organic material RDX, and the synthesized particles showed increased crystal quality and reduced sensitivity to friction activation.

## $CO_2$ and $H_2O$ Dissociation

There are many other chemical reaction pathways that have demonstrated the potential benefits of nonthermal plasma processing. One noteworthy reaction of interest is carbon dioxide reduction and reformation. $CO_2$ dissociation and conversion to products, such as syngas, methanol, and higher hydrocarbons has been demonstrated in nonthermal plasmas.[62, 63] Combined methane and $CO_2$ conversion to $H_2$, CO, and small amounts of higher hydrocarbons has also been successfully carried out.[64]

Some primary investigations have been conducted for the $CO_2$ dissociation to generate products like syngas, methanol and hydrocarbons using corona discharge[65, 66] and dielectric barrier discharge.[67] In addition to the dry reforming of methane discussed earlier, direct $CO_2$ hydrogenation reactions in nonthermal plasams can generate several

kinds of oxygenated products, including methanol, aldehydes, acetic acid and some other oxygenates.[68, 69] Nonthermal plasma $CO_2$ hydrogenation in the presence or absence of a catalyst has been shown to produce methanol, and the comparative experiments showed that the simultaneous presence of nonthermal plasma and catalyst shifted the temperature range of the maximum catalyst activity from 493K to 373K.[69]

Nonthermal plasmas have been used in water splitting reactions, where results show energy efficiencies and hydrogen production rates that are comparable to and better than photocatalytic methods.[70, 71]

## Liquid Phase Reactions in Nonthermal Plasmas

The generation of nonthermal plasmas in condensed phases has been a heavily explored topic in the last decade. Several recent works have effectively reviewed and summarized these efforts and as a result liquid phase reactions in association with nonthermal plasma will not be covered in detail here. Bruggeman and Leys thoroughly reviewed non-thermal plasmas in and in contact with liquids.[77] Locke et al. has reviewed the generation of electrohydraulic discharges and the use of nonthermal plasmas for wastewater treatment applications.[76]

The small body of work that uses plasma to generate excited species that are active in oxidesulfurization has positive preliminary results. In one study, an oxygen plasma gas stream was passed onto a liquid surface.[89] The use of dielectric barrier discharge to generate excited oxygen species that then react in the liquid system with $MnO_2$ catalysts has also been investigated.[90]

# Nonthermal Microplasmas in Chemical Reaction Engineering: A Review

**Peter B. Kreider, Justin Pommerenck, Alexandre F.T. Yokochi**

**School of Chemical, Biological, and Environmental Engineering, Oregon State University**

*In Preparation*

## Abstract

Nonthermal plasmas generate high concentrations of excited species that can simultaneously exist at high energy and far from thermodynamic equilibrium, making them useful tools in chemistry and engineering. Microplasmas, plasmas that are generated within sub-millimeter dimensions, provide enhanced stability, improved excited species density, increased nonequilibrium properties, higher electron temperature, and better energy efficiency along with reduced onset voltages compared to traditional nonthermal plasmas, making them a promising tool for plasmachemical processing pathways. This review summarizes the use and performance of nonthermal microplasmas in commonly studied gas phase chemical reactions and discusses the advantages gained by generating nonthermal microplasmas in constricted spaces, on reduced timescales, and with engineered electrodes.

**Keywords:** plasmachemistry; microplasma; nonthermal plasma; reaction engineering; electrical discharge

# Introduction

Plasmas, as tools in the field of chemistry and engineering, provide three main features that are useful in application.[91]

1. The temperature and energy density of at least one component of the plasma often exceed those of other, more conventional processes.
2. Plasmas create high concentrations of activated or excited species, such as electrons, ions, atoms, radicals, excited states, and photons.
3. Plasmas can operate far from thermodynamic and chemical equilibrium, allowing for the existence of excited states and activated species while the bulk media remains at or near room temperature.

Collectively, these properties make plasmas interesting as chemical processing tools that provide reaction environments that are strikingly different from traditional methods. In essence, plasmas can create high density, high energy environments that activate reactions differently from traditional methods, all while existing far from thermodynamic equilibrium. This unique environment has shown promise in many different fields and has demonstrated performance that surpasses traditional thermocatalytic processing. Most research in plasma chemistry for reaction engineering has focused on several select areas, including reactions involving the transformation of methane and other hydrocarbons,[3, 5-18, 25] VOC destruction and the removal of hazardous compounds,[26-41] ammonia synthesis and nitrogen fixation,[42-52] nanoparticle and other material synthesis,[53-61] and carbon dioxide reduction and water splitting.[62-71] Atmospheric pressure plasmas have many other uses not covered in detail here, including gas cleaning, gas sensing, surface cleaning, surface etching, surface activation, powder treatments, surface coatings (oxides, polymers, carbon), material machining, and as photon sources and detectors.[72-75] There has also been a great deal of research done on plasmas generated above, in, and in contact with condensed phases for chemical treatment and wastewater treatment applications which will also not be discussed here.[76, 77]

In chemical processing, microreaction systems offer several fundamental advantages over macroscale systems. The use of components and structures on the microscale creates

strong gradients with respect to temperature, concentration, pressure, and reactive species.[1] This enables rapid heat and mass transfer within the system. These properties open new processing regimes that are especially beneficial for reactions involving fast reaction times and unstable intermediates, which complement plasmachemical systems well. The fast heat and mass transport capabilities of microreaction systems are further enhanced by their intrinsically large surface to volume ratios. The large surface to volume ratio has implications in chemical synthesis, as surfaces can play a large role in how chemical reactions proceed. In addition, microreaction systems are characterized by fast changes in temperature and concentration and by efficient heat and energy management. In plasma systems, rapid heat transfer usually results in a stabilization of the discharge and contributes in maintaining nonthermal properties of the plasmas at the microscale. Plasmas that are generated and confined within sub-millimeter spaces in at least one dimension are often referred to as microplasmas. The confined spatial scale associated with microplasmas can impart plasma properties that are substantially different from macroscale plasmas: namely, small physical size, high pressure stability, and non-thermal plasma properties such as non-Maxwellian electron energy distributions, non-equilibrium thermodynamics, and high electron energy and high electron density.[56] Chemical process intensification using microplasma reactors has shown promising results in methane reforming, and is likely a viable route for many other chemical processes.[92] At high pressure, microplasmas can have significantly different plasma component populations due to an increase in three-body processes and volumetric recombination.[93] Generally, microplasmas provide enhanced stability, improved excited species density, increased nonequilibrium properties, higher electron temperature, and better energy efficiency along with reduced onset voltages compared to traditional nonthermal plasmas, making them promising tools for plasmachemical processing pathways.

There are many different configurations of microplasma generators and most have names derived either from the general geometry of the system or from the method used to induce the plasma. These include certain forms of dielectric barrier discharge (DBD), capillary plasma electrode discharges (CPED), inverted square pyramid microplasma (ISP), square cross sectional cavity microplasma (SCSC), radio frequency inductively

coupled discharge (RFIC), micro-hollow cathode discharge (MHCD), and cathode boundary layer microplasma (CBL), among others.[94] There are works in literature that use microplasmas generated in systems that do not directly fall into the above named categories, and include simple discharge gaps, point-to-plane geometry, and simple electrode spacings that are smaller than one millimeter.

## Background

Plasmas are necessarily multi-component systems, and typically exist as a mixture of electrons, ions, and both excited and neutral species. In electrically generated plasmas, energy is first accumulated by electrons and then transferred to heavier species via collisions, providing the energy for ionization, dissociation, and excitation. The collisions that occur can be either elastic collisions, which are simply a redistribution of kinetic energy, or inelastic collisions that result in energy transfer between the kinetic energy and internal energy of the colliding components. The rates of the collision driven processes such as ionization depend on the number electrons with sufficient energy to activate the given process. The energy distribution of plasmas is often characterized by a temperature, and the temperature of plasmas is determined by the average energy of the plasma constituents and their relative degrees of freedom (i.e. translational, rotational, vibrational, and electronic excitations). Each component of the plasma (e.g. electrons, neutrals, ions, etc.) can exhibit their own characteristic temperature.

### *Energy Distributions in Plasma*

The temperature differences between electrons and heavy neutrals is characterized by the square of the ratio of the electric field, $E$, to the gas pressure, $p$. At small values of $E/p$, the temperature of heavy particles approaches the temperature of electrons and creates what is referred to as local thermodynamic equilibrium.[91] Local thermodynamic equilibrium requires chemical equilibrium, and a given point in the plasma can be characterized by a single temperature. Ionization and chemical processes are determined by that temperature, and these quasi-equilibrium plasmas are referred to as *thermal plasmas*. Thermal plasmas include lightning and electric arcs. Plasmas are at non-equilibrium when the electron temperature far exceeds the temperature of ions and

neutral particles ($T_e >> T_0$), and as a result ionization and chemical processes are determined by the electron temperature. When conditions allow the power transfer between components in the plasma to enable such disparity in electron temperature and the temperature of heavy species, the plasmas are referred to as *non-thermal plasmas.* The temperatures of various components in non-thermal plasmas can be complex, but in general follow a common trend: the electron temperature is the highest ($T_e$), followed by the temperature of vibrational states ($T_v$), and the lowest temperature is common between the gas temperature ($T_0$), ions ($T_i$), and rotational states ($T_r$).[91] ($T_e > T_v > T_0 \approx T_i \approx T_r$) Electron energy distribution functions (EEDFs) are used to describe the electron energy populations. The EEDFs depend strongly on the electric field and the gas properties. Quasi-equilibrium systems can be described using the Maxwell-Boltzmann distribution function, shown in equation 1. Here, ε is the electron energy, $T_e$ is the electron temperature, and $k$ is the Boltzmann constant.[91]

$$f(\varepsilon) = 2\sqrt{\frac{\varepsilon}{\pi(kT_e)^3}}\, e^{-\frac{\varepsilon}{kT_e}} \tag{1}$$

The mean electron energy in the Maxwell-Boltzmann distribution is defined as follows in equation 2.[91]

$$f(\varepsilon) = \int_0^\infty \varepsilon f(\varepsilon)\, d\varepsilon = \frac{3}{2}T_e \tag{2}$$

The Maxwell-Boltzmann distribution applies specifically to a system of particles that is assumed to have reached thermodynamic equilibrium. Nonthermal plasmas can exist far from thermodynamic equilibrium, and their respective EEDFs can be vastly different from the Maxwell-Boltzmann distribution and other distributions, such as the Druvyvesteyn distribution, are commonly employed to describe non-equilibrium systems. In most systems, the mean electron energy ranges from 1 to 5 eV. Even in nonequilibrium plasmas, the average electron energy can be correlated with the reduced electric field ($E/n_0$), where $E$ is the electric field and $n_0$ represents the number density of the system. Equation 3 can be used to define the electron temperature, and this relation is in good agreement with both Maxwell and Druvyesteyn distributions, where $\delta = 2m/M$ ($m$ being the mass of an electron and $M$ being the mass of the bulk gas), $E$ is the electric field

strength, and λ is the electron mean free path.[91] The correlation is qualitatively linear, but can be more complicated in real systems.

$$T_e = \frac{eE\lambda}{\sqrt{\delta}}\sqrt{\frac{\pi}{12}} \tag{3}$$

Here, it is useful to rearrange some of the terms to define the electron temperature in terms of reduced electric field and the interaction cross section of the electron-neutral collisions, $\langle\sigma_{en}\rangle$, to yield equation 4.[91]

$$T_e = \left(\frac{E}{n_0}\right)\frac{e}{\langle\sigma_{en}\rangle}\sqrt{\frac{\pi}{12}} \tag{4}$$

*PLASMACHEMISTRY AND ELECTRON IMPACT IONIZATION*

There are several parameters that can be used in describing collisions in plasmas, including the probability of collision, the mean free path of a species (λ), interaction frequency between species (υ), reaction rates and reaction rate coefficients, and the reaction cross section (σ). Most notable of these parameters is the cross section, which can be described as an imaginary circle of area σ around a component that defines a boundary, where if another collision component crosses that boundary an elementary reaction occurs. Electron-impact cross sections as a function of electron temperature can be found for many common plasma components in the NIST Chemistry WebBook.[95, 96] The cross section can be used in the derivation of other important parameters such as the mean free path, which is the average distance traveled by a moving particle between collisions. The mean free path of A with B is shown in equation 5, where $n_B$ is the number density of species B, and σ is the cross section of component A.[91]

$$\lambda = {}^{1}/_{n_B\sigma} \tag{5}$$

The interaction frequency (υ) of A with B, where *v* is velocity, is given in equation 6.[91]

$$\upsilon_A = n_B\sigma v \tag{6}$$

This relation can also be written with a velocity distribution and with cross section dependence on velocity, shown in equation 7.[91]

$$\upsilon_A = n_B\int \sigma(v)\, v f(v) dv = \langle\sigma v\rangle n_B \tag{7}$$

The number of elementary reactions (ω) which take place per unit volume per unit time is called the elementary reaction rate, and is simply the product of interaction frequency with the number density of the component (equation 8).[91]

$$\omega_{A+B} = \upsilon_A n_A \tag{8}$$

From this, the reaction rate coefficient of an elementary reaction in electron impact driven reactions can written as shown in equation 9.[91]

$$k_{A+B} = \int \sigma(v)\, vf(v)dv = \langle \sigma v \rangle \tag{9}$$

The key process in plasmas is the conversion of neutral components into electrons and positively charged ions. In electronegative gases, negative ions can also form in appreciable amounts. The ionization events via electron impact in plasmas can proceed through one of several basic mechanisms: Direct ionization by electron impact, which can be dissociative or non-dissociative, and stepwise ionization.

**Direct ionization by electron impact** (equation 10) is the ionization of neutral and unexcited species by an electron with high enough energy to ionize in one collision.[91]

$$A + e \rightarrow A^+ + e + e \tag{10}$$

Direct ionization is most important in non-thermal discharges, where electron energy and electric field strength are high but excitation level is moderate. Occurs when the energy transferred (Δε) is greater than the ionization potential of valence electrons, *I*, with the number of valence electrons $Z_v$. The Thomson formula (equation 11) gives the ionization cross section for all values Δε > I, where *e* is the charge of an electron, *ε* is the electron energy, and $\varepsilon_0$ is the permittivity of free space.[91]

$$\sigma_i = \frac{1}{(4\pi\varepsilon_0)^2}\frac{\pi e^4}{\varepsilon}\left(\frac{1}{I} - \frac{1}{\varepsilon}\right)Z_v \tag{11}$$

If the electron energy distribution can be defined by the Maxwellian EEDF, the direct ionization rate coefficient can be calculated in terms of the electron temperature and the geometric cross section ($\sigma_0$) and mass (*m*) for the ionized atom or molecule, shown in equation 12.[91]

$$k_i(T_e) = \sqrt{{}^{8T_e}/_{\pi m}}\,\sigma_0 e^{-\frac{I}{T_e}} \tag{12}$$

The approximate geometric cross section of the ionized atom or molecule is given below in equation 13. The value for $N_2$ is approximately $10^{-16}$ $cm^2$.[91]

$$\sigma_0 = \frac{Z_v \pi \varepsilon^4}{I^2 (4\pi\varepsilon_0)^2} \tag{13}$$

**Non-dissociative ionization** occurs when electron energy does not greatly exceed ionization potential. Equation 14 shows an example non-dissociative ionization reaction.[91]

$$e + AB \rightarrow AB^+ + e + e \tag{14}$$

**Dissociative ionization** via electron impact occurs when electron energy greatly exceeds ionization potential and thus creates an excited state that results in the decay of the molecular ion (AB+)*. Equation 15 shows an example dissociative ionization reaction.[91]

$$e + AB \rightarrow A + B^+ + e + e \tag{15}$$

**Stepwise ionization by electron impact** is simply the ionization of previously excited species. Stepwise ionization is more important in thermal plasmas or systems that are in thermodynamic equilibrium and typically occurs mostly in high plasma density with high concentrations of excited neutrals. The excited neutrals can be excited again and again, eventually leading to ionization even when the electron energy is less than the ionization potential. Stepwise ionization can also occur much more readily than direct ionization when the electron energy is much less than the ionization potential. Equations 16 and 17 show stepwise ionization by electron impact with a model compound A.[91]

$$e + A \rightarrow A^* \tag{16}$$

$$e + A^* \rightarrow A^+ + e + e \tag{17}$$

Ionization can also occur via collisions with heavy particles, such as ion-atom or ion-molecule collisions, or collisions of electronically or vibrationally excited species with high enough energies to enable ionization. These ionization events are not important in most plasma systems since they do not occur easily due to the adiabatic principle. Essentially, it is difficult for high energy ions to effectively impart energy to electrons inside an atom, and the probability of this collision occurring is exponentially small until

the ion energy is about three orders of magnitude greater than the ionization potential (~10 to 100 KeV).[91]

Photo-ionization, ionization as a result of a neutral-photon collision that results in an electron-ion pair, can also occur. These events are most important in thermal plasmas and in some propagation mechanisms for nonthermal discharges.

Surface ionization from electron emission occurs when ionization is driven by electron emission from a surfaces as a result of electron, ion, and photon collisions with the surface or simply by surface heating.

Vibrational and electronic excitations play the most important role in the stimulation of endothermic processes in plasma. The vibrational excitation cross section of molecules by electron impact is given in equation 18, where *m* is mass of electron, *M* is mass of neutral, $\sigma_0$ is the gas-kinetic cross section, $\varepsilon$ is the electron energy, and *I* is the ionization potential.[91]

$$\sigma_{vib}^{elastic} \approx \sigma_0 \frac{\varepsilon}{I} \sqrt{\frac{m}{M}} \tag{18}$$

Vibrationally excited molecules can undergo elementray reactions, with rates given by equation 19. The rate coefficient of elementary reactions of a vibrationally excited molecule with vibrational energy $E_v$ and a translational gas temp $T_0$, where $\Theta$ is the Heaviside function (1 when positive inside, 0 when negative inside), $\alpha$ is the efficiency of excitation energy in overcoming the activation barrier (tabulated or theoretically calculable) and $k_{R0}$ is the pre-exponential factor.[91]

$$k_R(E_v, T_0) = k_{R0} e^{-\frac{E_a - \alpha E_v}{T_0}} \Theta(E_a - \alpha E_v) \tag{19}$$

In addition to the ionization reactions, there are also recombination and attachment reactions. Reactions that occur with positive ions are typically recombination reactions.

**Dissociative electron-ion recombination**, where the recombination energy goes into dissociation of the intermediately formed molecule and then on to the excitation of dissociation products. An example dissociation electron-ion recombination is shown in equation 20.[91]

$$e + AB^+ \rightarrow (AB)^* \rightarrow A + B^* \tag{20}$$

**Three-body electron-ion recombination**, where the third body partner is a free electron (heavy particles are ineffective third-body partners). The example in equation 21 is in an atomic gas in the absence of molecular ions.[91]

$$e + e + A^+ \rightarrow A^* + e \tag{21}$$

**Radiative electron-ion recombination**, where the recombination energy is converted to radiation. Equation 22 is an example radiative electron-ion recombination reaction.[91]

$$e + A^+ \rightarrow A + h\nu \tag{22}$$

Reactions that occur with negative ions, which regularly occur in electronegative gases, are usually attachment reactions. Dissociative attachment occurs regularly when the products have positive electron affinity. For example, the dissociative attachment of electrons is shown below in equation 23.[91]

$$e + AB \leftrightarrow (AB^-)^* \rightarrow A + B^- \tag{23}$$

The dissociative attachment rate coefficient, $k_a$, can be approximated as a function of the resonance parameters for dissociative attachment (equation 24). The parameters $\varepsilon_{max}$, $\Delta\varepsilon$, and $\sigma_{d.a.}^{max}$ can be calculated but are also tabulated and are 6.7 eV, 1 eV, and $10^{-18}$ $cm^2$ for the dissociative attachment of $O_2$, respectively.[91]

$$k_a \approx \sigma_{d.a.}^{max}(\varepsilon_{max}) \sqrt{\frac{2\varepsilon_{max}}{m}} \frac{\Delta\varepsilon}{T_e} e^{-\frac{\varepsilon_{max}}{T_e}} \tag{24}$$

Three-body electron attachment, occurs readily at pressure above 0.1 atm and when the electron energies are not high enough for the dissociative attachment.[91] Equation 25 is an example three body electron attachment reaction.

$$e + A + B \rightarrow A^- + B \tag{25}$$

The specific example of three-body attachment with oxygen is important in atmospheric-pressure non-thermal discharges in air and oxygen.[91] This reaction is shown in equation 26.

$$e + O_2 + M \rightarrow O_2^- + M \tag{26}$$

This process proceeds via the two-stage Bloch-Bradbury mechanism, and starts with the formation of a negative ion in an unstable auto-ionization state (equation 27), where $\tau$ is the time of collisionless detachment.[91]

$$e + O_2 \xrightarrow{k_{att},\tau} (O_2^-)^* \quad (27)$$

The second stage of the Bloch-Bradbury mechanism includes collisions with the third body particle M (number density $n_0$), leading to the stabilization (equation 28) or collisional decay (equation 29) of the unstable ion.[91]

$$(O_2^-)^* + M \xrightarrow{k_{st}} O_2^- + M \quad (28)$$

$$(O_2^-)^* + M \xrightarrow{k_{dec}} O_2 + e + M \quad (29)$$

Taking the two steps into account, the rate coefficient for the total attachment process is given by equation 30.[91]

$$k_{3M} = \frac{k_{att}k_{st}}{\frac{1}{\tau} + (k_{st} + k_{dec})n_0} \quad (30)$$

This reaction rate coefficient for electron attachment is tabulated[91] for different three-body partners, and for $O_2$ is greater than $10^{-29}$ $cm^6/s$ for methane, $1.6 \cdot 10^{-31}$ $cm^6/s$ for nitrogen, and $2.5 \cdot 10^{-30}$ $cm^6/s$ for $O_2$ as third-body partners. The rate for three-body attachment processes is greater than dissociative attachment once the gas number density reaches a certain threshold value. For oxygen, this value is for a number density greater than $10^{18}$ $cm^3$, which corresponds to a gas pressure greater than 30 torr.[91]

### *TYPES OF ELECTRICAL DISCHARGES*

In discussing electrically generated plasmas, it is useful to first briefly cover fundamental discharge modes in DC discharges. When a voltage high enough to cause electric breakdown is applied to a discharge gap, the different fundamental discharges modes can be segregated in terms of current density. These current-voltage relations for simple DC discharge systems can be seen in figure 4.

At very low currents, the discharges start as intermittent current pulses owing to the random action of external ionizing sources such as x-rays and cosmic rays. When the current is allowed to increase, these current pulses reach a saturation point and, with increasing current, eventually transition from externally sustained driven discharges to self-sustained electron avalanche discharges (Townshend discharge). All of the discharges up until this point operate in what is commonly referred to as the dark discharge regime. At higher discharge currents, the self-sustained discharges begin to

emit light, and at this point they enter the glow discharge regime. In highly non-uniform electric fields and at high pressures the corona discharge is the first to form, while the glow discharge is the first to form in low pressure environments. As current continues to increase the normal glow discharge transitions to the abnormal glow discharges, and finally to the arc/spark discharge.[97] Transition from the intermittent to the steady state is sometimes rapid and is described as the onset of steady discharge.[98] It is immediately apparent that these relationships are highly dependent on gas pressure, but also on the geometry of the electrode system, which has a direct impact on the electric field of the system.

It is useful to list some commonly encountered definitions here, most of which are taken or adapted from *Fundamentals of Gaseous Ionization and Plasma Electronics* by Nasser.[99]

**Geiger Regime**– under a constant radiation level, current increases with voltage until a plateau known as the saturation current is reached. Intermittent irradiation will change the current, and this regime is referred to as the Geiger regime. All current is a consequence of external volume ionization. (current pulses less than $10^{-16}$ amps)

**Townsend Discharge** – After the Geiger regime, increasing voltage does not affect current until some point where the current increases exponentially, to the $10^{-12}$ amp regime. Ionization as a result of collision starts to occur.

**Electron avalanche**–the process of one accelerated free electron colliding with gas molecules and causing further ionization, with the number of electrons increasing continuously from the cathode to anode.

**Breakdown**– collapse of voltage across the gap accompanied by an over exponential increase in current as a result of a rapid change in the electrical resistance of the gap. Current becomes independent of external radiation and is referred to as self-sustained. There are two fundamental mechanisms that describe the breakdown.

> **Townshend breakdown mechanism**– electron avalanche mechanism for discharge, collision of accelerated electrons with gas molecules yield further ions. Accurately describes many phenomena, but has some limitations, most

noteworthy is that the formation of self-sustaining discharge occurs much faster than the Townshend model can predict in some cases.

**Streamer breakdown mechanism** – during the electron avalanche, gas molecules are being excited as well. As these molecules return to ground state, they emit photons that head in all directions and are absorbed varying distances from their origin. Some of these photons lead to photoionization which creates photoelectrons that are available in the gas but separate from the original avalanche. This process creates auxiliary avalanches. The auxiliary avalanches all have the ability to create third generation avalanches, and this behavior leads to the branching that is often seen with streamer formation. This explains the limitations of the Townshend mechanism, where only one point of avalanche origin is considered.

**Corona discharge** – any manifestation of locally confined ionization and excitation processes that occur before the complete voltage breakdown between electrodes, associated with non-uniform electric fields where the local potential is strong enough to create ionization events but not strong enough to cause arcing/sparking across the gap. Partially overlaps with the definition of glow discharge.

**Glow discharge** – generic term for any gaseous electrical discharge that produces luminosity, most commonly applied to continuous, low power plasmas that exhibit traditional "glow discharge" qualities, namely (1) Aston dark space (2) Cathode glow (3) Cathode dark space (also called Crookes dark space, or Hittorf dark space) (4) Negative glow (5) Faraday space (6) Positive column (7) Anode glow (8) Anode dark space

**Spark** – short lived plasma channel with high current density

**Arc** – a continuous plasma channel with high current density

**Onset voltage** – voltage at which specific phenomena occur in a system. Corona onset occurs where the system exhibits a corona.

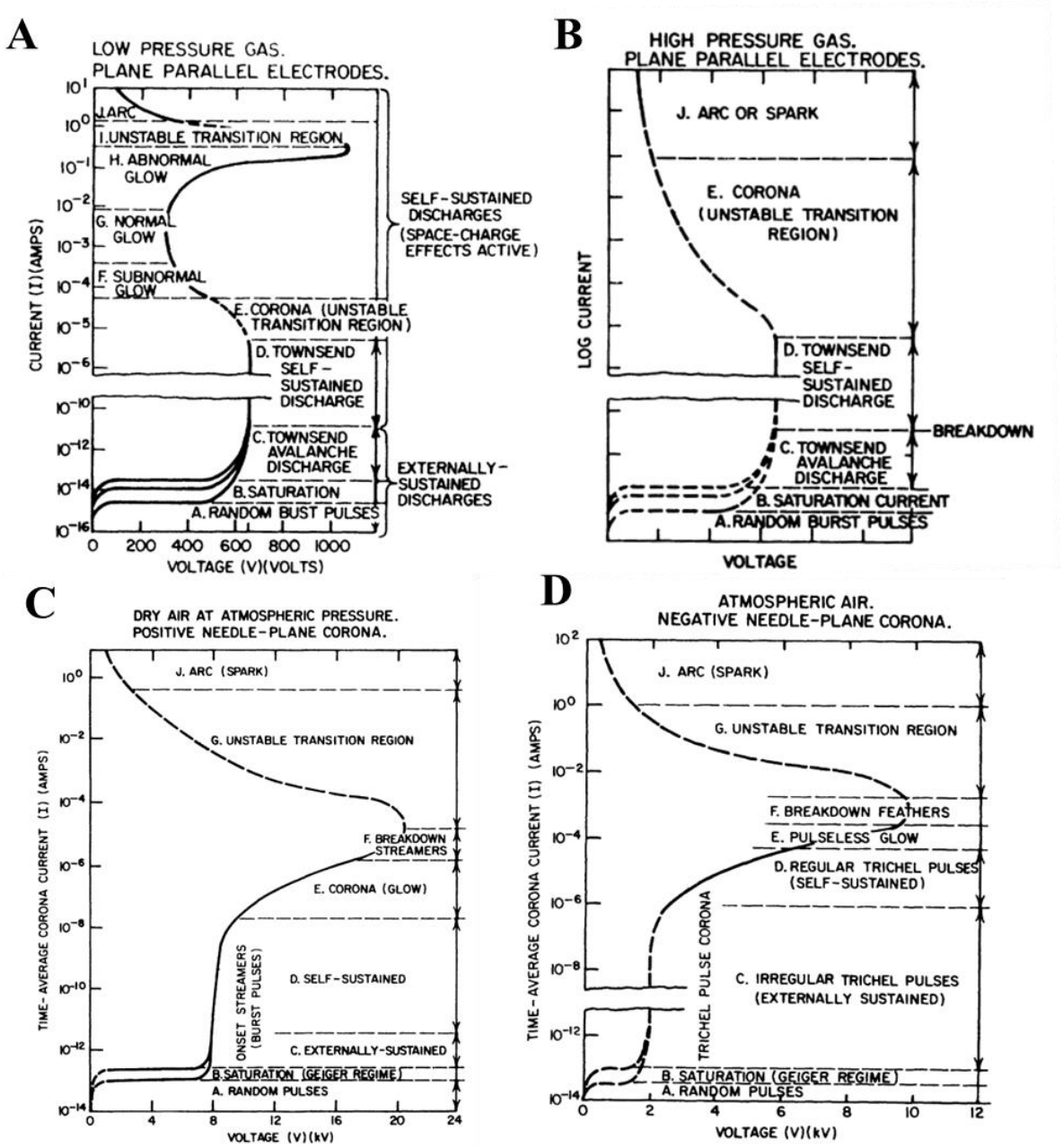


Figure 4: Representative current-voltage relation for DC discharges. Curves are shown for discharges in A) low pressure neon (1 torr) with 2 cm disk electrodes at 50 cm gap spacing and B) high pressure (1 atm or greater) gases between plane-parallel electrodes with a current-limited DC voltage. Current-voltage relation for dry air in an atmospheric pressure needle-to-plane geometry with C) positive DC voltage applied to the needle with 0.5 mm tip radius and gap spacing of 8 cm and D) negative DC voltage applied to the needle with 6 mm gap spacing (insensitive to needle radius between 0.003 and 0.05 mm). These figures are collected and compiled from *Coronas and gas discharges in electrophotography* by Gallo[113] (© 1975 IEEE) and built upon data and figures in *Fundamentals of Gaseous Ionization and Plasma Electronics* by Nasser.[112]

The voltage-current curves shown in figure 4 are useful tools in understanding how DC generated plasmas behave, especially nonthermal plasmas in non-uniform electric fields as shown in Figure 4C and 4D. These curves also eloquently differentiate the operating regimes of the low pressure and atmospheric pressure plasmas. However, it is important to note that these curves are generated in a very specific system and are only generally representative. While the different types of electrical discharge can be vastly different in properties and performance, they all share similar trends in the voltage current relationship. It is worth noting explicitly that the corona and glow type discharges are not stable in plane parallel systems at high pressure (fig. 4B), as their formation typically requires either low pressure environments (fig. 4A) or highly non-uniform electric fields (fig. 4C and 4D). The unstable transition regime shown in figure 4B-D can exhibit a stable region for microplasma systems with very small discharge gaps.

Both the spark and arc discharges are typically thermal plasmas, but are not necessarily thermal in nature. The corona discharge is the classical example of nonthermal plasma, and is closely related to the glow discharge. The current density increases from the corona to the glow, and these nonthermal plasmas are usually lower in electron energy distribution but not necessarily lower in electron density. Either of these modes of plasma may become thermal with increasing energy density. The glow discharge has traditionally implied low pressure operation, but more recent work in the field has definitively show that the glow discharge can operate at atmospheric pressure.

The dielectric barrier discharge (DBD) is a special case, and is the name given to plasmas that employ a dielectric material covering all or part of an electrode material and an applied electric potential at frequencies that range from kHz to MHz. DBD is a type of electrically generated plasma but not a fundamental plasma mode as it can occupy any of the fundamental forms that nonthermal plasma typically displays, including filamentary streamer formation, corona, glow, and diffuse glow forms, as shown in figure 5.

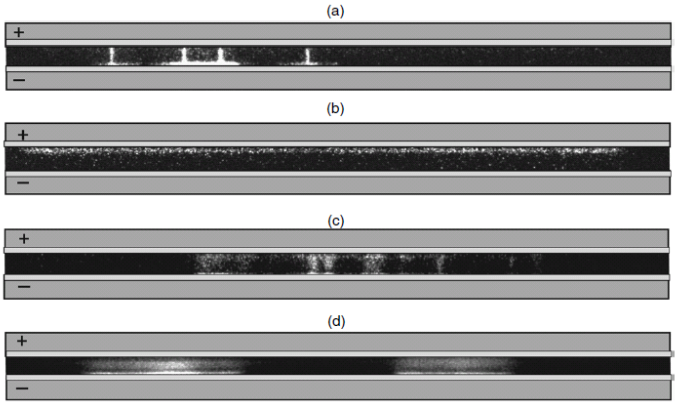


Figure 5: Images of different plasma modes in a DBD system. (a) Stationary filaments; (b) Townsend discharge; (c) non-stationary microdischarges; (d) glow discharge. The discharge gap is 0.9 mm and the lateral electrode size is 40 mm. In all images, the instantaneous anode is positioned at the top while the instantaneous cathode is at the bottom. Exposure time is 5 ns for each image. (© IOP Publishing. Reproduced with permission. All rights reserved. doi:10.1088/0963-0252/18/4/04502)[100]

## Microplasmas

In general, microplasmas provide enhanced stability, increased nonequilibrium properties, and better energy efficiency than macroscale plasmas. These properties make microplasmas a promising tool for plasmachemical processing pathways, and as such have been used in the synthesis of aerosol nanoparticles (NPs), nanostructured thin films, nanocomposites, carbon nanotubes, and colloidal NPs.[56] Microplasmas have also been used in $NO_x$ and $SO_x$ remediation, VOC destruction, bio-decontamination, sterilization, and in gas and surface analysis.[101] In addition, it has been suggested that microplasmas have favorable properties as visible/UV emission sources, as photodetectors, and in decontamination, surface modification, etching, film deposition, and plasmachemical synthesis.[75, 102]

There are three major considerations to account for in a thorough discussion of microplasma generation and utilization. These are: (1) the spatial scale at which the plasma is generated, (2) the time scale for plasma initiation and sustainment, and (3) the geometry and properties of the electrodes used in the system. Adjusting these three properties of the microplasma system gives rise to a high level of control of plasma properties. Highly controlled plasmas permit chemical processes to be selectively driven in a desired direction, with a certain level tunability in reaction mechanism and product distribution.[91]

*MICROPLASMAS AND SPATIAL CONFINEMENT*

Studies have shown that there are definite benefits to confining atmospheric pressure plasmas in small physical spaces. As the size of the generated plasma decreases, the surface area to volume ratio increases. This ratio has implications in the energy balance of the plasma system and the corresponding energetic stability of the plasma.[56] On the microscale, plasma-surface interactions become important, where improved heat and energy transfer to surfaces result in enhanced plasma stability and an overall increase in energy efficiency.[101, 103] The transition from glow to arc discharge can be avoided with small spatial dimensions.[75] Physical confinement has a strong influence on the energy distribution among different species in the plasma (electrons, ions, neutrals, etc.) and on the physical structure of the plasma.[56] Figure 6 depicts the atmospheric pressure glow discharge at varying electrode spacings. The negative glow region near the bottom electrode (cathode) in figure 6 fills nearly the entire discharge volume at a discharge gap of 100 microns.

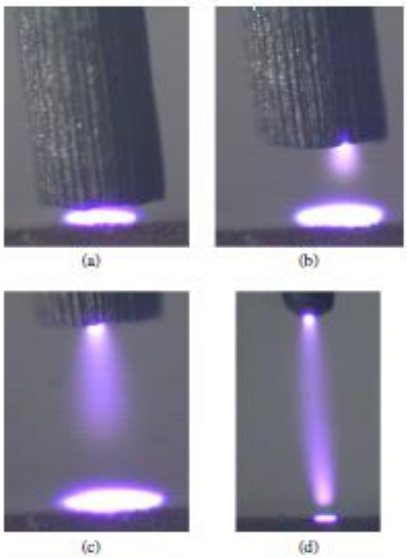


Figure 6: Images of the atmospheric pressure glow discharge in air. Shown at discharge gaps of a) 0.1 mm, b) 0.5 mm, c) 1mm, and d) 3mm. (© IOP Publishing. Reproduced with permission. All rights reserved. doi:10.1088/0963-0252/14/4/009)[104]

Electrical plasmas have a classically well-known interplay between pressure and distance. The type and stability of the discharge has a direct impact on the spatial distribution of energetic electrons. Since both the type of discharge and discharge stability strongly depend on the pressure-distance product (*Pd*), spatial considerations are

critical when designing microplasmas at atmospheric pressure.[105] The current-voltage characteristics of the space scales for wire point to plate geometry have been explored near the Paschen minimum (from ~20μm to 1.5mm).[104] Shrinking space scales and rising pressure leads to situations where the dimensions of the device approach the mean free path of electrons and the Debye length of the plasma, and at this point traditional concepts like breakdown and scaling laws may no longer apply.[75] Effects such as field emission and electron tunneling start to cause substantially different plasma behavior at lower breakdown voltages, and this behavior can be drastically altered by small changes in operating parameters.[75] The characteristics of these microplasmas are also highly dependent on input power, electrode geometry, gas composition, and space velocity.[56]
It has been shown that as the size of a microplasma decreases, the gas temperature and electron temperature diverge from one another, as illustrated in figure 7.[106] This allows for chemical reactions to be driven by the electron temperature while the temperature of the bulk media and heavier species remains at or near room temperature. The spatial scale itself stabilizes the microplasma while the external circuit reactance and the power supply also interact with the distance scale at atmospheric pressure to reduce or impart thermal stability.[107]

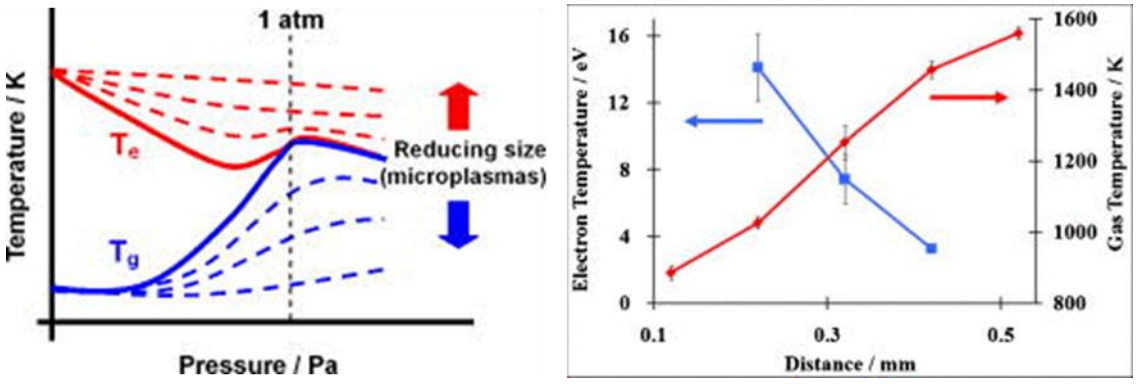


Figure 7: The spatial scale of the discharge can directly impact the energy distribution of excited species. Left) Electron and gas temperature divergence with decreasing microplasma size. Right) Also from "Nonequilibrium and effect of gas mixtures in an atmospheric microplasma", effect of discharge "height" on *effective* gas temperature and electron temperature in a 450 MHz plasma at a power of 7W. (Reprinted with permission from "Nonequilibrium and effect of gas mixtures in an atmospheric microplasma", *Applied Physics Letters* Copyright 2008, AIP Publishing LLC.)[106]

Evidence suggests that there are two distinct groups of electrons with mean energies of 0.6 eV and 5 eV, where the electron density is on the order of $10^{15}$ $cm^{-3}$ in DC

discharges.[105] Observations in various gas microplasmas show that the gas temperature is dependent on the gas studied and its pressure.[105]

### *Microplasmas and Temporal Restriction*

Plasmas are complicated, multi-component systems, where the different components can accumulate energy at varying rates and propagate through the discharge at different speeds. The timescale in plasmas can span multiple orders of magnitude, ranging from the accumulation of energy in plasma components to the chemical reaction kinetics of the processes that the excited species are driving. As a result, the time scale for the electrical properties of the plasma can be of significant interest, particularly in the interactions between the electrical properties of the discharge and the lifetimes for physical and chemical processes that occur in the plasma.

Plasmachemical systems and fundamentally multi-timescale and span several orders of magnitude, as shown in figure 8. The figure provides a simple visualization of the characteristic time scales of the physical and chemical processes that occur in plasmachemical systems.

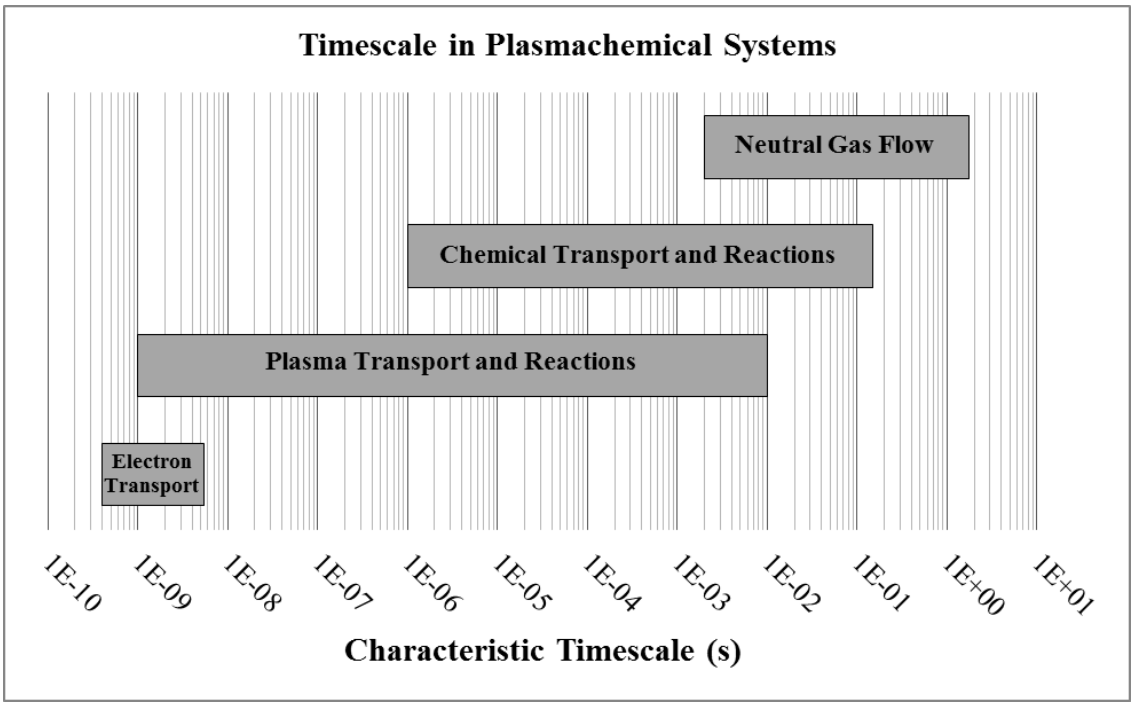


Figure 8: Characteristic timescale for reactions and transport phenomena ins plasmachemical systems, reproduced combining information from a paper on plasma modeling by Farouk et al.[108] and the COMSOL Plasma module user's guide.[109]

When discussing electrically generated plasmas, the time scale for the electric field generation is usually controlled via the frequency of applied electric potential. Simple DC generated corona discharge plasmas can have inherent pulsing frequencies on the order of 1 to 1000 Hz, but most electrically generated plasma studies that discuss pulsing frequency do so in the context of applied pulse frequency modulation.[99] The pulse frequency is typically slow compared to the time scale required for the plasma to develop during a pulse. The partially ionized filament from the previous discharge can interact with the next discharge. This has the net effect of increasing the charge density and can change some of the fundamental properties of the plasma and can even change the mode of the plasma. In microreaction volumes, extremely fast residence times with commonly encountered flow rates can lead to residence times that are as fast as or faster than excited species transport in the plasma. For this reason, the timescale for plasma generation and sustainment becomes important in determining the chemical processes that occur in the plasma.

In both DC and AC circuits, the discharge frequency can change the discharge from glow or corona modes to spark or arc modes just as does applied electric potential, and this relationship can be visualized in figures 9 and 10.

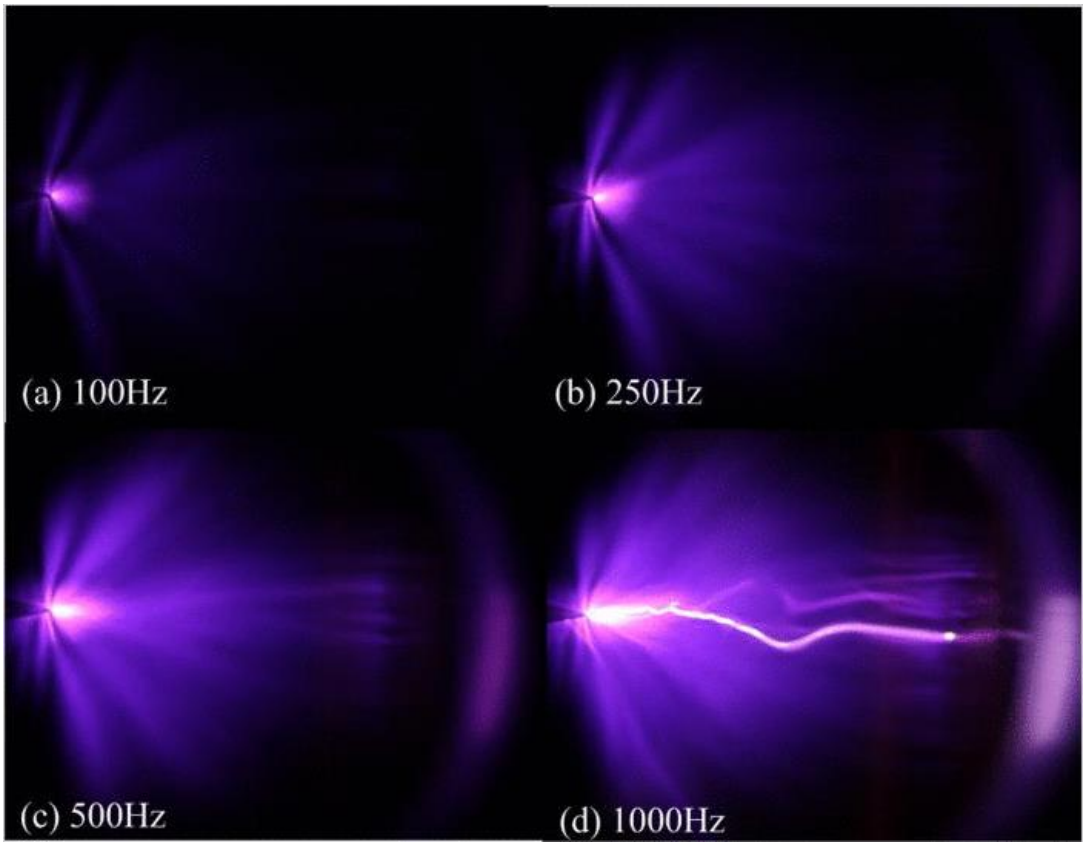


Figure 9: Images showing the appearance of discharges with varying pulse repetition frequency at 120 kV in atmospheric pressure air with an 8 cm discharge gap. The applied nanosecond pulses had a rise time of 15 ns and a FWHM of 30-40 ns. a) corona mode, b) and c) discharges bridge the gap and the authors describe the discharge as being in "diffuse mode", d) gap bridged by one spark channel along with diffuse discharge.[110](Reprinted with permission from "Diffuse discharge produced by repetitive nanosecond pulses in open air, nitrogen, and helium", *Journal of Applied Physics.* Copyright 2013, AIP Publishing LLC.)

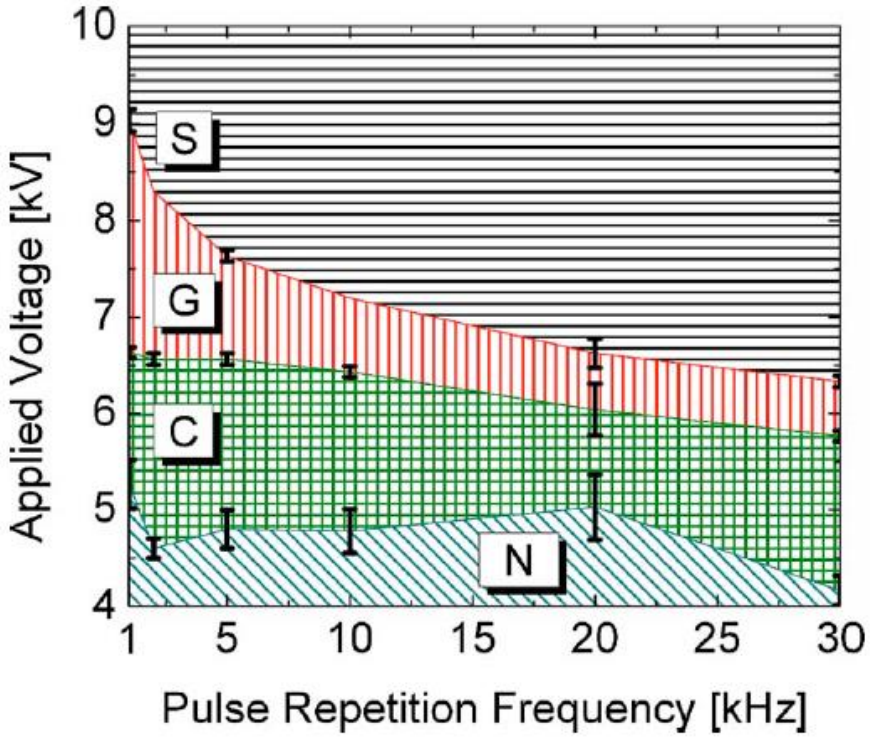


Figure 10: Fundamental discharge mode dependence on applied potential and the frequency of applied 10 ns potential pulses, where S = spark, G = glow, C = corona, and N = no discharge. This map is generated in 1000K air flowing at 1.6 m/s in a discharge gap of 5 mm. (Reprinted with permission from "Transitions between corona, glow, and spark regimes of nanosecond repetitively pulsed discharges in air at atmospheric pressure", *Journal of Applied Physics*. Copyright 2010. AIP Publishing LLC.)[111]

One strategy to temporally control and tailor plasma modes is to reduce the pulse duration to the nanosecond timescale at several hertz. This inhibits each discharge from fully developing and prevents interaction between different discharges. In nanosecond DC pulsed discharges, the frequency of the applied electric potential is very closely related to the type of discharge mode, as are applied potential, discharge gap length, and system geometry.[110, 111] This has been demonstrated at 5mm with pulsed glow discharges at atmospheric pressure.[112] This effect has been observed with a 45 kV signal from 100 to 1000Hz with pulse duration of 100ns for separation gaps of 4.5 cm to 2 cm.[113] Figure 5 shows the transition of the discharge from corona to sparking by changing the frequency of applied potential from 100 Hz to 1000 Hz, demonstrating visually that applied frequency and the timescale of the discharge directly affects the properties of the

generated plasma. Several discharge pins have also been able to generate stable diffuse glow with 30 ns, 28 kV pulses at 90Hz operation in ambient conditions at the 1mm scale.[114]

One study investigating methane oxidation in pulsed nonthermal plasma showed the generation of ~6% liquid oxygenates at moderate pulsing frequencies.[9] However, at low and at high pulsing frequencies, the production of liquid oxygenates disappeared, which may be indicative of the physical construction of the plasma interacting with excited species from previous discharges at moderate pulsing frequencies. However, it is certainly possible that different modes or types of non-thermal plasma lend themselves to certain reactions through the necessary impact ionization or photo-ionization processes which are required for certain radical intermediates.[9]

The diffusivity and homogeneity of the non-thermal plasma can be fundamentally influenced by using nanosecond pulsed dielectric barrier discharge.[115] The more uniform nanosecond dielectric barrier reactors have reported improvements in the partial oxidation of methane to methanol at one pass yields of 10% at 25°C and atmospheric pressure in a reproduced experiment in a 1mm diameter flow-through glass tube.[116] Pulse widths of 600ns or shorter are required for primary mode discharge generation of glow non-thermal plasma using a 6mm gap and DC pulsed waveforms at a pulse frequency of 1kHz. The applied waveform affects the discharge current significantly if shorter than 600 ns.[117] Dielectric barrier discharge driven with DC excitation nanosecond pulses is inherently more efficient than AC excitation because of energy deposition and the higher reduced electric field from overpotentials.[118] DC pulsed operation of microdischarge non-thermal plasma at nanosecond temporal scales is two to three times more efficient than standard DC operation.[119]

### *MICRO- AND NANO-STRUCTURED ELECTRODES*

The behavior of electrical discharges, especially discharges that form in highly non-uniform electric fields such as the corona discharge, depends highly on the geometry of the electrode system. This geometry includes the relative size and shape of the electrodes, in addition to the spacing between each electrode. For relatively uniform electric fields, an applied potential will be reached at which a spark will form and create a plasma channel for charge flow. In highly non-uniform electric fields at certain electrode separation distances, accelerated free electrons near the "sharp" electrode will begin to ionize gas molecules before the potential at which spark-breakdown occurs for the entire electrode gap. In addition to effects associated with electrode geometry, electrode material and the micro/nanostructure of the electrode play a large part in the specifics of electric breakdown and in determining the fundamental mode of the discharge. The different modes each have their respective energy distribution, electron density, temporal development rates, and spatial patterns.

The creation of either nano or micro structures on electrode surfaces provides several benefits in the generation of nonthermal plasma, and a variety of techniques to modify electrode surfaces to achieve enhanced performance have been investigated. High aspect ratio materials, such as carbon nanotubes, silicon nanowires, or patterned arrays of microstructures, can create extremely strong electric field gradients, which in turn enable plasma inception at reduced total applied electric potential. Research has also shown that these nanostructured electrodes allow for discharges to occur more frequently and with a higher degree of uniformity. These enhancements yield increased energy efficiency and improved performance in nonthermal plasmachemical reactions.

Multi-walled carbon nanotube enhanced electrodes are able to generate pulsed corona discharge at 365 V DC and a gap separation of 40 μm.[120] Pulses occur on the order of once every 50 μs (20 kHz) with carbon nanotube electrodes, and on the order of once every 100 μs (10 kHz) with plain aluminum electrodes.[120] Carbon nanofiber and tungsten oxide nanowire modified electrodes have also successfully enhanced microplasma reactor performance.[121] These modifications result in a reduction in the breakdown voltage and an increase in the frequency of microdischarges when an unmodified DC potential is

applied.[121] The lowered onset voltage coupled with increased discharge frequency results in higher power input to the reaction volume at the same potential compared to flat plates.[121] Silicon nanowire electrodes have demonstrated breakdown in atmospheric air at 38 volts and 1.5 $E^{-7}$ amps with a gap width of 0.5 μm.[122] The emissive characteristics of nanoscale features have long been studied with applications in sensing and optics, and have only recently begun generating increasing interest for chemical conversion applications.

Dielectric barrier discharge with modified electrodes has operated successfully at the 1 to 2 mm scale using widely available fabrication techniques. The application of nickel oxide nanowires significantly reduces the inception electric potential for the formation of non-thermal plasma.[123] This allows stable operation at the macroscales or increased efficiency and stability at the microscale. Hydrogen production under dielectric barrier discharge in a discharge gap of 10 mm using nickel oxide nanorods chemically converts methane at selectivities near 100%.[123]

Nano and microsctructures that function as field emitters provide multiple, equally well defined discharge points which collectively intensify local electric fields. These locally-intensified electric fields at the structured electrode enable breakdown at lower potentials and, as a result, then define macroscopic electrical breakdown. The inception electric field requirement for stable DC glow discharge is reduced and the glow region physically widens with increasing electric potential when using 1D nanostructured emitter electrodes, where uniform glows of $1cm^2$ in area are sustained by 300V to a Paschen minimum of 0.1Torr-cm.[124]

Nanotube bundles have been used to provide electron emission at low fields of 1V/μm.[125] These nanostructures can be the basis for pixelated flat panel displays.[126] The cold cathode emission of carbon nanotube in polymer composite matrixes also displayed emission characteristics which were altogether unique to these nanomaterials.[127] An eighteen percent increase in photonic emission for a total radiative efficiency of 8.8% at 700Torr has been demonstrated for noble gas light emitting microplasmas. The inception voltage is 220V for a 200μm microplasma device.[128] Increases of 6-9% in the 300-800nm wavelength emission can be achieved using carbon nanotube electrode emitters.[129] Metal

oxide nanowires have also been utilized with dielectric barrier discharge in a discharge gap of 500μm.[121] Figure 7A shows the surface glow on a stainless steel cathode covered with carbon nanotubes. The emissive characteristics are generally improved, and figure 7B demonstrates the increase in emission of the Hα line. There is evidence that carbon nanotubes are degraded in the presence of oxygen plasmas, so metal and metal oxide nanostructures are of particular interest for future efforts.[130]

Microelectromechanical systems (MEMS) devices are usually designed and fabricated with micron size geometries, and as a result these devices often experience failure as a result of the electric breakdown of gases on the microscale.[131] Significant deviations from Paschen's law are observed at smaller gap widths approaching 5 μm and smaller, likely as a result of the electric field becoming strong enough to induce strong field emission.[131-133] Other work using various structures and curvature of MEMS structures suggest that these deviations from the Paschen curve might be driven by the Townsend discharge process rather than field emission.[134] The conclusion can be reached that at smaller gap distances (around 5 μm), field emission becomes an important effect when using metal electrodes, but is much less important when using other materials like silicon. It has been suggested that the Townsend mechanism is not sufficient in explaining breakdown behavior in microgaps and that quantum-tunneling of electrons from metal electrodes must be considered, in addition to ion-enhanced field emission.[135] Inter-digitated and comb-like microplasma generator designs have also been investigated, where titanium electrodes and titanium electrodes treated with diamond-like graphite and nitriding treatments have been studied.[136, 137] These designs have potential to operate below the classical breakdown criteria and thus utilize less energy and be suitable for use as miniature mass spec, gas sensing, and microscale electrohydrodynamic applications.[136] Modified titianium electrodes have demonstrated longer lifetimes than pure titanium.[136, 137]

### *Chemical Processes in Microplasmas*

The use of microplasmas in volumetric chemical processing is still a relatively unexplored field. There have been several studies using microplasma reactors for chemical conversion, but they rarely focus on how plasma operating parameters and

specific microplasma properties affect chemical conversion, selectivity, and energy efficiency in driving chemical reactions. Beyond the stability and efficiency advantages of microdischarges, there exists the potential to adjust reactivity and selectivity of desired chemical reactions along with microplasma properties. In the body of research work done in the field of plasmachemical reactions, there is evidence to suggest that changes in temporal and spatial parameters of plasmas on the microscale has a direct impact on chemical conversion and the distribution of products.

Nonthermal plasma reactors have been used to generate ozone for many years. Recently, nonthermal microplasma reactors have been investigated for ozone production, with an example reactor shown in figure 11. The microplasma ozone generator, where each channel is 200 μm in width and 3 cm long, can produce ozone at rates and energy efficiencies that meet or exceed the performance of conventional DBD or corona ozone reactors.[103, 138] These microplasma ozone reactors are also considerably smaller than traditional ozone production systems, and offer a full order of magnitude reduction in volume along with considerable reductions in weight.

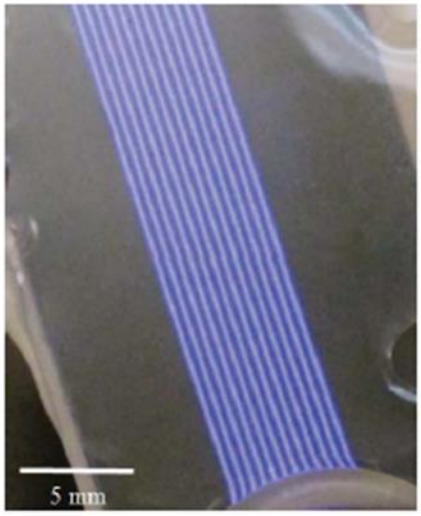


Figure 11: Photograph of an array of 12 microchannel plasma ozone generating devices operating in oxygen at 1 atm with a 0.5 slm flowrate. Each channel is fabricated in nanoporous alumina and has a width of ~200 μm and a length of 3 cm. Borrowed with permission from Plasma Science and Technology in the Limit of the Small: Microcavity Plasmas and Emerging Applications[103] (© 2013 IEEE). This device is discussed in more detail in Efficient generation of ozone in arrays of microchannel plasmas by Kim et al.[138]

Kinetics studies on microplasma ozone reactors shows the potential for increased yield at lower powers compared to traditional nonthermal plasma reactors.[139] Kinetic modeling of the plasmolysis of water vapor also shows competitive energy efficiency to traditional methods, along with reduced equipment size.[71] These kinetic studies suggest that microplasmas should be effective and efficient in driving reactions as long as the reaction rate of the desired reaction is faster than the ambipolar diffusion times (10 to 100 ms) in the submillimeter microplasma zone.[139]

Studies of methane partial oxidation in nonthermal plasma reactors have shown that increases in the reduced electric field strength can shift the products of reaction.[8] Higher amounts of methanol were created in the direct partial oxidation of methane in stronger electric fields, suggesting that higher average electric field strength and smaller discharge gaps lead to higher methanol yield.[140] It has been suggested that no methanol formation will be seen below an electric field strength of 21.3 kV/cm, and that the yield of methanol in the products increases with increasing electric field strengh.[141] Other works in methane conversion to hydrogen in nonthermal plasmas reach maximum hydrogen yields at higher electric field strengths in discharge gaps around 500 μm, suggesting that increased electric field intensity can influence both conversion and selectivity.[142] [143] Larkin and Chen both demonstrated higher selectivity (~20%) and yield for methane partial oxidation to methanol (~0.3% improvement to 2.2%) with diminishing plasma spatial scales at room temperature and near atmospheric pressures for dielectric barrier discharge at 1mm scales.[144]

Single step methane conversion into synthetic fuels in a microplasma reactor using methane, oxygen, and water has been investigated with single pass methane conversion of 40%. Syngas and liquid oxygenates (methanol, formaldehyde, and formic acid) were obtained at low operating temperatures.[145] Micro Hollow Cathode Discharge (MHCD) has demonstrated 50% methane conversion with solid carbon, $H_2$, $C_2H_2$, $C_2H_6$, $CO_2$ as products.[146] Using a MHCD in a 200 μm space, Hsu and Graves showed that a microplasma reactor induces significant chemical modifications with both ammonia and carbon dioxide as reactant gases.[147] The observed chemical decomposition rates are equivalent to thermal decomposition at temperatures above 2000 K. Qiu et al. performed

similar work decomposing $NH_3$ in a MHCD reactor to generate $H_2$, and achieved conversions of about 20% in a residence time of 5 μs.[148] Microplasma carbon dioxide decomposition in microchannel reactors using DC voltage less than 800 V and less than 12 mA with gaps of 25 or 100 μm has also been demonstrated.[149] Device lifetime, from seconds to a few hours, induces variability in reaction outcomes. It has been suggested that conversion is directly linked to input power, more specifically to specific energy input (the ratio of input power to gas flow rate).[149] For $CO_2$ decomposition, 100% conversion could be reached at an input energy of 400 J/mL, yielding an energy efficiency of 3.16%.[149] Specific energy input can potentially be much higher when reaction volumes are smaller, which provides motivation for generating plasmas at the microscale. Improved $CO_2$ conversion has been demonstrated by using enhanced electrodes.[121]

The volume to surface ratio of the discharge significantly affects the performances of the microplasma system in terms of reactivity and energy efficiency in methane processing.[78] The microscale promotes the effect of surfaces and diminishes the impact of volumetric considerations. Beyond the fact that the discharge can be stabilized by transferring thermal energy to reactor walls, the reactor walls themselves can participate directly in reaction pathways. In both plasma chemical ammonia synthesis and methane partial oxidation, it has been shown that the material properties and temperature of reactor walls directly affect the selectivity and conversion.[8, 47]

Capillary plasma electrode (CPE) discharge can successfully decompose model VOCs toluene, ethylbenzene, and m-xylene.[150] Microplasmas have also been shown to be effective in the synthesis of high-quality nanomaterials, including metals, semiconductors, oxides, and bimetallic or alloyed nanoparticles.[151] The development of the non-thermal plasma at microscales is receiving attention in order to accurately characterize the microplasma process and observe intermediates as they pertain to chemical conversion.[152]

## Conclusion

Overall, the field of chemical reaction engineering using microscale nonthermal plasmas has not been extensively studied. Many publications study nonthermal plasmas that are

generated at centimeter and millimeter scales, and the these works generally show that plasmas generated on the microscale provide enhanced stability, improved excited species density, increased nonequilibrium properties, higher electron temperature, and better energy efficiency along with reduced onset voltages. Little attention has been given to DC or DC pulsed non-thermal plasma at low electric potentials at confined (10 to 500μm) spatial scales for chemical conversion. Generally, nonthermal plasmas meet or exceed the performance of traditional chemical processing systems, while microplasmas have shown the potential to outperform macroscale nonthermal plasma chemical systems. Of the studies that use microplasmas to drive chemical reactions, many report improved conversion, higher selectivity towards desirable products, and increased energy efficiency.

Electric field strength, and thus the energy distribution among excited states, can directly affect product selectivity in nonthermal plasma systems. This adds further motivation to generating these plasmas at the microscale, where small adjustments in geometry and applied potential can greatly impact electric field strength while maintaining energy efficiency.

Plasmacatalysis is an effective method to improve yields and to tailor selectivity to desired products. In nonthermal plasma reaction systems, the materials of construction seem to directly affect reaction products. This further suggests that catalysis combined with plasma processing could be very effective at the microscale. Surface interactions become important in imparting energetic stability to plasmas generated at the microscale, and since the walls and surfaces affect product distribution, this synergistic effect could be engineered to not only stabilize the active plasma but also tune reactions to yield different products.

The generation of nanoparticles and nanomaterials using nonthermal plasmas benefit from improved quality, higher crystallinity, and enhanced properties in catalysis and semiconductor devices. Plasma processing appears to be capable of generating novel particle morphologies. It is possible that other material properties could be adjustable based on plasma parameters.

The frontier of low energy, non-thermal plasma chemical processing appears to be in confined microscale technology utilizing pulsed nanosecond power. The question still remains as to whether discharge regime and electrical properties of the plasma can be used to control chemical reaction pathways. Future studies should focus on the depth analysis of the relationship between plasma operating parameters and the effect they have on chemical reactions driven in nonthermal plasmas, namely reaction mechanisms, reaction kinetics, and chemical conversion and product selectivities.

# Materials and Methods

## Procedures

### *Methane Partial Oxidation*

The gas phase, flat plate microreactor consists of two electrode plates (corrosion resistant 316 stainless steel, 1 1/16" x 2" x 1/8" thick), each connected to terminals of the power supply (Glassman High Voltage Series EQ 10 kV Power Supply) and separated by a Teflon ® PTFE spacer (250 μm or less), sandwiched between impact resistant polycarbonate support plates (2" x 3" x ½" OR 3" x 4" x ½"). Both stainless steel plates are cleaned to ensure a clean reaction environment and to improve the adhesion of deposited materials (see Stainless steel cleaning procedure) One of the stainless steel plate electrodes is first coated with a thin film of nickel via electroplating, and then multiwalled carbon nanotubes are grown on the surface to enhance the electric field gradient around the electrode and enable electrical breakdown at lower potentials (see Ni Electroplating Procedure and Carbon Nanotube Growth Protocol). The flat plate reaction system is shown in figure 12.

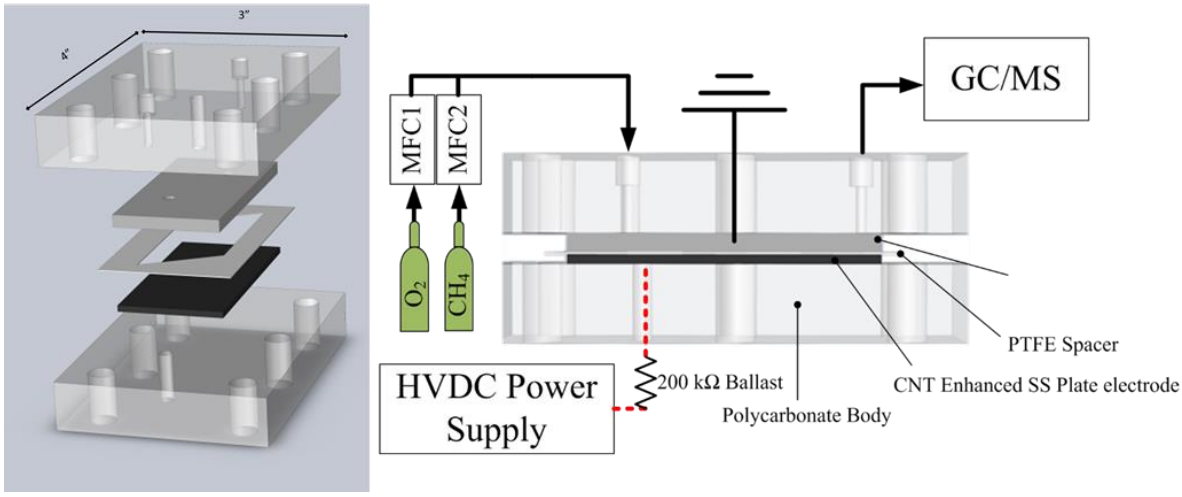


Figure 12: Flat plate gas phase reactor design schematic. Left) Exploded view of (top to bottom) polycarbonate body with gas flow and electrical connection holes, stainless steel plate electrode, Teflon spacer with parallelogram reaction volume, bottom stainless steel plate with a MW-CNT thin film, bottom polycarbonate body. Right) Experimental schematic of the assembled reactor.

The support plates are tightened down using six threaded bolts (ASTM A193 Grade B7 Alloy Steel Threaded rods, plain finish, ¼”-28 thread) secured with nuts and washers. A high-voltage differential oscilloscope probe (Keysight N2891A 70 MHz High-voltage Differential Probe with an HP 54542A Oscilloscope) is connected across the reactor to measure the electrical behavior of the reactor. The circuit current is measured with an in-line multimeter or with a second oscilloscope probe connected to small resistor. Product gas temperature was measured using an OMEGA 1/16” Type K ungrounded thermocouple (Part#CASS-116U-12-NHX). Two mass flow controllers (Brooks 4800 series) are used to control the flow rates of methane and oxygen in the system. A labview data-acquisition box (NI USB-6008) is used to monitor the flow rates and send setpoint signals to the MFCs using a custom LabView VI. The MFCs were calibrated using a graduated cylinder and a large bucket, to correlate set-point voltage with actual gas flow rates. (See appendix for more detailed information.)

The point-to-plane reactor design, shown in figure 13, is very similar in form and function to the flat plate design, with the notable difference of the reaction zone.

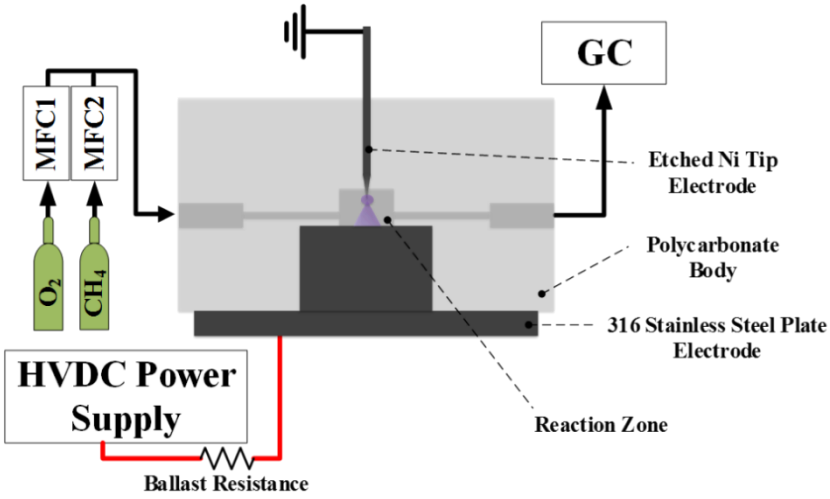


Figure 13: Point-to-plane gas phase reactor design and experimental schematic.

The main body of the reactor is machined out of acrylic or polycarbonate, and includes 10-28 fittings for 1/16” tubing and the 1/16” sharpened tip electrode. The plate electrode is a flat piece of stainless steel that is held in place against the polycarbonate body with an aluminum plate and bolts that tighten into the polycarbonate body. The back wall, the

top wall, and the inlet/outlet side walls of the reaction zone are provided by the polycarbonate body, while the bottom wall is the stainless steel plate electrode. The front wall is a piece of quartz glass, held in place by two aluminum arms that can be tightened down by bolts extending into the polycarbonate body. The reaction zone dimensions are 1.5mm (D) x 1.5mm (H) x 3.5mm (W).

Both gas phase reaction systems are use the same experimental procedure. First, the reactor is fully assembled and undergoes thorough leak tests to ensure that the system is sealed. Then the electrical lines are connected to the reactor and tested, to make sure that there is electrical conductivity to both electrodes without any sort of electrical short across the discharge gap. If a ballast resistance is inserted into the circuit, it typically goes on the positive high voltage side of the power supply. The oscilloscope probe measuring circuit current should be on the grounded side of the system so that it experiences smaller potentials and does not damage the probe. After passing start up tests, all analytical equipment is set up and prepared for experimental testing (e.g. Oscilloscope probes on and connected, GC warmed up and steady baseline, etc.). After the set-up is complete, the mass flow controllers are used to start the flow of reactant gases at the appropriate flow rates. Once gases are flowing, the high voltage power supply is turned on, and the high voltage interlock switch is pressed to start the application of high voltage power. The system is properly connected when you can see the applied potential across the reactor increase on the HV Oscope probe readout with the readout on the front of the power supply. The potential is steadily increased until electrical breakdown occurs, and then the power supply (Glassman High Voltage Series EQ 10 kV Power Supply) is adjusted to the appropriate operating voltage. It should be noted that the power supply has both voltage and current limiting capabilities. For the experiments conducted herein, the current limit on the power supply is not engaged, and all power control is through applied voltage. Gas chromatography of gas phase samples is accomplished through a sampling valve connected to downstream gas connections. Optical emission spectra are collected through viewing windows or through holes created in the reactor assembly to enable viewing. All electrical properties are recorded by hand or via the save disk in the oscilloscope.

### *Ni Electroplating Procedure*

A Watts solution of nickel chloride ($NiCl_2.6H_2O$), boric acid ($B(OH)_3$) and nickel sulfate ($NiSO_4.6H_2O$) was used in all nickel electroplating procedures. The Watts solution is used in decorative plating solutions and for protection against corrosion. Nickel sulfate in the solution is used to provide the needed concentration of nickel ions, while boric acid is used to maintain the pH of the solution by acting as a weak buffer. Nickel chloride is used to increase conductivity and improve anode corrosion.

1. 250 g/L $NiSO_4$, 40 g/L $NiCl_2$, 35 g/L Boric Acid.
2. 3 Volts applied, 2 kΩ resistor for a maximum current of 1.5 mA
3. Growth for 6.5 minutes to plate 15 nm on a 1x1" substrate.

### *Carbon Nanotube Growth Protocol via CVD*

MTI Corporation OTF 1200X-S tube furnace with 50mm OD quartz tube. Gas flow rates controlled by calibrated rotometers. Temperature ramp and gas flows according to the following recipe.

1. N2/H2 at 200/20 SCCM from 25 to 775 C over 70 minutes.
2. C2H4/H2 at 250/20 SCCM at 775 for 5 minutes.
3. N2 at 200 SCCM from 775 to 25 over approx. 3 hours.

### *Ni Tip Etching Procedure*

The following procedure is used to create sharpened metal tips to be used as electrodes in the point-to-plane reactors.

2 M KCl solution and 1/16" Ni Rods from ESPI Metals (Alloy 201, stock#: Knd1141) Cover the top and bottom surface of the Ni Rod with electrical tape with an approximately 2 cm gap exposed. Submerge the Ni rod in the 2 M KCl solution so that the exposed Ni surface is centered at the solution surface. A stainless steel ring (1cm diameter) is suspended right at the surface of solution so that the Ni rod hangs vertically and is centered through the ring and the ring is covered in solution via surface tension. A 3 V power supply with the positive terminal attached to the top of the Ni rod and the negative terminal attached to stainless steel ring. The stainless steel ring will start to bubble hydrogen gas when the power is turned on, and NiCl2 will start to form in

solution. For a 1/16” rod, the etch process takes approx. 35 minutes. The KCl solution is refilled after 10 minutes. At 25 minutes, the process is paused and the Ni rod is rinsed with DI water and the KCl solution is replaced. The rod should break right around 35 minutes into the etching process, allowing the bottom part to fall into solution. At this point the power is immediately turned off and the both pieces of the Ni rod are retrieved and thoroughly rinsed in DI water and isopropyl alcohol. This process is adapted from “Electrochemically etched nickel tips for spin polarized scanning tunneling microscopy” by Cavallini and Biscarini.

### *316 Stainless Steel Cleaning Procedure*

Allows improved performance during heat treatment steps and for much better adhesion of electroplated metals and subsequent CNT thin films.

1. Rinse with DI water.
2. Sonication for 10 minutes in 1% alconox solution.
3. Rinse with DI water.
4. Sonication for 10 minutes in DI water.
5. Rinse with DI water.
6. Sonication for 10 minutes in ethanol.
7. Dry under vacuum or $N_2$ flow.

### *Oscilloscope Operation*

An HP 54542A Oscilloscope (2 GSa/s 500 MHz) with a TekP6121 10 MOhm 11.0 pF 10X 1.5M probe and a Keysight N2891A 70 MHz High-voltage Differential Probe was used to collect specific electrical behavior of the discharge systems. Voltage (y-axis) and time (x-axis) are adjusted using the knobs on the front of the unit to suit the characteristics of the electrical signal. The specifics of each probe, such as attenuation and maximum collection speed, can be programmed into the oscilloscope unit so that the readout on the screen is the actual voltage of the system. Collection of electrical signals is done by pressing the “stop/single” button on the front and storing the data on a 3.5” diskette. This is done by pressing the blue shift button, and pressing waveform save (disk), selecting “store scope” as xy-pairs, and then naming the file to be stored on the disk, and selecting “execute” when a single waveform is captured on screen. In collecting

values for reactor voltage (operating voltage during steady glow discharge or pulsed behavior), the $V_{avg}$ function is used and the $V_{avg}$ value is recorded.

### *Gas Chromatography for Gas Phase Experiments*

An SRI 8610C gas chromatograph equipped with a helium ionization detector (HID) and a thermal conductivity detector (TCD) is attached the reactor effluent for the analysis of gas phase products. The GC is controlled through the computer program PeakSimple, and all post processing of data is accomplished using the tools built in to PeakSimple. Plotting, analysis of peak height/area, and application of calibration curves is done afterwards in Excel.

**Flat Plate Reactor:** The GC system uses a 6' x 1/8" SS Hayesep Q Packed column with 10 psi He carrier pressure setpoint and 30 psi He make-up pressure setpoint. The temperature ramp program for the flat plate reactor experiments was 1min at 40 °C, followed by a 30 s ramp to 100 °C, with the remainder of the experimental run operating at 100 °C. The effluent gas is analyzed using the HID detector, operating at a current setpoint of 100 with gain set to "high".

**Singe Point-to-Plane Reactor:** Same as flat plate reactor, with 6' x 1/8" SS Hayesep D Packed column and a temperature program set to a constant 120 °C.

### *Optical Emission Spectra*

An Avantes (AvaSpec 3648-USB2-FCPC, grating: UA, from 200 nm to 1100 nm, options: DUV3648-coating, DCL-UV/VIS-200, Slit-10, OSC-UA with FC-UV400-2-SR fiber optic cables) spectrometer is used to capture optical emission spectra of the discharges, either via direct viewing or through the front glass window of the needle-to-plane reactor. Avasoft 8.0 software is used to collect the emission spectra. A dark spectrum is recorded, and data is then collected in the scope minus dark ($S_{-d}$) mode. Typically, the reported spectra herein are the average of 3 scans collected for a full 1000 ms, but these values are adjusted based on detector saturation and other factors to obtain the best spectra possible for each experimental situation. The spectra are normalized to their respective maximum intensities before comparison. The identification of emission bands was accomplished using "The Identification of Molecular Spectra" by Pearse.[153]

### *Digital Photography*

Many images shown in this document were taken with a Canon EOS Rebel T3i DSLR Camera. The digital copies of all photos used herein contain EXIF data, which includes camera make and model, date/time, and specifics for the actual individual exposure, including resolution, focal length, aperture setting, and ISO setting.

Images of the small reaction systems used additional equipment, namely a Fotodiox Macro Extension tube (28 mm) and a Polaroid Close-up 10X 58 mm filter.

### *Electron Microscopy*

All SEM images were taken at the Oregon State University Electron Microscopy Facility. Field emission-scanning electron microscope (FE-SEM) analysis was conducted using a FEI Quanta 600 operating at 15–30 kV accelerating voltage.

Where applicable (appendix and other non-dissertation papers), TEM imaging was conducted either at the Oregon State University Electron Microscopy Facility (FEI Titan 80-200) or at the CAMCOR facility at the University of Oregon's high resolution transmission electron microscopy (HRTEM) (FEI Titan 80-300).

### *Dibenzothiophene Oxidation in Decane*

The flat plate and point-to-plane reaction systems used in gas phase experiments were also used in liquid phase experimental runs. The liquid phase flat plate reaction system is summarized in figure 14, and the liquid phase point-to-plane reaction system is summarized in figure 15.

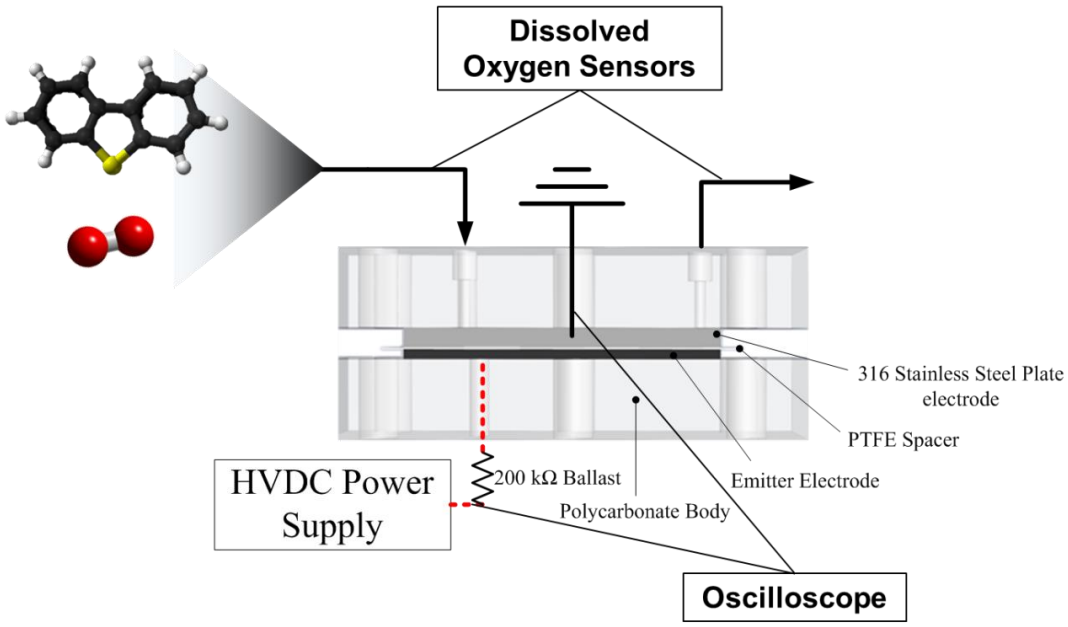


Figure 14: Experimental schematic of dibenzothiophene oxidation experiments in a flat-plate type reaction system.

A Syringe Pump (Harvard Apparatus Pump 33, Cat#: 55-3333) is used to flow a solution of n-decane with small amounts of dissolved dibenzothiophene through the designed flow-through reactor. The inlet and outlet of the reactor are equipped with NEOFOX-GT Oxygen Phase Fluorimeters to measure dissolved oxygen concentration (1000 micron spot size bifurcated borosilicate fiber assembly and the HIOXY-R oxygen sensors on 1000 micron fiber in 1/16" OD SS ferrules). The microreactor itself consists of two electrode plates, each connected to terminals of the power supply (Glassman High Voltage Series EQ 10 kV Power Supply OR Life Technologies Gibco BRL 4001P Programmable Electrophoresis Power Supply) and separated by a Teflon ® PTFE spacer (250 μm or less), sandwiched between impact resistant polycarbonate support plates. The electrode plates are corrosion resistant 316 stainless steel, 1/8" thick. One of the plates is cleaned stainless steel with a mirror finish, while the "emitter electrode" is patterned with a high aspect ratio material to facilitate the formation of corona-type discharges. The emitter electrode is either patterned with MWCNT (same as gas phase) or with a silver epoxy with embedded carbon nanotubes (emulating Kevin Caple's Master's Thesis work) The support plates are tightened down using threaded bolts (ASTM A193 Grade B7 Alloy Steel Threaded rods, plain finish, ¼"-28 thread) secured with nuts and washers. A

high-voltage differential oscilloscope probe (Keysight N2891A 70 MHz High-voltage Differential Probe with an HP 54542A Oscilloscope) is connected across the reactor to measure the electrical behavior of the reactor. The circuit current is measured with an in-line multimeter.

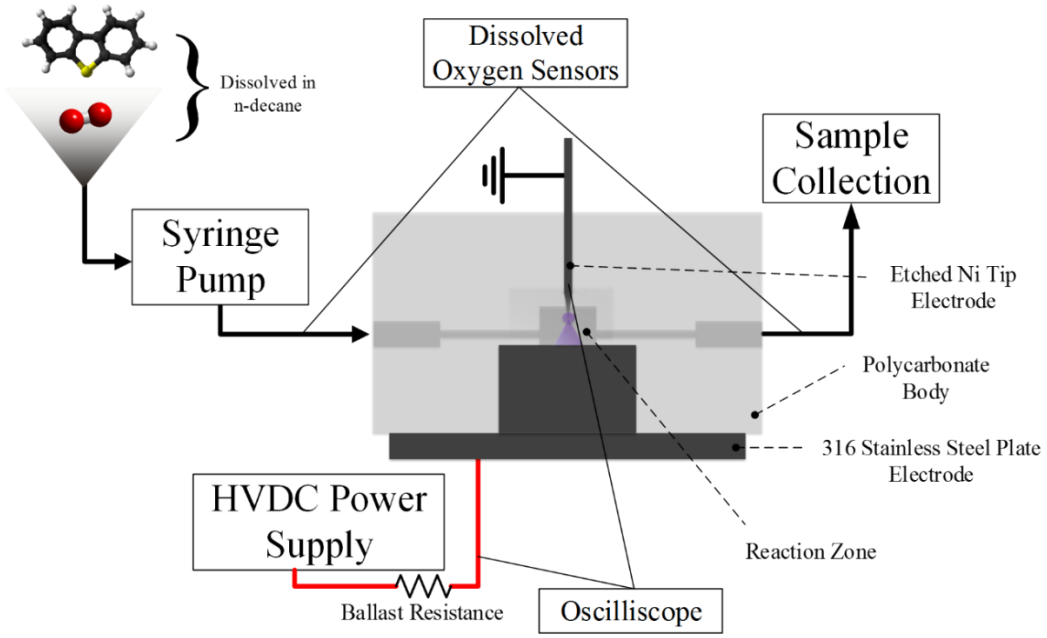


Figure 15: Experimental schemiatc of dibenzothiophene oxidation experiments in a point-to-plane reaction system.

The discharge experiments in n-decane that take place in the point-to-plane microreactor are set up in a very similar manner to the flat plate experiments, and only use the Glassman HV DC power supply.

### *Silver Epoxy CNT Plate electrode*

A flat plate of stainless steel (1 1/16" X 2" X 1/8" thick) was cleaned (see stainless steel cleaning method) and coated with a thin layer of conductive silver epoxy, referred to henceforth as Ag/SS. The coating method was simple, using a razor blade to apply a thin, relatively uniform layer of silver epoxy (MG Chemicals Silver Conductive Epoxy Cat. No. 8331-14G). A similar electrode was constructed, with the notable difference of the addition of carbon nanotubes grown in a tube furnace mixed into the silver epoxy before application to the electrode surface, referred to from now on as CNT/Ag/SS. Both electrodes were subjected to an $O_2$ plasma treatment for 35 seconds at 24 W for

activation (plasma etcher). According to Caple, the plasma etcher removes the top "inactive" layer of the epoxy mixture. The fabricated electrodes were inserted into the flat plate reaction system with a 50 micron Teflon spacer with a narrow, rectangular flow channel cut out of the spacer.

### *Dissolved Oxygen Sensors*

NEOFOX-GT Oxygen Phase Fluorimeters to measure dissolved oxygen concentration (1000 micron spot size bifurcated borosilicate fiber assembly and the HIOXY-R oxygen sensors on 1000 micron fiber in 1/16" OD SS ferrules). The Neofox Viewer software is used to collect data from the fluorimeters. The calibrations for dissolved oxygen reading as a function of temperature are specific for each sensor, and a sensor's identity is signified by a letter and 3 numbers etched into the metal at the base of the fluorimeter assembly. Ocean Optics calibrated the 2 HIOXY and 2 FOXY sensors, and the calibration data can be found on a CD with the NEOFOX equipment. More information in the appendix.

### *FTIR*

FTIR spectra were collected on a Bruker Vertex 70 FTIR with an ATR attachment, using 4 $cm^{-1}$ resolution. 256 sample scans and 64 background scans in the 4000 to 400 $cm^{-1}$ range.

### *Gas Chromatography for Liquid Phase Experiments*

An SRI 8610C GC equipped with an FID detector a sulfur wavelength specific filter FPD detector was used to analyze decane and DBT/DBTO/$DBTO_2$ mixtures. A capillary column at 250 °C was used to perform the separation (30m x 0.53mm ID 1 micron film thickness MXT-5 Capillary Column, Restek).

### *HPLC*

The HPLC system used herein is an HPLC: Dionex RSLC system (SRD-3400 UltiMate 3000 Integrated Solvent and Degasser Rack, HPG-3200RS UltiMate 3000 Binary Rapid Separation Pump, WPS-3000SL Analytical and WPS-3000RS Autosampler Series) The corona aerosol detector is not in working condition, so an analog UV detector (Gilson Model 111B Uv Detector at 254 nm in the 0-0.2 Abs range) is been integrated into the

HPLC system using the Dionex UCI-50 Universal Chromatography Interface. A C18 column was used with a liquid flow rate of 1 mL/min 80/20 acetonitrile/water mobile phase.

### *Ni Etching Procedure for MEMS Style Reactor (from Han Song, OSU EECS)*

1. The substrate is 1" x 2" glass substrate. Clean the substrate with Acetone, IPA, and DI water, and dehydrate for 10 min at 200 °C before sputtering.

2. The sputtering is done in the Microproducts Breakthrough Institute (MBI) here in Corvallis. The sputter tool is AJA ATC Orion sputter system. The Ni target is from Lesker, 99.9% pure, 2" diameter, 0.125" thick. The Ni sputtering operates at 5 mTorr pressure, 20 sccm Ar. The 300 nm Ni thin film is achieved by sputtering Ni target at 300 W for 2000 sec. The thickness is verified by a Tencor AlphaStep 100 Profilometer.

3. The photoresist used for photolithography is Microposit S1818 Photoresist. Spin on the photoresist at 4000 rpm for 30 sec. Then put the sample on a hot plate, 115 degC for 1 min. Expose the photoresist for 10 sec. Then develop the photoresist in 1:4 351 developer solution (10 ml Microposit 351 Developer and 40 ml DI water) for 10 sec.

4. Wet etching of Ni thin film uses 1:4 HNO3 solution (10 ml 70% HNO3 and 40 ml Di water). The etching takes about 2 min.

# Reactor Design

## Annular Design

Historically, corona discharges have been associated with small diameter wires at elevated potentials. From this reasoning, the concentric cylinder concept seemed a reasonable starting point for microscale corona discharge generation. In this annular design (figure 16), a 1/8” diameter (Super corrosion resistant stainless steel type 316/316L 1/8” rod) stainless steel rod is used as the discharge electrode. The 1/8” rod is inserted into a larger diameter section of tubing (Seamless ¼” stainless steel tubing, either 1/4” OD x 0.035” wall OR 1/4” OD x 0.049” wall) that is connected to a tee at both ends. The discharge gap distance can be adjusted by changing the wall thickness of the outer tubing. The tee allows for gas connections to flow into the larger tube that surrounds the smaller rod, creating a contained reaction volume in the space between the tube inner wall and the surface of the rod. The inner rod is secured in a PTFE compression fitting reducing union on the outer connection of the tee and extends slightly farther than the compression fitting. This allows for an electrical connection to be made to the inner rod while allowing it to be fully insulated from the rest of the metal reactor assembly. The outer surface of the tube containing the 1/8” rod is grounded, completing the circuit. The generated electrical discharge originates at the inner rod and terminates at the inner surface of the containing tube electrode. In order to facilitate the formation of corona-like discharges at lower onset voltages, the inner rod electrode is patterned with multi-walled carbon nanotubes. The carbon nanotubes were grown via CVD on the inner electrode surface that is first coated with a thin layer of nickel via electrodeposition.

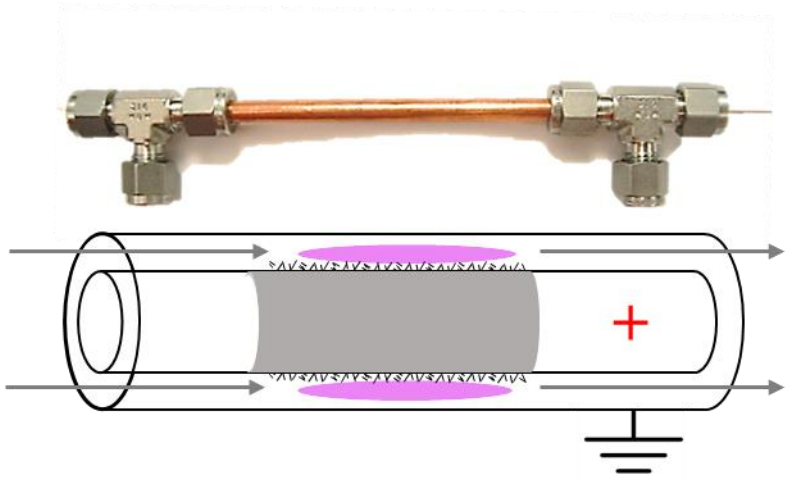


Figure 16: Image and theoretical representation of the annular reactor design. The inner electrode rod is coated with carbon nanotubes to enable corona type discharge phenomena (pink ovals) to occur in the discharge gap.

The annular reactor design failed to reliably reproduce consistent spacing between the electrodes, which resulted in a single hot spot at the smallest discharge gap distance. This hot spot regularly led to the formation of carbon deposits that rapidly short the reactor.

## Flat Plate Design

The flat plate reactor design sought to overcome some of the limitations of the annular design. The compression of two flat metal sheets with a spacer between them allows for reliable, consistent spacing between the electrodes. In this design, the emitter electrode was covered with carbon nanotubes grown by the nickel electrodeposition followed by CVD nanotube growth. The “sharpness” of carbon nanotube tips can generate extremely strong electric field gradients. The flat plate reactor design is shown in an exploded view schematic below (figure 17), with call-outs showing an SEM image of the CNTs grown on the surface and a COMSOL model the electric field generated by a single CNT tip in the system.

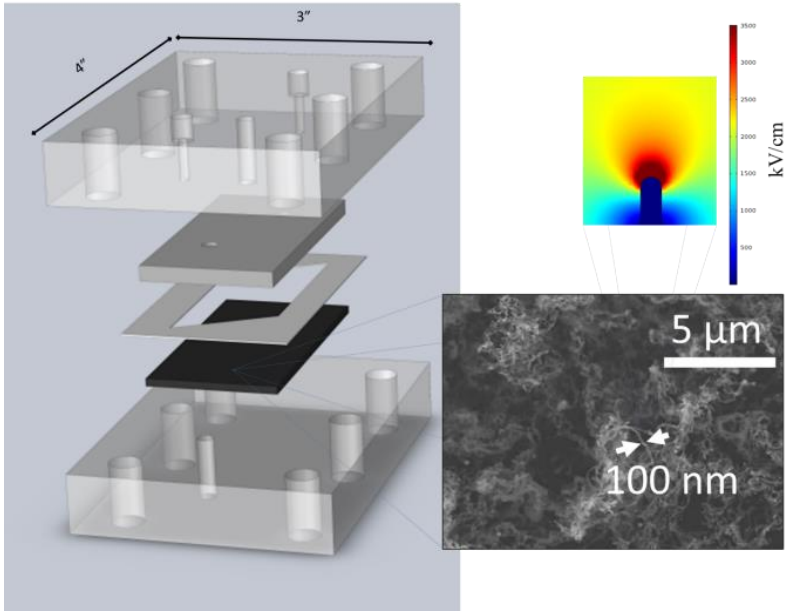


Figure 17: The flat plate reactor design, exploded view. The bottom stainless steel plate (black) is coated with a thin-film of MWCNTs via CVD. The MWCNTs are approximately 100 nm in diameter. The COMSOL model represents a single CNT, 100 nm in diameter, placed in a discharge gap of 1 mm, with an applied potential of 1 kV. The maximum calculated electric field gradient exceeds 3000 kV/cm.

The flat plate reactor design was able to generate a discharge in the sealed reaction volume, and merited further experimental investigation. The first step in characterizing these electrical discharge systems is to create a current-voltage relationship curve. The curve for the flat plate reactor can be seen in figure 20. The generated curve represents the behavior for both positive and negative polarity DC discharges. Positive polarity discharges occur when the positive DC potential is applied to the “sharp” CNT covered electrode, and negative polarity discharges occur when the positive DC potential is applied to the simple stainless steel electrode.

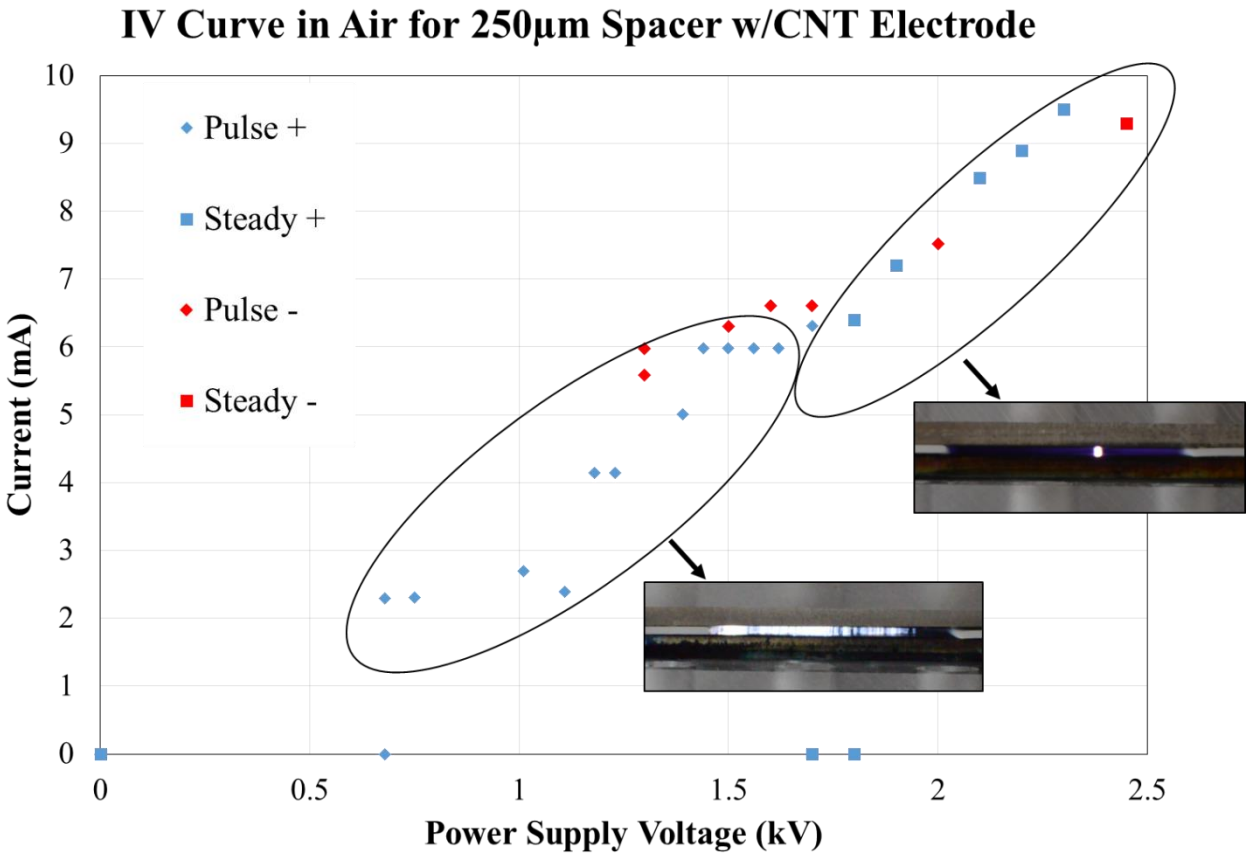


Figure 18: Current-Voltage (I-V) curve for both positive and negative polarity discharges in the flat plate microreactor in air. There are two distinct modes of operation: a pulsing mode where current can only be seen using a high-speed oscilloscope and a steady mode where the discharge stabilizes. The images shown are taken from the side view of the reactor, with one side of the PTFE spacer removed in order to directly view the discharge. The images are only approximations of actual discharge behavior in the closed system.

Current-voltage relationships for the flat plate reactor were collected in an attempt to more fully understand the fundamental behavior of electrical discharges in the constructed system. Pulse values were collected using an oscilloscope and the maximum value of a reproducible current pulse is used as the plotted point in figure 18. The steady current values are circuit current measurements made using the readout on the power supply. The pictures related to the callouts on the chart are representative images for both pulsed and steady operation in the system. The images are taken with part of the spacer in between the flat plates removed, and as such the actual discharge in a completely sealed system could appear differently. The oscilloscope traces, shown in figure 19, provide some insight in the behavior inside the closed system.

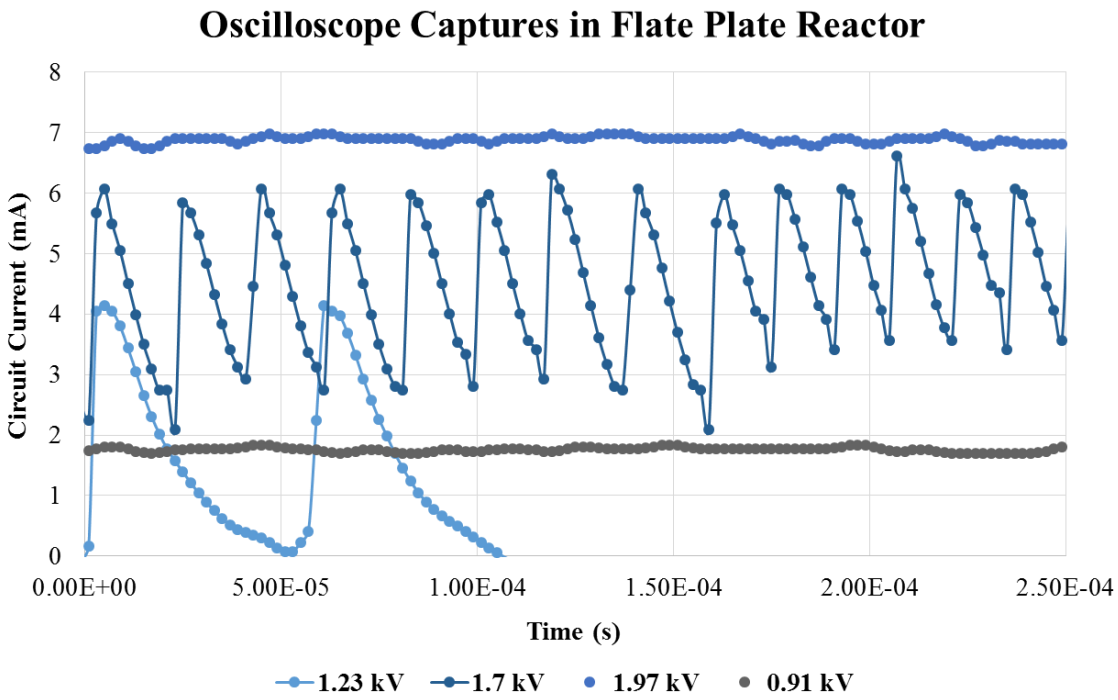


Figure 19: Oscilloscope captures of the discharges as they occur in the flat plate microreactor.

Voltage is applied and continuously increased to the flat plate reactor, and at a value of approximately 1.2 kV, the occurrence of short lived pulses becomes apparent. At 1.7 kV, the pulses occur regularly and the discharge current remains at a non-zero value. At 1.97 kV, the discharge enters a stable operation mode, likely a glow discharge or a localized arc-like discharge. At this point, the power supply voltage can be lowered while maintaining a stable discharge. In this experimental run, the discharge was maintained at an applied potential even lower than initial pulse streamer onset, and was still stable at 0.91 kV.

While the flat plate reaction system was superior in design and performance to the annular reaction system, it was not without faults. The first issue to arise was an apparent degradation in performance at extended operation times. The required onset voltages became higher and higher over time, and eventually the pulsed behavior disappeared and the reaction system would function in an altogether different manner than with freshly grown CNT plates. Figure 20 shows the CNT electrode before and after being used in the flat plate reaction system.

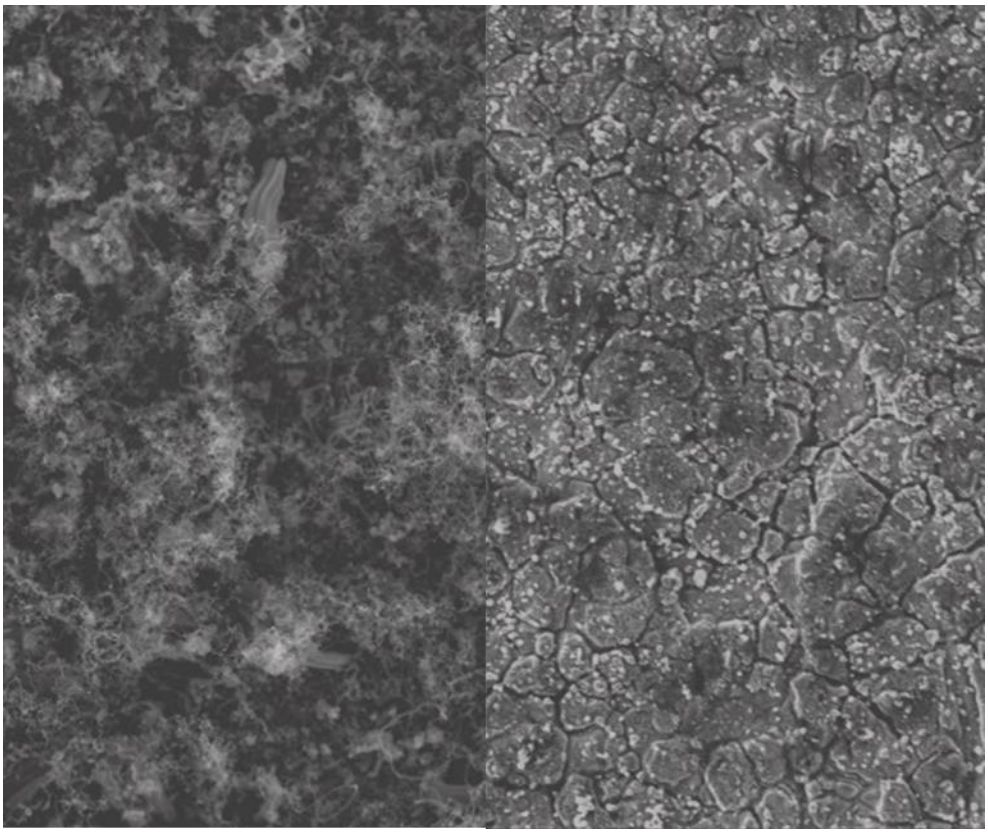

Figure 20: The carbon nanotubes deposited on the electrode before (left) and after (right) use in the reaction system.

It is obvious, both visually and using an electron microscope, that the CNT thin film is degraded over time. There is evidence in literature for anhydrous CNT oxidation in glow discharges containing $O_2$.[130] While the CNTs are present, the flat plate reactor is able to turn on and process methane to create products. After CNT degradation, which occurs on the time scale of ten minutes to an hour of operation, the reactor no longer behaves in the same way. This degradation limits the lifetime and reproducibility of the CNT enhanced flat plate reactor design. However, preliminary results in methane processing were obtained and are discussed in the *Methane Partial Oxidation Results* section.

After operation, the system can be disassembled and inspected. While the flat plate design does have issues with reproducibility and degradation of the CNT enhanced electrode, it does seem to function as intended for the duration of its useful life. Figure 21 below shows and SEM image of the deposition of carbonaceous solids near the flat plate reactor outlet. Solid carbon deposits on the electrode materials can lead to the reactor

shorting as the carbon eventually bridges the discharge gap and creates a conductive path through the solid. Methane decomposition is the likely source of carbon deposits on the electodes.[84]

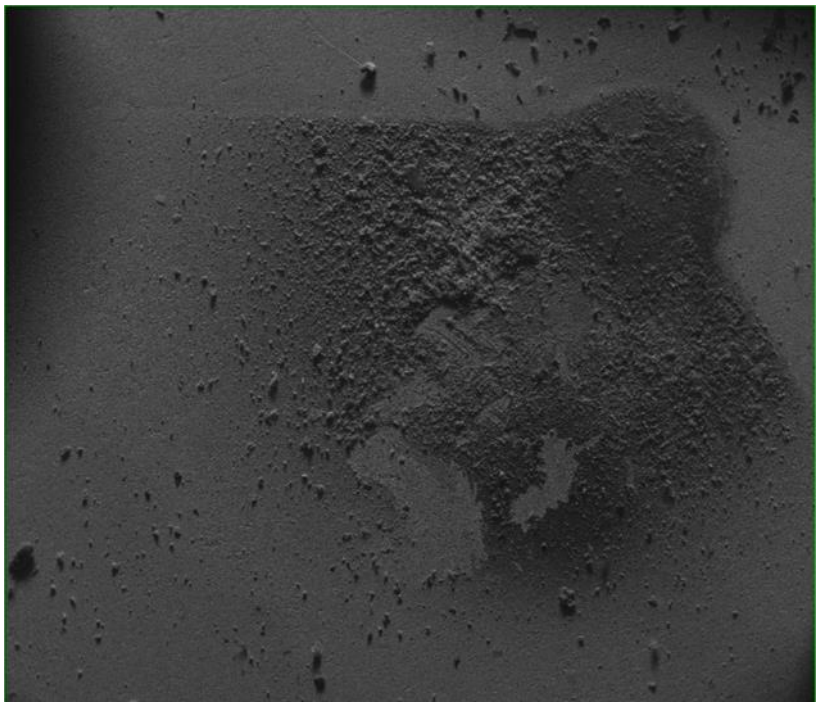

Figure 21: Carbon deposition on the bare stainless steel cathode after use in the reaction system. The exit of the reaction system can be seen as the circular portion in the upper right.

The stainless steel electrode that acts as the ground electrode in the flat plate reaction system can provide information on how the discharge physically appears in the closed system. The discoloration of the stainless steel plate appears to be distributed over the entire reaction volume, with darker discoloration towards the reactor outlet and lighter discoloration towards the inlet, as seen in figure 22. FTIR spectra of the stainless steel surface before and after discoloration were obtained in order to elucidate further details on the origin of the discoloration. The FTIR spectra showed that the discolored stainless steel was cleaner (i.e. lack of any organic or IR active groups) than the stainless steel before operation in the reactor, suggesting that the discoloration is an alteration to the stainless steel, perhaps formation of iron oxide.

Figure 22: The 316 stainless steel electrode positioned opposite of the stainless steel electrode after use in the reactor. This electrode retains an "imprint" of what was active plasma are during operation. The upper right is the gas flow inlet, and the low left is the gas outlet.

The discharge can sometimes be seen at the reactor outlet, as shown in figure 23. It is difficult to determine how the system is operating in the entire reaction volume based on visual inspection of the outlet, but it is useful to see that the discharge manifests itself at the correct locations.

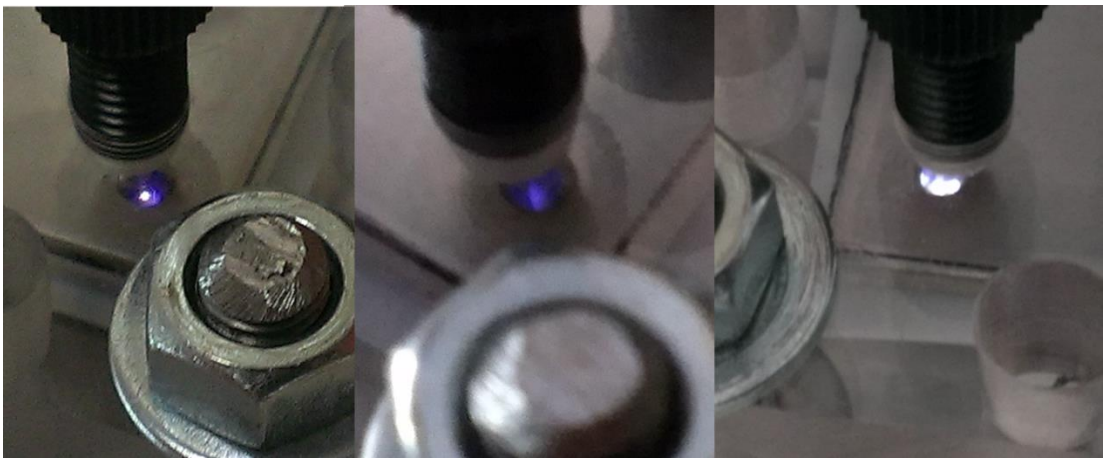

Figure 23: Images of discharges occurring in the flat plate reactor, as seen from the reactor outlet. Left) A spark forming near the exit of the reactor. Middle) A more diffuse glow is visible from the reactor exit. It becomes difficult to discern the difference between a desirable diffuse glow activation and a spark or arc that emits light that can be seen from the exit. Right) The discharge visible when the reactor is active in methane/air mixtures.

Visual inspection is difficult in a sealed system, and visual verification of the active discharge is one of the most straightforward and reliable ways to determine if the system is behaving as intended. The images shown in figure 23 can be helpful in verifying that

the discharge is occurring, but they do not lend any insight into the shape and diffusivity of the active discharge zone. The degradation of the CNTs on the electrode is detrimental, as it is effective failure of the constructed reactor. The accounting of any carbon based products (e.g.. solid carbon, CO, $CO_2$) also becomes difficult as the products could originate from the methane feed or from the deposited CNT thin film. Additionally, the gradual removal of the electrode that facilitates plasma formation hinders the reliability and reproducibility of the system. Even without CNT removal, the flat plate design does not guarantee that the formation of a stable plasma will occur at the same location from run to run. Figure 24 demonstrates this limitation of the reactor design, and shows that the effective reaction volume can change as a result of the first electric breakdown point and as a function of flow rate through the reaction volume.

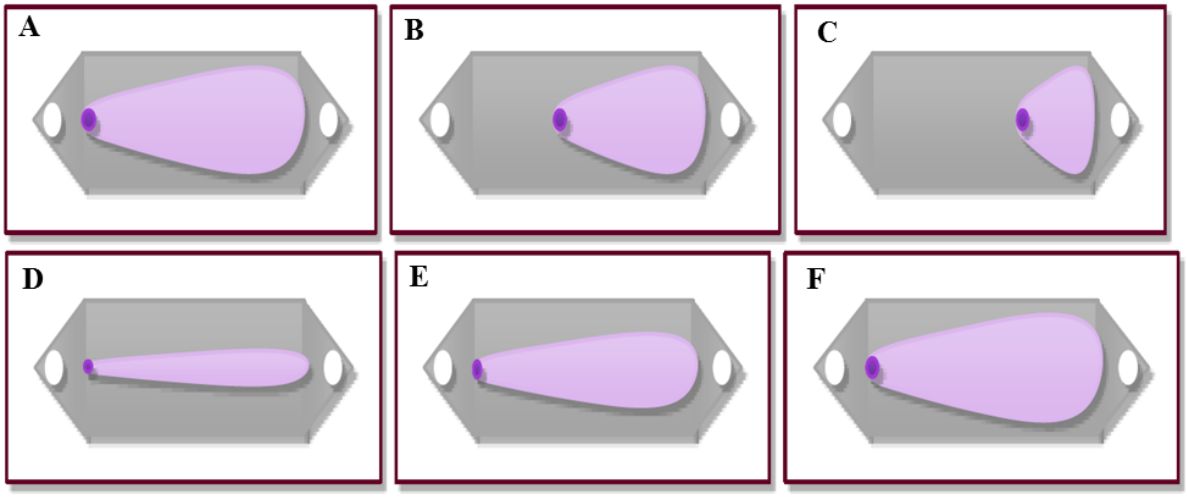


Figure 24: Variation in potential active plasma volume in the flat plate reactor design. A, B, and C demonstrate how the active volume could easily change based on where the steady discharge filament first forms. D, E, and F show how the active plasma plume can change depending on the gas flow rate through the system, with the progression D-F being faster to slower flow rates. This figure is borrowed from the Yousef Alanazi's Master's Work at Oregon State University, in which he used the same flat plate reaction system to carry out ethylene oxidation.

## MEMS Style Interdigitated Reactor Design

The simple flat plate reactor suffered from three main limitations: 1) The lack of a way to visually inspect the discharge, 2) electrode degradation over time, and 3) difficulty in generating a reproducible reaction environment. The fabrication techniques associated with microelectromechanical systems (MEMS), namely sputtering and wet etching, are

able to create fine metallic and semiconductor structures with good reliability. Depositing these structures on a glass slide would allow for simple visual inspection, and it was thought that metallic structures should be more robust in the plasmachemical reaction environment. Since the MEMS design could, in theory, overcome the three main limitations of the flat plate design and still fit into the flat plate design's housing, it was the logical next step. The MEMS-style microplasma reactor, created via sputter deposition of nickel on a glass slide followed by wet chemical etching procedures, is shown in figure 25. Information on the procedure can be found in *Materials and Methods*. The Ni film is 300 nm thick, and the Ni "fingers" are 100 μm wide with 50 μm spacing between them and extend 13 mm from the electrode contact base.

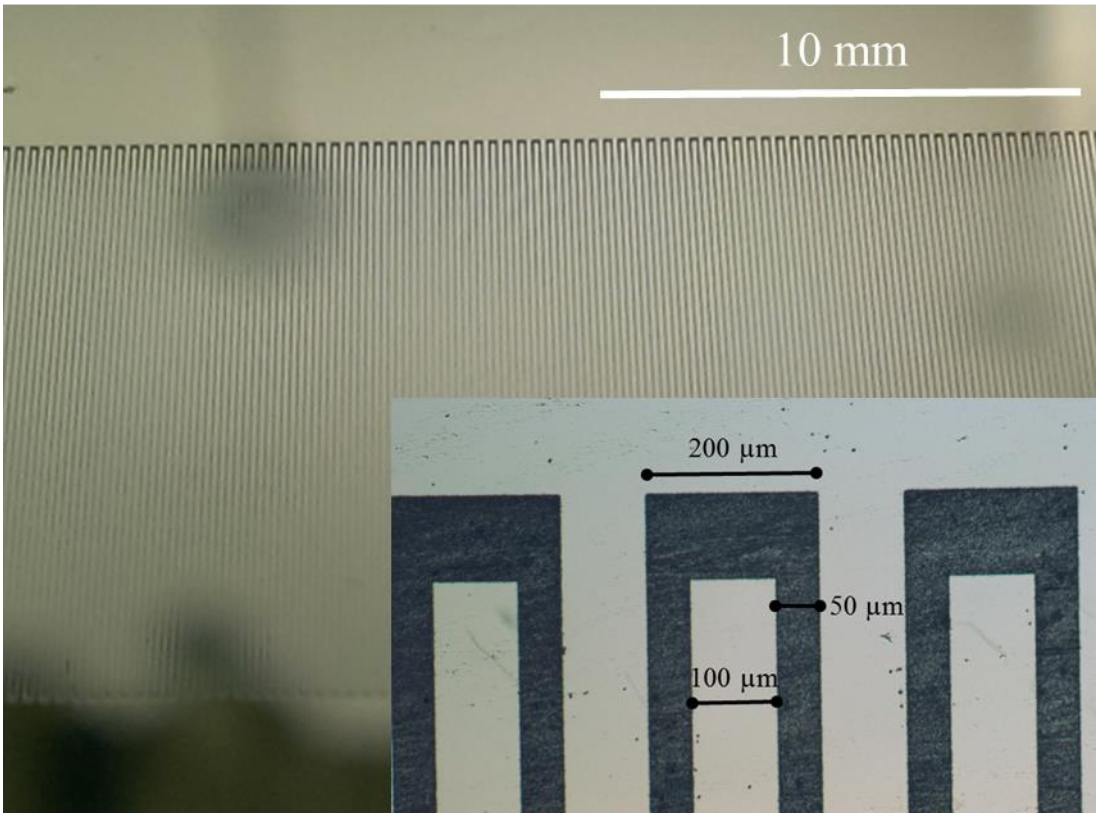


Figure 25: Images of the interdigitated MEMS style reactor design. The interdigitated nickel fingers extend from a solid layer on either side and can act as either the cathode or anode. A microscopic view (insert) of the constructed MEMS-style electrode surface. In the insert, the Ni thin film appears white.

The MEMS style reactor was set up in the same way as the flat plate design, and was intended to fit into the flat plate design's reactor body in place of the CNT enhanced electrode. The MEMS style electrode was attached to the high voltage DC power supply

in the same way as the flat plate design, with the exception that the ground and high voltage potential are applied to the same side flat plate system. Potential was gradually increased until electric breakdown occurred, shown in figure 26A. Increased applied potential creates more discharge points and increases the discharge current, resulting in the discharge points glowing more brightly (figure 26B). After about 10 seconds operation time at the conditions shown in figure 26B, the discharge becomes thermally destructive (figure 26C) and results in the irreversible damage of the etched Ni fingers in the MEMS design (figure 26D).

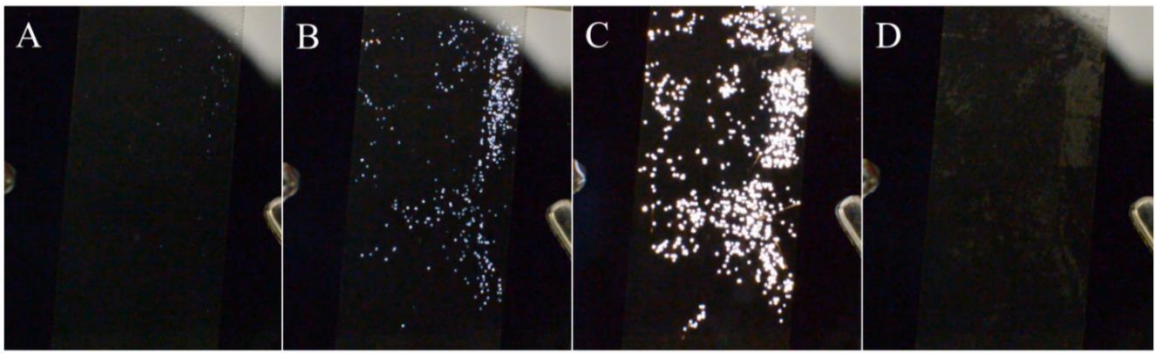


Figure 26: Discharges using a high-voltage DC source with the constructed MEMS device and a ballast resistance of 200 kΩ. At lower potentials, (A) the discharges can be faintly seen, (B) begin to develop in greater number and at higher intensity as the voltage increases, and (C) eventually become thermally destructive around 250 V. (D) Areas of the etched Ni are destroyed and the device is irreversibly damaged.

The failure mechanism for the MEMS style reactor design was investigated using a metallographic microscope. An image of the destroyed etched Ni plate is shown in figure 27 below.

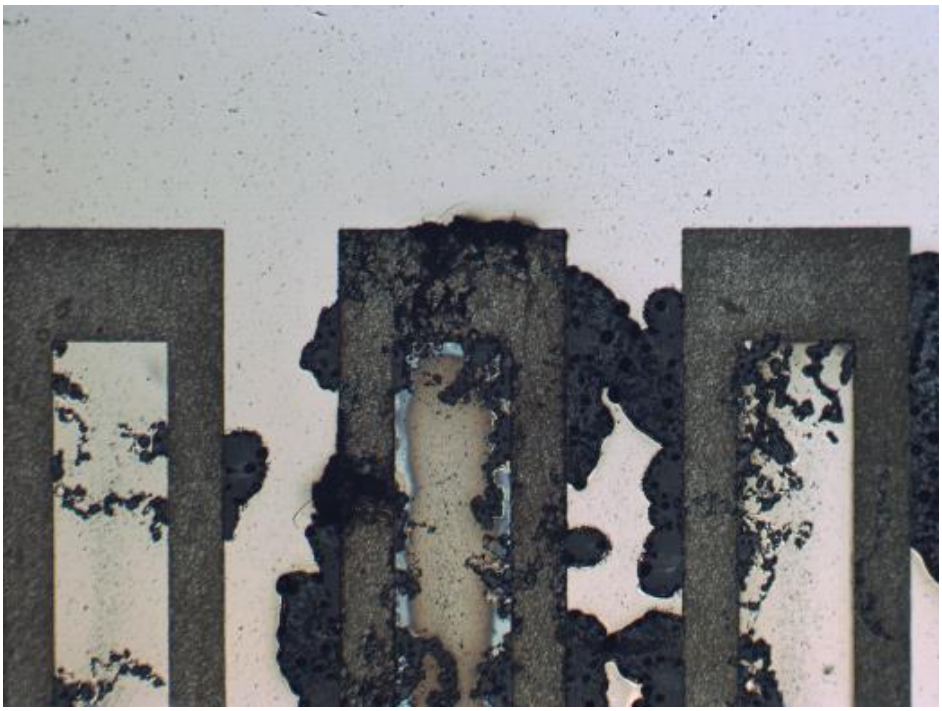

Figure 27: The MEMS device after failure at ~300 V operation. The top digits (anode) tend to show more damage than the bottom digits (cathode).

Multiple attempts were made to operate the MEMS style microreaction system. However, operation of any discharge between the interdigitated nickel electrodes resulted in thermal failure on the first experimental run.

## Point-to-plane Design

The MEMS style microreactor design was not robust, and failed on the first trial run multiple times. The added time and complications from the fabrication process made it so that further exploration was not merited. Most of the classically cited papers that study electrical discharges used a simple point-to-plane system to characterize electrical discharges. Most of these point-to-plane systems in literature use discharge gaps that range from 1 to 50 cm, and only a select few venture below the 1 mm length scale. The design process for the point-to-plane (PTP) microreactor was simply the effective miniaturization of a simple sharpened metal point electrode positioned above a flat plane electrode. The first pass at the PTP design positioned three sharpened 1/16” metal tips within 1 mm of the flattened surface of larger ¼” stainless steel rods, as shown in figure 28.

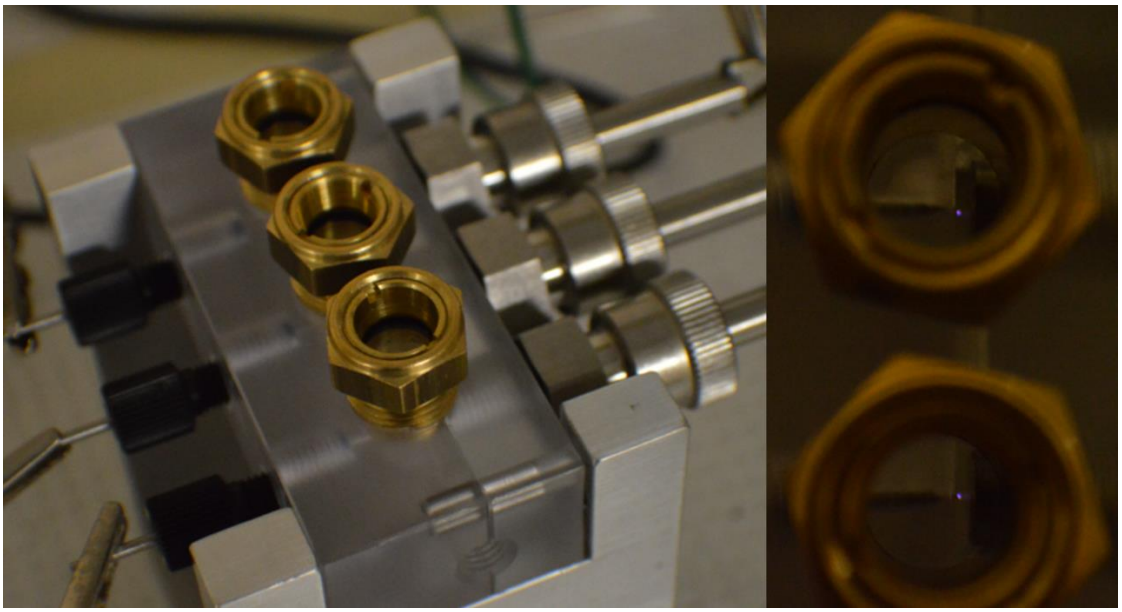

Figure 28: First generation point-to-plane microreactor. Left) First generation point-to-plane microreactor system with discharge pins on the left and larger "plane" electrodes on the right and viewing windows on the top. Gas inlet/outlet holes can be seen at the front (similar fittings on the back), and the body is held together by the stainless steel stand. The underside of the system has 3 ports that align with the viewing windows for the installation of collimating lenses for OES. Right) Picture showing that multiple discharge pins can be activated simultaneously.

This system could generate stable discharges at multiple sharpened point electrodes, and maintain those discharges in reacting gas flows. The glass viewing windows allowed for simple visual verification, and the series design of the system allowed for one, two, or three points to be active at the same time. The sharpened tips can be virtually any conducting material that can withstand the plasma environment generated at the electrode and sustain the discharge. Our lab has used steel, tungsten, and nickel electrode materials. The majority of the work shown here was carried out using 1/16" nickel rods that have been electrochemically etched to create fine points as seen in the SEM image figure 29.

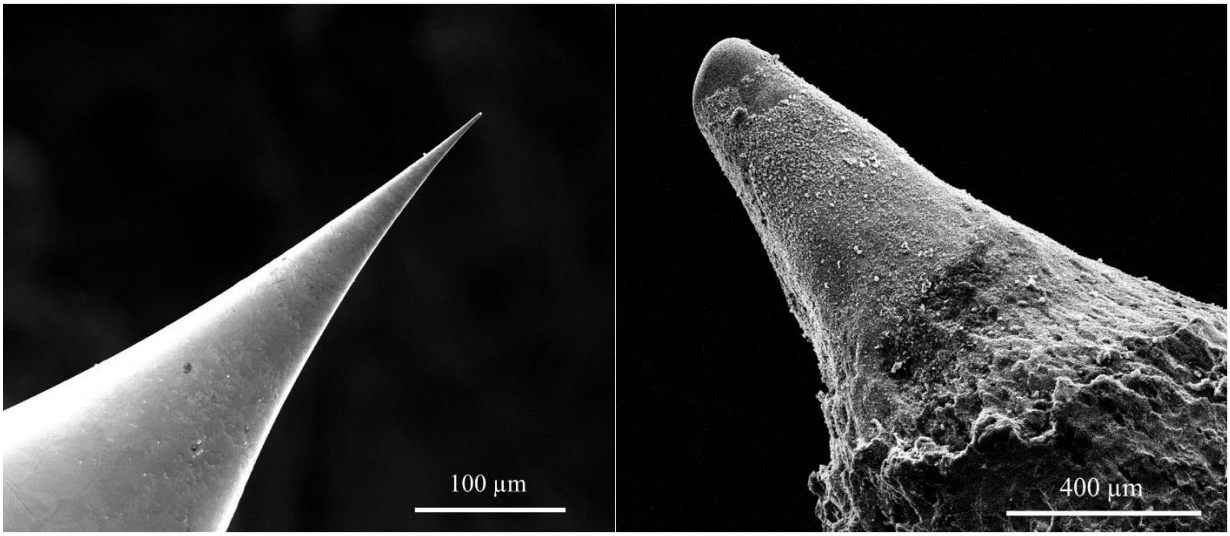


Figure 29: SEM image etched nickel tips. Left) A 1/16" nickel rod that has been electrochemically etched in 2M KCl solution. The tip diameter at its finest point is approximately 4 µm, and Right) A similar Ni tip after several hours operation in the discharge system, with the tip diameter of approximately 150 µm. The Ni tips do sustain wear over time, but are still adequately sharp to create electric breakdown, only with increasing required applied potential.

The etched Ni points are degraded over the course of several hours operation time, as shown in figure 29. The degradation happens quickly at first (within the first minutes of operation) and begins to slow as the tip becomes less sharp. The degradation of the Ni tip electrode occurs as a result of electrons and ions eroding the metal surface. The very small volumes of eroded Ni are deposited on other parts of the reactor.

In this point to plane system, the generated discharges could be effectively changed from corona modes, to glow modes, and finally to spark/arc modes by changing the electrical parameters of the system, namely applied potential and discharge current. This progression can be seen in figure 30.

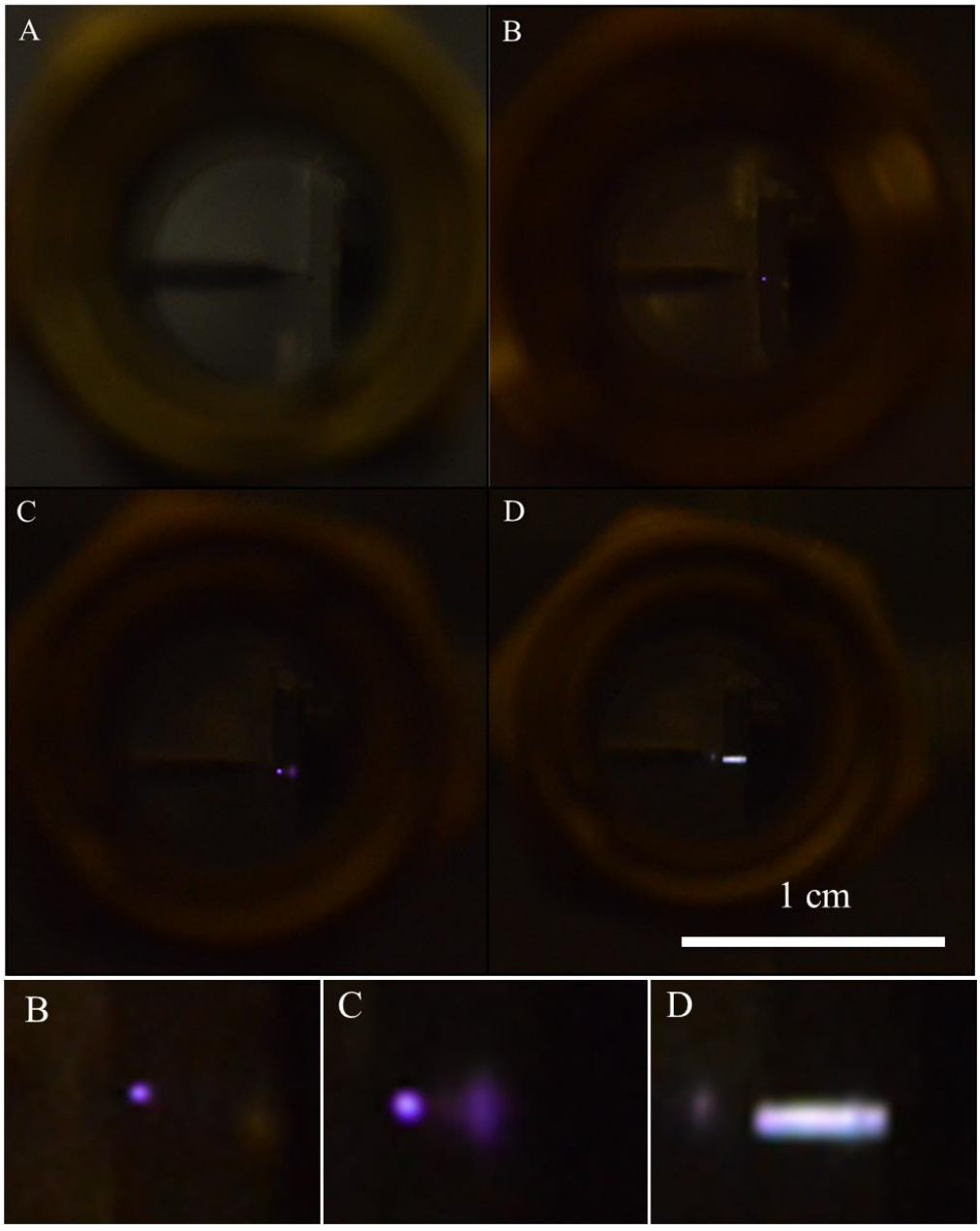


Figure 30: Images of the point-to-plane electrodes in atmospheric air. The discharge gap is approximately 1 mm. Images are taken from above through a glass viewing window, with the etched point electrode extending through the polycarbonate reactor body into the discharge gap on the left, and the larger "plane" electrode on the right. A) With the power supply off. B) The discharge in corona mode. C) The discharge in a pulseless glow mode. D) The discharge in a spark or arc mode.

The initial results of the point-to-plane reactor are quite good, in that they enable stable discharge in a reproducible, reliable manner. Additionally, the visual verification allows for very straightforward classification of the discharge modes. The etched metal tip electrodes do degrade over time, but not nearly to the degree of the CNT electrodes

studied previously, and can provide stable operation for at least multiple hours. The discharges are reproducible, with the only noticeable change in operation parameter being the required electric breakdown voltage. As the tips degrade, the required electric breakdown voltage increases. However, there is no noticeable change in sustaining voltage during operation. The designed system has only one major flaw, and that was its large dead volume to reactive volume ratio. Since a large portion of the reactant gas flows around the active discharge region, conversions were low and detection of product gases in the effluent was difficult to quantify.

## Point-to-plane Design: Mark II

The next generation point-to-plane reactor design is essentially the same as the previous design, simply with smaller dead volume and a larger active volume to dead volume ratio and only one discharge pin. This next generation design is modular in nature and can be coupled with another identical unit for multiple discharge studies.

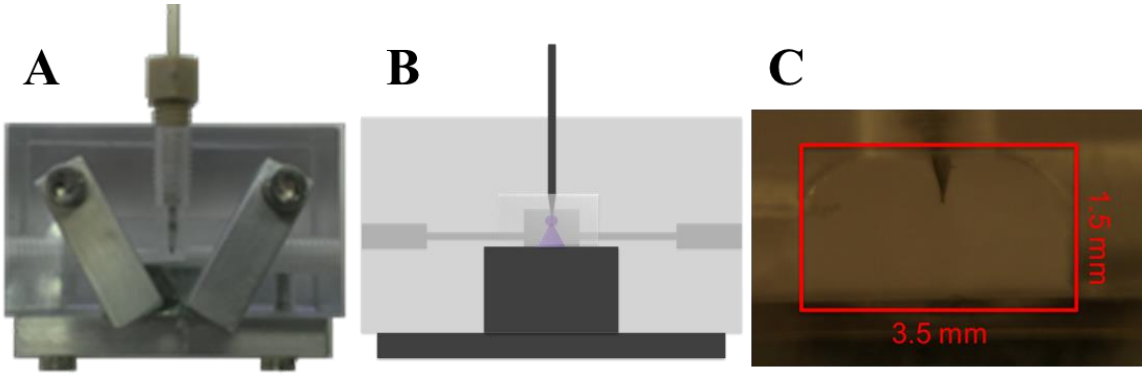


Figure 31: Second generation point to plane reactor design. A) An image of the assembled reactor. B) A simplified depiction of the reactor for clarity. C) Magnified view of the physical reaction zone with dimensions. The depth of the reaction zone is 1.5 mm. The sharpened tip electrode is visible and extends into the reaction zone. In this image, the discharge gap is approximately 1 mm.

The main body of the reactor is machined out of polycarbonate, and includes #10-32 PEEK tube compression fittings for 1/16” (1.5875 mm) tubing and the 1/16” sharpened tip electrode. The plate electrode is a flat piece of grade 316 stainless steel that is held in place against the polycarbonate body with an aluminum plate and screws that tighten into the polycarbonate body. A tight fit between the plate electrode and the recess in the reactor body provides necessary sealing. Using the orientation of the reactor in figure 31,

the rear wall, top wall, and inlet/outlet side walls of the reaction zone are provided by the polycarbonate body, while the bottom wall is the stainless steel plate electrode. The front chamber side is formed by a piece of glass, held in place by two aluminum arms that can be are tightened held down by bolts screws extending into the polycarbonate body. A piece of clear silicone rubber is used as the seal between the glass and polycarbonate body, and it is cut to size in order to keep the glass viewing window as the wall of reaction zone. The reaction zone dimensions are 1.5mm (D) x 1.5mm (H) x 3.5mm (W). The inside corners of the chamber are radiused from the cutting tool, which is 3/64" diameter resulting in a 0.6 mm radius. As a result, reaction chamber volume is approximately 10 $mm^3$.

The performance of the second generation point-to-plane reactor is markedly improved from the first generation. Figure 32 shows images taken of the discharges obtained in oxygen and nitrogen flows with various size ballast resistors. The negative polarity discharges are much more stable than the positive polarity discharges, and the 1 MΩ ballast resistor seems to enable easiest access to the steady glow discharge regime.

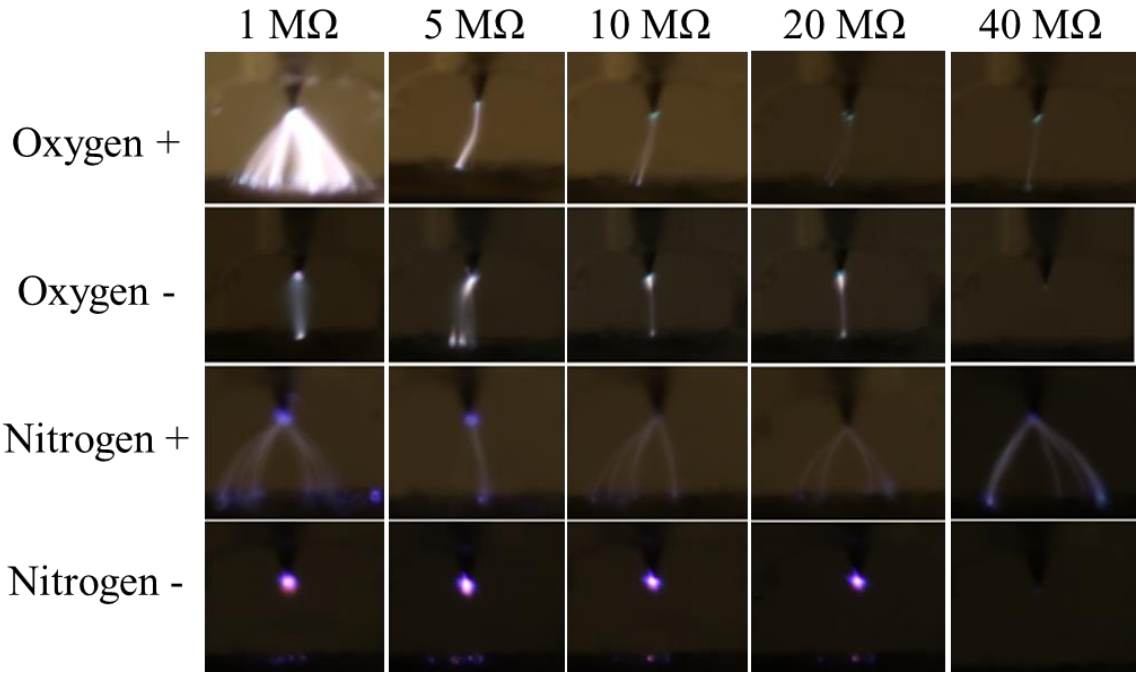


Figure 32: Images of the DC discharge generated in oxygen and nitrogen gases for both positive and negative polarity. The circuit current is limited by the ballast resistor, ranging from 1 MΩ to 40 MΩ for the images shown here. In general, the negative polarity DC discharges are typically stable glows or coronas while the positive polarity discharges exhibit pulsing behaviors and streamer formation. Note: Changes in

the brightness/darkness of the background result due to the required change in camera shutter speed. These discharges occur at different speeds, and the camera settings need to change to accurately capture the phenomena.

Figure 33 shows steady circuit current as a function of the circuit ballast resistance in a negative polarity oxygen plasma, where the images on the right relate to the points on the curve. The images and the current values obtained here are for the discharges that occur at first breakdown, and it should be noted that differing discharge behaviors can be obtained by changing applied potential and thus, total input power to the reactor. This study simply shows what the default state of the discharge is with differing ballast resistances. Based on this information, the discharge at point A is of the most interest, as it is a steady glow discharge. The corona discharge at point E is also of interest, but will likely lead to much lower chemical conversion than the glow discharge at point A.

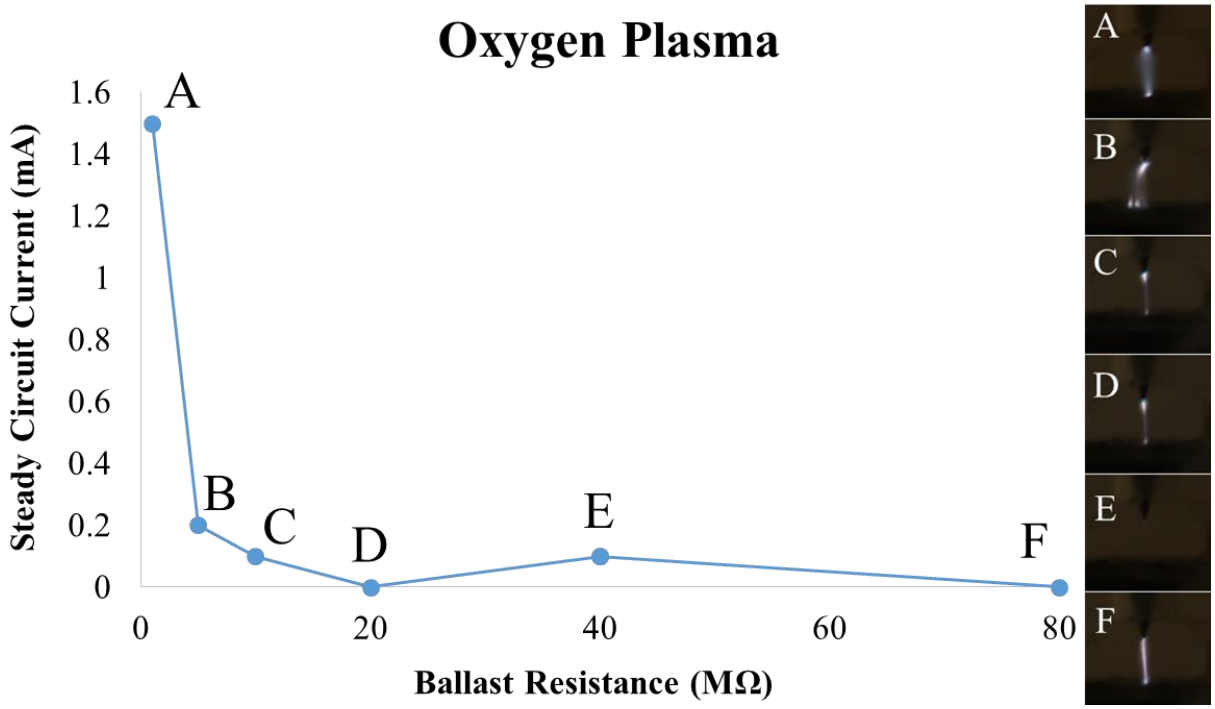


Figure 33: Steady circuit current at breakdown voltage in pure oxygen flow in the point-to-plane system as a function of the ballast resistance used in the circuit. The points on the curve correspond to the images on the right, which are all depicting the discharge behavior in a negative polarity DC discharge in oxygen flow. A) Steady glow discharge. B) Glow discharge with pulsed streamer formation. C) Pulsed streamers, image is for one occurrence. D) Pulsed streamers, occurring much less regularly than in C. E) Corona discharge at the sharpened tip electrode. F) Spark discharge, occurs infrequently.

## Reactor Design Conclusions

Several reactor designs were explored and evaluated for their effectiveness in generating reproducible, stable, non-thermal plasma that enable chemical processing. The constructed devices all needed to be able to generate a stable discharge, allow flow through a reaction zone and also allow for the conduction of electricity only through the desired pathway and not into parts of the device that are not associated with the reaction zone.

Ultimately, the point-to-plane reactor designs were the best designs for reliably producing stable nonthermal plasmas in a repeatable manner. The use of singular sharp points creates an equally singular origination for the actual discharge, which was important in reproducibility of experimental run conditions. The result of this single point-to-plane active discharge zone is a reproducible discharge that can be observed visually and characterized electrically and spectroscopically. Additionally, the point-to-plane designs are very simple, which facilitates modeling efforts, minimizes manufacturing costs, and simplifies experimental work and data analysis.

Monitoring of the generated nonthermal plasmas can be accomplished with electrical measurements, notably circuit current, total applied potential, and the sustaining voltage drop across the reaction zone with a differential oscilloscope probe. However, in completing this work it became apparent that the best way to reliably determine the discharge regime and corresponding shape, size, luminosity, and behavior of the discharge is *via* visual inspection through a viewing window. The presence of a viewing window also allows for optical emission spectroscopy, which is a useful tool in probing plasmachemistry and reactivity of the discharge.

Materials of construction for nonthermal microplasma reactors are of serious concern. The best reactors constructed here were machined out of polycarbonate, which was cheap and easy to achieve. However, reactor failure as a result of melting and burning polycarbonate became a problem at high discharge current and with highly exothermic reactions. Materials such as glass and machinable ceramic are the most promising moving forward in this field. Electrode materials are also of concern, as their properties can affect not only the discharge properties but also directly influence product

distributions. Ni was predominantly used as the sharp tip electrode due to ease of electrochemical etching, and stainless steel was used as the flat plate electrode due to ease of access with stainless steel materials. Future work should consider the effect these materials have in the reaction system.

Further exploration into more sophisticated reactor designs, specifically those designs that aim to reduce bypass flow and incorporate multiple discharge points in series should be seriously considered. The energy calculations carried out in our lab suggest that reactors capable of high throughput will be the most energy efficient and more easily applicable to industrial purposes. The use of already developed microplasma generators, such as the microhollow cathode discharge, may also be of interest if they can be adapted to chemical processing.

# Methane Partial Oxidation Results

The construction and characterization of an experimental corona discharge activated reactor was the first objective in this work. Both the flat plate reactor design and the second generation point-to-plane reactor design will be the only designs further discussed, as both designs have been used in the experimental objectives in this work. The experimental evaluation of the corona discharge reactor performance in the partial oxidation of methane is discussed in this section.

## Flat Plate Reactor

The flat plate reactor design, while problematic in reproducibility and reliability, did manage to provide some interesting experimental results in methane processing. The flat plate reaction system used herein is shown in detail in figure 34.

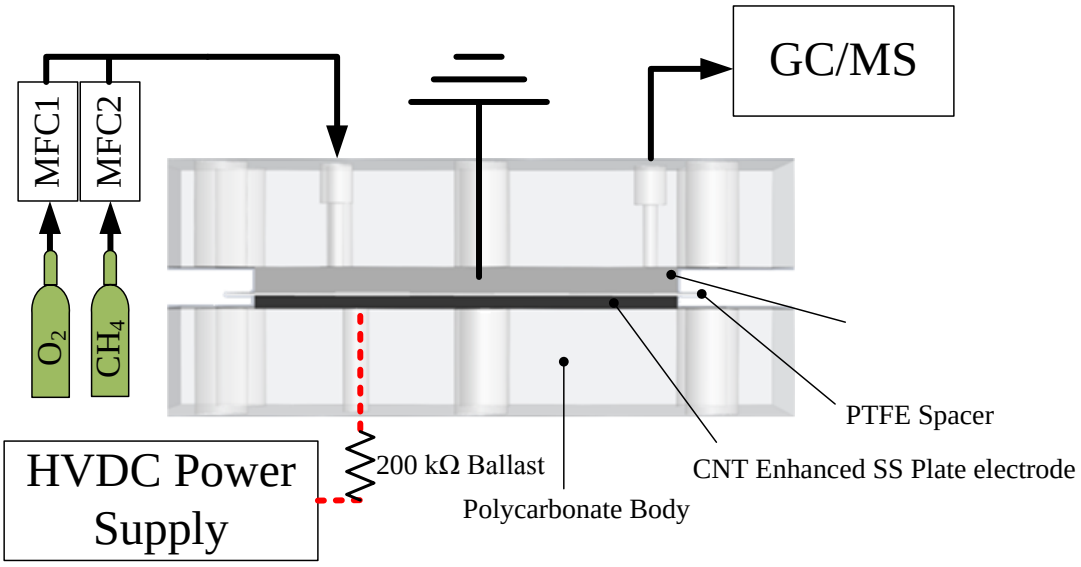


Figure 34: The flat plate reaction system used in the analysis of corona discharge activated methane partial oxidation. Here, the flow through reaction volume is a parallelogram cut out of the PTFE spacer insert.

The electrical discharges generated in this system have been explored and characterized (see *Reactor Design* section). Figure 35 depicts characteristic discharges in the pulse operation and steady operation modes. The methane partial oxidation experiments were predominantly conducted in the steady discharge operation mode (figure 35 bottom).

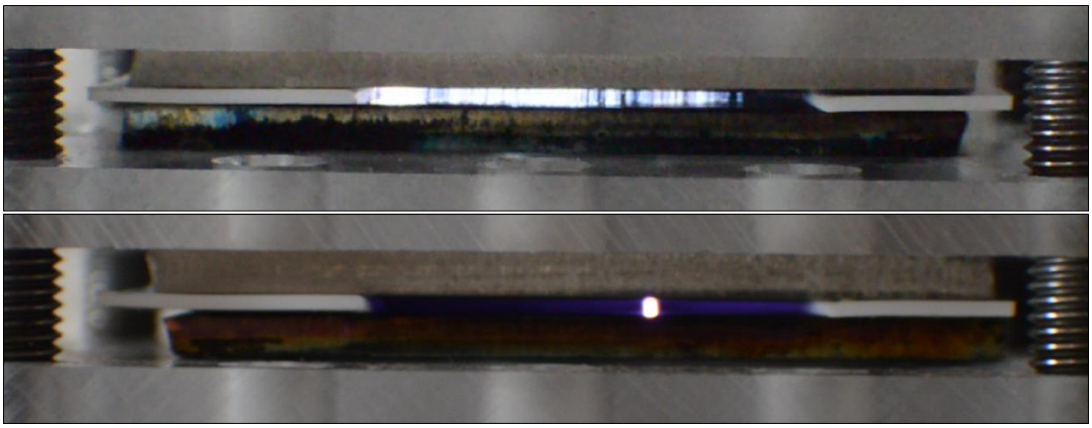

Figure 35: Larger view of the discharges in the flat plate microreactor, as shown in figure 18. The following data was obtained with the reactor operating in the steady discharge regime, as depicted by the bottom image above. Again, it should be noted that these images are taken with a piece of the Teflon spacer removed, so actual discharges could appear significantly different in the sealed system.

Flows of methane with an oxygen source such as air or pure oxygen were passed through the reaction zone with an active discharge, and the chemical products were analyzed using in-line gas chromatography. Typical GC traces for the products of methane and oxygen source cofeeds are shown in figure 36.

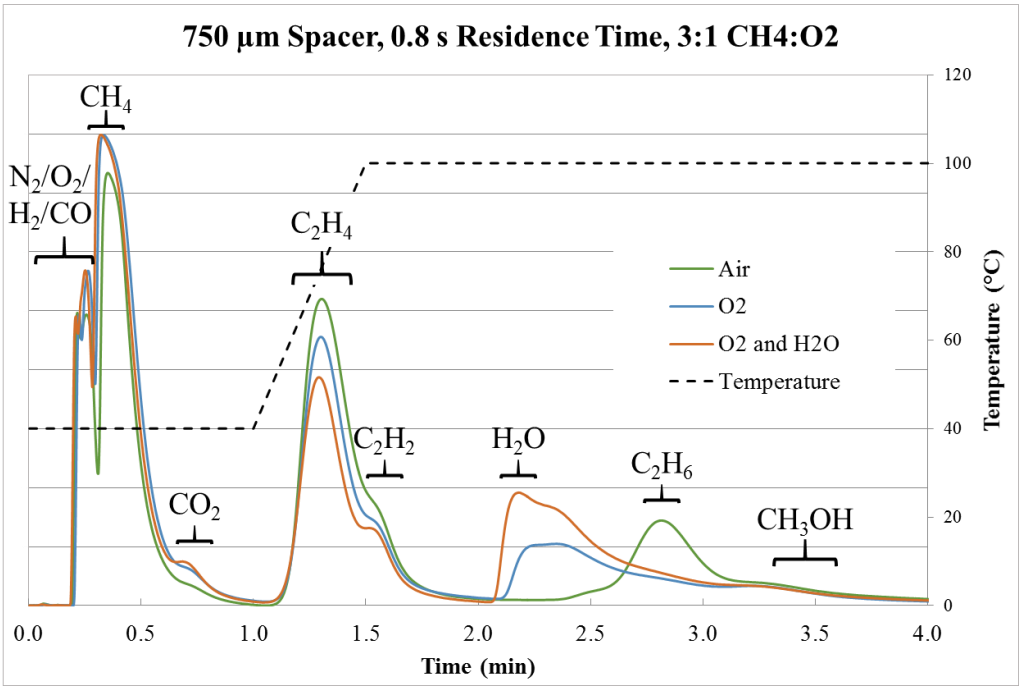


Figure 36: GC trace from the HID detector for methane partial oxidation experiments in the flat plate microreactor system.

This system was used to carry out a $2^3$ factorial design experiment in order to gain an initial understanding of methane processing in electrical discharges. The factors investigated were flow rate (mL/min), reactant gas feed ratio (mol methane to mol oxygen), and the discharge gap (μm thickness of the Teflon spacer). The responses were methane conversion and product selectivities. Gas flow rates were calculated based on the molar ratios between methane and oxygen. The details of the $2^3$ factorial design are shown in table 1, including factor levels and response values.

Table 1: Factor values and response values for the simple $2^3$ factorial design experimental investigation of the flat plate reactor.

| Methane/Air Flat Plate Discharge System: $2^3$ Factorial Design | | | | | | | | |
|---|---|---|---|---|---|---|---|---|
| Factors | | | | | | | | |
| Flow Rate (mL/min) | 15 | 15 | 17.5 | 17.5 | 150 | 150 | 175 | 175 |
| Gas Ratio CH4:O2 (mol:mol) | 5 | 5 | 3 | 3 | 5 | 5 | 3 | 3 |
| Discharge Gap (um) | 250 | 750 | 250 | 750 | 250 | 750 | 250 | 750 |
| Randomized Run Number | 1 | 3 | 8 | 5 | 6 | 2 | 7 | 4 |
| | | | | | | | | |
| Response | | | | | | | | |
| **Methane Conversion** | 1.24% | 11.91% | 9.43% | 15.44% | 1.05% | 3.03% | 1.79% | 3.92% |
| | | | | | | | | |
| **Selectivity** | | | | | | | | |
| CO2 | 13.0% | 1.3% | 1.5% | 0.4% | 40.1% | 3.8% | 7.1% | 4.7% |
| Ethylene | 28.0% | 76.0% | 63.2% | 72.3% | 22.3% | 46.7% | 43.0% | 48.4% |
| Acetylene | 11.2% | 13.6% | 15.2% | 12.7% | 2.2% | 15.5% | 10.7% | 15.5% |
| Ethane | 47.8% | 9.1% | 20.1% | 14.7% | 35.3% | 34.0% | 39.2% | 31.4% |
| | | | | | | | | |
| **Yield** | | | | | | | | |
| CO2 | 0.2% | 0.2% | 0.1% | 0.1% | 0.4% | 0.1% | 0.1% | 0.2% |
| Ethylene | 0.3% | 9.1% | 6.0% | 11.2% | 0.2% | 1.4% | 0.8% | 1.9% |
| Acetylene | 0.1% | 1.6% | 1.4% | 2.0% | 0.0% | 0.5% | 0.2% | 0.6% |
| Ethane | 0.6% | 1.1% | 1.9% | 2.3% | 0.4% | 1.0% | 0.7% | 1.2% |

The results from the factorial design experiment show that co-feeds of methane and oxygen in the flat plate reaction system can chemically convert methane to C2 hydrocarbons, with very little $CO_2$ in the product gases. The HayeSep Q column used in the GC analysis resulted in overlapping $H_2$, CO, and air peaks, so quantification of CO and $H_2$ was not possible.

Figure 37 is the normal plot of the effects studied in the 23 design. For the un-replicated design, there are no significant effects on the 95% confidence interval.

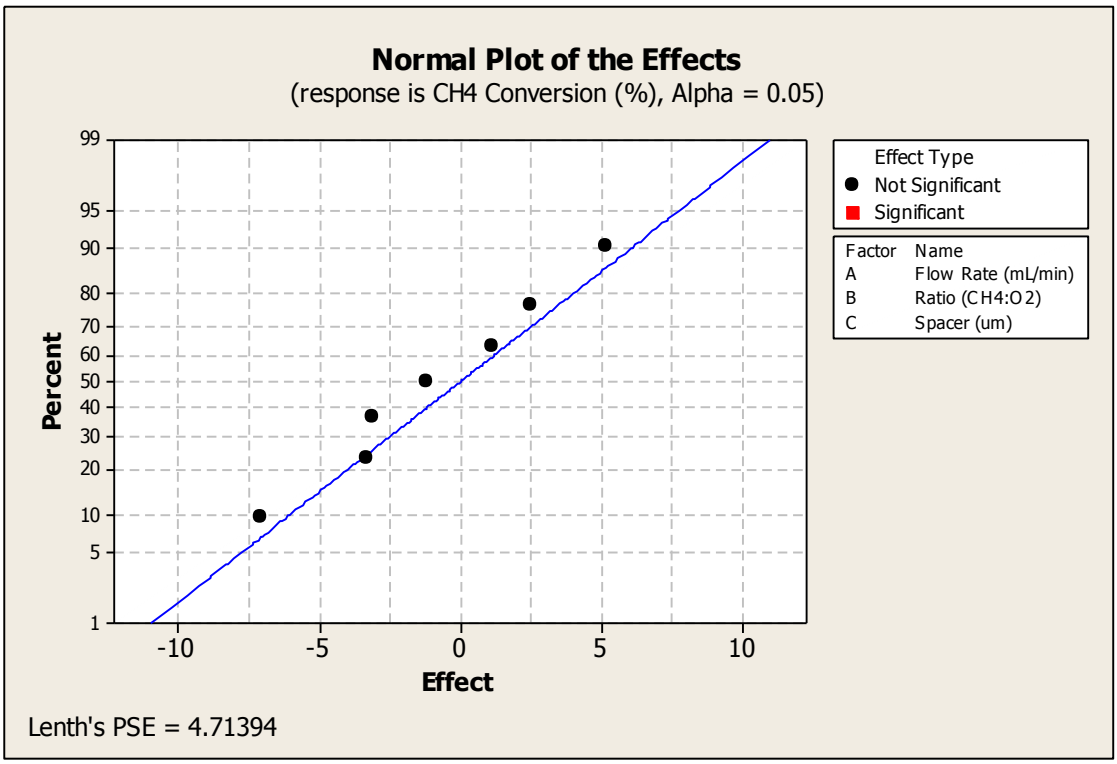


Figure 37: Normal effects plot for the $2^3$ factorial experiment using the flat plate reaction system in methane partial oxidation. For a single replicate, there were no statistically significant effects at the 95% confidence interval.

Randomized run number 5 resulted in the largest methane conversion (15.44%) and large gas phase selectivities to C2 hydrocarbon products, acetylene (12.7%), ethylene (72.3%) and ethane (14.7%). Run 5 corresponds to a slow flow rate (17.5 mL/min), a methane to oxygen feed ratio of 3:1, and a larger discharge gap (750 μm). These selectivities do not include solid carbon formation, as there was no reliable method to measure solid carbon deposition. The proportion of product that forms solid carbon in a single GC sample is likely so small that it does not affect the results significantly. Further studies were undertaken at the same conditions as randomized run 5, namely an investigation to the effect of using pure oxygen in place of air and the effect of adding water vapor to the feed. The results for the further studies are shown in table 2.

Table 2: A simple further investigation into the run conditions at the highest conversion in the 23 factorial design. Run 5 in the factorial design was carried out with air. The same experimental run was also carried out with pure oxygen and pure oxygen saturated with water vapor.

**Run 5 Comparison**

| | Air | $O_2$ | $O_2$ and $H_2O$ |
|---|---|---|---|
| Flow Rate (mL/min) | 17.5 | 17.5 | 17.5 |
| Gas Ratio CH4:O2 (mol:mol) | 3 | 3 | 3 |
| Discharge Gap (um) | 750 | 750 | 750 |
| | | | |
| **Methane Conversion** | 15.44% | 12.43% | 10.93% |
| | | | |
| **Selectivity** | | | |
| CO2 | 0.4% | 1.4% | 1.4% |
| Ethylene | 72.3% | 76.7% | 73.9% |
| Acetylene | 12.7% | 12.9% | 12.1% |
| Ethane | 14.7% | 9.0% | 12.5% |
| | | | |
| **Yield** | | | |
| CO2 | 0.1% | 0.2% | 0.2% |
| Ethylene | 11.2% | 9.5% | 8.1% |
| Acetylene | 2.0% | 1.6% | 1.3% |
| Ethane | 2.3% | 1.1% | 1.4% |

The results in table 2 correspond with the GC traces shown in figure 36. Here, it would appear that no real benefit is gained from using pure oxygen feeds or from adding water vapor to the feed gas flow. Interestingly, the generation of ethane in the products largely disappears when using pure oxygen.

While the factorial design did not determine any statistically significant effects on the responses, methane conversion and product selectivity responses, there are some trends that are worth noting. The contour plots in figure 38 show the methane conversion as a function of the spacer thickness compared to both the gas flow rate and the methane:oxygen feed ratio. While there were no statistically significant effects on the 95% CI, methane conversion in the flat plate reaction system does appear to follow some general trends. Generalizing the results shown in the contour plots, methane conversion increases with a larger discharge gap, increases with smaller gas flow rates, and increase

with increasing oxygen content in the feed. Smaller flow rates and larger oxygen content logically result in higher methane conversion. Larger discharge gaps resulting in increased conversion could have to do with the way that gas flows in and around the active discharge zone. Another consideration is residence time in the active discharge zone, and larger discharge gaps could lead to a longer residence time in the chemically active area.

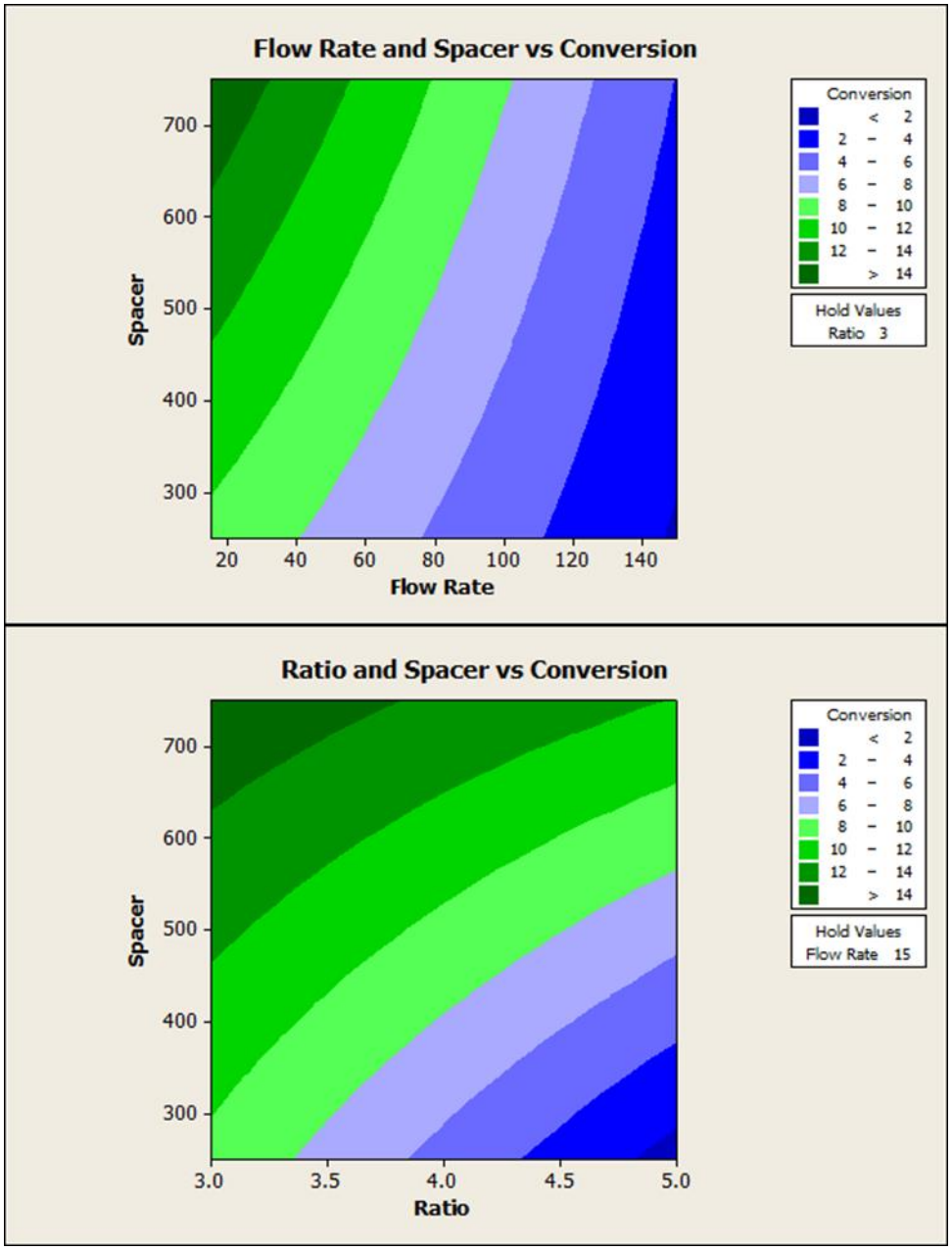


Figure 38: Contour plots of methane conversion vs the gas flow rate [mL/min] and the discharge gap/ spacer thickness [µm] (top) and methane conversion [%] vs the gas composition ratio [$CH_4$:Air] and the

discharge gap/ spacer thickness (bottom). While the single replicate factorial design did not find any statistically significant effects, the contour plots do suggest that there is a patterned change in methane conversion with respect to the studied factors.

The flat plate reaction system was ultimately not adequate to generate reliable, reducible data, and as a result was abandoned for later reactor designs. However, the flat plat system was able to demonstrate methane conversions up to 15.44% in a flat plate corona discharge microreactor enhanced with a CNT electrode. The low conversion is likely a result of localized discharges. As a result, next generation reactor designs that create more controlled discharges in a larger percentage of the reaction volume should enable much higher methane conversions. Our initial results in this flat plate system show that the nonthermal plasmas favor $C_2$ hydrocarbon products in methane/air and methane/oxygen flows.

## Point to Plane Reactor

The experimental data generated with the point-to-plane reactor platform was also worthwhile, and in many ways superior to the data generated with the flat plate reactor. Many of the advantages of the point-to-plane reaction geometry are discussed in the *Reactor Design* section. Not least of these advantages is the incorporation of a glass viewing window into the reaction zone, which allows for visual inspection of the discharge. The glass window also allows for the collection of optical emission spectra from the discharges, which is useful in identifying excited species and corroborating data collected with other analytical methods, such as gas chromatography.

The following paper, titled “Methane Coupling in an Atmospheric Pressure DC Discharge Microreactor”, does an excellent job summarizing data collection for methane and oxygen flows in the point-to-plane microreaction platform.

# Methane Coupling in an Atmospheric Pressure DC Discharge Microreactor

Peter B. Kreider, Justin Pommerenck, Alexandre F.T. Yokochi

*In Preparation*

**Abstract**

Nonthermal plasmas generate high concentrations of excited species that can simultaneously exist at high energy and far from thermodynamic equilibrium, making them useful tools in chemistry and engineering. The reaction environment generated by nonthermal plasmas is well suited for the activation of non-spontaneous gas phase reactions. Microplasmas, roughly defined as plasmas that are generated within sub-millimeter dimensions, provide enhanced stability, improved excited species density, increased nonequilibrium properties, higher electron temperature, and better energy efficiency along with reduced onset voltages compared to traditional nonthermal plasmas, making it a promising tool for plasmachemical processing pathways. In this work, a microreactor capable of generating low power atmospheric pressure glow discharges is used in methane and oxygen processing. The reactor effectively performs methane coupling to $C_2$ hydrocarbons with 20% methane conversion and 90% selectivity to C2, achieving one pass yields of 18% with no traditional catalysis or downstream processing.

**Keywords**

Microreactor, nonthermal plasma, methane coupling, plasmachemical

## Introduction

The direct chemical conversion of methane to more valuable products has been actively studied since the early 1900s.[2] Methane is difficult to transport and store and is not easily accessible in chemical synthesis. As a result, methane is often processed into syngas via steam reforming, a process that requires large amounts of energy and further downstream processing. Many researchers have investigated the direct chemical activation of methane reactions that target organic oxygenates like methanol or higher hydrocarbons via methane coupling. The direct conversion of methane to methanol and catalytic oxidative methane coupling to $C_2$ hydrocarbons and have both been extensively studied.[2, 154] In general, traditional catalytic methane reactions have difficulty activating the methane C-H bond without simultaneously enabling the activation of deep oxidation products like CO and $CO_2$ and typically suffer less than desirable yields to target products.[2, 154] Several more recent efforts have investigated the plasmachemical activation of methane as an alternative to thermocatalytic methods, usually employing electrically generated nonthermal plasmas. These efforts have focused on dielectric barrier discharge (DBD)[3, 5-8], corona discharge[5, 9-12], the combination of a plasma and traditional catalysis[13-16], and occasionally other plasma sources such as gliding arc discharges or microwave generated plasmas.[17, 18] Nonthermal plasmas are of interest because they can generate high concentrations of excited species that exist at high energy while the bulk of the media remains cool, enabling the activation of reactions at or near room temperature. Recently, microplasmas, roughly defined as plasmas that are generated within sub-millimeter dimensions, have begun to attract attention because they can provide enhanced stability, improved excited species density, increased nonequilibrium properties, higher electron temperature, and better energy efficiency along with reduced onset voltages compared to traditional nonthermal plasmas, making them a promising tool for plasmachemical processing pathways.[56, 91, 101, 103] Microreaction technology and the use of components and structures on the microscale creates strong gradients with respect to temperature, concentration, pressure, and reactive species.[1] This enables rapid heat and mass transfer within the system and a finer degree of control over reaction parameters. These properties open new processing regimes that are especially beneficial for reactions

involving fast reaction times and unstable intermediates, such as plasmachemical systems.

Herein, a simple microplasma reactor is used to investigate plasmacatalytic oxidative coupling of methane. The designed system operates at low powers, at high flowrates, and with no downstream catalysis, and as a result generally outperforms many other methane coupling reaction pathways currently studied.

**Materials and methods**

The reaction system employed in this study is an effective miniaturization of the traditional point-to-plane atmospheric pressure corona discharge electrode system, and consists of a discharge gap of 1mm or less and a reaction volume of approximately 10 $mm^3$. Most of the point-to-plane systems in literature use discharge gaps that range from 1 to 50 cm, and only a few venture below the 1 mm length scale.[138, 142-144, 146-149] The microplasma reactor system consists of the machined microreactor body, a high voltage power supply, and downstream analytical equipment, shown in figure 39.

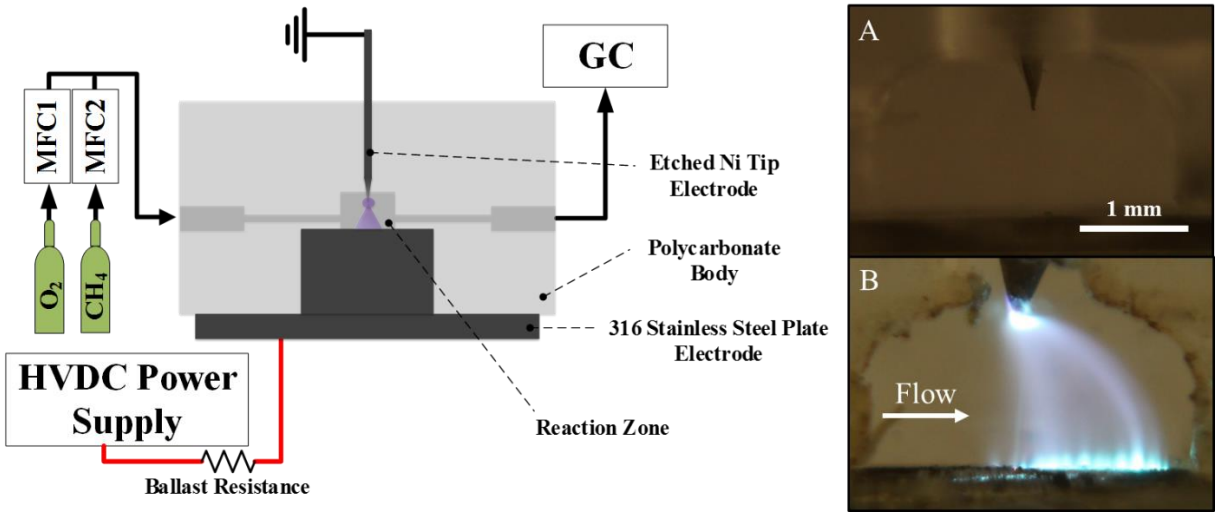


Figure 39: Experimental schematic for the flow-through plasma microreactor system. A) The reaction zone before experimental operation with an unused Ni tip electrode and B) a steady glow discharge in 3:1 CH4:O2 flow at 40 mL/min with a sustaining voltage of ~600 V and 2.1 mA discharge current after several hours operation time.

The microreactor itself is machined out of polycarbonate with inlet and outlet gas connections for 1/16” #10-32 fittings and a microreactor zone with two electrode contacts and a glass viewing window. The reaction zone is milled out of the polycarbonate body

with a 0.078” drill bit, allowing for inner dimensions 1.651 mm deep, 1.651 mm tall, and about 3.5 mm from end to end. The total reaction volume is approximately 10 $mm^3$. A 316 stainless steel plate electrode forms the bottom of the flow through channel, and a piece of soda lime glass is held in place to form the front wall of the reaction zone to allow for optical analysis. The top wall of the reaction zone has a 1/16” clearance hole to allow the high aspect ratio electrode to be inserted into the reaction zone at various discharge gap distances. The high aspect ratio electrode can be a variety of materials, but in this system is an electrochemically etched 1/16” Ni rod (1/16” Ni Rods from ESPI Metals (Alloy 201, stock#: Knd1141)). The nickel etching procedure is adapted from the methods reported in Cavallini and Biscarini.[155] The etched Ni electrode is very sharp and provides strong electric field gradients that enable corona and glow discharge modes in the microreaction system (figure 1A). The tip is degraded over time and is considerably less sharp after extended use, but still functional as an electric field strength enhancer (see figure 1B). The degradation of the Ni tip electrode occurs as a result of electrons and ions eroding the metal surface. The very small volumes of eroded Ni are deposited on other parts of the reactor. The high voltage DC power supply (Glassman High Voltage Series EQ 10 kV Power Supply) is attached to the stainless steel plate electrode for negative polarity dc discharges. A ballast resistor is present to limit circuit current after electrical breakdown occurs in the reaction zone. The ballast can vary in size, but for this system is 1 MΩ (Vishay Dale Rox-3) and allows for steady state current in the ~1-5 mA range. An HP 54542A Oscilloscope (2 GSa/s 500 MHz) is used to probe the electrical properties of the discharge along with a high-voltage differential probe (Keysight N2891A 70 MHz) to directly measure voltage drop across the reactor after electrical breakdown. Methane and oxygen reactant gases are supplied to the system with two mass flow controllers (Brooks 4800 series Mass Flow Controllers, O2, 0-500 SCCM) that are controlled and monitored with a custom LabView program and a data acquisition box (NI USB-6008 DAQ). An SRI 8610C GC equipped with an HID detector is used for downstream gas analysis. The GC system uses a 6’ x 1/8” SS Hayesep D Packed column with 10 psi He carrier pressure and 30 psi He make-up pressure with a column oven temperature of 120 °C. A spectrometer is used to capture optical emission spectra of the

discharge through the front glass window. (AvaSpec 3648-USB2-FCPC, grating: UA, from 200 nm to 1100 nm, options: DUV3648-coating, DCL-UV/VIS-200, Slit-10, OSC-UA with FC-UV400-2-SR fiber optic cables). A typical experimental run involves setting a flow rate from the mass flow controllers and applying a steadily increasing voltage to reaction system shown in figure 1 until electric breakdown occurs in the discharge gap, typically around 2 kV. In this system, using a ballast resistance of 1 MΩ, the discharge is typically in a steady glow mode at a sustaining reactor voltage in the range of 500 to 1000 V. Circuit current is adjusted by changing the total applied potential at the power supply.

**Results and Discussion**

Ideally, methane coupling reactions could take place in the absence of oxygen, and in fact we have demonstrated significant production of C2 hydrocarbons in pure methane feeds. However, at methane feed percentages above 80%, the discharge becomes spatially very narrow and generates a carbon filament that grows across the discharge gap, eventually creating a carbon bridge that shorts the reactor and extinguishes the plasma. One of the carbon filaments was recovered and imaged using SEM, and is shown in figure 40.

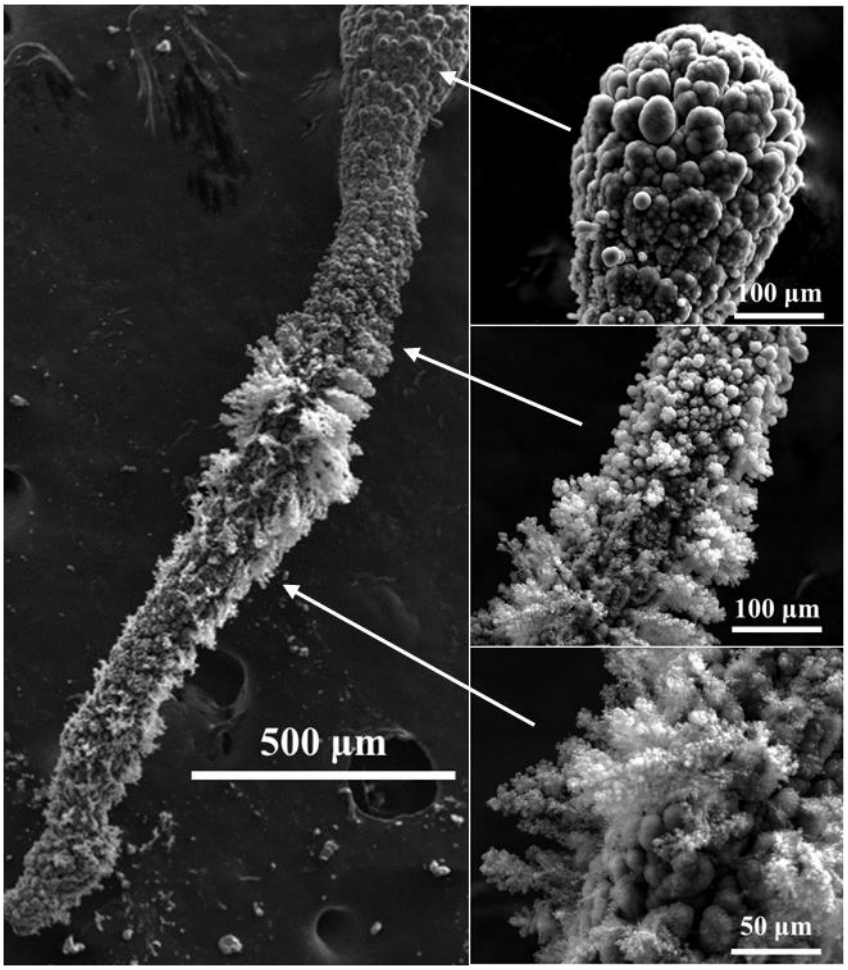


Figure 40: SEM image of a carbon filament formed in the filamentary discharge in methane rich flows. The rounded head of the filament grows and extends towards the sharp electrode tip functioning as the cathode. Towards the middle of the filament and continuing down towards the anode, feather-like carbon nanostructures appear.

The presence of oxygen in the gas stream prevents the formation of the carbon filament and, interestingly, does not seem to necessitate the formation of large amounts of CO or $CO_2$. Based on this preliminary study with atmospheric pressure DC glow discharges, the optimum $CH_4$:$O_2$ volumetric feed ratio (mL:mL) is approximately 3:1, where methane conversion is maximized at 19.5% and $C_2$ product selectivites are 90.7%, for $C_2$ product yields around 17.7% for a single pass process. The effect the methane to oxygen feed ratio at discharge powers around 1.5 watts can be seen in figure 41.

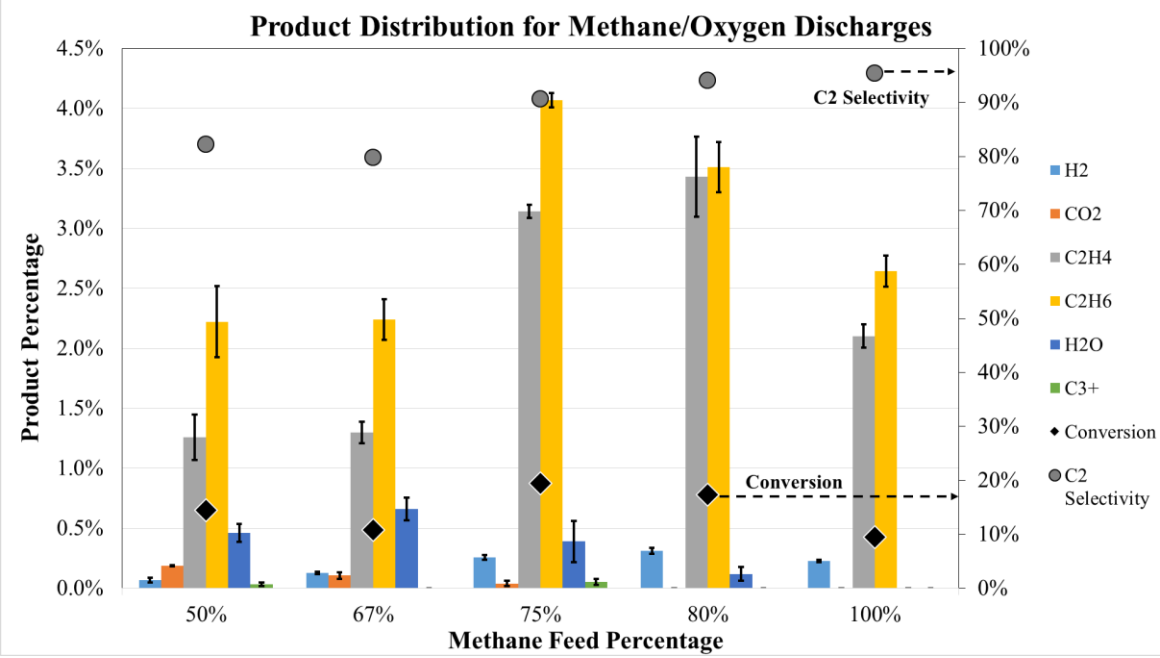


Figure 41: Product distributions and methane conversion for varying feed compositions of oxygen and methane, ranging from a 50/50 mixture to pure methane feed gas. While electrical properties vary slightly with feed gas composition, typical operating conditions are approximately 750 V sustaining voltage and 2 mA discharge current for approximate discharge power of 1.5 W.

The carbon balance for the reaction system varies depending on specific reaction conditions but generally greater than 80% and often greater than 90%. Assuming that there is some error in the analytical equipment as a result of calibrations, imperfect sample flows to the sample loop, and changes in HID sensitivity as runs progress, there is no more than 10% of the carbon in the methane feed that remains unaccounted for. This 10% is likely attributable to losses from solid carbon (C) deposited on reactor components or as carbon monoxide (CO) which is not directly measured using the GC as it co-elutes with oxygen.

The current that passes through the discharge should have a significant effect on product distributions and chemical conversion. The effect of discharge current in 3:1 $CH_4$:$O_2$ flow

can be seen in figure 42.

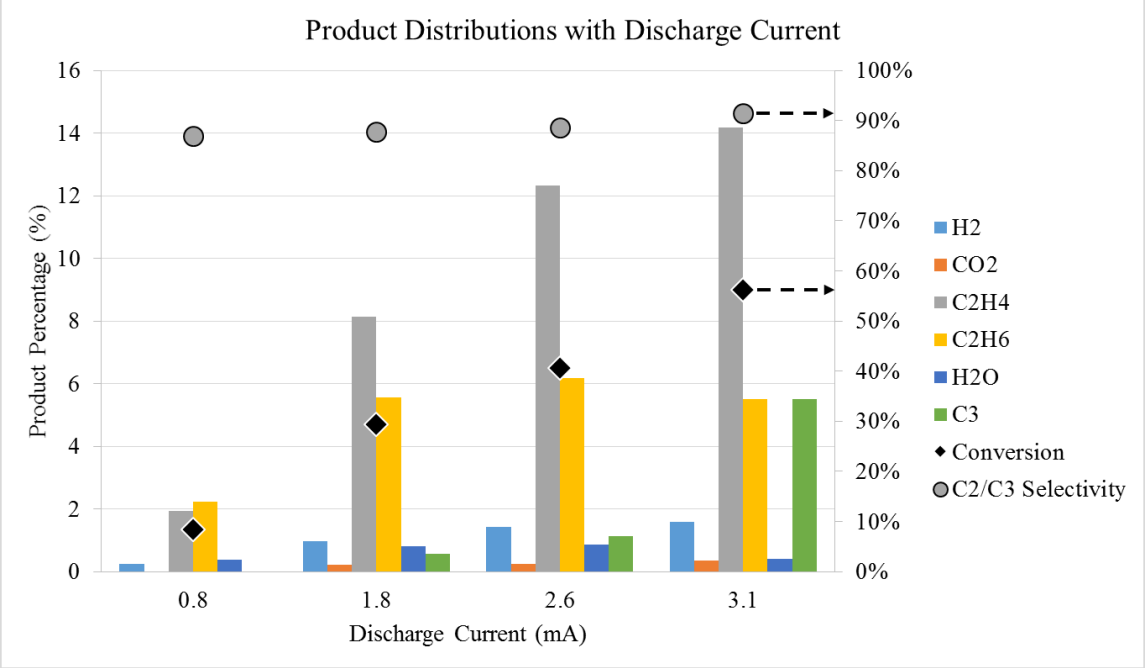


Figure 42: Product distributions as a function of discharge current in a 3:1 methane: oxygen mixture flowing at 40 mL/min, equivalent to a 15 ms residence time in the reaction system.

The discharge current controls the operating regime of the plasma and is directly related to the density of electrons and thus excited species in the discharge. As the discharge current increases, methane conversion increases linearly. The selectivity of methane condensation products (i.e. C2 and C3 hydrocarbons) is relatively constant at ~90%. At higher discharge currents, C3 hydrocarbons start to appear more readily. A current of 0.8 mA is a reasonable starting point as it is slightly above the minimum discharge current needed to enable a steady glow discharge. At discharge currents higher than about 4 mA, the methane:oxygen flow begins to generate more solid carbon on the electrodes, which then glow orange and heat the reaction zone, often leading to reactor failure. At a discharge power of 2.5 watts (3.1 mA and 800 Volts), methane conversion reaches 56.2% and C2/C3 hydrocarbon selectivity reaches 91.5% for one pass yields of 51.4% for C2/C3 hydrocarbons.

Optical emission spectra (OES) for the discharges were collected through the front viewing window of the microreaction system. Spectra in the 300 to 800 nm range for pure oxygen, pure methane, and a 3:1 mixture of methane:oxygen are shown in figure 43.

The emission spectrum for the 3:1 $CH_4$:$O_2$ mixture appears very similar to the pure methane emission spectrum and the emission line for O at 757 nm is absent. The $C_2$ swan system ($A^3\Pi_g \rightarrow X^3\Pi_u$ transition) provide most of the visible emission bands.[153] The Hα emission line at 656 nm is readily identified. CH species can also be easily seen, notably the 4300Å series ($A^2\Delta \rightarrow X^2\Pi$ transition) and the 3900Å series ($B^2\Sigma^- \rightarrow X^2\Pi$ transition).[153]

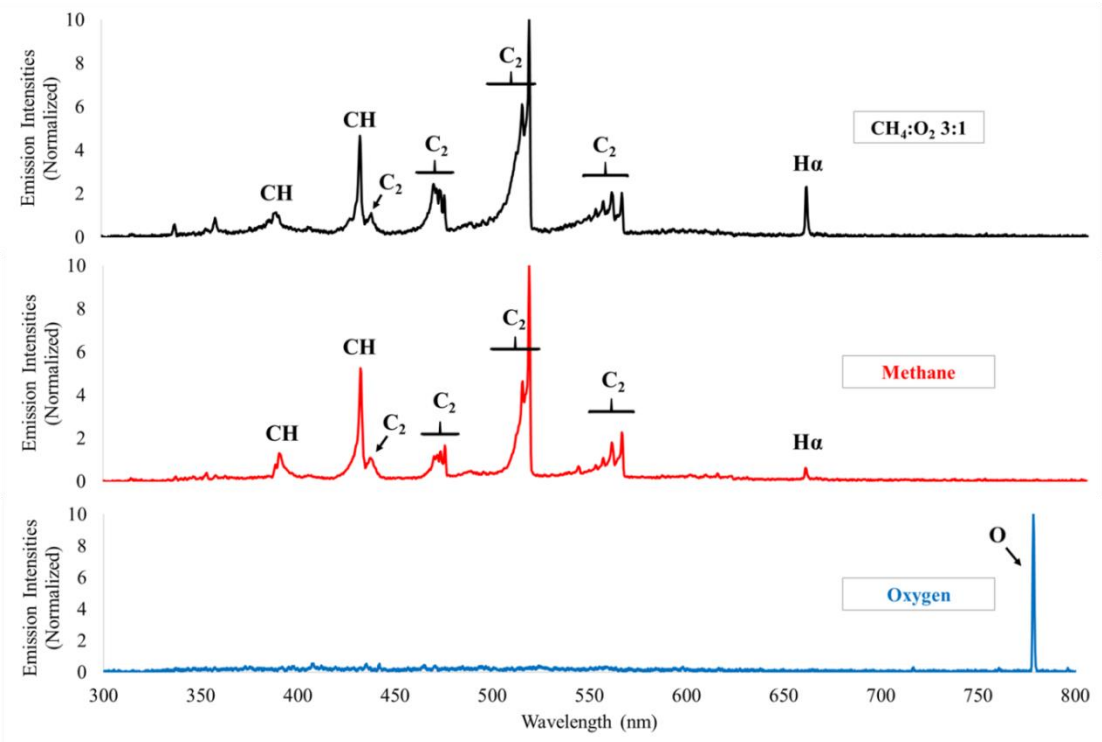


Figure 43: Normalized optical emission spectra discharges in pure $O_2$, pure $CH_4$, and a 3:1 $CH_4$:$O_2$ mixture. Emission bands for the C2 Swan system, the CH 4300 Å system, and Hα can be identified when methane is present in the discharge. A single emission line at 757 nm is seen in pure oxygen flows.

Using a continuous OES sampling approach, the emission intensities for the identified bands can be tracked as a function of discharge current. These emission intensities can be correlated with the products quantified via gas chromatography, shown in figure 44.

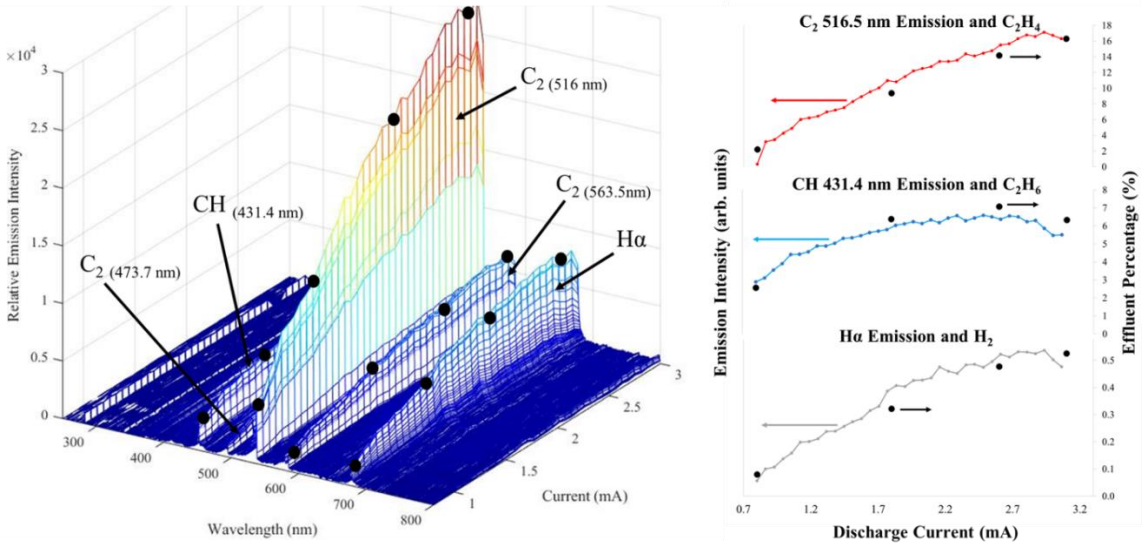


Figure 44: Optical emission spectra and product percentages as a function of discharge current. A) The emission band intensities as a function of discharge current in a 3:1 $CH_4$:$O_2$ reactant gas. The 5 major emission bands are identified. The dots on emission lines represent the values of discharge current where GC samples were taken, and correspond to 0.8 mA, 1.8 mA, 2.6 mA, and 3.1 mA. B) C2 Swan emission intensity at 516.5 nm with the concentration of $C_2H_4$ in the product gas. C) The CH 4300 Å system emission intensity at 431.4 nm with the concentration of $C_2H_6$ in the product gas. D) Hα emission intensity at 656.28 nm with the concentration of $H_2$ in the product gas.

The $C_2$ Swan emission band at 516.5 nm trends with the amount of $C_2H_4$ in the product stream. The emission band for CH at 431.4 nm mirrors the effluent concentration of $C_2H_6$, and not surprisingly, the emission intensity of the Hα line follows closely with the amount of $H_2$ gas produced. The emission band peak intensity values have been correlated with product percentages in the effluent gas. C2 Swan emission intensity at 516.5 nm correlated with the concentration of $C_2H_4$ in the product gas with a correlation coefficient of 0.991. The CH 4300 Å system emission intensity at 431.4 nm correlated with the concentration of $C_2H_6$ in the product gas with a correlation coefficient of 0.989. The Hα emission intensity at 656.28 nm correlated with the concentration of $H_2$ in the product gas with a correlation coefficient equal to 0.961. The other prominent emission bands generally increase with increasing discharge current.

The OES data, coupled with GC analysis, provides a complete picture of the reacting flows in methane coupling. The emission spectra allow for an *in situ* method for chemical analysis and measurement of the product distribution. Additionally, the chemical

signatures seen in the emission bands can be used to propose possible reaction mechanisms and demonstrate the presence of reaction intermediates, such as CH.

**Conclusions**

A microreaction system that can generate stable atmospheric pressure glow for volumetric chemical processing has been developed. The developed system is an effective platform for the oxidative coupling of methane to C2 and C3 hydrocarbons. In this preliminary study on methane processing with oxygen co-feed, the optimum operating point for methane oxygen systems lies around a 3:1 methane:oxygen ratio, where conversion is maximized, selectivity to C2 products remains high, and the formation of a carbon filament, and as a consequence solid carbon deposition, in the discharge gap is greatly diminished.

Methane conversion increases linearly with increasing discharge current and selectivity to longer chain hydrocarbons remains high at varying discharge currents. At higher discharge currents above 3 mA, C3 hydrocarbons start to become major reaction products. Methane processing reactions with to up 56.2% methane conversion, 91.5% selectivity for C2/C3 products, for one pass yields of 51% for C2 hydrocarbons have been achieved. Optical emission spectroscopy as an *in situ* technique for measuring product distributions. In the methane/oxygen discharges, the $C_2$ Swan emission band at 516.5 nm, CH emission at 431.4 nm, Hα emission line at 656.28 nm are correlated with the effluent concentration of $C_2H_4$, $C_2H_6$, $H_2$, respectively.

**Future Work**

The experimental results obtained here will be used to develop a detailed kinetic model of methane reactions in microplasmachemical systems. The OES data could provide insight into the mechanistic reaction pathway. The data suggests that longer hydrocarbon chains C3 and greater could be generated in this reaction system, perhaps at higher discharge power or with several reaction zones in series.

# Plasmachemical Oxidative Coupling of Methane: Performance and Energy Considerations

The oxidative methane coupling results shown here compare favorably in both catalytic performance and energy consumption to recent similar works.[85, 156] In summary, the reaction platform here generates a glow discharge that is sustained by 800 V and 1.8 mA (1.44 watts) for one discharge point. The single point can process methane/oxygen flows at 40 mL/min (residence time of 15 ms) and generate C2 hydrocarbons at ~90% selectivity at methane conversions of 20% in $CH_4$:$O_2$ mixtures at a 3:1 ratio, with higher conversions achievable with higher discharge current. A paper published recently on oxidative methane coupling in a plasmacatalytic system by Delavari et al. is summarized here for comparison in table 3.[156] Their system generated a corona discharge sustained by 3 kV and 10 mA (30 watts) over 5 needle points that could process flows at a 4 mL/min flowrate of $CH_4$:$O_2$ mixtures at a 4:1 ratio. The published work also used a downstream zeolite catalyst to increase conversion/selectivity, and was able to achieve ~70% selectivity to C2 and ~85% methane conversion.

Table 3: Comparison of performance for this work and a recent similar work by Delavari et al.[156] in the oxidative coupling of methane. Ethylene is used as a model compound for values such as molecular weight in these calculations.

| | This Work | Delavari et al. (2014) |
|---|---|---|
| **Voltage (V)** | 800 | 3,000 |
| **Current (mA)** | 1.8 | 30 |
| **Power (W)** | 1.44 | 30 |
| **Power (kW)** | 0.0014 | 0.03 |
| | | |
| **Flow Rate (mL/min)** | 40 | 4 |
| **Flow Rate (mL/s)** | 0.67 | 0.07 |
| **Flow Rate (mol/s)** | 3.0E-05 | 3.0E-06 |
| **Flow Rate (kg/s)** | 8.3E-07 | 8.3E-08 |
| | | |
| **$CH_4$ Conversion** | 20% | 85% |
| **C2+ Selectivity** | 90% | 70% |
| **C2+ Product Yield** | 18% | 60% |
| | $\textbf{Energy per Product} = \frac{\textbf{Power}}{\textbf{Flow Rate} * \textbf{Yield}}$ | |
| **Energy Calculations** | | |
| **Flow Rate C2+ (mol/s)** | 5.36E-06 | 1.77E-06 |
| **Energy per Product (kJ/mol)** | 269 | 16,941 |
| **Energy per Product (MJ/kg)** | 9.6 | 604 |

Many works that employ electrically generated plasmas do so without great consideration for energy expenditure in the plasma. Naturally, many authors discuss energy use and efficiency within the context of their work, but few attempt to minimize energy dissipation in the plasma from the outset. A fundamental reduction in onset voltage was one of the goals of this work from the beginning. Figure 45 is a simple reconstruction of the classical IV curve for atmospheric pressure point-to-plane DC discharge, along with a simple transformation of the curve to power as a function of discharge current. Figure 46 is the same figures, but with power plotted on a log scale.

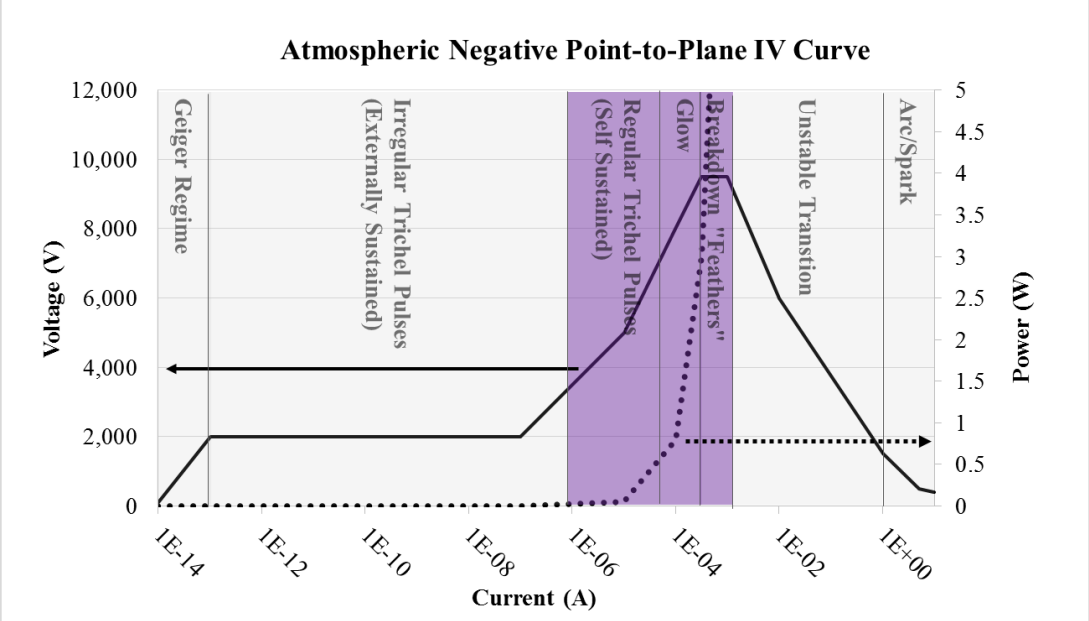


Figure 45: A reworking of the classical IV curve for an atmospheric pressure, negative polarity DC discharge. The voltage-current curve is a transcription of the classic curve, also shown in figure 4D. The power-current relation is shown with the dotted line and the target discharge regimes are highlighted in purple.

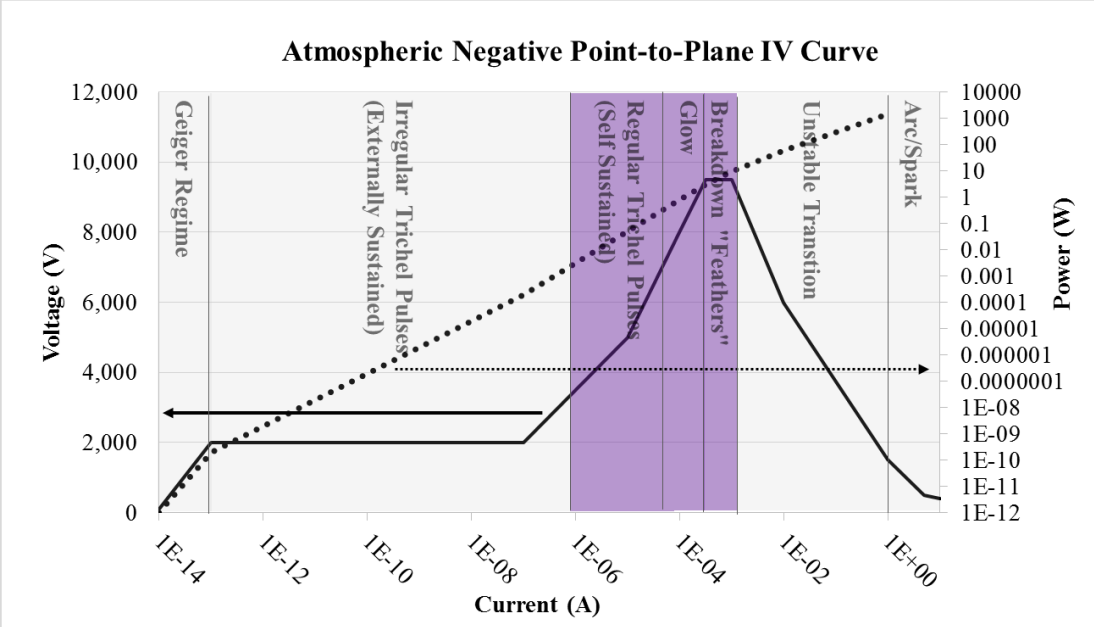


Figure 46: Replotting figure 45 with both power and current on a log scale.

The target operating point is somewhere in the regular self-sustained discharge modes, labeled as regular trichel pulses, glow, and breakdown feathers and colored purple in

figures 45 and 46. These discharge modes are self-sustained, have electron energies high enough to drive chemical reactions, and minimize dissipated power in the discharge. Figure 47 contains images of a glow discharge in a 50/50 mixture of methane and oxygen at varying gas flow rates, and shows how gas flow rates and residence affect power consumption and chemical conversion.

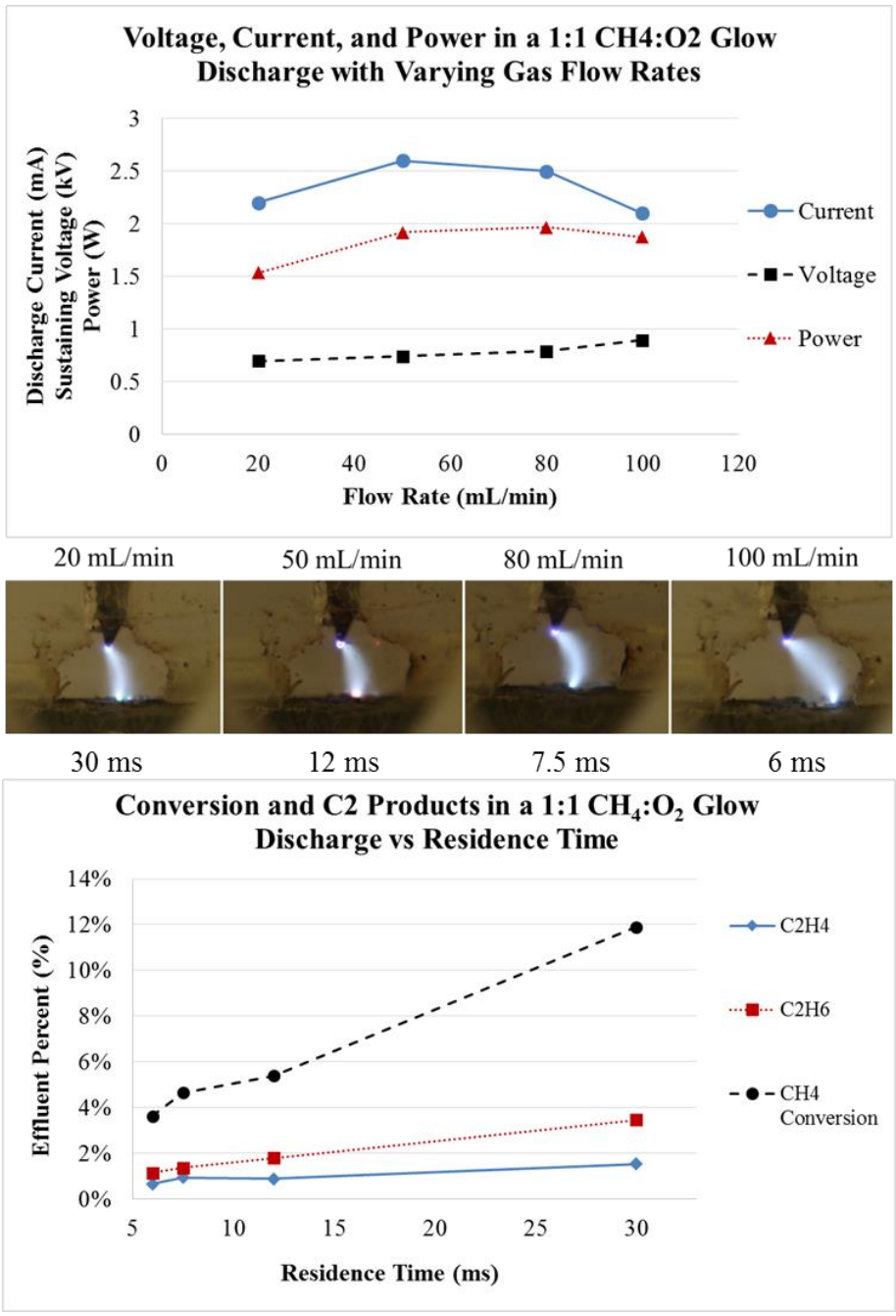


Figure 47: Glow discharge in 1:1 $CH_4$:$O_2$ flows at varying gas flow rates (top) and the effect of residence time on conversion and C2 species production (bottom).

State-of-the-art thermocatalytic methane coupling catalysts have difficulty achieving C2 yields greater than 23%.[157] $Mn/NaWO_4/SiO_2$ catalysts provide the highest selectivity and yields for OCM compared to other catalysts, including the commonly encountered catalysts based on Li/MgO, Mo-based oxides, $Sm_2O_3$, and $La_2O_3$.[157, 158 159, 160]

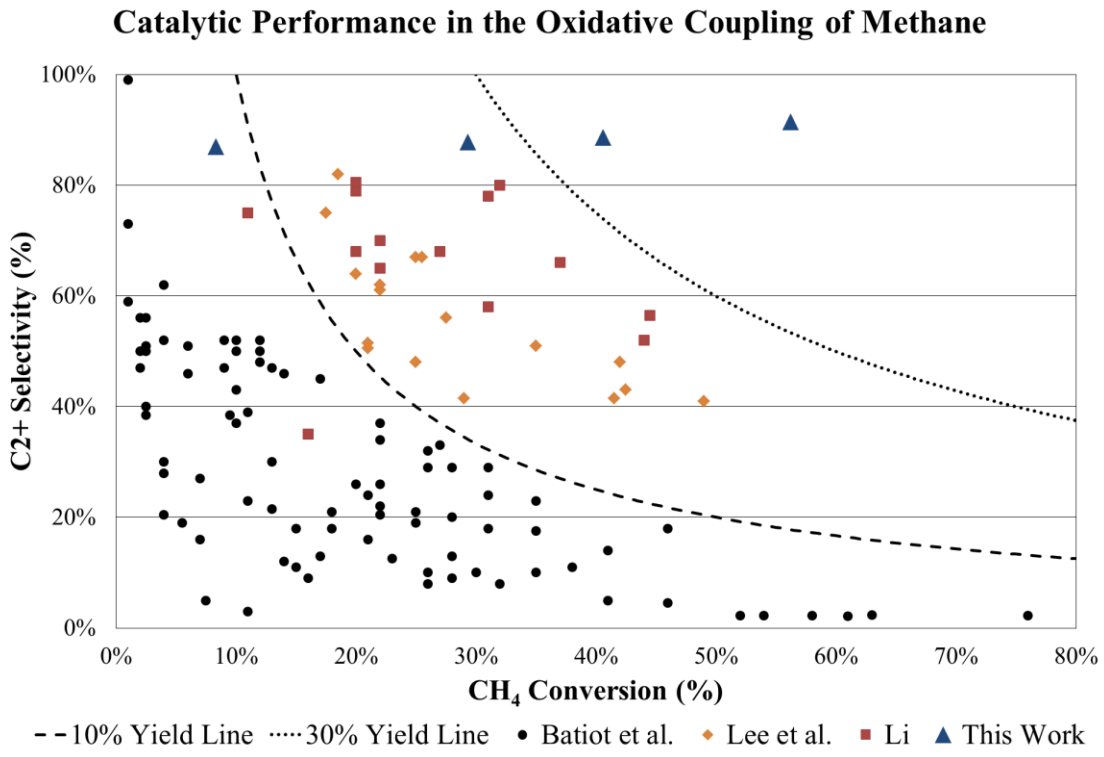


Figure 48: Catalytic performance in the oxidative coupling of methane, partially reproduced from Takanabe.[157] The plotted data is based on work with Li/MgO and MoO based catalysts by Batiot et al.[158] (circles), Li/MgO, $Sm_2O_3$, $La_2O_3$, etc. catalysts by Lee et al.[159] (diamonds), and $Mn/Na_2WO_4/SiO_2$ catalysts by Li[160] (squares), and this work (triangles).

Recent works in plasmachemical methane coupling, including this work, seem to suggest that plasmachemical processing has the capacity to overcome this low yield limitation.[5, 9, 156] Catalysts used in the oxidative methane coupling have difficulty surpassing ~25% yield to C2 hydrocarbons. Generally, if the catalyst enables high methane conversion, it will also have low selectivity to C2 hydrocarbons and generate increased amounts of $CO/CO_2$. If the catalyst has high selectivity to C2 hydrocarbons, the system almost always has relatively low methane conversions. These trends can be seen in a work with typical OCM catalysts using both $O_2$ and $N_2O$ as oxidizing agents.[161] C2+ product yields in OCM reactions with various catalysts reported in the literature are also summarized by Takanabe.[157]

Several works in plasmachemical processing suggest that specific energy input (*SEI*), the ratio of input power (W) to volumetric flow rate ($\dot{v}$), can be used as an indicator of conversion and selectivity.[116, 149, 162]

$$SEI = \frac{W}{\dot{v}} \tag{5}$$

Nozaki et al. generated figures that show both C2/C3 selectivity and $CO_2$/CO selectivity as a function of specific energy input in methane steam reforming reactions in DBD.[162] Those figures have been recreated here in figure 49, along with added data generated in this work. It should be noted that the data points from Nozaki et al. are generated with methane and water co-feed, and the data from this work is generated with methane and oxygen co-feed. However, the trends associated with specific energy input are still interesting and potentially useful in understanding plasmachemical behavior in these discharge systems.

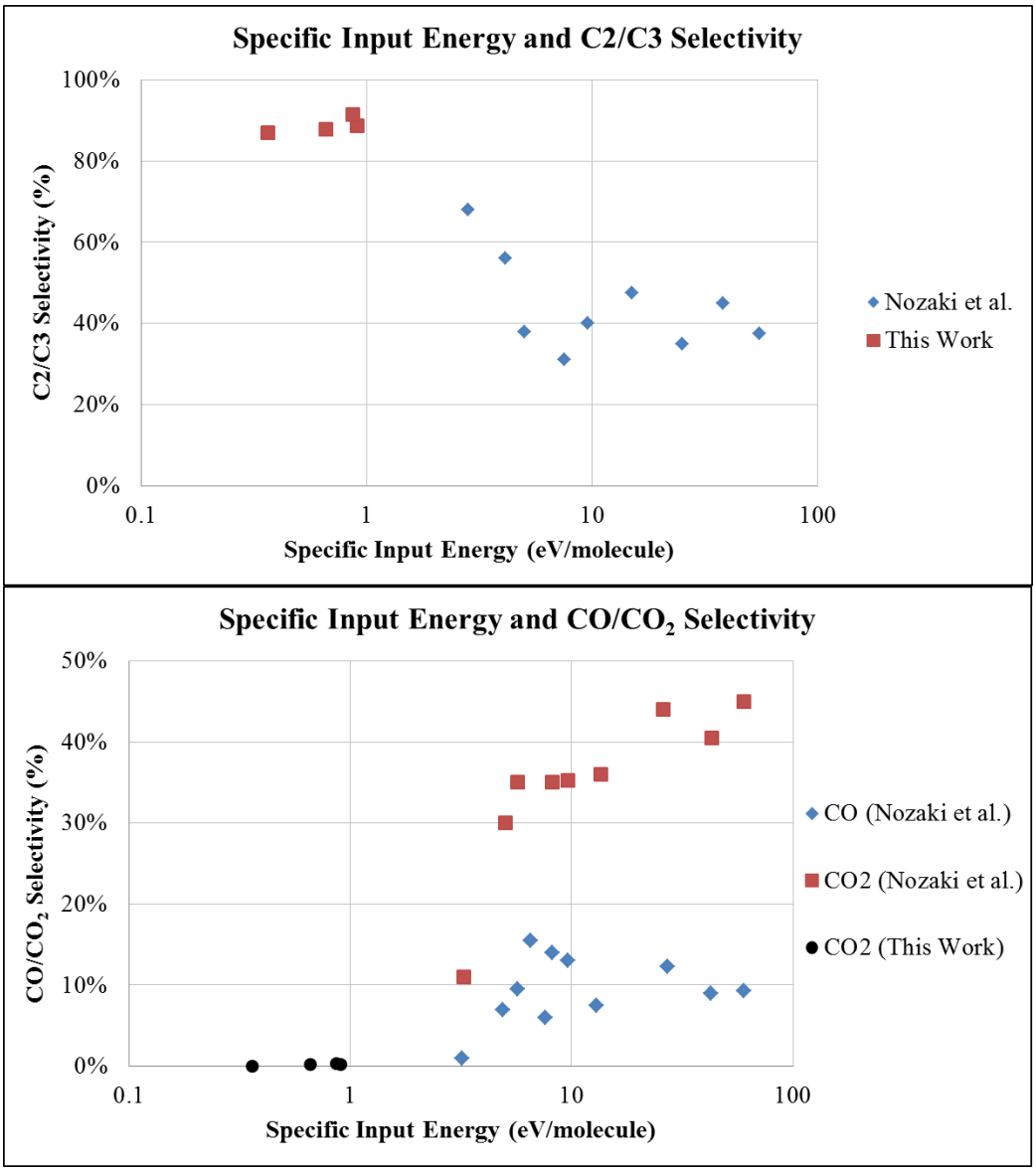


Figure 49: Product selectivities as a function of specific input energy in electron volts per molecule of gas processed, from Nozaki et al. and this work.[162] Data from Nozaki et al. is generated with methane and water feed, data from this work is generated with methane and oxygen feed. Top) C2/C3 selectivities as a function of specific input energy with Nozaki et al. (diamonds) and data from this work (squares). Bottom) $CO/CO_2$ selectivities from Nozaki et al. (CO: diamonds, $CO_2$: squares) and data from this work (CO: triangles, $CO_2$: circles).

The chemical conversion and selectivitiy in plasmachemical methane processing does appear to follow a trend based on specific input energy. Nozaki et al. suggested that at lower specific input energies, C2/C3 selectivity increase and $CO_2$/CO selectivity decrease.[162] Plotting their data in figure 49 along with data generated in this work reinforces that concept, and indeed, at specific input energy less than 1 eV/molecule,

selectivity towards $CO_2$ products is essentially zero and C2/C3 selectivity is greater than 90%.

The bulk gas temperature from the reactor effluent during a discharge in pure oxygen was measured using an ungrounded thermocouple. Typical grounded thermocouples are not compatible with these plasmachemical systems as charged particles influence the voltage reading from the junction potential. Average gas temperature rise in atmospheric pressure glow discharges is reported to be about 20-40 K, which agrees closely with the observations shown here in figure 50.[163]

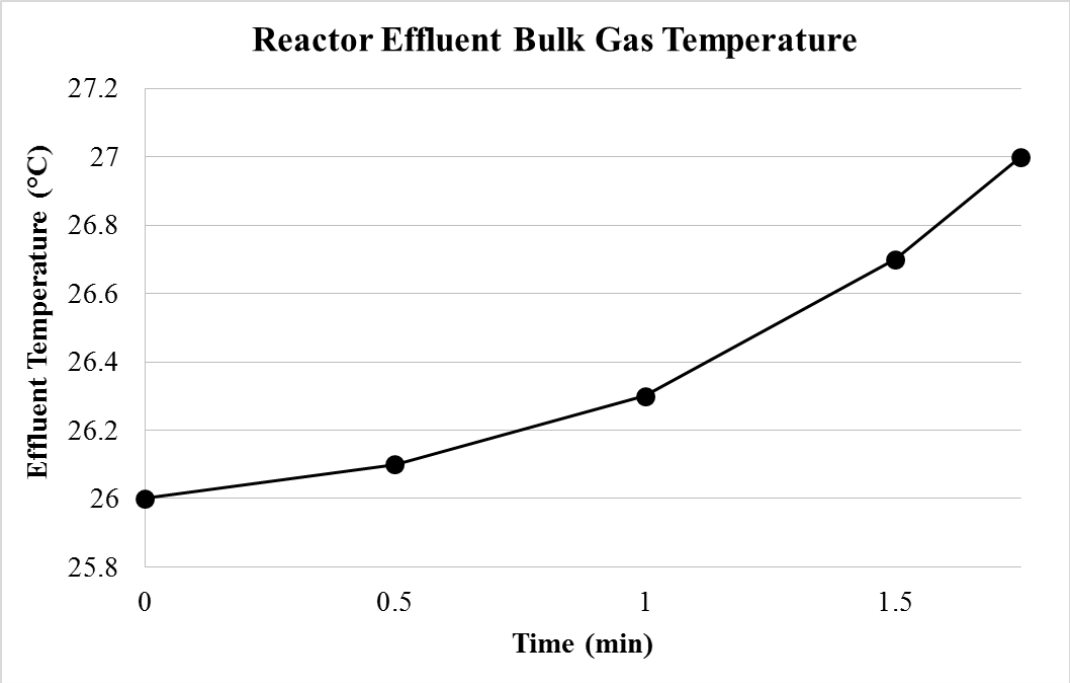


Figure 50: Effluent bulk gas temperature from the point-to-plane reactor during glow discharge in pure oxygen flow.

In depth discussions of the plasma-catalytic activation of methane processing and energy considerations, including energy efficiency calculations, are presented in "Non-thermal plasma catalysis of methane: Principles, energy efficiency, and applications." by Nozaki et al.[85] The equation below, the same one used by Nozaki et al., shows the overall energy efficiency calculation for plasma processing. Here, $\Delta H_{rxn\_i}$ is the enthalpy of the reaction for methane to product *i*, $N_i$ is the number density of the specific product *i*, and $W$ is the total power consumption of the plasma.

$$\eta = \frac{\sum(\Delta H_{rxn\_i} N_i)}{W} \quad (5)$$

Using the standard enthalpies of formation for the C2 and C3 product production, we can obtain the reaction enthalpies, summarized in table 4.

Table 4: Enthalpies of formation and reaction enthalpies for methane coupling reactions.

| | | |
|---|---|---|
| $\Delta H_f$ $CH_4$ | -74.87 | kJ/mol |
| $\Delta H_f$ $C_2H_6$ | -84.68 | kJ/mol |
| $\Delta H_f$ $C_2H_4$ | 52.4 | kJ/mol |
| $\Delta H_f$ $C_2H_2$ | 227.4 | kJ/mol |
| $\Delta H_f$ $H_2O$ | -285.8 | kJ/mol |
| $\Delta H_f$ $C_3H_8$ | -103.85 | kJ/mol |

$$2\,CH_4 \rightarrow C_2H_6 + H_2$$

$\Delta H_{C2H6}$ = 65.06 kJ/mol

$$2\,CH_4 \rightarrow C_2H_4 + 2\,H_2$$

$\Delta H_{C2H4}$ = 202.14 kJ/mol

$$3\,CH_4 \rightarrow C_3H_8 + 2\,H_2$$

$\Delta H_{C3H8}$ = 120.76 kJ/mol

Using the same data that is reported in figure 42 for oxidative methane coupling in a glow discharge as a function of discharge current, we can calculate energy efficiency for the plasmachemical methane coupling reactions. Table 5 summarizes the energy efficiency calculations, and figure 51 shows these results in graphical form.

Table 5: Energy efficiency calculations for methane conversion to C2 and C3 products in the glow discharge microreactor with reaction enthalpies shown in table 4.

| | | | | | | |
|---|---|---|---|---|---|---|
| 40 | mL/min flow | | | | | $\eta = \frac{\sum(\Delta H_{rxn\_i} N_i)}{W}$ |
| 0.0018 | mol/min @ STP | | | | | |
| **2.98E-05** | **mol/s, *N*** | | | | | |
| Reactor Voltage (V) | Discharge Current (mA) | **Plasma Power (W), *P*** | **% $C_2H_6$** | **% $C_2H_4$** | **% $C_3H_8$** | **Efficiency, η** |
| 1,300 | 0.8 | **1.04** | **2.2** | **1.9** | **0.0** | **15.4%** |
| 1,050 | 1.8 | **1.89** | **5.6** | **8.2** | **0.6** | **32.7%** |
| 1,000 | 2.6 | **2.6** | **6.2** | **12.3** | **1.1** | **34.7%** |
| 800 | 3.1 | **2.48** | **5.5** | **14.2** | **5.5** | **46.7%** |

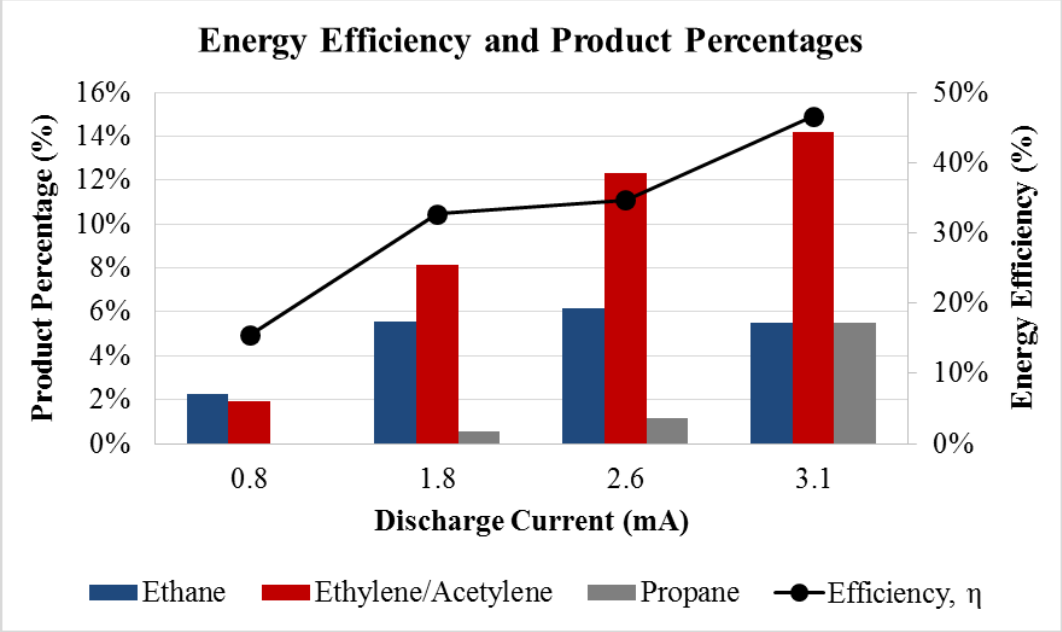


Figure 51: Energy efficiency as a function of discharge current, along with the product percentages for C2 and C3 hydrocarbons.

Literature reports that methane decomposition energy efficiency about 1% for dielectric barrier discharge and the atmospheric pressure glow discharge (APG).[163] The calculations here use the same calculations that many authors use for computing plasma energy efficiency. However, it is important to note that this is a simple calculation that ignores the obvious fact that methane is co-fed with oxygen in this system, and these energy efficiency calculations fail to capture the energy sink that occurs as a result of water formation as opposed to pure hydrogen in pure methane feeds. If water formation is used in the enthalpy calculations, the energy efficiency calculations become negative, and the plasma acts only as a reaction initiator.

## Performance and Energy Efficiency Conclusions

The performance of the nonthermal microplasma reactor developed in this work compares favorably in both catalytic performance and energy consumption to other oxidative methane coupling technologies. This is due in part to targeting discharge regimes that optimize power consumption while maintaining an excited species density that remains suitable for the activation of chemical reactions.

Investigating the effect of flow rate and in turn, residence time in the reaction zone shows that faster flows lead to lower chemical conversion. This is the expected result, as more time spent in the presence of the activating discharge should yield higher concentrations of products. However, the consumed power in the discharge reaches a local maximum and midrange flow rates and is lower at higher flow rates, which suggests potential for energy efficient high flow-rate processing with reduced single pass conversion. Nonthermal microplasmachemical oxidative methane coupling has demonstrated superior performance than traditional thermocatalysis, with conversions greater than 50% and selectivites to C2/C3 products greater than 90%. The reactor effluent bulk gas temperature remains near room temperature during active glow discharge operation. This low power operation leads to low specific energy inputs, the ration of input power to processed volume, which allows for high C2/C3 selectivites and suppresses deep oxidation products CO and $CO_2$. This nonthermal microplasma system results in energy efficiencies that approach 50% in methane coupling reactions. It should be noted that this is due in part to the presence of oxygen in the reaction flows, which creates water as a product and provides thermodynamic driving force to products.

# Preliminary Results in Methane Dry Reforming

Methane processing with $CO_2$, regularly referred to as dry reforming, is of significant interest here. The generation of valuable products from a co-feed of methane and carbon dioxide is of great interest, mainly due to upgrading the waste product carbon dioxide while simultaneously enabling the conversion of methane to more valuable products. Additionally, natural gas is regularly recovered from the ground along with $CO_2$, so the ability to process methane and $CO_2$ together directly would provide additional benefit. The nonthermal microplasma reactor platform developed for methane processing can be easily applied to the exploration of methane dry reforming.

The first investigation into this field was an observation of an electrical discharge through pure $CO_2$. The image in figure 52 shows negative polarity DC discharges in pure $CO_2$ flow at 40 mL/min.

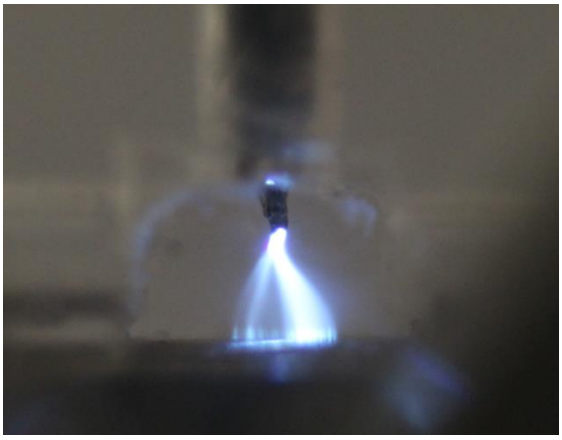

Figure 52: Typical $CO_2$ discharge appearance with blue emissions from the $CO_2$+ transitions.

The pure $CO_2$ discharge is sustained by 2.5 mA and 719 volts, and has a distinct blue hue and striations similar in appearance to the $CH_4$:$O_2$ mixtures studied previously. The traditional target products from dry reforming methane are $H_2$ and CO, so the discharge characteristics of a 1:1 stoichiometric mixture of $CH_4$ and $CO_2$ were also observed. The discharge in 1:1 $CH_4$:$CO_2$ flow at 40 mL/min is sustained by 2.3 mA and 630 volts and shown in figure 53.

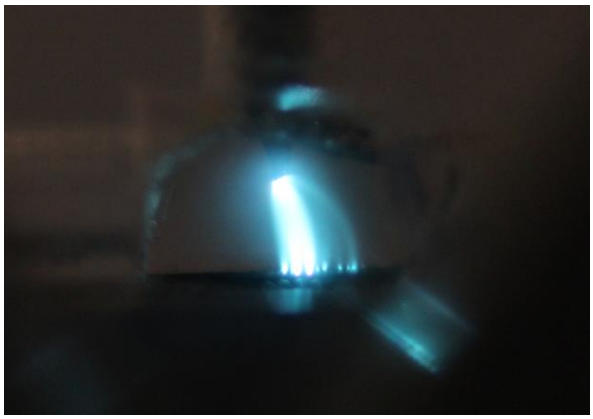

Figure 53: Typical 1:1 $CH_4$:$CO_2$ discharge appearance. The discharge is brighter than in pure $CO_2$, so the background of the image is darker to show more details in the bright discharge.

Simple images are good starting points for discussion, but provide little insight as to chemical species and reaction activation. Optical emission spectra were collected for both pure $CO_2$ and 1:1 $CH_4$:$CO_2$ discharges, shown in figure 54.

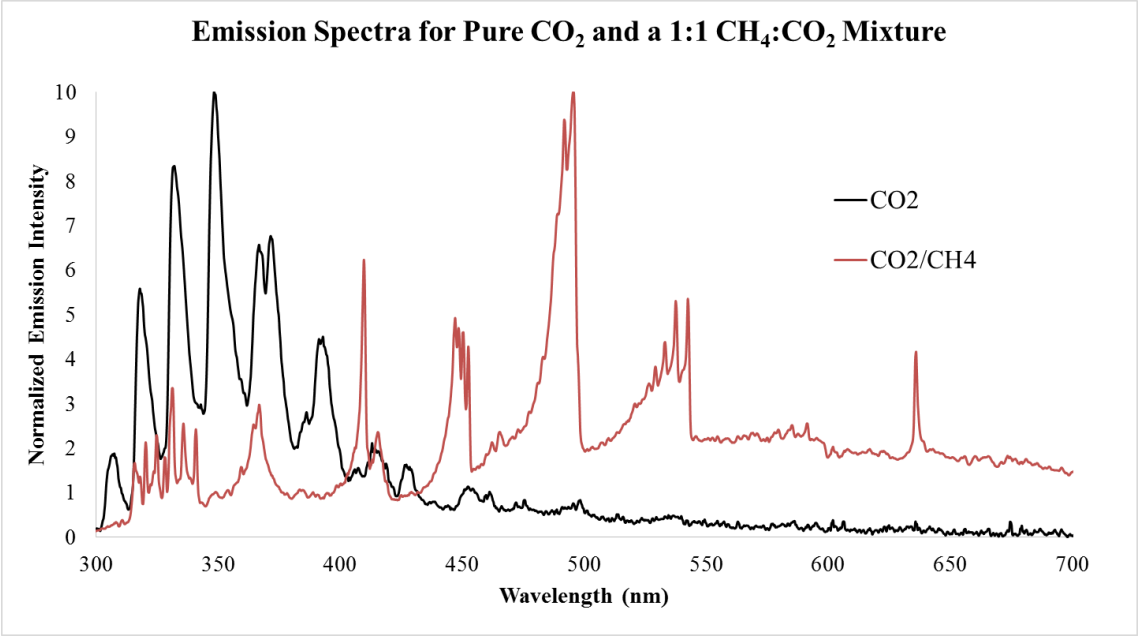


Figure 54: Optical emission spectra for a discharge in pure $CO_2$ and a discharge in a 1:1 $CH_4$:$CO_2$ mixture.

The $CO_2$ emission spectra is almost solely a result of the $CO_2^+$ $A^2\Pi_u \rightarrow X^2\Pi_g$ transition.[164] The 1:1 $CH_4$:$CO_2$ mixture has an emission spectrum that is very similar to $CH_4$:$O_2$ mixtures. The 1:1 $CH_4$:$CO_2$ emission spectrum has an increased baseline emission, due in part to blackbody emission from heated carbon deposits in the discharge. The direct comparison between a 3:1 $CH_4$:$O_2$ and the 1:1 $CH_4$:$CO_2$ can be seen in figure 55.

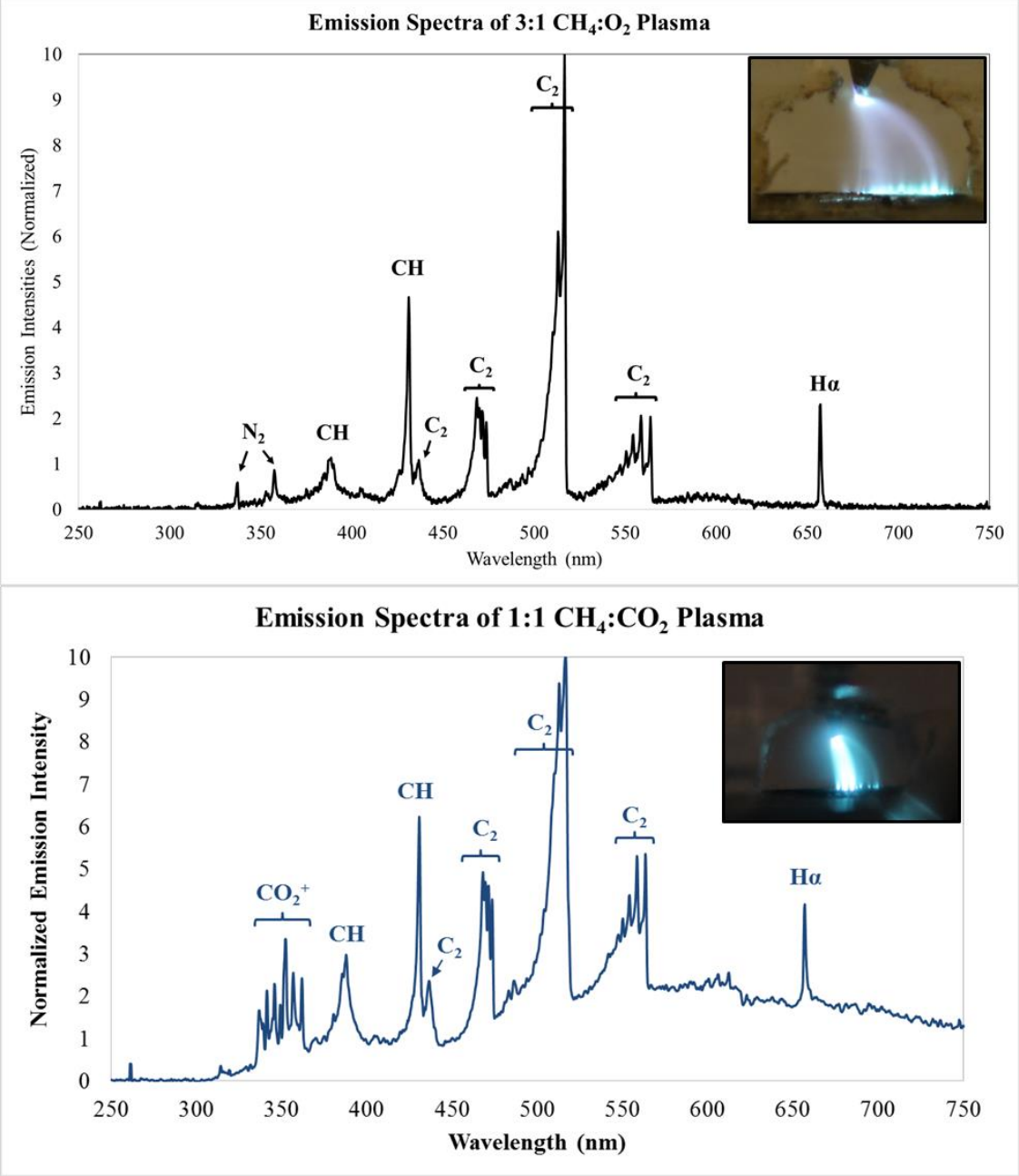


Figure 55: Emission spectra of $CH_4$:$O_2$ 3:1 and $CH_4$:$CO_2$ 1:1 mixtures in a glow discharge. Inset images taken under the same flow conditions for each discharge. The CH4:$CO_2$ mixture is significantly brighter, as evidenced by the increased baseline in the emission spectra. This is due in part to formation of coke on the Ni tip electrode in the $CH_4$:$CO_2$ discharge, which emits blackbody radiation and glows orange.

Collected GC data on the products formed in glow discharges for pure $CO_2$ flows and stoichiometric $CH_4$:$CO_2$ flows are presented in figure 56. The dominant products in pure $CO_2$ are the direct breakdown products of CO and $O_2$, with trace amounts of water vapor, which could be from impurities in the reactor or gas lines. In a 1:1 mixture of $CH_4$:$CO_2$,

observed products include $H_2$, $CO/O_2$, $C_2H_4$, $C_2H_6$, $H_2O$, and some small amounts of C3 hydrocarbons. These results are evidence that the constructed microplasma reactor could be a promising platform for methane dry reforming.

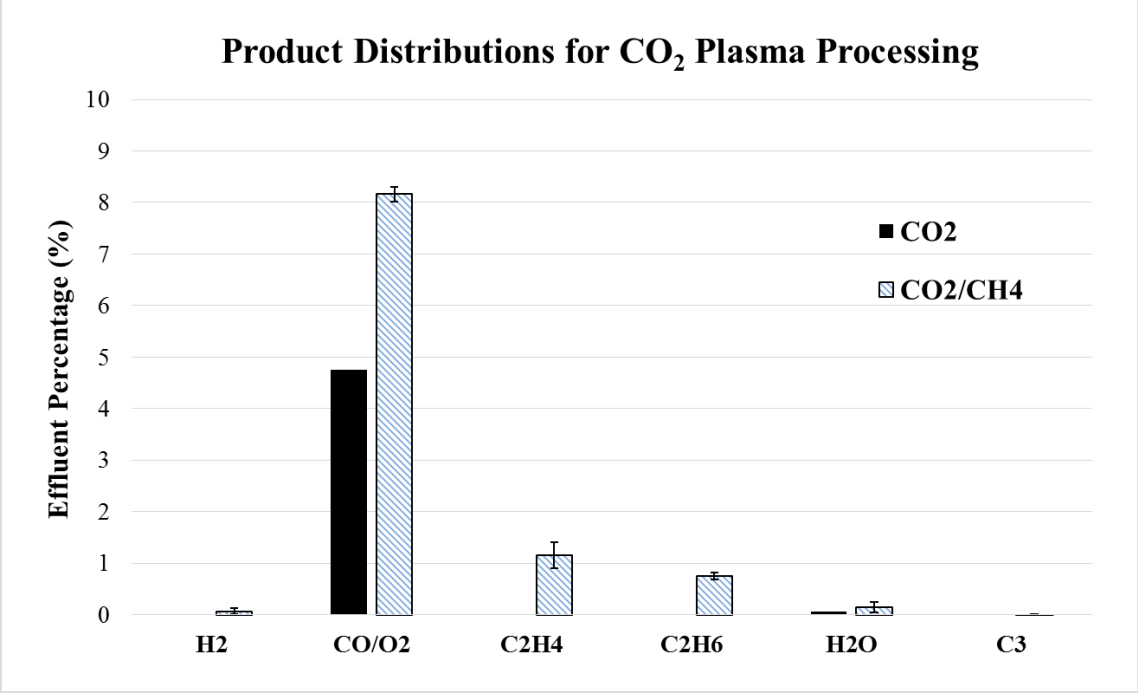


Figure 56: Product distributions for a pure $CO_2$ flow and a flow of $CH_4$:$CO_2$ 1:1, where the balance of the reactor effluent is $CO_2$ and a 1:1 mixture of $CH_4$:$CO_2$, respectively.

Figure 57, which depicts the formation of carbon deposits in methane dry reforming and the subsequent removal of carbon deposits in pure $CO_2$ discharges, suggests that the dominant mechanism for carbon deposition is methane decomposition. Future work using DC discharges for methane dry reforming should reduce the concentration of methane in the feed gas to reduce the amount of coke formation in the reactor. An additional concept worth exploring is a feed of both $CO_2$ and $H_2O$ with $CH_4$ for combined methane reforming.

Figure 57: Discharge behavior in 1:1 CH4:$CO_2$ mixtures. Left) Formation of carbon deposits on the Ni tip, the orange emission from the heated carbon is prominent. Middle) Immediately after the plasma is extinguished by removing applied potential from the power supply. Carbon deposits are easily visible. Right) Initiating discharge again in pure $CO_2$ flow, the carbon deposits are removed quickly and the discharge returns to the characteristic blue glow

## Methane Dry Reforming Conclusions

Discharges in both pure $CO_2$ and a co-feed of 1:1 $CO_2$:$CH_4$ create products that warrant further investigation into microplasma $CO_2$ processing. For pure carbon dioxide feed streams, single pass dissociation to CO and $O_2$ is observed. $CH_4$/$CO_2$ mixtures show more $CO_2$ dissociation and the formation of C2 hydrocarbons. A 1:1 $CH_4$:$CO_2$ mixture quickly forms coke on the sharp tip electrode, so future explorations should explore reaction mixtures that have higher $CO_2$ concentrations in the feed gas.

# Desulfurization

In addition to methane processing, the constructed nonthermal microplasma systems have been used to evaluate the feasibility of electrical discharge driven oxidation of refractory sulfur compounds in fuel-like media. Traditionally, refractory sulfur compounds like dibenzothiphene are removed using a process called hydrodesulfurization. Oxidative desulfurization, the process of selectively oxidizing and subsequently removing sulfur compounds is explored as an alternative, using electrically generated discharges as the oxidation mechanism. For this purpose, n-decane is used as the "fuel-like media", and dibenzothiophene is chosen as the model refractory sulfur compound.

Historically, several catalysts for the oxidative desulfurization process have been studied. Work with $Mo/Al_2O_3$ catalysts showed decreasing reactivity of refractory sulfur compounds, with dibenzothiophene (DBT) being the most reactive, followed by 4-methyl dibenzothiophene (4-MDBT), then 4,6-dimethyldibenzothiophene (4,6-DMDBT), and simple benzothiophene (BT) being much less reactive than the dibenzothiophenes (DBT > 4-MDBT > 4,6-DMDBT >> BT), with the results suggesting that the oxidative reaction of each sulfur compound can be treated as a first-order reaction with activation energy around 28 ± 1 kJ/mol.[165] An iron based catalyst study proposes that hydroxyl radicals are main driving force for the oxidation reactions.[20] Oxovanadium (IV) polymer-supported catalysts for the oxidation of thiophene, benzothiophene, dibenzothiophene, and 4,6-dimethyldibenzothiophene in a continuous flow system with 1 to 10 mL/hr flow rates were able to achieve conversions greater than 70%.[166] Pd and supported $Cr_2O_3$ and Co-Mo catalysts with $H_2O_2$ have also shown promise in oxidesulfurization.[167] Mn and Co oxides on $Al_2O_3$ using air at 130-200 °C were able to reach 40-60 ppm sulfur reduction after separation.[168] The study with Mn and Co oxides showed decreasing trends in reactivity in oxidation as follows: Trialkylsubstituted dibenzothiophene > dialkyl-substituted dibenzothiophene > monoalkyl-substituted dibenzothiophene > dibenzothiophene. This result suggests that the sulfur compounds that are most difficult to remove via HDS processing are, conversely, possibly the most active in catalytic oxidation pathways.

Studies of oxidative desulfurization have been extended into more exotic systems, including magnetic ionic liquids, ultrasonic processing, recoverable emulsion catalysts,[169] polyoxometalates,[170] visible light and UV photochemical activation,[171, 172] and organometallic catalysts based on Ni and Pt compounds.[173] One study used combined catalysis for oxidation and subsequent extraction of oxidized refractory sulfur compounds (benzothiopehene) using magnetic ionic liquids.[174] The use of ultrasound assisted oxidative desulfurization using tetraoctylammonium bromide and phosphotungstic acid, $H_2O_2$ was able to achieve 98% sulfur removal with ~85% oil recovery.[175]

The few studies utilizing plasma processing for oxidative desulfurization typically use electric discharges to generate radical oxygen species that then react with a liquid phase containing sulfur compounds. For instance, Liu et al. used an RF oxygen plasma that then passes onto a liquid surface chilled to -85 °C that contains ethyl mercaptan, ethyl thioether, and thiophene.[89] Ma et al. studied deep oxidative desulfurization via dielectric barrier discharge plasma oxidation using $MnO_2$ catalysts and combination of ionic liquid extraction.[90] Lili et al. investigated using DBD operating at 16 kV in air to provide oxygen radicals to drive oxidation followed by an ionic liquid extraction step, with results showing a DBT > 4,6-DMDBT > BT reactivity trend.[176] Ban et al. also used DBD operating at 15+ kV, along with a $FeCl_3/SiO_2$ catalyst, and showed up to 98.4%, 94.8%, and 92.7% removal of DBT, BT, and 4,6-DMDBT.[177]

The corona discharge activated oxidation of refractory sulfur compounds in decane has been demonstrated in our lab previously, but without detailed investigation into the characteristics of the electrical discharge or the specific reaction mechanism.[178] Here it is useful to summarize Kevin Caple's work and discuss a replication of his work.

Caple showed that the electrically driven oxidation of DBT occurs in a flat plate reaction system with stainless steel electrode surfaces, where one electrode was coated with a conductive silver epoxy/CNT mixture. Using small flow rates of low concentration DBT in decane and varying amounts of the oxidatnt *tert*-butyl peroxide, Caple observed the oxidation of DBT to DBTO and $DBTO_2$ with increasing oxidation rates of with increasing current. He also noted that significant amounts of DBT oxidation occurred

without the presence of the oxidizing agent, *tert*-butyl peroxide. These findings suggest that the oxidation of thiophenes in the electrically driven microreaction system occurs as a result of dissolved oxygen in the fuel-like media. However, there was no direct evidence to support the claim that the reactions were the cause of an electrical discharge. Herein, the characteristics of the electrical discharge in decane will be investigated in order to achieve a more complete understanding of the oxidation of dibenzothiophene in fuel-like media.

Replication of the experiments conducted in Kevin Caple's Master's work is a logical first step. The work described as follows is simply an elementary recreation of his experimental system. Refer to his thesis for amore in depth discussion of his experimental methods and results.[178]

A flat plate of stainless steel (1 1/16" X 2" X 1/8") was cleaned and coated with a thin layer of conductive silver epoxy, referred to henceforth as Ag/SS. A similar electrode was constructed but with carbon nanotubes grown in a tube furnace (the same CNTs used by Caple) mixed into the silver epoxy before application to the electrode surface, referred to from now on as CNT/Ag/SS. Both electrodes were subjected to an $O_2$ plasma treatment for 35 seconds at 24 W for activation. According to Caple, the plasma etcher removes the top "inactive" layer of the epoxy mixture. The fabricated electrodes were inserted into the flat plate reaction system with a 50 micron Teflon spacer with a narrow, rectangular flow channel cut out of the spacer.

The fabricated AG/SS ans CNT/Ag/SS electrodes were used in the flat plate reaction system shown in figure 58 (described in detail in materials and methods).

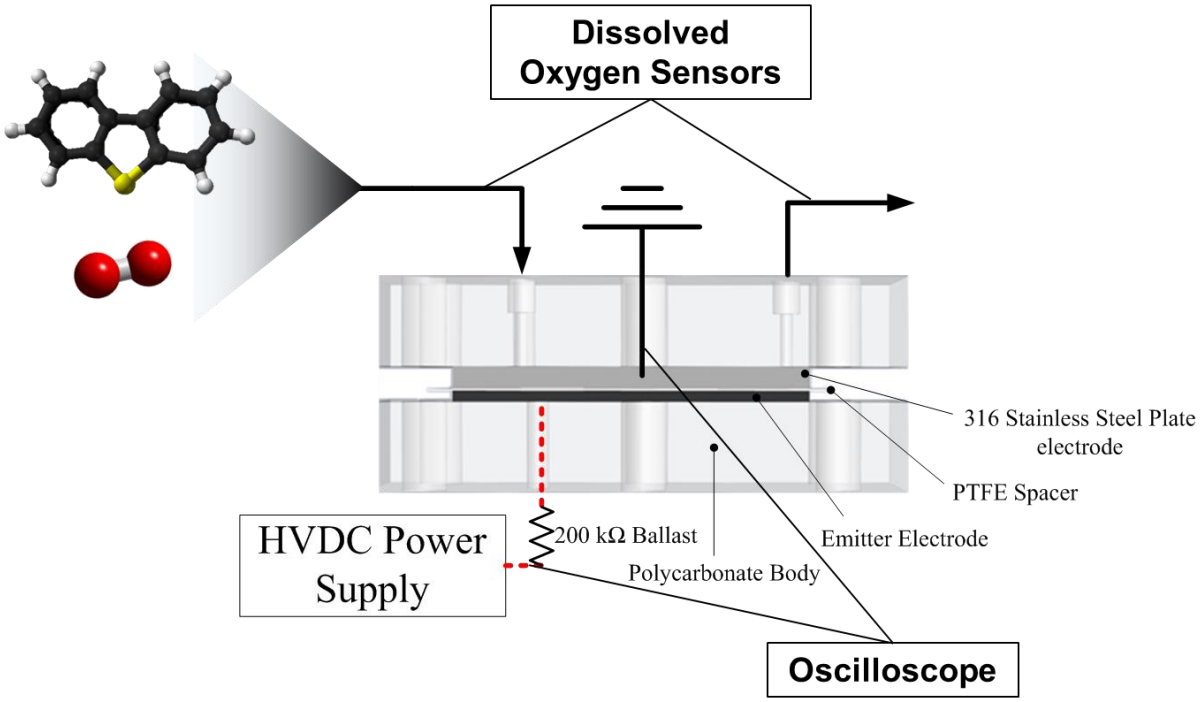


Figure 58: Experimental system used to replicate Kevin Caple's master's work: oxidation of dibenzothiophene to biobenzothiophene sulfone and dibenzothiophene sulfoxide in a corona discharge microreactor.

The first experimental trial run utilized the Glassman HV power supply. In those experimental runs, discharge could only be obtained in the flat plate reaction system at elevated voltages above 6 kV, and those discharges were pulsed and very infrequent. The first experimental trials showed inadequate performance and were not a good analog to what Caple observed.

The second experimental trials utilized the same power supply that Caple used in his work, the Life Technologies Gibco BRL 4001P Programmable Electrophoresis Power Supply. This power supply has a built in system to detect if the system is electrically open, and will not apply voltage unless it detects that the circuit is complete. Since decane is an excellent insulating fluid, the power supply would not engage in the designed system. In order for the power supply to engage, the flat plat system had to be tightened to a much more severe degree than usual for operation in order for the circuit to be complete. This means that in all the experiments reported here, the two flat plate electrodes are substantially closer together than 50 µm. Multimeter measurements of the

resistance between electrodes still indicated that the circuit was open, but the power supply was able to recognize a circuit and was able to apply potential.

The Ag/SS electrode was used in the described reaction system with a 1 mL/min flow of a 500 ppm DBT solution in n-decane. The power supply was able to engage and deliver 3.5 mA of current to the reaction system, and the voltage drop across the reactor was 1.2 volts. Applied voltage and measured voltage drop across the reactor was measured, and summarized in figure 59.

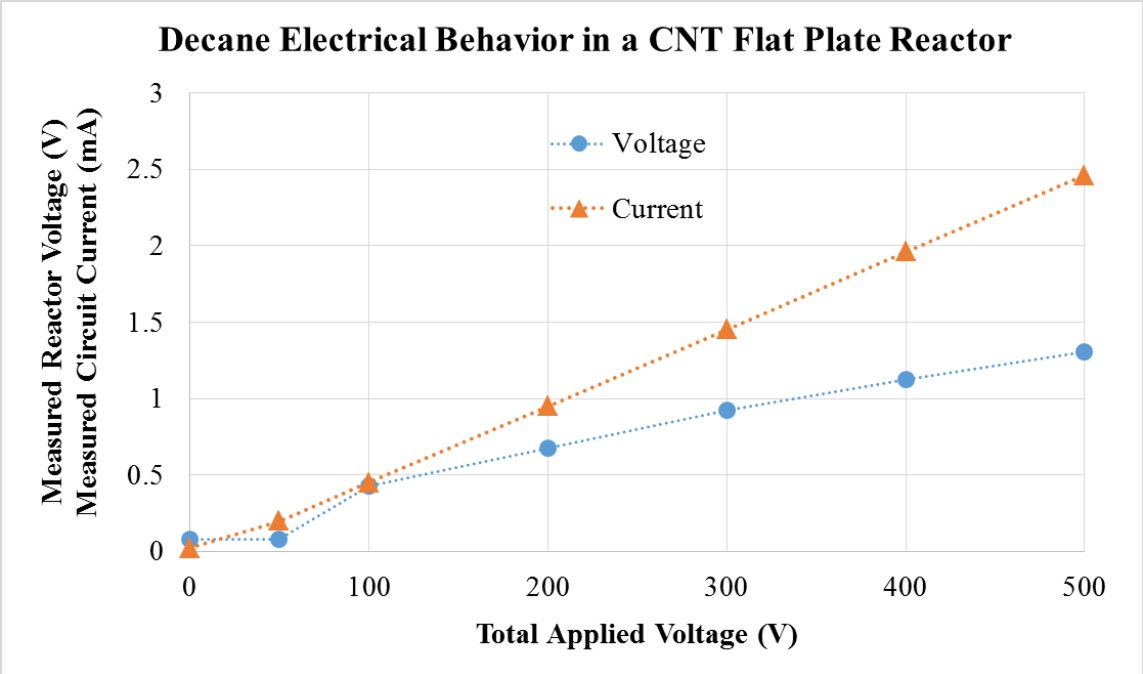


Figure 59: Current and voltage measurements in the flat plate DBT oxidation reaction system.

The voltage-current relation of the flat plate reaction system that emulates Caple's work shows that the voltage drop across the reactor is in the range of 0-1.5 volts, which is not in the range of voltages expected in electrical discharge reactions. Voltages around 1 volt are more typical of electrochemistry. However, the behavior that Caple observed does not suggest that his reactions are the result of electrochemistry. This voltage/current relationship could be indicative of an oxidation/reduction reaction occurring on the electrode materials. Figure 60 is the SEM image of the Ag/SS plate used the run, with the inset image of the Ag/SS plate after being used in the reaction system.

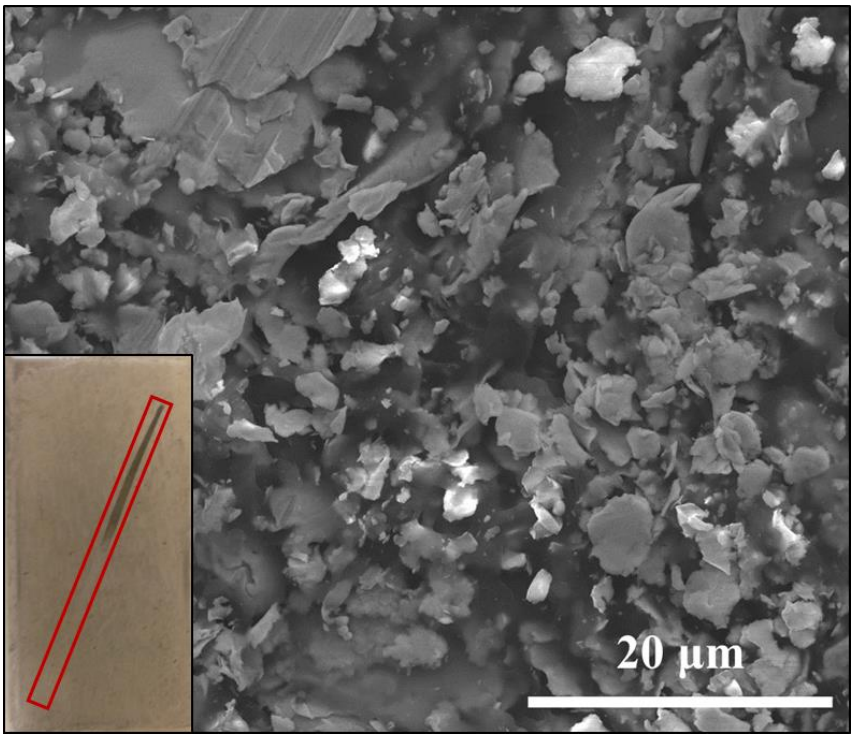


Figure 60: SEM image of the silver epoxy film on a stainless steel substrate after $O_2$ plasma treatment. The inset is an image of the Ag/SS electrode after use in the reaction system, with exposed reaction volume surface highlighted in red. The discolored area is likely silver oxide.

The discolored portion of the plate mirrors the reaction zone cut out of the Teflon spacer, but only for about half of the total reaction zone. The discoloration is likely the oxidation of silver in the silver epoxy to silver oxide, and could be the dominant source of electrochemical current flow. However, the circuit is completed with DBT/decane fluid flowing through the system, which is a promising sign in trying to replicate Caple's work. The signal from the dissolved oxygen sensors on the inlet and outlet of the reaction system was also monitored during the experiments. The inlet signal remained constant for all conditions, as expected, and is not shown here. The dissolved oxygen signal for the reactor effluent is shown in figure 61 below.

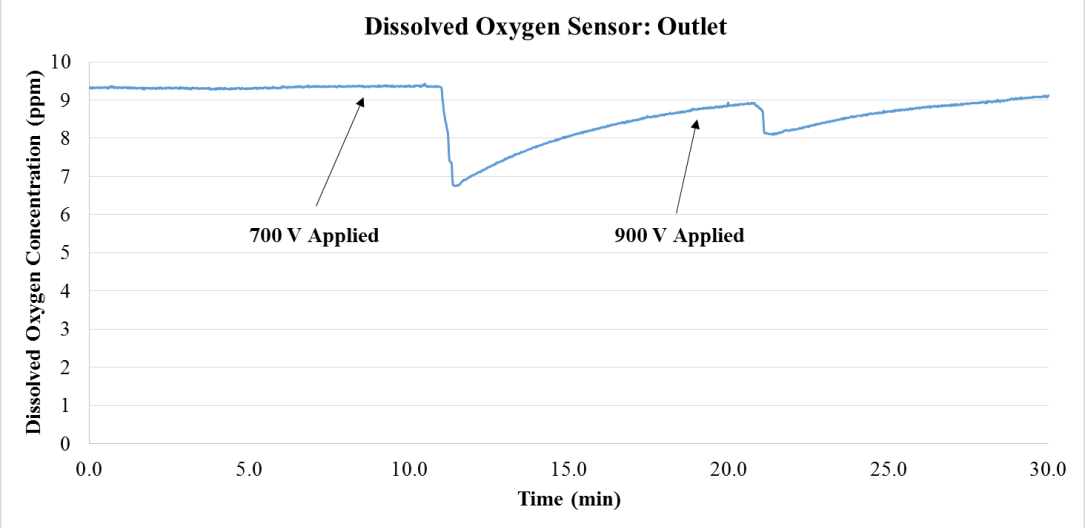


Figure 61: Dissolved oxygen sensor reading for reactor effluent during an experimental run with an Ag/SS electrode.

There was no current flow below a total applied potential of 700 volts. At 700 volts applied potential, 3.5 mA current began to flow into the system and a few minutes later the effluents DOS decreased by about 3 ppm and began to steadily return to baseline values. At this point, the voltage was increased to 900 volts, and the dissolved oxygen peak again dipped by about 1 ppm as the current increased to 4.51 mA. The source of the change in dissolved oxygen concentration is unknown. The inlet dissolved oxygen concentration did not change significantly over time and did not respond to any of the changes to the reaction system, so variations in pressure and flow can likely be ruled out as sources of change in dissolved oxygen signals on the fluorimeters. There were no observed changes in temperature of the effluent, so temperature fluctuations can also be ruled out. Bubble formation is a possibility, as a bubble passing in front of the fluorimeters would disrupt the signal, but the bubble would likely not leave as a steady change in signal as seen here. The signal change is likely as a direct result in a change in dissolved oxygen concentration. In order to ensure that no chemical reactions are happening with n-decane, pure n-decane was passed through the reaction system with applied potential and current flow. The FTIR spectra for n-decane before and after passing through the active reaction system are shown in figure 62. There is no discernable chemical change.

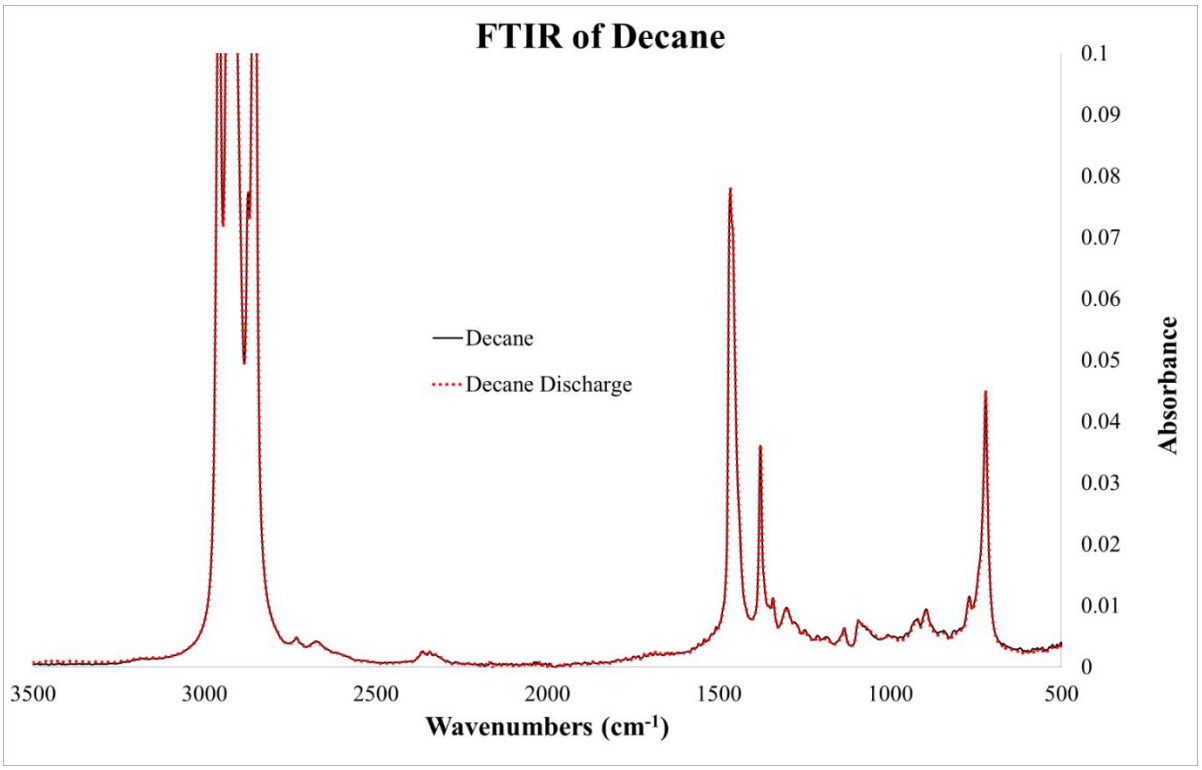


Figure 62: FTIR spectra for n-decane, and n-decane after passing through the active reaction system.

Chemical analysis of the dibenzothiophene oxidation products proved to be more difficult than expected. FTIR-ATR was used as a first pass at quantification of the products from the reactor effluent. Figure 63 the FTIR spectra for DBT and $DBTO_2$ dissolved in n-decane with the n-decane background scan removed. The black lines are the NIST standard IR spectra for DBT and $DBTO_2$.

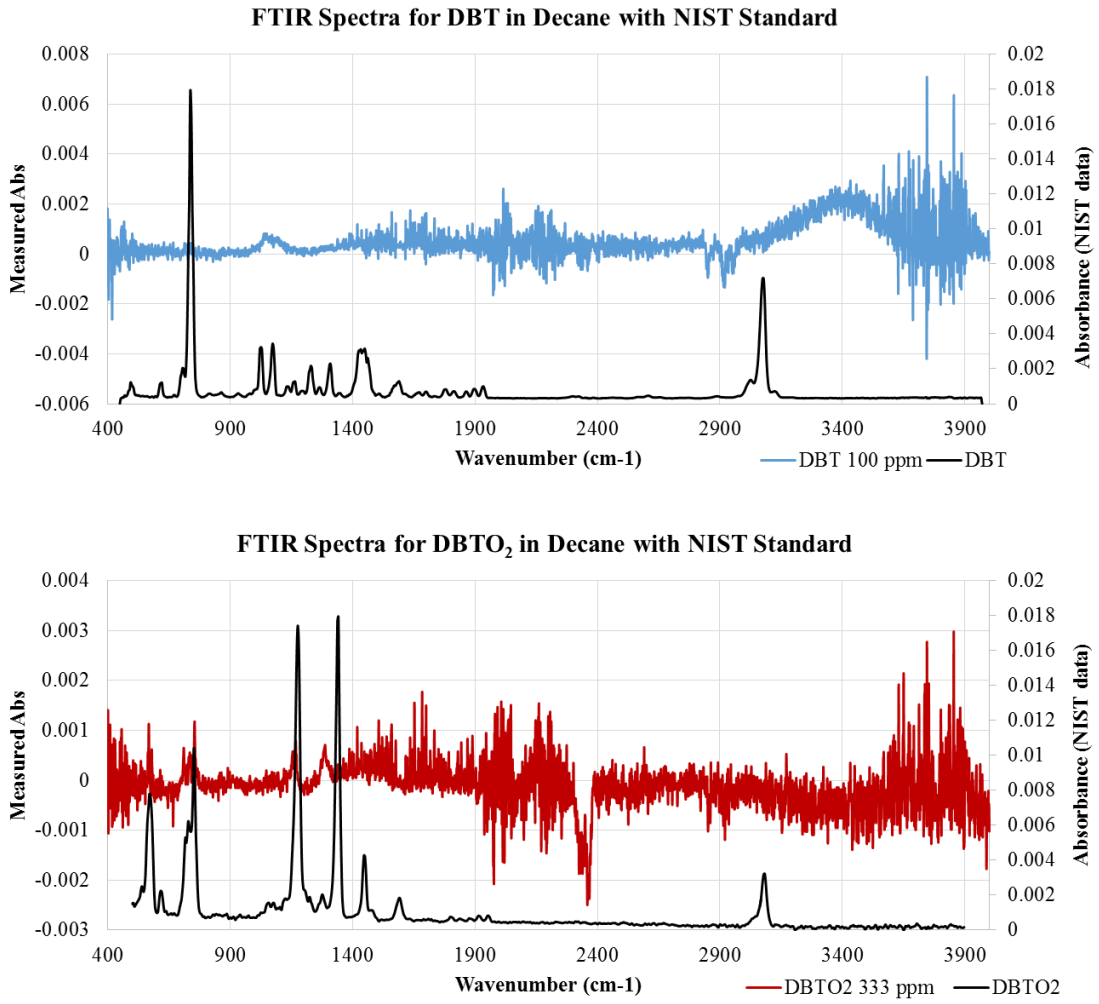


Figure 63: FTIR spectra for both Dibenzothiophene (top) and dibenzothiophene sulfone (bottom) dissolved in decane with a pure decane background scan as a baseline. The NIST Chemistry WebBook FTIR standards are shown for comparison.

The FTIR spectra could not resolve the peaks associated with the dissolved thiophenic compounds to a degree suitable for quantification. Using an extraction method to pre-concentrate the sulfur compounds before analysis would improve this analysis method. However, a direct measurement method would be more desirable for data collection and quantification. As a result, gas chromatography was used in an attempt to improve the quantification methodology. An SRI 8610C GC with a MXT-5 capillary column (details in materials in methods) was used to separate thiophenic compounds from decane. The FPD detector with a window specifically made to single out sulfur compounds was used

as the main detector, along with an FID detector to complement the FPD. The resulting chromatograms from the GC system are shown in figure 64 below.

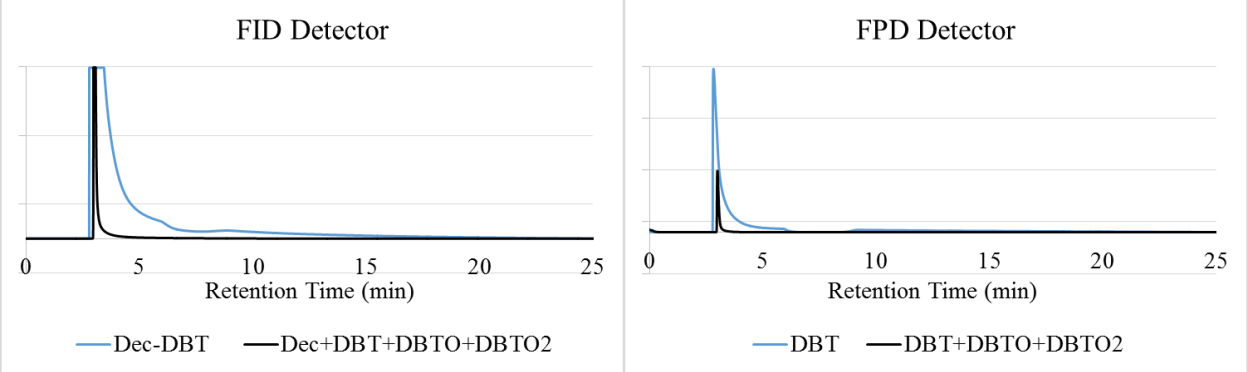


Figure 64: Gas chromatogram of some decane/DBT/DBTO/DBTO mixtures. Even with the sulfur specific FPD detector, the only obvious peak is due to decane, and no usable data was obtainable from this analytic system.

Figure 64demonstrates the inability of the GC system used to adequately measure and quantify DBT/DBTO/$DBTO_2$ mixtures. The type of column and operating conditions were selected based on a review of the dibenzothiphene compound GC separation techniques reported in literature and summarized in the NIST Chemistry WebBook. Dibenzothiophene has many entries suggesting that a DB-5/MXT-5 capillary column operating around 250 °C is a good choice for this separation. Dibenzothiopehne sulfoxide and dibenzothiophene sulfone do not have entries for gas chromatagoprahy in the NIST Chemistry webbook, but there are reports in literature suggesting that GC can be used in the analysis of DBTO and $DBTO_2$.[179] The inability of the GC system to detect and quantify sulfur compounds could be a result of the FPD detector not operating as intended. The sulfur-wavelength specific FPD window was replaced with a new one, with no improvements in performance.

Caple used HPLC in his analysis of DBT oxidation, so I turned to the same analysis method in order to finally detect sulfur compounds in an adequate manner. The HPLC system available in Merryfield was not in working order, and the unplanned for delay in time between sample collection in the previous experiment and the arrival of a usable HPLC system rendered the samples taken from the Ag/SS and CNT/Ag/SS plates unreliable and ultimately not useable.

The HPLC system used herein is a combination of the ultimate 3000 HPLC system with a Gilson Model 111B UV detector installed as the detection system using the universal chromatography interface (Dionex UCI-50). This system can separate and quantify all three compounds, DBT, DBTO, and $DBTO_2$, and since decane is transparent to UV, the solvent peak does not appear in the chromatogram. Figure 65 shows a sample chromatogram for DBT/DBT/$DBTO_2$ separation.

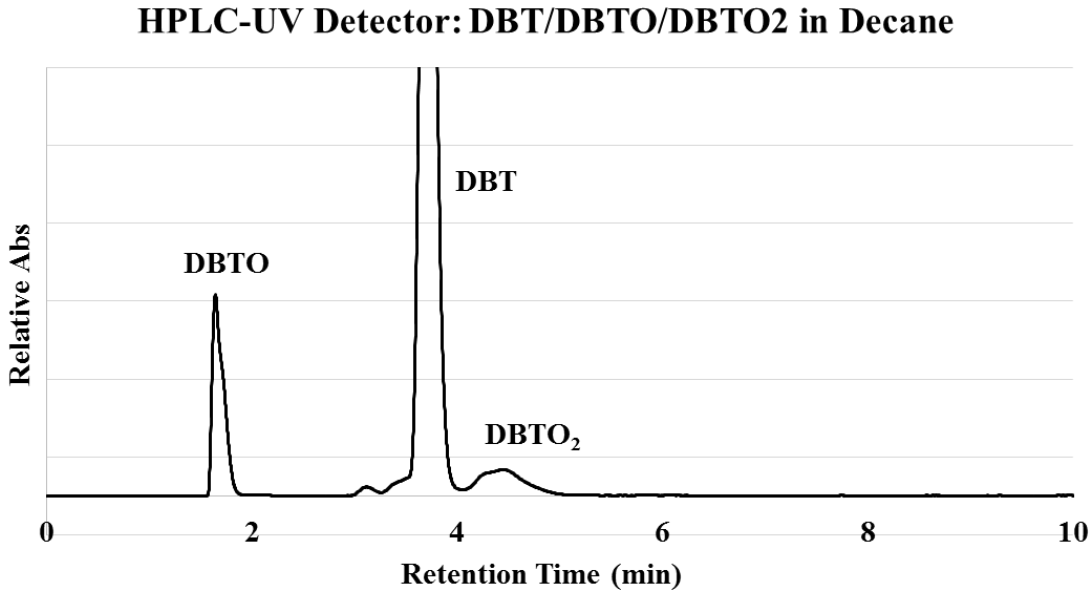


Figure 65: HPLC run with a mixture of 315/167/111 ppm DBT/DBTO/$DBTO_2$ in decane at 1mL/min with an 80/20 ACN/$H_2O$ mobile phase, as seen by a UV detector at 254 nm.

The experimental investigation of electrical discharge enabled oxidation of thiophenes in fuel-like media could benefit from an exploration of simple DC discharges in the model fuel-like system, n-decane. To this end, the point-to-plane microreactor used in the gas phase experiments was used to carry out some simple, exploratory experiments. The point-to-plane reactor with a freshly sharpened Ni tip in a discharge gap of ~250 μm is filled with n-decane, and a 1mL/min flowrate of 2000 ppm DBT in n-decane is continuously pumped through the system, as shown in figure 66. A steadily increasing voltage is applied to the system and electrical breakdown occurs in the range of 6 to 7 kV and generates a gas bubble and a discharge with a blue hue. During this time, the

dissolved oxygen content of the reactor effluent drops off sharply. The discharge rapidly generates a carbon filament that shorts the reactor

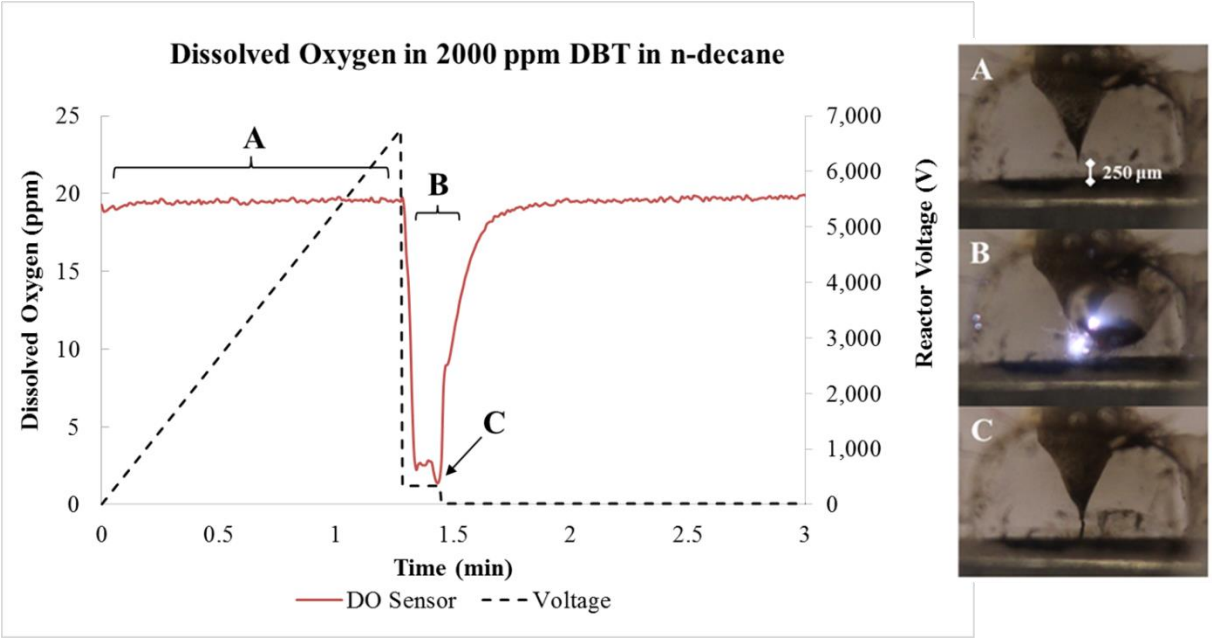


Figure 66: Discharges in the point-to-plane microreactor with a 1mL/min flowrate of 2000 ppm DBT in n-decane. The discharge gap is approximately 250 µm. A) A steadily increasing voltage is applied to the system, B) electrical breakdown occurs in the range of 6 to 7 kV and generates a gas bubble and bluish discharge filament that operates around 335 volts (see figure 67). During this time, the dissolved oxygen content of the reactor effluent drops off sharply. C) The discharge rapidly generates a carbon filament that shorts the reactor, and the DOS reading rises back to the baseline.

An oscilloscope capture of the short-lived discharge in decane is shown in figure 67.

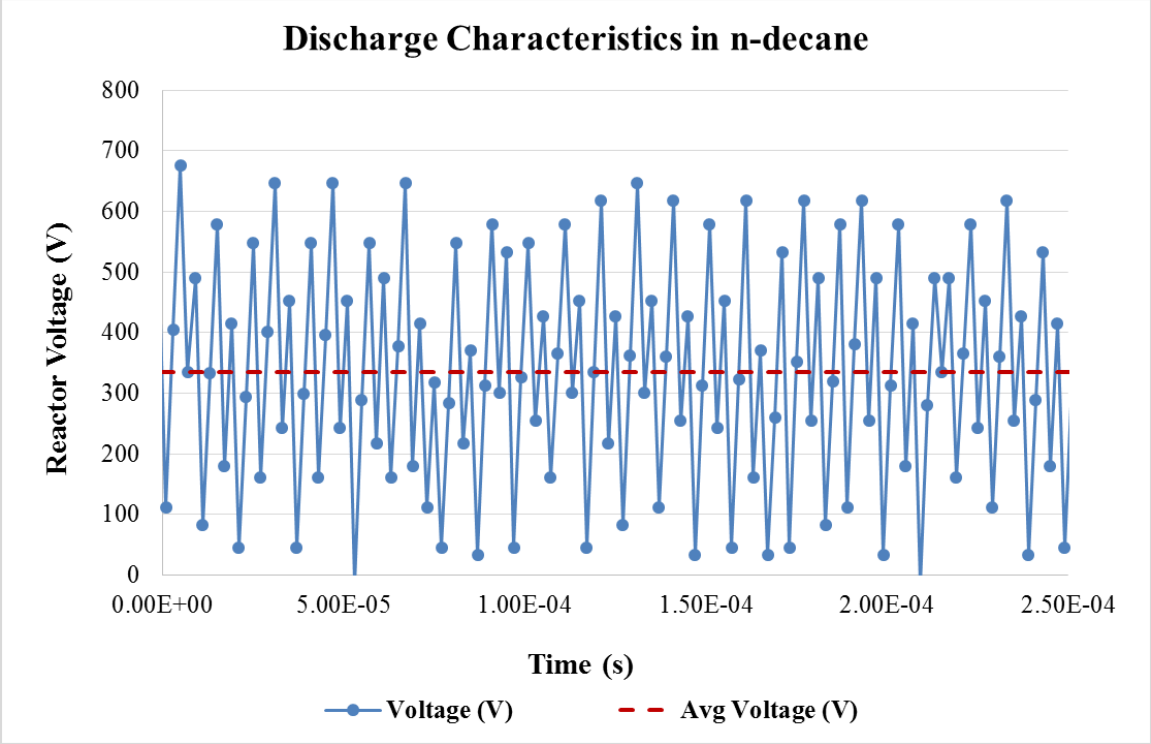


Figure 67: HV differential oscilloscope trace for the discharge as it occurs in n-decane, shown in figure 66.

The oscilloscope trace seems to indicate a pulsed discharge behavior where the voltage drop across the reactor builds up to the 500-700 volt range, and then collapses to the 100-300 volt range. This results in an average discharge voltage around 334 volts, and the discharge current corresponding to this oscilloscope capture was approximately 1 mA. Samples were collected from the reaction system during the short-lived discharge, analyzed, and compared to a fresh sample using the HPLC system. Chromatograms for a standard mixture solution of DBT/DBTO/DBTO2, the blank DBT sample, and the DBT sample passed through the active discharge are shown in figure 68.

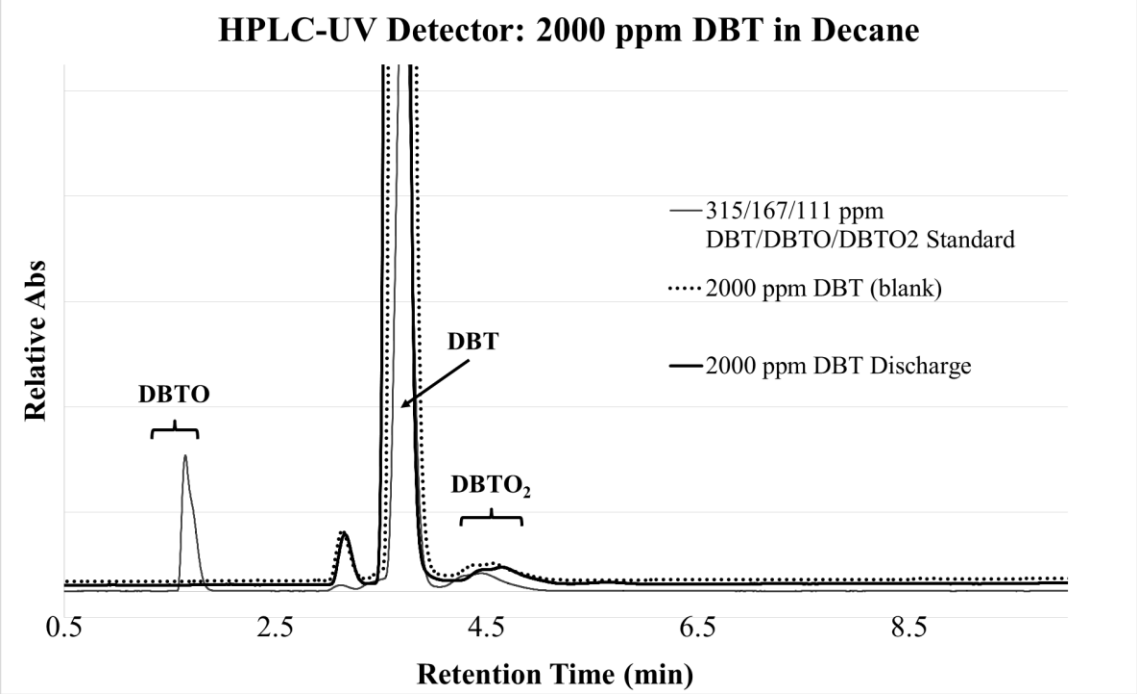


Figure 68: HPLC UV detector signal for DBT/DBTO/DBTO2 standards and a 2000ppm DBT solution before and after exposure to the discharge shown in figure 66.

Figure 68 clearly shows that there is no significant difference between the standard 2000 ppm DBT solution and the 2000 ppm DBT solution that passed through the active discharge. The DBT peak remains the same, there is no DBTO peak, and the tiny, nebulous hump associated with $DBTO_2$ is present even before passing through the reactor. It is interesting to note the presence of a fourth, unknown peak just before the DBT peak that appears in the 2000 ppm DBT solution but not the stock solution of the DBT/DBTO/$DBTO_2$.

## Desulfurization Conclusions

In a simple replication Kevin Caple's Master's work, a flat plate reactor with a conductive silver epoxy coating on one electrode was able to complete an electrical circuit through flows of DBT in n-decane at electrode spacings smaller than 50 µm. In this system, dissolved oxygen content from the reactor effluent decreases as a result of

electrical current. However, it has not been shown whether this electrical current effectively mediates any oxidation of sulfur compounds in fuel-like media. Literature reports effective oxidative desulfurization with silver-based catalysts and the selective adsorption of thiophenes on silver surfaces in hydrocarbon mixtures.[180, 181] One study showed that the degree of oxidation of sulfur compounds in oxidative desulfurization is greater in the presence of an electric field, and that the silver electrodes are more easily corroded in sulfur containing hydrocarbon environments.[182] Observations of this reaction system and studies in literature suggest that at least part of the electrical current draw into this system drives the oxidation or electrochemical corrosion of the silver epoxy coating on the electrode surface. There are also works that suggest pi-complexing occurs between $Ag^{+}$ and aromatic groups such as those in thiophenes and benzene.[183] Additionally, coordinative adsorption of thiophenic sulfur compounds on $Ag^{0}$ has been identified.[184] It is likely that these interactions are of consequence in both the reaction system developed here and the reaction system in Caple's work. At the conclusion of the experimental work with a flat plate reactor design, Caple's work was not able to be reproduced. However, I was able to observe similar electrical phenomena to those reported by Caple. The interaction of aromatic sulfur compounds with silver could explain the oxidative desulfurization phenomena observed by Caple. This implication suggests that future research efforts should explore electrically driven oxidative desulfurization with silver catalysts.

In a point-to-plane discharge system with a discharge gap of 250 μm, electrical breakdown of 2000 ppm DBT in n-decane occurs around 6.5 kV. The resulting discharge forms a carbon filament between the electrodes, effectively shorting the reactor and limiting the duration of the generated discharges to lifetimes on the order of 10 seconds. There is no observable oxidation of dibenzothiopehene using this simple point-to-plane DC discharge in 2000ppm DBT/n-decane flows.

# Modeling

The use of mathematical models is almost always of use in understanding physical systems. This work is most definitely a multiphysics problem, and touches on many aspects of science and engineering that can benefit from modeling, including fluid flow, mass transfer, electrostatics, and chemical kinetics. The reactors described within this work are relatively simple in design, but the larger scope of the project ultimately seeks to design microreation systems that are much more optimized and amenable to real world applications. To that end, COMSOL multiphysics was employed to develop some fundamental insights into a designed nonthermal microplasma reactor platform. The first and most straightforward aspect of these microplasma reactors is the electric field.

## Electric Field

One of the goals of this project, and of the related projects in this field currently underway at Oregon State University, is to create a microscale plasma reactor that can process large volumes with multiple active discharge zones. The creation and construction of micoreactors is a complicated undertaking and only becomes more so when trying to accommodate the generation of DC microdischarges into the design. One of the most important aspects of stable DC discharges is the electric field strength, which is the source of continued generation of excited species that sustain the discharge. In most of the studies in literature that explore DC discharges, the generation of the discharge is a given. In other words, the reaction systems are typically designed and then operated at an applied potential, discharge current, and power dissipation that create desirable results. When the electrical properties of the discharge are of secondary concern, energy efficiency is difficult to optimize. In this work, and in others at OSU, the microplasma reactors are designed with energy efficiency in mind from the outset, and modeling can be a useful tool in that design process.

The electrostatics module in COMSOL can be used to study electric fields in static conditions. For the purposes of this work, electrostatics can be used to study the electric field strength of the reactor design prior to electric breakdown. Here, the developed model simulates a microreaction system with a discharge gap of slightly less than 1 mm

and a patterned array of discharge points that create strong electric fields to generate DC discharges in the microgap. The reactor gap length is kept constant at 1 mm with sharp features that are 100 µm in height, for a discharge gap of 0.9 mm. The studies presented here use an applied potential of 1000 volts, air as the gas in the discharge gap, and stainless steel as the material of construction for the electrodes and electrode features. The following model investigates the effect of the "sharpness" of the features and the spacing between features. See figure 69 for images of the electric field model.

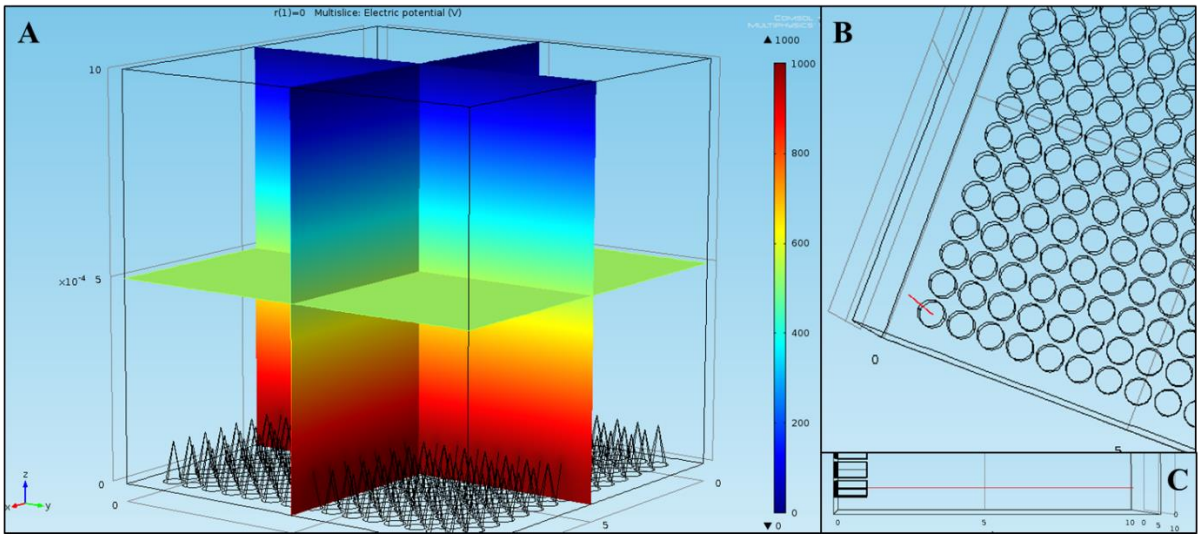


Figure 69: COMSOL electric field modeling. A) 1000 volts applied to the bottom plate, which consists of a square array of 15x15 cones with 50µm radius base and a height of 100 µm. This array sits inside a discharge gap of 1 mm, where the top plate is flat and acts as a ground for the modeled electrostatic system. B) The array as cylinders, with a cut line rising straight out of the cylinder on the corner of the array. C) Side view of B. The cutline is used to probe electric field strength.

The generated 3D model provides valuable data in the analysis of these DC microplasma systems. 2D cutlines are used to select a linear portion of data points extending from the base of the electrode at 1000V (x = 0) into the discharge gap towards the ground electrode (x = 1mm).

The cones shown in figure 69 are 25µm in radius and 100µm tall. In the close-packed arrangement, the distance from center to center for each cone-shaped feature is 35 µm for a spacing distance of 10 µm. In the staggered arrangement, every other feature is removed from the array, with alternating removal from line to line so that every feature is surrounded on four sides by an empty feature location. This results in a lienar spacing of

70 µm in the up, down, left, and right directions, and approximately 50 µm spacing in the four diagonal directions. The values for electric field gradient in kV/cm along a 2D cutline are prodived figure 70.

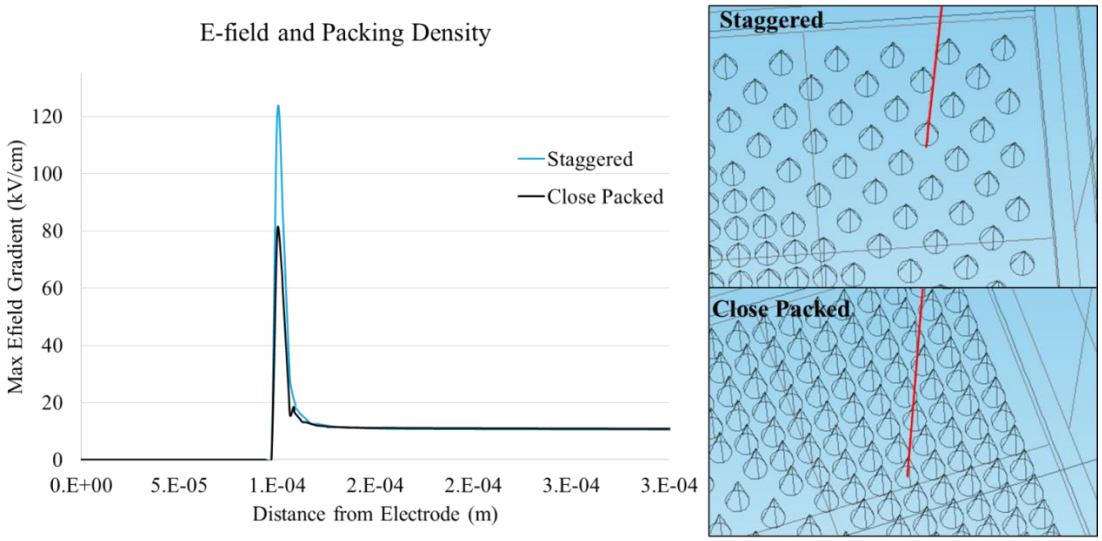


Figure 70: Packing density and Efield gradient directly above the cone shaped features.

The threshold value of electric field gradient for electric breakdown in air is approximately 30 kV/cm. In both the staggered and close packed arrangements, the electric field strength directly above the cone-shaped features exceeds the electric breakdown threshold for air. This indicates that a closely packed arrangement of sharp features with a spacing of 10 µm would be suitable for large scale activation of many discharge points.

While exceedingly sharp features like cones (or electrochemically etched Ni tips in the experimental sections) are capable of generating electrical breakdown in these systems, it would be useful to know what degree of sharpness is required to achieve satisfactory performance. To this end, the model was used to carry out a parametric sweep of feature sharpness, controlled by varying the tip radius of cylindrical features: 25 µm tip radius represents a true cylinder, while a tip radius of 5 µm represents a very finely sharpened cone-shaped feature. Figure 71 shows 2D cut-planes taken 1 µm above the surface of the electrode features for different feature radii. The figure also shows a 2 value re-scaling of the surface values of electric field gradient, with red showing values that exceed the

electric breakdown potential for air (30 kV/cm) and blue showing values that fall below the electric breakdown potential.

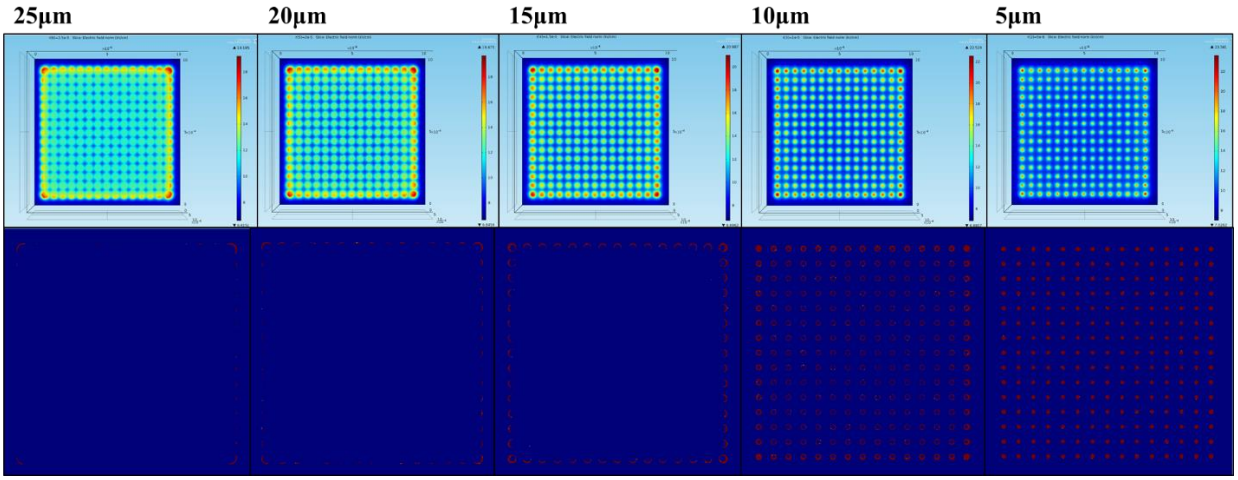


Figure 71: Electric field strength cutplanes in the parametric sweep of cylinder tip radius, with cylinders of 25µm radius and 100µm height. Distance from center to center is 35 µm for a spacing distance of 10 µm. Top: Left to right, tip radius values are 25, 20, 15, 10, and 5 µm. Cut plane is take 1 micron above the surface of the features. Bottom: Same system, with two value color scale above and below the Efield breakdown threshold values for air, 30 kV/cm. Red is above the threshold for electric breakdown, and blue is below.

Figure 72 is a graphical representation of the data in figure 71.

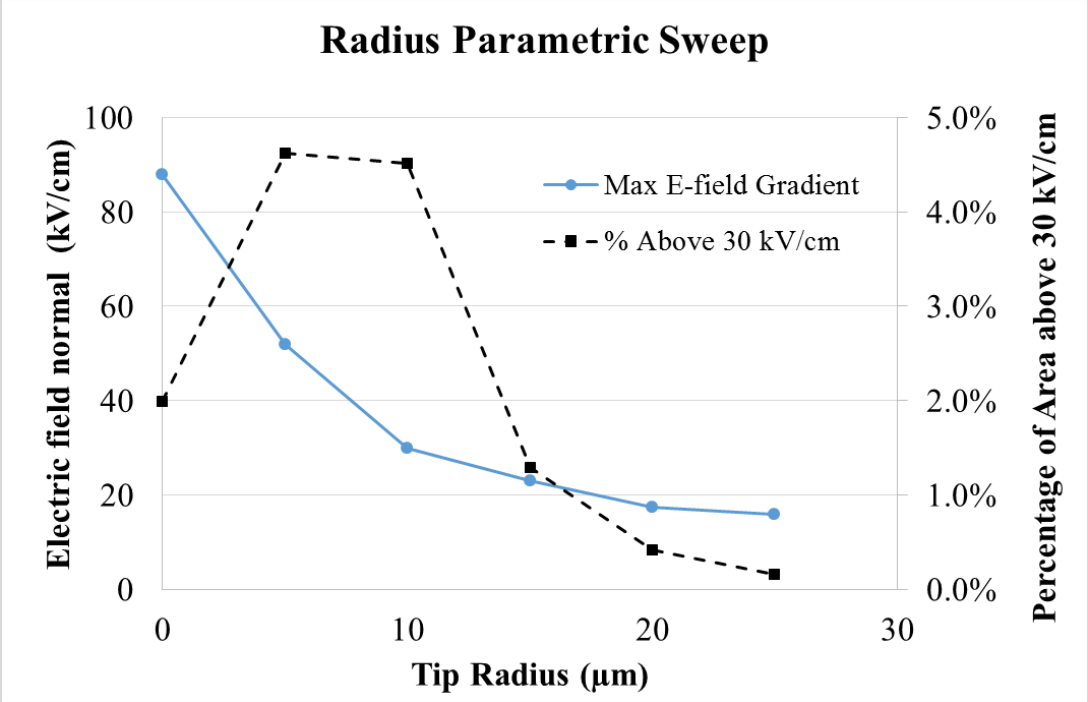


Figure 72: Graphic depiction of the parmetric sweep of feature radius, with the maximum value of electric field gradient of the 2D cutline above the features plotted along with the percentage of the studied area that has an electric field strength strong enough to cause electric breakdown.

It should be noted that when the value of the max E-field gradient falls below 30 kV/cm in figure 72, the strongest points in the electric field are no longer as a result of the sharp point directly above the feature but of the sharp edges of the cylinder, and as such are no longer part of the 2D cutline that extends directly above the center of the feature. At this point, there is no longer a benefit to sharpening the tips. The percentage of the area above the threshold value of 30 kV/cm is not evenly distributed until the feature radius is 10 µm or less, so for the arrangements studied here it makes sense to have an emitter tip with a tip radius smaller than or equal a value around 10 µm.

## Kinetics

Modeling of the reaction kinetics involved in plasmachemical systems is complex, with many mechanisms, reaction pathways, and behaviors that are still not completely understood. The fourth objective of this work involves the development of kinetic model that can describe the performance of the constructed microplasma reaction platform. The kinetic studies here revolve around methane processing with some theoretical discussion

of plasma kinetics provided first, followed by reaction kinetics models developed in COMSOL multiphysics.

*PLASMACHEMISTRY KINETICS*

The key process in plasmas is the conversion of neutral components into electrons and positively charged ions. The ionization events via electron impact in plasmas can proceed through one of several basic mechanisms: Direct ionization by electron impact, which can be dissociative or non-dissociative, and stepwise ionization. In order to calculate any of these simple kinetic values, the electron energy distribution must be known, or at least approximated. The following (equation 31) can be used as a simplified approximation of EEDFs, where $\bar{\varepsilon}$ is the average electron energy (eV), ε is the electron energy (eV), and Γ is the incomplete gamma function. x = 1 for a Maxwell-Boltzmann distribution and x = 2 for a Druyvesteyn distribution.[185]

$$f(\varepsilon) = \bar{\varepsilon}^{-\frac{3}{2}}\beta_1 exp\left(\left(-\frac{\varepsilon\beta_2}{\bar{\varepsilon}}\right)^x\right) \quad (31)$$

$$\beta_1 = \Gamma(5/2x)^{3/2}\Gamma(3/2x)^{-5/2} \quad \beta_2 = \Gamma(5/2x)\Gamma(3/2x)^{-1}$$

The electron energy distribution in nonthermal plasmas determines the reactivity of the plasma and is important when discussing modeling plasmachemical behavior. Electron energy distribution functions are useful ways to model electron energy. Typically, the Maxwell-Boltzmann distribution models thermal plasmas and the Druvyvesteyn distribution has been used to model nonthermal plasmas. However, it should be noted that nonthermal plasmas, especially nonthermal microplasmas, can have true EEDFs that deviate significantly from these models. The Maxwell-Boltzmann distribution and Druyvesteyn distribution in figure 73 are representative EEDFs with an average electron energy of 5.6 eV.

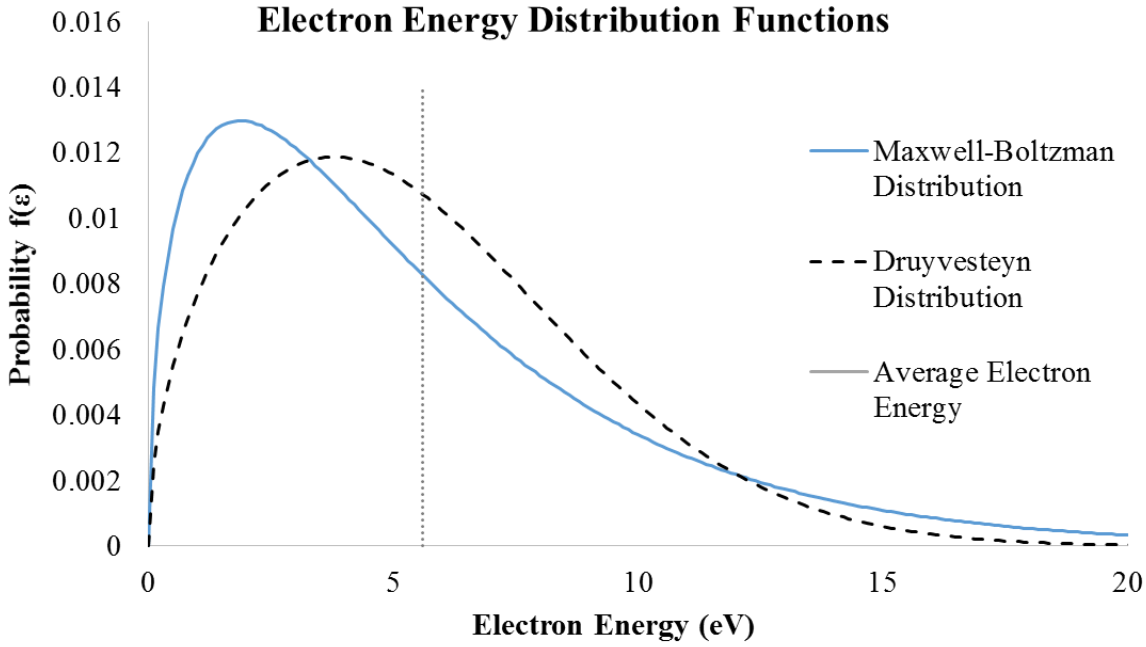


Figure 73: EEDFs for an average electron energy of 5.6 eV.

In addition to the electron energy distribution, it is important to have values for electron-impact cross sections for the various species that can be present in the system. The NIST Physical Measurement Laboratory provides an Electron-Impact Ionization Cross Section database where the electron impact ionization cross sections for various neutral molecules and excited species have been experimentally measured and theoretically modeled.[96] The ionization cross sections as a function of electron energy for relevant species are shown in figure 74.

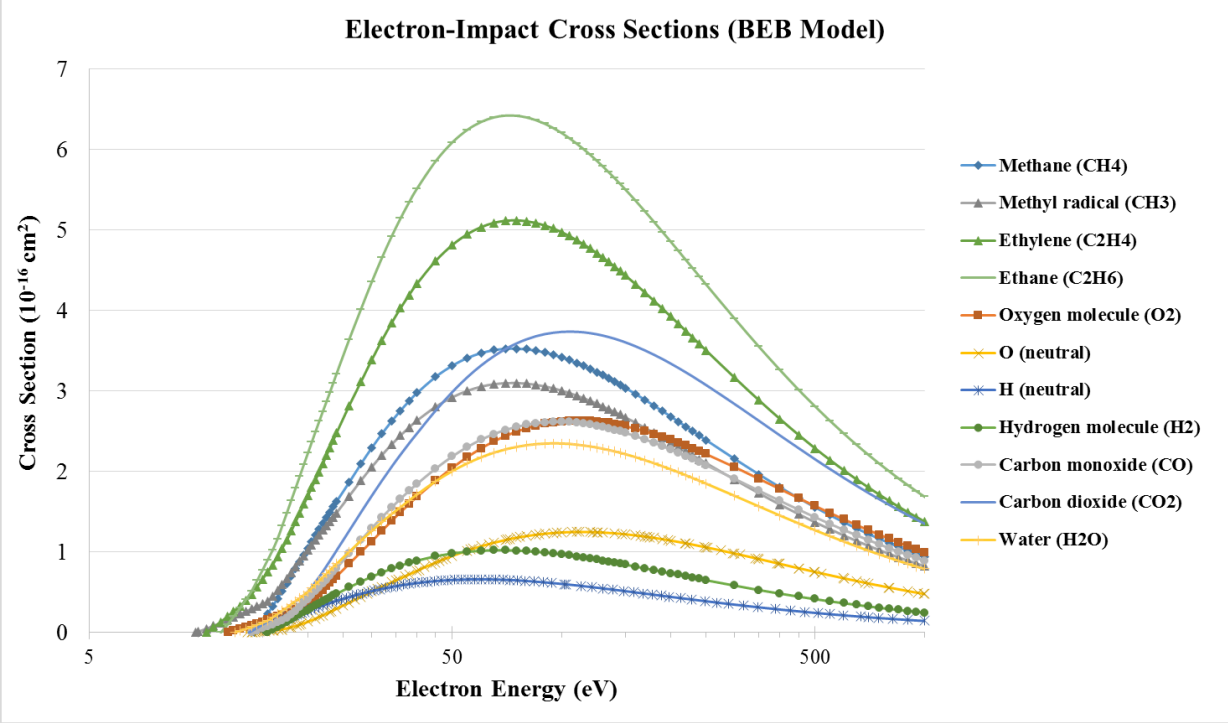


Figure 74: Electron impact cross sections for selected species, derived from the Binary-Encounter-Bethe (BEB) Model

### *COMSOL Plasma Module: Trial Run*

Due to the complexity of coupling the electrostatic field to the transport of electrons and heavy species, the Plasma Module provides a multiphysics interface specially designed for DC discharges. The complicated coupling between the electron transport, heavy species transport, and electrostatic field is handled automatically by the software. Furthermore, the secondary emission flux from ion bombardment on an electrode is automatically computed and used in the boundary condition for electrons. This makes it easy to model things such as positive columns and DC glow discharges. The physics of DC discharges can be further complicated when a strong, static magnetic field is present. This can lead to highly anisotropic transport properties for the electrons. The DC Discharge interface can automatically compute the tensor form of the electron mobility. This makes it possible to model things such as magnetron discharges and hall thrusters. DC discharges require reaction rates to be specified in terms of Townsend coefficients rather than with reaction rate coefficients, largely because Townsend coefficients provide a better description of the physics in the cathode fall region. The discharge is sustained by

secondary emission, rather than a time varying electric field. Therefore, secondary emission effects from surfaces must be included in any DC discharge model otherwise the plasma simply self-extinguishes.

The **DC discharge interface** couples the Drift Diffusion, Heavy Species Transport, and Electrostatics interfaces. It is used to study discahrges that are sustained by a static electric field, and Townshen coefficients can be used instead of rate coefficients for electron source terms.

The d**rift diffusion** interface solves for the electron density and mean electron energy for any type of plasma. Can handle secondary emission, thermionc emission, and wall losses.

The **heavy species transport** interface is a mass balance interface for all non-electron species. This allows the addition of electron impact reactions, chemical reactions, and surface reactions, which can include charged, neutral, and electronically excited species.

The **electrostatics** interface is used to compute the electric field, the electric displacement field and potential distributions in dielectrics under conditions where the electric charge distribution is explicitly prescribed.

The **Terminal node** provides a boundary condition for connection to external circuits, to transmission lines, or with a specified voltage or charge. By specifying zero charge, a floating potential condition is obtained. The Terminal node also enables the computation of the lumped parameters of the system, such as capacitance. **Quick circuit settings** are available when Voltage is selected as the Terminal type: None (the default), Series RC circuit, Ballast resistor, or Blocking capacitor

The **electron impact reaction** node sets up the reaction rate for a reaction involving an electron and a target species. These collision reactions can be specified as elastic (default), excitation, attachment, or ionization reactions. The reaction rate for these reactions can be supplied via Arrhenius parameters, rate constants, a look up table (table of source coefficient vs. mean electron energy), or by importing cross section data.

The **Cross Section Import** node allows you to import collision cross section data into the model. For each electron impact reaction, the lookup table of electron energy (eV) versus collision cross section ($m^2$) allows electron transport properties and source coefficients to be computed.

The plasma module, specifically the DC discharge interface, is probably the ideal way to model the chemical reaction processes that occur in our microplasma systems. Modeling in this way would allow for an insightful look into not only reaction mechanisms and chemical products but also electrical properties such as electric field strength, material properties like secondary emission coefficients (work function related) of the electrodes, and circuit properties like ballast resistance and circuit capacitance. However, in terms of simple kinetic modeling, the plasma module has far too many input parameters and input requirements. If this project is to continue into complicated modeling with COMSOL, subjects like plasma physics need to be more heavily considered. For example, pure argon systems still require 3 species and at least 7 reactions to be modeled effectively. These reactions and kinetic values only become more complicated at higher pressures and in multi-component systems. The parameters below can all be important in the DC discharge interface, and this list does not include fluid flow or heat transfer parameters, which can couple with the plasma module.

- Input parameters for the drift diffusion interface
    - Electric potential
    - Collisional power loss
    - Neutral number density
    - Magnetic flux density
    - Electron density and energy, which can have up to 4 independent inputs such as
        - Electron mobility
        - Electron diffusivity
        - Electron energy mobility and diffusivity
    - Electron production rate
    - General power deposition
- Input parameters for the heavy species transport interface
    - Temperature
    - Pressure
    - General parameters (for ion of neutral species)
        - Molecular weight
        - Charge
        - Potential characteristic length
        - Potential energy minimum
        - Dipole moment

        - Thermal diffusion coefficient
        - Diffusion coefficient
    - Electron parameters
        - Electron density
        - Mean electron energy
        - Initial electron density
    - Kinetic values for all reactions
        - electron impact (elastic, excitation, ionization, excitation, relaxation, etc)
        - volume reactions, surface reactions

*0D KINETIC MODEL*

Moving forward *without* the COMSOL Plasma module, the first model created to simulate the single point-to-plane microreactor performance was a simple OD kinetic model using the COMSOL reaction engineering module. The kinetics being studied in this system are incredibly fast, and as a result the numerical solver has a difficult time converging even in a simple 2D space when coupled to diffusion and fluid flow physics. Employing a 0D kinetic model to further study the kinetics of the system is a useful way to move forward in this scenario.

Homogenous gas phase reaction kinetics and mechanisms have been studied for oxidative methane coupling.[186-188] The kinetics of oxidative coupling in pulsed microwave plasmas have also been studied.[189] The body of literature involving the methane partial oxidation and the oxidative coupling of methane is well developed for thermocatalytic methods, where many of the most important reaction steps involve surface species. The plasmachemical methane processing reaction mechanisms are much more poorly understood, but that is not to say that there is no groundwork done in the field. Methyl radicals ($CH_3$) can be produced from methane-electron collisions, and those methyl radicals serve as precursors to $CH_2$ and CH radicals.[190, 191] Oxygen, when present in the feed gas, is very effective at removing deposited carbon in the discharge system and stabilizes the discharge.[190] A collection of 23 reactions, summarized in table 6, have been compiled building off of these works in kinetic modeling of homogenous methane processing. The simple methane reactions are the likely reactions that would occur in pure methane based on literature and experimental results. The oxygen reactions add a simple reaction pathway involving oxygen species. The $C_2H_5$ reactions involve the

component $C_2H_5$, which could be a major player in the formation of C2 and C3 hydrocarbons.

Table 6: Summary of reactions used in the kinetic modeling of methane processing in oxygen.

**Simple Methane Reactions**

1) $CH_4 \rightarrow CH_3 + H$ *e* impact
2) $CH_4 + H \rightarrow CH_3 + H_2$
3) $CH_4 + CH_3 \rightarrow C_2H_6 + H$
4) $2\,CH_3 \rightarrow C_2H_6$
5) $2\,CH_3 \rightarrow C_2H_4 + H_2$

**Oxygen Reactions**

6) $O_2 \rightarrow 2O$ *e* impact
7) $CH_4 + O \rightarrow CH_3 + OH$
8) $OH + O \rightarrow O_2 + H$
9) $2\,OH \rightarrow H_2O + O$
10) $2\,OH \rightarrow H_2 + O_2$
11) $CH_4 + OH \rightarrow CH_3 + H_2O$
12) $CH_3 + OH \rightarrow CH_4 + O$
13) $H_2 + O \rightarrow H + OH$

**$C_2H_5$ Reactions**

14) $CH_3 + CH_4 \rightarrow C_2H_5 + H_2$
15) $C_2H_5 + O \rightarrow C_2H_4 + OH$
16) $C_2H_5 + H \rightarrow C_2H_6$
17) $C_2H_5 + H \rightarrow C_2H_4 + H_2$
18) $C_2H_5 + H \rightarrow 2CH_3$
19) $C_2H_5 \rightarrow C_2H_4 + H$
20) $C_2H_5 + OH \rightarrow C_2H_4 + H_2O$
21) $C_2H_5 + CH_3 \rightarrow C_3H_8$
22) $C_2H_5 + CH_3 \rightarrow CH_4 + C_2H_4$
23) $C_2H_6 + OH \rightarrow C_2H_5 + H_2O$

Reaction 1, the electron impact ionization of methane, and reaction 6, the electron impact excitement of the $O_2$ molecule, should only occur in the active discharge. Reactions 1 and 6 are likely much more complicated and involve intermediates such as vibrationally excited methane or an excited O2 molecule via electron attachment, but the simplified reactions shown here should be adequate in describing the reaction kinetics. As such, they are the initiators of reaction pathways and subject to the conditions of the discharge, including electric field strength and discharge current. Reactions 1 and 6 are treated as a special case in this simplified plasmachemical model, where the reaction rate constants are calculated theoretically based on the conditions of the generated plasma. The

remaining reactions (1-5 and 7-23) have parameters that are obtained from the NIST Chemical Kinetics database. These values are summarized in table 7 below.

Table 7: Reaction parameters for the 23 equations selected to be part of the model. All values are taken from the NIST Chemistry Webbook and the NIST Chemical Kinetics Database.[95, 192]

| Reaction # | Reaction | Reaction Type | Forward Reaction | | | | | | | Reverse Reaction | | | | | | |
|---|---|---|---|---|---|---|---|---|---|---|---|---|---|---|---|---|
| | | | ΔH$_{rxn}$ (kJ/mol) | A$_n$ | E$_a$ (kJ/mole) | n | K$_c$ (cm$^3$/molecules) | K$_c$ (m$^3$/mol/s) | ΔH$_{rxn}$ (kJ/mol) | A$_n$ | E$_a$ (kJ/mole) | n | K$_c$ (cm3/molecule/s) OR (1/s) | K$_c$ (m$^3$/mol/s) |
| 1 | $CH_4 \rightarrow CH_3 + H$ | electron impact | 438.56 | --- | --- | Theoretical Calculations | --- | --- | -438.56 | - | - | - | - | - |
| 2 | $CH_4 + H \rightarrow CH_3 + H_2$ | radical | 2.56 | 4.36E-13 | 36.63 | 3.16 | 1.69E-17 | 1.02E-01 | -2.56 | 6.86E-14 | -39.41 | 2.74 | 9.6E-21 | 5.78E-03 |
| 3 | $CH_4 + CH_3 \rightarrow C_2H_6 + H$ | radical | 63.18 | 4.95E-13 | 188 | 1 | 1.053E-22 | 6.34E-05 | -63.18 | 8.97E-20 | 48.64 | | 7.34E-23 | 4.42E-05 |
| 4 | $2CH_3 \rightarrow C_2H_6$ | radical | -375.38 | 1.03E-10 | 1.33 | -1.1 | 6E-11 | 3.61E+07 | 375.38 | 7.49E-20 | 392 | -8.24 | 2.8E-64 | 1.69E-46 |
| 5 | $2CH_3 \rightarrow C_2H_4 + H_2$ | radical | -238.91 | 1.66E-08 | 134 | - | 1.66E-13 | 1.00E+05 | 238.91 | - | - | - | - | 0.00E+00 |
| 6 | $O_2 \rightarrow 2O$ | electron impact | 498.36 | --- | --- | Theoretical Calculations | --- | --- | -498.36 | - | - | - | - | - |
| 7 | $CH_4 + O \rightarrow CH_3 + OH$ | radical | 10.37 | 2.26E-12 | 31.76 | 2.2 | 6.12E-18 | 3.68E+00 | -10.37 | 3.22E-14 | 18.62 | 2.2 | 1.75E-17 | 1.05E+01 |
| 8 | $OH + O \rightarrow O_2 + H$ | radical | 179.01 | 2.4E-11 | - | -0.91 | 3.47E-11 | 2.09E+07 | -179.01 | 1.62E-10 | 62.11 | - | 2.48E-21 | 1.49E-03 |
| 9 | $OH + OH \rightarrow H_2O + O$ | radical | -70.626 | 1.02E-12 | -1.66 | 1.4 | 1.48E-12 | 8.91E+05 | 70.626 | - | - | - | - | 0.00E+00 |
| 10 | $OH + OH \rightarrow H_2 + O_2$ | radical | -77.98 | 3.32E-12 | 211 | 0.51 | 2.99E-49 | 1.80E-31 | 77.98 | - | - | - | - | 0.00E+00 |
| 11 | $CH_4 + OH \rightarrow CH_3 + H_2O$ | radical | -60.256 | 4.16E-13 | 10.24 | 2.18 | 6.68E-15 | 4.02E+03 | 60.256 | 1.2E-14 | 62.19 | 2.9 | 1.82E-25 | 1.10E-07 |
| 12 | $CH_3 + OH \rightarrow CH_4 + O$ | radical | -10.37 | 3.22E-14 | 18.62 | 2.2 | 1.75E-17 | 1.05E+01 | 10.37 | 2.26E-12 | 31.76 | 2.2 | 6.12E-18 | 3.69E+00 |
| 13 | $H_2 + O \rightarrow H + OH$ | radical | 7.81 | 3.44E-13 | 26.27 | 2.67 | 9E-18 | 5.42E+00 | -7.81 | 6.89E-14 | 16.21 | 2.8 | 1.05E-16 | 6.32E+01 |
| 14 | $CH_3 + CH_4 \rightarrow C_2H_5 + H_2$ | radical | 48.18 | 1.66E-11 | 96.45 | - | 4.33E-14 | 2.61E+04 | -48.18 | - | - | - | - | 0.00E+00 |
| 15 | $C_2H_5 + O \rightarrow C_2H_4 + OH$ | radical | -276.72 | 6.31E-12 | -1.65 | 0.03 | 1.23E-11 | 7.41E+06 | 276.72 | - | - | - | - | 0.00E+00 |
| 16 | $C_2H_5 + H \rightarrow C_2H_6$ | radical | -421 | 1.66E-10 | - | - | 1.6E-10 | 9.64E+07 | 421 | 8.11E+17 | 427 | -1.23 | 1E-57 | 6.02E-40 |
| 17 | $C_2H_5 + H \rightarrow C_2H_4 + H_2$ | radical | -284.53 | 3.01E-12 | - | - | 3.01E-12 | 1.81E+06 | 284.53 | 1.69E-11 | 285 | | 3.75E-61 | 2.26E-43 |
| 18 | $C_2H_5 + H \rightarrow 2CH_3$ | radical | -45.62 | 1.25E-10 | - | - | 1.25E-10 | 7.53E+07 | 45.62 | 1.46E-11 | 44.4 | 0.1 | 2.4E-19 | 1.45E-01 |
| 19 | $C_2H_5 + OH \rightarrow C_2H_4 + H$ | radical | 151.47 | - | - | - | 5.56E-15 | 3.35E+03 | -151.47 | 1.25E-11 | 6.07 | 1.07 | 1.1E-12 | 6.62E+05 |
| 20 | $C_2H_5 + OH \rightarrow C_2H_4 + H_2O$ | radical | -347.346 | 4E-11 | - | - | 4E-11 | 2.41E+07 | 347.346 | - | - | - | - | 0.00E+00 |
| 21 | $C_2H_5 + CH_3 \rightarrow C_3H_8$ | radical | -369.39 | - | - | - | 1.99E-23 | 1.20E-05 | 369.39 | 2.78E+18 | 371 | -1.8 | 7.48E-47 | 4.50E-29 |
| 22 | $C_2H_5 + CH_3 \rightarrow CH_4 + C_2H_4$ | radical | -287.09 | - | - | - | 1.9E-12 | 1.14E+06 | 287.09 | - | - | - | - | 0.00E+00 |
| 23 | $C_2H_6 + OH \rightarrow C_2H_5 + H_2O$ | radical | -77.816 | 8.53E-13 | 3.1 | 2.22 | 2.44E-13 | 1.47E+05 | 77.816 | 2.06E-14 | 84.81 | 1.44 | 3.56E-29 | 2.14E-11 |

The calculations for the electron impact ionization of methane depend strongly on the energy of the electrons in the discharge. The Druyvesteyn EEDF can be used as an

approximation of the electron energy in nonequilibrium plasmas. In order to generate a distribution, an average electron energy value is required. Even in nonequilibrium plasmas, the average electron energy can be correlated with the reduced electric field ($E/n_0$). This correlation is shown in equations 3 and 4, reproduced here.

$$T_e = \frac{eE\lambda}{\sqrt{\delta}}\sqrt{\frac{\pi}{12}} \tag{3}$$

Here, it is useful to rearrange some of the terms to define the electron temperature in terms of reduced electric field and the interaction cross section of the electron-neutral collisions, $\langle\sigma_{en}\rangle$, to yield equation 4.[91]

$$T_e = \left(\frac{E}{n_0}\right)\frac{e}{\langle\sigma_{en}\rangle}\sqrt{\frac{\pi}{12}} \tag{4}$$

The electric field strength for a discharge gap of 1 mm operating at 700 V is 7000 V/cm. The average electron energy can be estimated from this electric field strength to be approximately 5.6 eV. In figure 75 below, the Druyvesteyn distribution with an average electron energy of 5.6 eV is plotted with the electron impact cross section for the methane molecule.

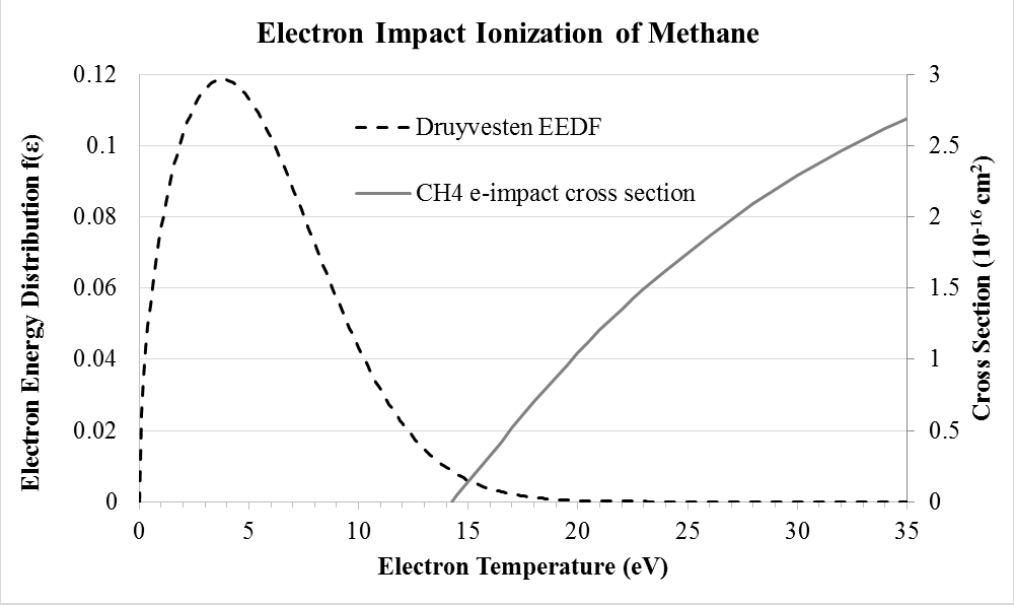


Figure 75: Electron impact ionization cross section for the methane molecule and a characteristic Druyvesteyn EEDF. The overlapping section of the plot is a graphical representation of the electron impact driven reaction rate of methane in the model system.

This figure graphically depicts how electron impact driven chemical reaction kinetics can be theoretically calculated. Here, the area underneath where the two curves overlap represents the physical space where electrons have enough energy to directly ionize methane. Ionized methane and vibrationally excited methane can then decompose into CH3 and H, as per reaction 1. The rate constant for the electron impact ionization of methane can be calculated using the values of the curves in figure 75, where $\sigma$ is the value of the electron impact cross section as a function of electron velocity, $v$. The electron velocity is directly proportional to the electric field strength, which is directly related to the electron energy, modeled here by the EEDF which is essentially the probability of an electron moving at a certain velocity. The elementary reaction rate can be calculated with these values using equation 9 (reproduced here).

$$k_{A+B} = \int \sigma(v)\, vf(v) dv = \langle \sigma v \rangle \tag{9}$$

The calculations for the excitement of oxygen in the discharge are similar in nature to the calculations for methane. Reactions that occur with negative ions, which regularly occur in electronegative gases, are usually attachment reactions. Dissociative attachment occurs regularly when the products have positive electron affinity. The dissociative attachment rate coefficient, $k_a$, can be approximated as a function of the resonance parameters for dissociative attachment (equation 24, reproduced here). The parameters $\varepsilon_{max}$, $\Delta\varepsilon$, and $\sigma_{d.a.}^{max}$ can be calculated but are also tabulated and are 6.7 eV, 1 eV, and $10^{-18}$ $cm^2$ for the dissociative attachment of $O_2$, respectively.[91]

$$k_a \approx \sigma_{d.a.}^{max}(\varepsilon_{max}) \sqrt{\frac{2\varepsilon_{max}}{m}} \frac{\Delta\varepsilon}{T_e} e^{-\frac{\varepsilon_{max}}{T_e}} \tag{24}$$

The rate for three-body attachment processes is greater than dissociative attachment once the gas number density reaches a certain threshold value. For oxygen, this value is for a number density greater than $10^{18}$ $cm^3$, which corresponds to a gas pressure greater than 30 torr. The Bloch-Bradbury mechanism is important in nonthermal plasmas that have relatively low electron energies. This calculation would be used in systems with lower calculated electron energy systems, but for the estimate of an average electron energy 5.6 eV here, the dissociative attachment reaction rate is used instead.

The rate coefficients for the electron impact mediated reactions can be calculated as outlined above, and for a discharge with an average electron energy of 5.6 eV yield the values in table 8.

Table 8: Theoretical reaction rate constants for electron impact mediated reactions.

| Reaction | Rate Coefficient, $k$ |
|---|---|
| $CH_4 + e \rightarrow CH_3 + H$ | 1.88e8 [$m^3$/mol/s] |
| $O_2 \rightarrow 2\,O$ | 8.32e8 [$m^3$/mol/s] |

The selected reactions outlined in table 7 and the theoretical kinetic values derived here were used to generate a 0D kinetic model using the reaction engineering module in COMSOL. The concentration profiles over time from the 0D model are shown in figure 76.

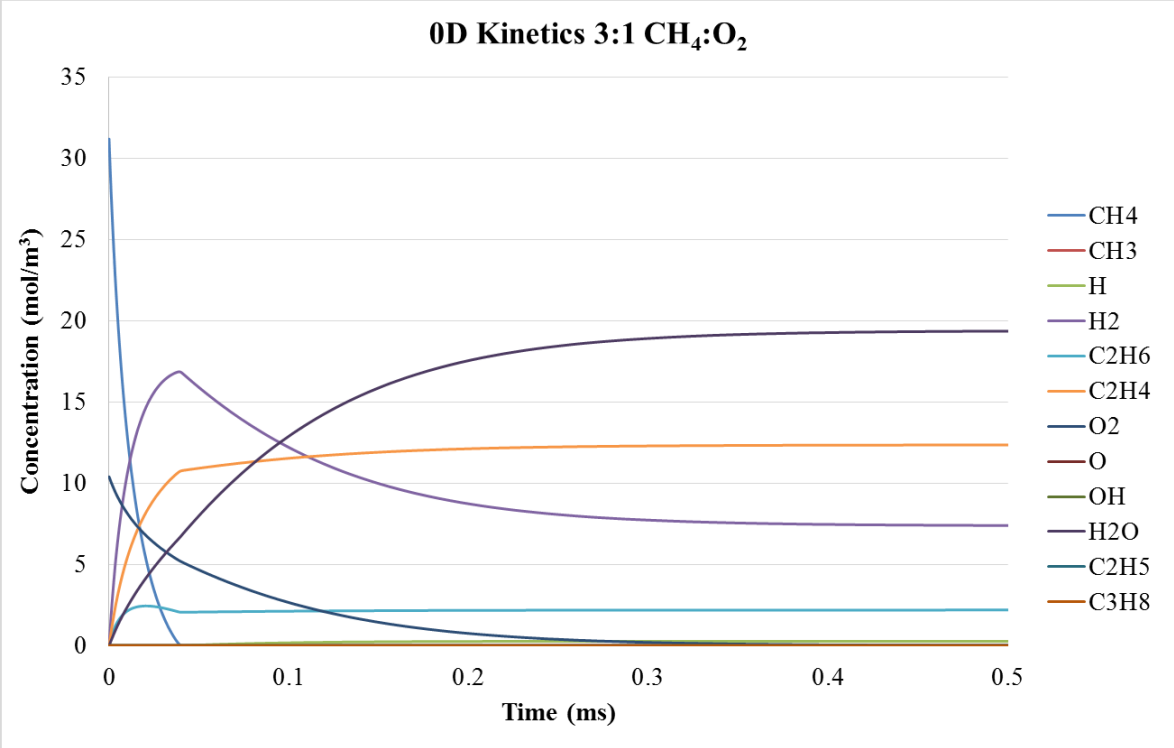


Figure 76: 0D kinetic model concentration profiles as a function of time for a 3:1 $CH_4$:$O_2$ mixture in the active discharge for all 23 reversible reactions outlined in tables 6, 7, and 8.

The 0D model system is for the reactions taking place in the active discharge, so it is important to note that these are the products that would result if the reactants and

products were allowed to stay in the active discharge as time progresses. At times longer than ~50 μs, $H_2O$, $H_2$, $C_2H_4$, and $C_2H_6$ become the dominant products. These results agree closely with the experimental results obtained with the constructed microreactor. Figure 77 shows that the dominant reaction products in the 0D model for pure methane flows are $H_2$, $C_2H_6$, and $C_2H_4$.

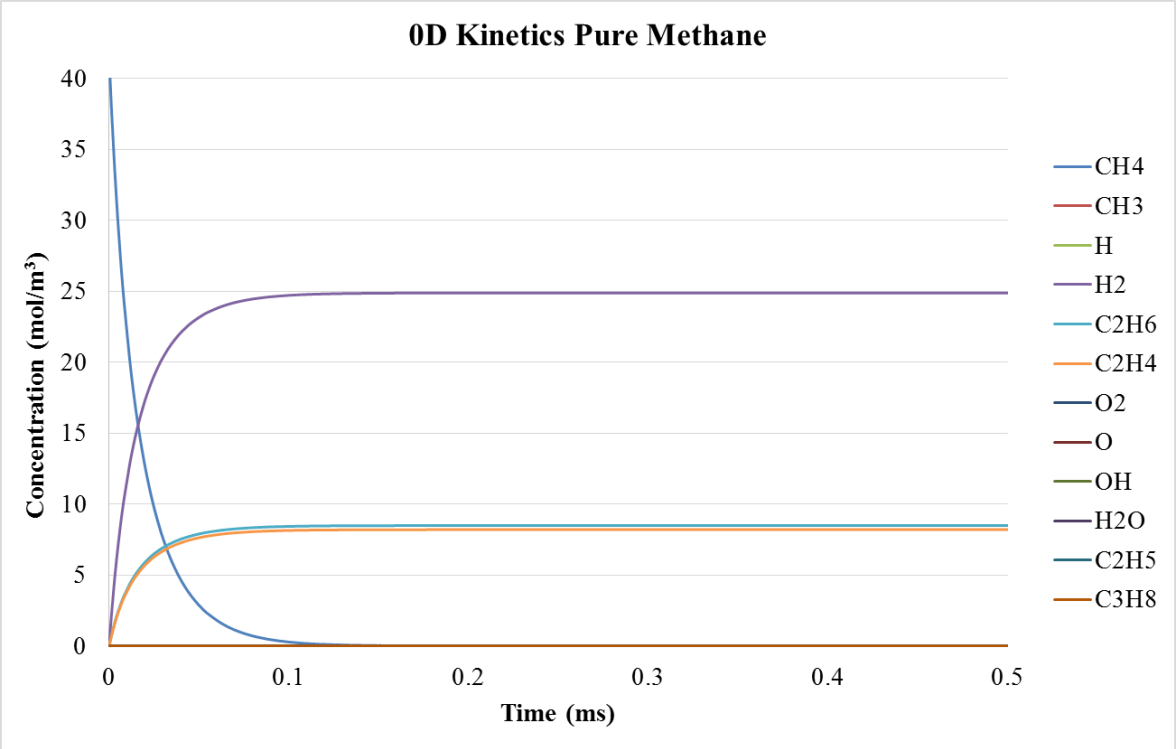


Figure 77: 0D kinetic model concentration profiles as a function of time for pure methane in the active discharge for all 23 reversible reactions outlined in tables 6, 7, and 8.

Figure 78 shows the 0D kinetic model in a 1:1 $CH_4$:$O_2$ flow. This suggests that as oxygen content in the feed stream increases the dominant product shifts to $C_2H_4$ alone as the oxygen content is greater than required to enable reaction pathways to C2 species. Radical species such as O and H are still present at longer reaction times and continue to react with $C_2H_6$ and $H_2$ to form $H_2O$.

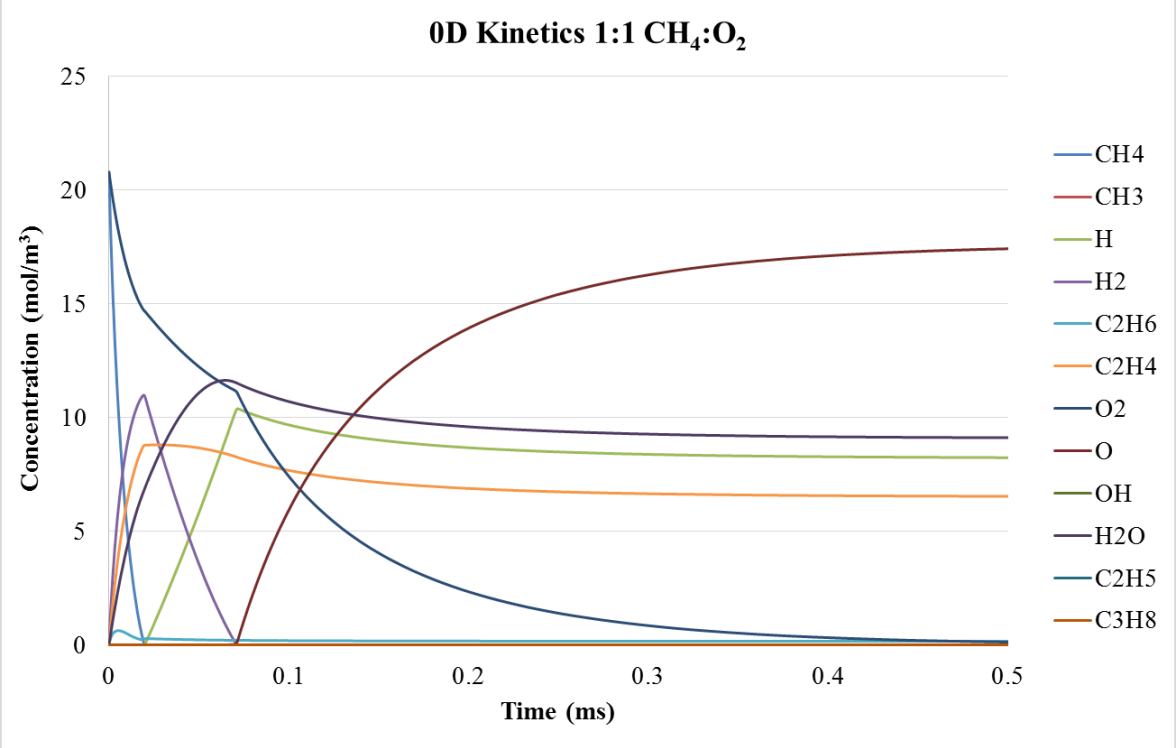


Figure 78: 0D kinetic model concentration profiles as a function of time for a 1:1 $CH_4$:$O_2$ mixture in the active discharge for all 23 reversible reactions outlined in tables 6, 7, and 8.

### *2D Kinetic Model*

A more realistic model of the constructed microreactor would include fluid flow and diffusion, along with the geometry of the reacting system. In order to accomplish a more realistic simulation, a 2D COMSOL model was developed. The 2D kinetic model incorporated the fluid flow and transport of concentrated species modules along with the basic kinetics of simple methane/oxygen reactions in the reacting flow generated by the glow discharge. Figure 79 shows the basic geometry of the 2D model.

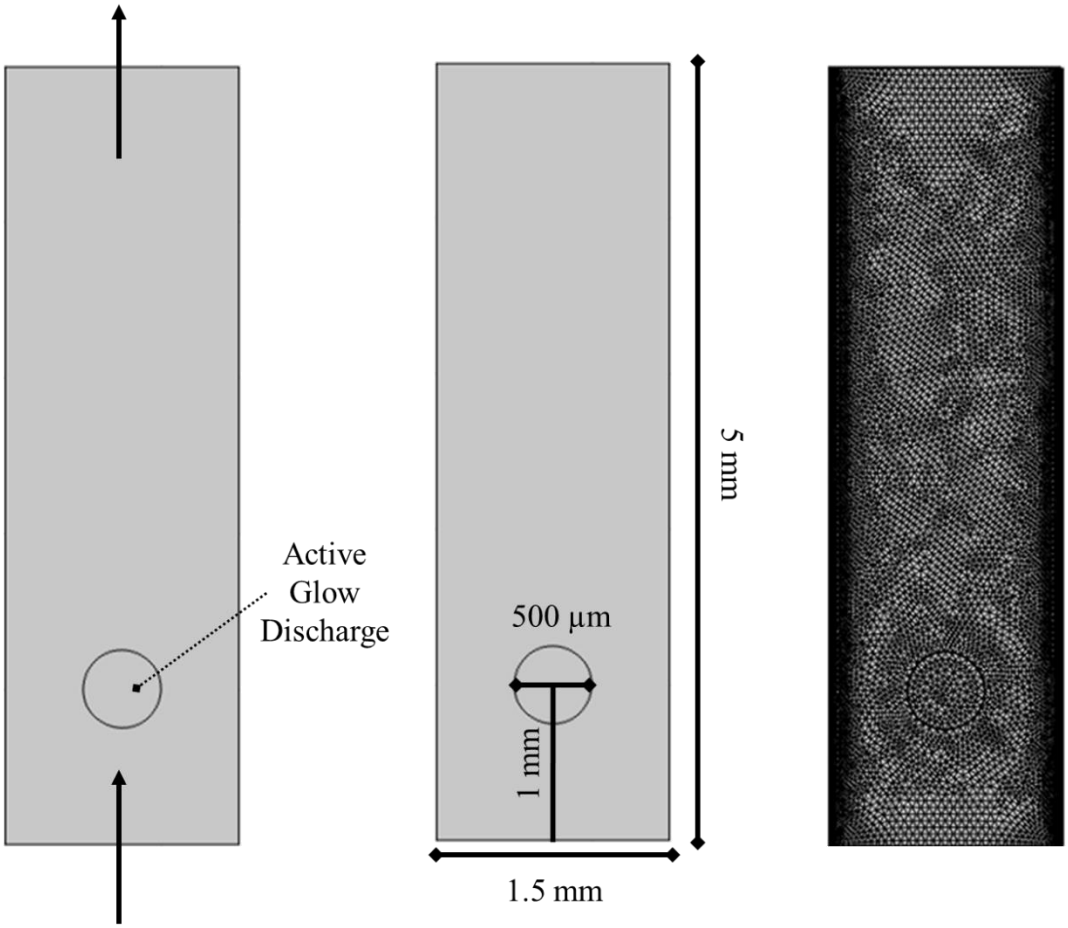


Figure 79: Basic geometry of the constructed 2D kinetic COMSOL model. Left) A simple schematic showing fluid flow path and the separation of the two reaction domains. The circle is the active discharge, and the remaining area is the reaction zone where there is no active discharge. Middle) Dimensions of the reaction system. Right) The reaction system with the solver mesh.

The simulated reactor consists of an inlet, and outlet, and a rectangle that represents the total reaction volume. The circle in the middle represents the active discharge where electron impact reactions are active. The circle is 500 µm in diameter, obtained by measuring the size of the active glow discharge in very slow oxygen flows. This value is a conservative approximation of the active discharge zone. The entire model space has the remaining radical reaction pathways active, so the flow continues to react after passing through the discharge.

The model was developed and initially run with pure methane as the reacting flow and used the "simple methane reactions" (reactions 1-5) outlined in table 6. The model was then updated with the oxygen reactions (reactions 6-13), and then further updated

including the reaction pathways that can include $C_2H_5$ (reactions 14-23) and run with a $CH_4$:$O_2$ mixture of 3:1 at a total flow rate of 10 mL/min. The kinetic parameters for the radical reactions used in these studies are predominantly taken from the NIST Chemical Kinetics Database, with the exception of the electron impact reactions, which are estimated using theoretical equations that employ plasma parameters such as the electron impact ionization cross section.[192] The two electron impact driven reactions, methane activation (reaction 1) and oxygen activation (reaction 6), are only active inside the circle in the reaction volume. The kinetic parameters for these radical reactions are much too fast for the solver to converge upon a solution when the system is coupled with fluid flow and diffusion. As a result, the k values for the studied reactions are reduced in magnitude by a factor of $10^5$ for the solutions presented in the 2D COMSOL model. The reactions still occur extremely quickly in the model. Additionally, the reverse reactions are essentially non-existent compared to the forward reactions. This reduction in magnitude of the kinetic parameters is an effective, although elementary way to reduce issues that the solver has with the extremely fast electron transport and plasmachemical reaction timescales (see figure 8).

Surface plots for concentrations in mol/$m^3$ of reactants ($CH_4$ and $O_2$) and major products ($C_2H_6$, $C_2H_4$, and $H_2$) from the 2D COMSOL model are shown in figure 80. These surface plots effectively shown how the reactants are consumed and products are generated in the active discharge and corresponding plasma plume that flows behind the active discharge zone. The figures also demonstrate how bypass around the active plasma results in overall lower chemical conversion to desired products.

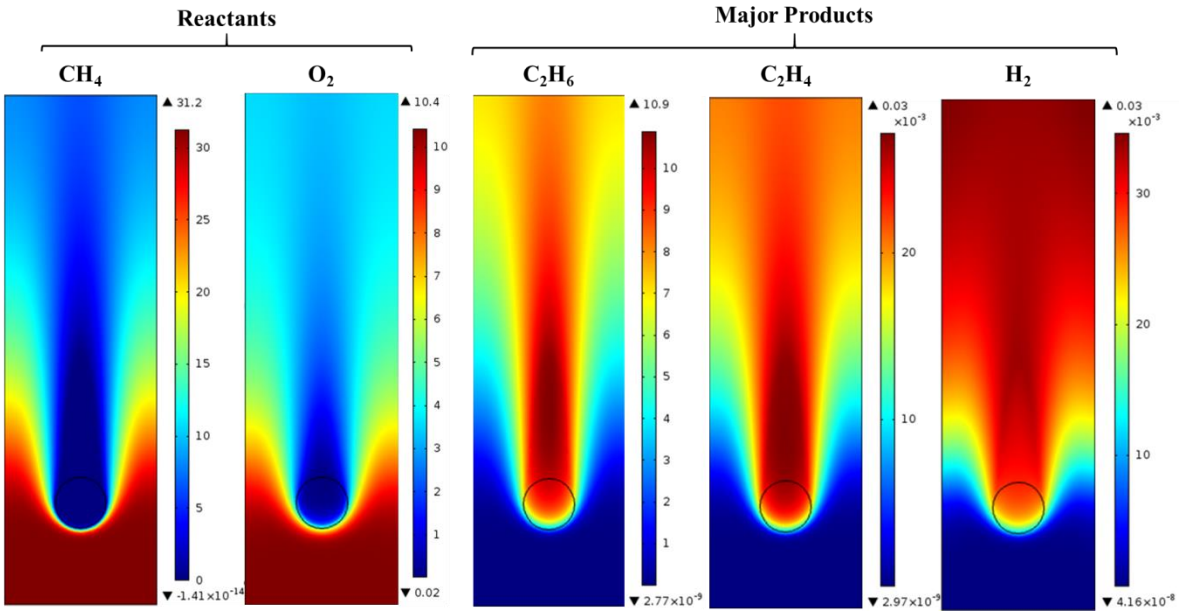


Figure 80: COMSOL surface plots for the concentration of reactants ($CH_4$ and $O_2$) and the major products ($C_2H_6$, $C_2H_4$, and $H_2$) in units of mol/$m^3$.

Taking an axial cutline down the centerline of the surface plots in figure 80, the concentrations along the reactor length can be plotted together, as is done in figures 81 and 82.

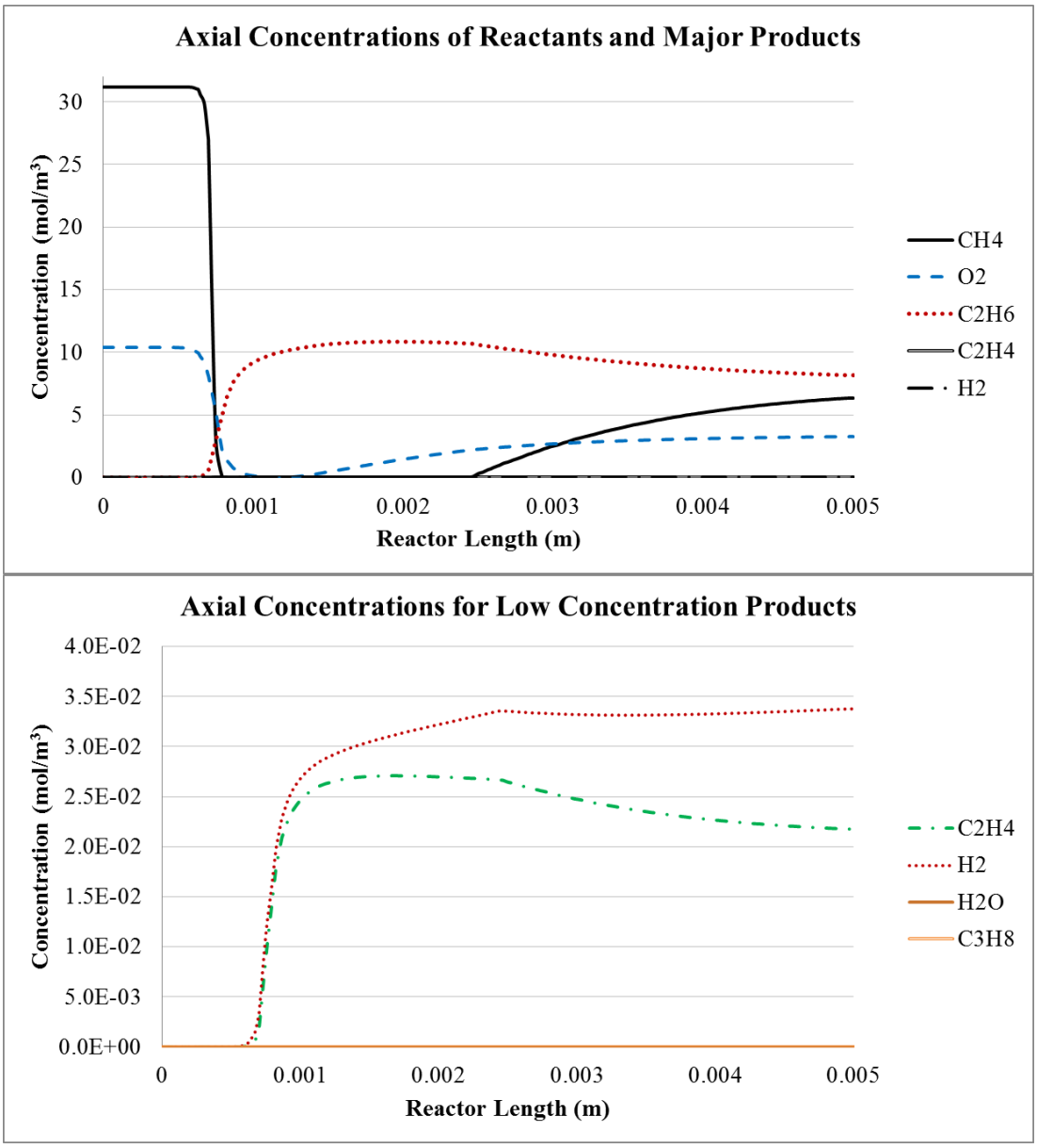


Figure 81: Axial concentrations (mol/m$^3$) in the 2D Comsol model. These values correspond to a cutline through the reactor centerline for each of the reactants and products shown in figure 78.

Both methane and oxygen are used up rapidly in the active discharge. This occurs as a result of the rapid electron-impact initiated reactions, and the equally rapid radical reactions that occur with the products of the electron-impact reactions. There is some bypass around the active discharge, and that bypass increases the reactant gas concentrations further down the reactor. $C_2H_6$ is the major product, with $C_2H_4$ and $H_2$ also being produced in appreciable quantities, although quantities much smaller than

$C_2H_6$. $H_2O$ and $C_3H_8$ are essentially nonexistent as products in this simplified model reaction system.

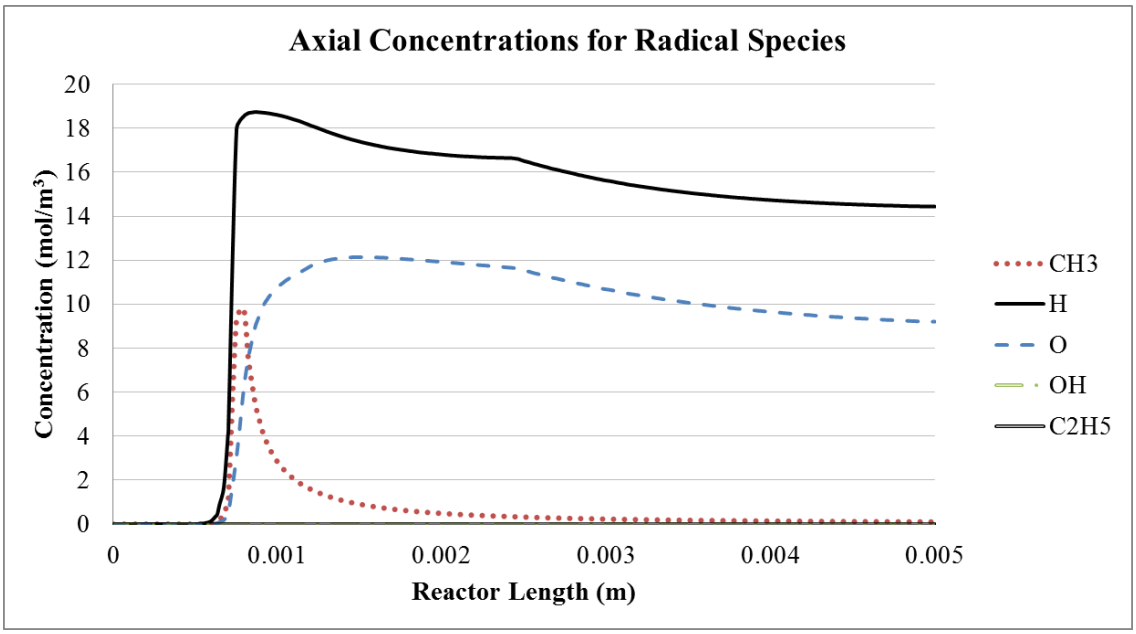


Figure 82: Axial concentrations for radical species in the reaction space.

Methyl radicals ($CH_3$) are rapidly generated by decomposing methane and subsequently rapidly consumed in the ethane formation reactions. Both H and O radicals still exist in appreciable quantities at the end of the 5 mm reaction zone. These radicals should continue to react with methane, oxygen, and formed products to generate water, ethylene, hydrogen, and other species in greater concentrations. However, experimental results do suggest that the majority of O radicals produced in the reaction zone reform the starting reactant, $O_2$ gas. In the 0D kinetic model, where all components remain in the active discharge area, ethylene, water, and hydrogen become much more prominent reaction products, suggesting that the actual active discharge area is larger than was used in the 2D model. Alternatively, the formation of $C_2H_4$, $H_2$, and $H_2O$ (and possibly $CO/CO_2$ products) could occur as a result of electron impact reactions with primary reaction products such as $C_2H_6$ or radical species.

## Modeling Conclusions

Taking the 0D and 2D models as a complete picture of the reacting system, the COMSOL simulations model the nonthermal plasma microreactors to a reasonable level of accuracy. The 2D model effectively predicts that ethane, ethylene, and hydrogen are the dominant products. The 0D model provides further insight, suggesting that if ethane is formed and continually exposed to the active discharge, products such as ethylene, hydrogen, and water become much more pronounced in the product stream, which agrees closely with the results seen in experimental runs.

Future iterations of the model should seek to include more thorough oxidative dehydrogenation reactions, which could play a large role in the formation of ethylene and acetylene from ethane. Also, $CH_2$ and CH species should be incorporated to give the most realistic model outputs, as it has been suggested that there are parallel reaction pathways to C2 products.[191] Even though the experimental investigations suggest that $CO_2$ and CO are minor products in this system, a thorough model should also include species and the reaction pathways that lead to deep oxidation. These improvements would make the model much more robust and useful in carrying out reactions in theoretical conditions. The use of the COMOSL Plasma module is the ideal way to improve the quality of the models that simulate the microplasma reactor. However, the complexity involved in preparing and building a COMSOL plasma module model for even a simple reaction like the oxidative coupling of methane is extreme, and would warrant a PhD dissertation in and of itself.

Models of the electric field surrounding an array of electrode features are useful in exploring theoretical electrode geometries and designs. The beginnings of the electric field models developed here suggest that proximity of packing is of secondary concern, and sharpness of the electrode features is important for activating many tips simultaneously. The tip radius of cone shaped electrode features should be on the order of 10 microns in diameter if the goal is simultaneous activation of many tips in a completely uniform array.

# Conclusions

## Nonthermal Plasmas Review

Overall, the field of chemical reaction engineering using microscale nonthermal plasmas has not been extensively studied. Many publications study nonthermal plasmas that are generated at centimeter and millimeter scales, and the these works generally show that plasmas generated on the microscale provide enhanced stability, improved excited species density, increased nonequilibrium properties, higher electron temperature, and better energy efficiency along with reduced onset voltages. Little attention has been given to DC or DC pulsed non-thermal plasma at low electric potentials at confined (10 to 500μm) spatial scales for chemical conversion. Generally, nonthermal plasmas meet or exceed the performance of traditional chemical processing systems, while microplasmas have shown the potential to outperform macroscale nonthermal plasma chemical systems. Of the studies that use microplasmas to drive chemical reactions, many report improved conversion, higher selectivity towards desirable products, and increased energy efficiency.

Electric field strength, and thus the energy distribution among excited states, can directly affect product selectivity in nonthermal plasma systems. This adds further motivation to generating these plasmas at the microscale, where small adjustments in geometry and applied potential can greatly impact electric field strength while maintaining energy efficiency.

Plasmacatalysis is an effective method to improve yields and to tailor selectivity to desired products. In nonthermal plasma reaction systems, the materials of construction seem to directly affect reaction products. This further suggests that catalysis combined with plasma processing could be very effective at the microscale. Surface interactions become important in imparting energetic stability to plasmas generated at the microscale, and since the walls and surfaces affect product distribution, this synergistic effect could be engineered to not only stabilize the active plasma but also tune reactions to yield different products.

The generation of nanoparticles and nanomaterials using nonthermal plasmas benefit from improved quality, higher crystallinity, and enhanced properties in catalysis and semiconductor devices. Plasma processing appears to be capable of generating novel particle morphologies. It is possible that other material properties could be adjustable based on plasma parameters.

The frontier of low energy, non-thermal plasma chemical processing appears to be in confined microscale technology utilizing pulsed nanosecond power. The question still remains as to whether discharge regime and electrical properties of the plasma can be used to control chemical reaction pathways. Future studies should focus on the depth analysis of the relationship between plasma operating parameters and the effect they have on chemical reactions driven in nonthermal plasmas, namely reaction mechanisms, reaction kinetics, and chemical conversion and product selectivities.

## Reactor Design

Several reactor designs were explored and evaluated for their effectiveness in generating reproducible, stable, non-thermal plasma that enable chemical processing. The constructed devices all needed to be able to generate a stable discharge, allow flow through a reaction zone and also allow for the conduction of electricity only through the desired pathway and not into parts of the device that are not associated with the reaction zone.

Ultimately, the point-to-plane reactor designs were the best designs for reliably producing stable nonthermal plasmas in a repeatable manner. The use of singular sharp points creates an equally singular origination for the actual discharge, which was important in reproducibility of experimental run conditions. The result of this single point-to-plane active discharge zone is a reproducible discharge that can be observed visually and characterized electrically and spectroscopically. Additionally, the point-to-plane designs are very simple, which facilitates modeling efforts, minimizes manufacturing costs, and simplifies experimental work and data analysis.

Monitoring of the generated nonthermal plasmas can be accomplished with electrical measurements, notably circuit current, total applied potential, and the sustaining voltage

drop across the reaction zone with a differential oscilloscope probe. However, in completing this work it became apparent that the best way to reliably determine the discharge regime and corresponding shape, size, luminosity, and behavior of the discharge is *via* visual inspection through a viewing window. The presence of a viewing window also allows for optical emission spectroscopy, which is a useful tool in probing plasmachemistry and reactivity of the discharge.

Materials of construction for nonthermal microplasma reactors are of serious concern. The best reactors constructed here were machined out of polycarbonate, which was cheap and easy to achieve. However, reactor failure as a result of melting and burning polycarbonate became a problem at high discharge current and with highly exothermic reactions. Materials such as glass and machinable ceramic are the most promising moving forward in this field. Electrode materials are also of concern, as their properties can affect not only the discharge properties but also directly influence product distributions. Ni was predominantly used as the sharp tip electrode due to ease of electrochemical etching, and stainless steel was used as the flat plate electrode due to ease of access with stainless steel materials. Future work should consider the effect these materials have in the reaction system.

## Plasmachemical Methane Processing

A microreaction system that can generate stable atmospheric pressure glow for volumetric chemical processing has been developed. The developed system is an effective platform for the oxidative coupling of methane to C2 and C3 hydrocarbons. In this preliminary study on methane processing with oxygen co-feed, the optimum operating point for methane oxygen systems lies around a 3:1 methane:oxygen ratio, where conversion is maximized, selectivity to C2 products remains high, and the formation of a carbon filament, and as a consequence solid carbon deposition, in the discharge gap is greatly diminished.

Methane conversion increases linearly with increasing discharge current and selectivity to longer chain hydrocarbons remains high at varying discharge currents. At higher discharge currents above 3 mA, C3 hydrocarbons start to become major reaction

products. Methane processing reactions with to up 56.2% methane conversion, 91.5% selectivity for C2/C3 products, for one pass yields of 51% for C2 hydrocarbons have been achieved. Optical emission spectroscopy as an *in situ* technique for measuring product distributions. In the methane/oxygen discharges, the $C_2$ Swan emission band at 516.5 nm, CH emission at 431.4 nm, Hα emission line at 656.28 nm are correlated with the effluent concentration of $C_2H_4$, $C_2H_6$, $H_2$, respectively.

## Performance and Energy Efficiency

The performance of the nonthermal microplasma reactor developed in this work compares favorably in both catalytic performance and energy consumption to other oxidative methane coupling technologies. This is due in part to targeting discharge regimes that optimize power consumption while maintaining an excited species density that remains suitable for the activation of chemical reactions.

Investigating the effect of flow rate and in turn, residence time in the reaction zone shows that faster flows lead to lower chemical conversion. This is the expected result, as more time spent in the presence of the activating discharge should yield higher concentrations of products. However, the consumed power in the discharge reaches a local maximum and midrange flow rates and is lower at higher flow rates, which suggests potential for energy efficient high flow-rate processing with reduced single pass conversion.

Nonthermal microplasmachemical oxidative methane coupling has demonstrated superior performance than traditional thermocatalysis, with conversions greater than 50% and selectivites to C2/C3 products greater than 90%. The reactor effluent bulk gas temperature remains near room temperature during active glow discharge operation. This low power operation leads to low specific energy inputs, the ration of input power to processed volume, which allows for high C2/C3 selectivites and suppresses deep oxidation products CO and $CO_2$. This nonthermal microplasma system results in energy efficiencies that approach 50% in methane coupling reactions. It should be noted that this is due in part to the presence of oxygen in the reaction flows, which creates water as a product and provides thermodynamic driving force to products.

## Plasmachemical Methane Dry Reforming

Discharges in both pure $CO_2$ and a co-feed of 1:1 $CO_2$:$CH_4$ create products that warrant further investigation into microplasma $CO_2$ processing. For pure carbon dioxide feed streams, single pass dissociation to CO and $O_2$ is observed. $CH_4$/$CO_2$ mixtures show more $CO_2$ dissociation and the formation of C2 hydrocarbons. A 1:1 $CH_4$:$CO_2$ mixture quickly forms coke on the sharp tip electrode, so future explorations should explore reaction mixtures that have higher $CO_2$ concentrations in the feed gas.

## Desulfurization

A flat plate reactor with a conductive silver epoxy coating on one electrode was able to complete an electrical circuit through flows of dibenzothiophene in n-decane at electrode spacings smaller than 50 µm. In this system dissolved oxygen content from the reactor effluent decreased as a result of electrical current. However, it has not been shown whether this electrical current effectively mediates any oxidation of sulfur compounds in fuel-like media. Observations of this reaction system and studies in literature suggest that at least part of the electrical current draw into this system drives the oxidation or electrochemical corrosion of the silver epoxy coating on the electrode surface. The interaction of aromatic sulfur compounds with silver could explain the oxidative desulfurization phenomena observed in previous works at OSU. This implication suggests that future research efforts should explore electrically driven oxidative desulfurization with silver-based catalysts. In a point-to-plane discharge system with a discharge gap of 250 µm, electrical breakdown in n-decane with 2000 ppm DBT occurs around 6.5 kV. The resulting discharge forms a carbon filament between the electrodes, effectively shorting the reactor and limiting the duration of the generated discharges to lifetimes on the order of 10 seconds.  There is no observable oxidation of dibenzothiopehene using this simple point-to-plane DC discharge in 2000ppm DBT/n-decane flows.

## Modeling

Taking the 0D and 2D models as a complete picture of the reacting system, the COMSOL simulations model the nonthermal plasma microreactors to a reasonable level of accuracy. The 2D model effectively predicts that ethane, ethylene, and hydrogen are the dominant products. The 0D model provides further insight, suggesting that if ethane is formed and continually exposed to the active discharge, products such as ethylene, hydrogen, and water become much more pronounced in the product stream, which agrees closely with the results seen in experimental runs.

Future iterations of the model should seek to include more thorough oxidative dehydrogenation reactions, which could play a large role in the formation of ethylene and acetylene from ethane. Also, $CH_2$ and CH species should be incorporated to give the most realistic model outputs, as it has been suggested that there are parallel reaction pathways to C2 products.[191] Even though the experimental investigations suggest that $CO_2$ and CO are minor products in this system, a thorough model should also include species and the reaction pathways that lead to deep oxidation. These improvements would make the model much more robust and useful in carrying out reactions in theoretical conditions. The use of the COMOSL Plasma module is the ideal way to improve the quality of the models that simulate the microplasma reactor. However, the complexity involved in preparing and building a COMSOL plasma module model for even a simple reaction like the oxidative coupling of methane is extreme, and would warrant a PhD dissertation in and of itself.

Models of the electric field surrounding an array of electrode features are useful in exploring theoretical electrode geometries and designs. The beginnings of the electric field models developed here suggest that proximity of packing is of secondary concern, and sharpness of the electrode features is important for activating many tips simultaneously. The tip radius of cone shaped electrode features should be on the order of 10 microns in diameter if the goal is simultaneous activation of many tips in a completely uniform array.

# Future Work

This body of work has taken reactor design, experimental evaluation, and modeling of nonthermal microplasmas to a point where works that build upon this foundation are easily imagined.

Further exploration into more sophisticated reactor designs, specifically those designs that aim to reduce bypass flow and incorporate multiple discharge points in series. The energy calculations carried out in our lab suggest that reactors capable of high throughput will be the most energy efficient and more easily applicable to industrial purposes. The use of already developed microplasma generators, such as the microhollow cathode discharge, may be of interest if they can be adapted to chemical processing.

The effect of discharge regime (i.e. corona, glow, transition) on conversion and product selectivity should be more thoroughly explored. Works involving plasmachemical reaction systems show results that suggest an interaction between discharge characteristics and chemical products. Future work would benefit from a better understanding of this interaction, specifically as it pertains to discharge mode and chemical conversion and selectivity. Literature suggests that the use of pulsed DC power at the nanosecond time scale is a promising method to both control the discharge regime and lower the power expenditure to turn on the plasma. The reader is referred to the research efforts of Justin Pommerenck for further insight on the subject as his work closely mirrors this work and explores the use of pulsed discharge systems.

Additionally, future work using different reactant gases, such as methane/water for steam reforming, the addition of $N_2$ or a noble gas to the discharge stream, methane/water/carbon dioxide for combined steam/dry reforming, or other gases of industrial interest would be interesting. Current work at OSU is already investigating $CO_2$ conversion to fuels, and the preliminary work presented here in methane dry reforming is promising.

The experimental results involving the oxidative desulfurization of dibenzothiophene using simple DC electrical discharges are not promising. However, the results obtained in this work and in the past using silver epoxy coated electrodes and an electrophoresis power supply enable a different phenomenon than does the simple HV DC discharge with a point-to-plane discharge system. This phenomena warrants further investigation.

A preliminary COMSOL model that simulates the point-to-plane microplasma reactor has been developed here, with reasonable outputs for chemical conversion in the oxidative coupling of methane. Future iterations of the COMSOL kinetic model should seek to include oxidative dehydrogenation reactions, which likely play a large role in the formation of ethylene and acetylene from ethane. Also, $CH_2$ and CH species should be incorporated to give the most realistic model outputs, as it has been suggested that there are parallel reaction pathways to C2 products. [191] [191] [190] Even though the experimental investigations suggest that $CO_2$ and CO are minor products in this system, a thorough model should also include species and the reaction pathways that lead to deep oxidation. These improvements would make the model much more robust and useful as a predicative tool for probing theoretical reaction conditions.

# Non-Dissertation Publications

## Two-step continuous-flow synthesis of $CuInSe_2$ nanoparticles in a solar microreactor.

**Peter B Kreider**, Ki-Joong Kim, Chih-Hung Chang.

*RSC Advances.*[193]

A novel method of copper indium diselenide nanoparticle ($CuInSe_2$ NP) synthesis using a two-step, continuous flow, solar microreactor is reported here. This method allows for exceedingly fast heating and short reaction times using only radiative heat transfer from simulated, concentrated solar radiation. Chalcopyrite and sphalerite $CuInSe_2$ phases have both been synthesized by changing nucleation temperature and residence time through the solar microreactor, with higher nucleation temperatures and longer residence times allowing for the formation of the chalcopyrite $CuInSe_2$ phase.

## Visible light sensitive nanoscale Au-ZnO photocatalysts.

Ki-Joong Kim, **Peter B Kreider**, Chih-Hung Chang, Chul-Min Park, Ho-Geun Ahn.

*Journal of Nanoparticle Research.*[194]

The role of gold nanoparticles supported on ZnO in photocatalytic activity for dye degradation was investigated. To this end, gold nanoparticles supported on ZnO (Au–ZnO) were prepared using a simple co-precipitation method. The prepared nanocatalyst was characterized by high-resolution transmission electron microscopy, X-ray diffraction, temperature-programmed reduction, X-ray photoelectron spectroscopy, UV–Vis absorption, and photoluminescence. The photocatalytic activity of Au–ZnO was examined by the degradation of methylene blue in aqueous solution using a light source that has more than 95 % (i.e., energy) of emitted photons between 400 and 800 nm. Highly enhanced photocatalytic degradation of methylene blue in air at room temperature was observed from these Au–ZnO nanocatalysts with gold particle size ranging from 2 to 7 nm, with an average size of 3.8 nm. The observed rate constant for MB degradation on Au–ZnO was 0.0118/min compared with 0.0007/min for pure ZnO. Furthermore, the charge transfer pathway for the degradation of methylene blue in Au–ZnO is suggested.

# Experimental modeling of hydrogen producing steps in a novel sulfur–sulfur thermochemical water splitting cycle.

Kevin Caple, **Peter Kreider**, Nicholas AuYeung, Alex Yokochi.

*International Journal of Hydrogen Energy.*[195]

One of the more well-known examples of thermochemical water splitting cycles is the sulfur-iodine cycle, which utilizes iodine and sulfur dioxide to transform water into hydrogen and oxygen. A novel sulfur-sulfur cycle has been developed based on the original sulfur-iodine cycle, seeking an overall more favorable chemical process. The initial stages of the original and novel cycles are the same, in using sulfur dioxide and iodine with an excess of water to form two strong acids, hydrogen iodide and sulfuric acid. The secondary reactions differ greatly and are based on a previously unwanted side reaction where the two strong acids regenerate iodine and water along with hydrogen sulfide, as shown in the equations below. The hydrogen sulfide can then be steam reformed to hydrogen and sulfur dioxide, completing the cycle. Excess sulfuric acid can also be treated to regenerate water and sulfur dioxide.

$$I_{2(l)} + SO_{2(g)} + 2H_2O_{(l)} \rightarrow 2HI_{(l)} + H_2SO_{4(l)}$$

$$8HI_{(l)} + H_2SO_{4(l)} \rightarrow 4I_{2(l)} + 4H_2O_{(l)} + H_2S_{(g)}$$

This study seeks to explore the reaction kinetics of this two-step reaction by altering the various reaction temperatures and the initial concentration of water and to develop a robust and simple predictive model based on the resulting experimental data. The results suggest that an increase in the initial concentration of water will increase the rate of both reactions substantially and that it is beneficial to carry them out in the same vessel. A predictive model was successfully developed that allows for monitoring the progression of iodine through the reaction system in a batch setting. The results of the experimental and modeling work warrants further development of this novel sulfur-sulfur thermochemical water splitting cycle.

## Visible-light-sensitive Na-doped p-type flower-like ZnO photocatalysts synthesized via a continuous flow microreactor.

Ki-Joong Kim, **Peter B Kreider**, Changho Choi, Chih-Hung Chang, Ho-Geun Ahn.
*RSC Advances.*[196]

A Na-doped p-type flower-like ZnO photocatalyst (Na:ZnO) that is highly visible-light-sensitive in air at room temperature was synthesized by a continuous flow microreactor, where NaOH was used as both the precipitating and doping agent. The results of various characterization techniques (XPS, ICP, ToF-SIMS, XRD, and HRTEM) indicated that the Na ions have been successfully doped into the ZnO lattice. The Na:ZnO demonstrated a much higher photocatalytic degradation rate of methylene blue under simulated sunlight (lmax = 494 nm) than the rates obtained from commercially available TiO2 photocatalysts (P-25) and pure ZnO. This much enhanced rate is likely a result of increased surface defect sites associated with oxygen when Na replaces Zn in the crystal structure. A possible mechanism of the photocatalytic degradation of methylene blue on the Na:ZnO is suggested.

## Plasmonics-enhanced metal–organic framework nanoporous films for highly sensitive near-infrared absorption.

Ki-Joong Kim, Xinyuan Chong, **Peter B Kreider**, Guoheng Ma, Paul R Ohodnicki, John P Baltrus, Alan X Wang, Chih-Hung Chang.
*Journal of Materials Chemistry C.*[197]

Combined plasmonic nanocrystals and metal-organic framework thin-films are fabricated for sensing gases in the near-infrared range. This nanocomposite thin-film shows a highly sensitive response in near-infrared absorption, which is attrributed to preconcentration of gas molecules in metalorganic framework pores causing close proximity to the electromagnetic fields at the plasmonic nanocrystals surface.

## High-rate synthesis of Cu–BTC metal–organic frameworks.

Ki-Joong Kim, Yong Jun Li, **Peter B Kreider**, Chih-Hung Chang, Nick Wannenmacher, Praveen K Thallapally, Ho-Geun Ahn.

*Chemical Communications.*[198]

The reaction conditions for the synthesis of Cu–BTC (BTC = benzene-1,3,5-tricarboxylic acid) were elucidated using a continuous-flow microreactor-assisted solvothermal system to achieve crystal size and phase control. A high-rate synthesis of Cu–BTC metal–organic frameworks with a BET surface area of more than 1600 $m^2$ $g^{-1}$ (Langmuir surface area of more than 2000 $m^2$ $g^{-1}$) and with a 97% production yield could be achieved with a total reaction time of 5 minutes.

## Continuous synthesis of colloidal chalcopyrite copper indium diselenide nanocrystal inks.

Ki-Joong Kim, Richard P Oleksak, Changqing Pan, Michael W Knapp, **Peter B Kreider**, Gregory S Herman, Chih-Hung Chang.

*RSC Advances.*[199]

A continuous synthetic method in a micro-tubular reactor is introduced for synthesizing mono-disperse and solution-stable chalcopyrite colloidal copper indium diselenide nanocrystal ($CuInSe_2$ NC) inks with potential scalability. It was found that the morphologies of the CuInSe2 NCs were dependent on the Cu/In/Se composition. The NC morphology changed from spherical to hexagonal to trigonal with increasing In or Se content, whereas trigonal morphologies synthesized at high temperature yielded chalcopyrite $CuInSe_2$ NCs. A laboratory-scale photovoltaic device with 1.9% efficiency under AM1.5G illumination was also fabricated to verify the utility of these inks

# Appendix

## General Materials

### *GASES*

- CP grade methane
- CP grade ethylene
- Ultra zero compressed air
- UHP $O_2$
- UHP $H_2$
- Compressed He
- Carbon dioxide UN 1013

### *CHEMICALS*

- n-Decane (>99%, TCI America)
- Dibenzothiophene (Alfa Aesar 98%)
- Dibenzothiophene sulfoxide (MP Biomedicals, cat #: 207702)
- Dibenzothiohene sulfone (97%, Sigma Aldrich)

### *METALS AND PLASTICS*

- Super corrosion resistant stainless steel (type 316/316L) 1/8" rod
- Seamless ¼" stainless steel tubing (1/4" OD x 0.035" wall & 1/4" OD x 0.049" wall)
- Corrosion resistant 316 stainless steel plate, (1 1/16" x 2" x 1/8" thick)
- ASTM A193 Grade B7 Alloy Steel Threaded rods, plain finish, ¼"-28 thread
- Teflon ® PTFE spacer @ 750 um and 250 um
- Impact resistant polycarbonate
- 1/16" Ni Rods from ESPI Metals (Alloy 201, stock#: Knd1141)

## General Equipment

- CNT growth furnace: MTI Corporation OTF-1200x-S w/50 mm quartz tube

- Brooks 4800 series Mass Flow Controllers, O2, 0-500 SCCM
    - MFCs hooked up to an NI USB-6008 DAQ box
- OMEGA 1/16” Type K ungrounded thermocouple: Part#CASS-116U-12-NHX
- Syringe Pump, Harvard Apparatus Pump 33 (Cat#: 55-3333)
- Technics Planar Etch II, Model 750 plasma generator
- Canon EOS Rebel T3i DSLR Camera
    - Canon EFS 18-55mm lens
    - Fotodiox Macro Extension Tube: 28 mm
    - Polaroid Close-up 10X 58mm filter

## Electrical Equipment

- Glassman High Voltage Series EQ 10 kV Power Supply
- Life Technologies Gibco BRL 4001P Programmable Electrophoresis Power Supply (Below 4000 V up to 300 W and/or 300 mA DC)
- HP 54542A Oscilloscope 2 GSa/s 500 MHz
    - TekP6121 10 MOhm 11.0 pF 10X 1.5M probe
    - Keysight N2891A 70 MHz High-voltage Differential Probe
- Resistors
    - Ohmite 100kΩ 50 W (L50J100KE)
    - Dale Rox-3
        - 10MΩ: 10MO FX 1225
        - 1 MΩ: 1 MO FX 1329
        - 5 MΩ: MB01 5M 1% 48/12
    - 20 MΩ: Ohmite 108E 20 Meg 1% 1351
    - 10 kΩ: LTO 100 10K 5% C2
    - 100 kΩ: MP925 100K 1% 1244

## Analytical Techniques

- SRI 8610C GC w/HID detector
    - 3’ x 1/8” SS PoraPak Q Packed column 8600-PKQA

- SRI 8610C GC w/FID and FPD detectors
    - 30m x 0.53mm ID 1 micron film thickness MXT-5 Capillary Column, Restek
- Field emission-scanning electron microscope (FE-SEM) analysis was conducted using an FEI Quanta 600 operating at 15–30 kV accelerating voltage
- X-ray diffraction (XRD) patterns were collected using a Bruker D8 Discover instrument with Cu-K$\alpha_1$ radiation (0.154 nm)
- Raman spectra were recorded using a WITec confocal Raman microscope with an Ar ion laser (514 nm) and CCD detector
- NEOFOX-GT Oxygen Phase Fluorimeter with 1000 micron spot size bifurcated borosilicate fiber assembly and the FOXY-R and HIOXY-R oxygen sensors on 1000 micron fiber in 1/16" OD SS ferrules.
- HPLC: Dionex RSLC system with Corona *ultra* Detector, SRD-3400 UltiMate 3000 Integrated Solvent and Degasser Rack, HPG-3200RS UltiMate 3000 Binary Rapid Separation Pump, WPS-3000SL Analytical and WPS-3000RS Autosampler Series, Corona Ultra - UltiMate 3000 RSLC Charged Aerosol Detector, UCI-50 Universal Chromatography Interface.
- Bruker Vertex 70 FTIR with an ATR attachment

## Mass Flow Controllers

The Brooks 4800 series MFCs were controlled with a custom LabView program. The block diagram is shown below.

Bubble volume measurements were used to calibrate the voltage/flow characteristics of the MFCs. The labview program, once properly setup, was used to set the MFC voltage signal to a set value. The flow corresponding to that value was collected for a set period of time in an inverted, submerged 500 mL graduated cylinder that is filled with water. The gas volume that bubbles into the graduated cylinder displaces water. After the collection time, the total volume of gas is measured on the graduated markings. The water level inside the cylinder must be at the same water level as the bucket to ensure that the pressure inside the cylinder is approximately atmospheric pressure. The total

collected volume of gas divided by the collection time is the flow rate. This procedure is repeated for varying voltage setpoints to create a calibration curve. The entire procedure is repeated for each MFC and for each different gas that will be flowed through the MFCs.

The calibration curves are linear for these MFCs. The slope and intercept of the line are used inside the labview block diagram to convert from a volumetric flowrate setpoint to setpoint voltage, and again to convert the flowrate signal voltage to a volumetric flowrate signal. This block diagram can control two MFCs at the same time. More MFCs could be controlled, but this setup is limited by the NI DAQ box which only has two analog outputs.

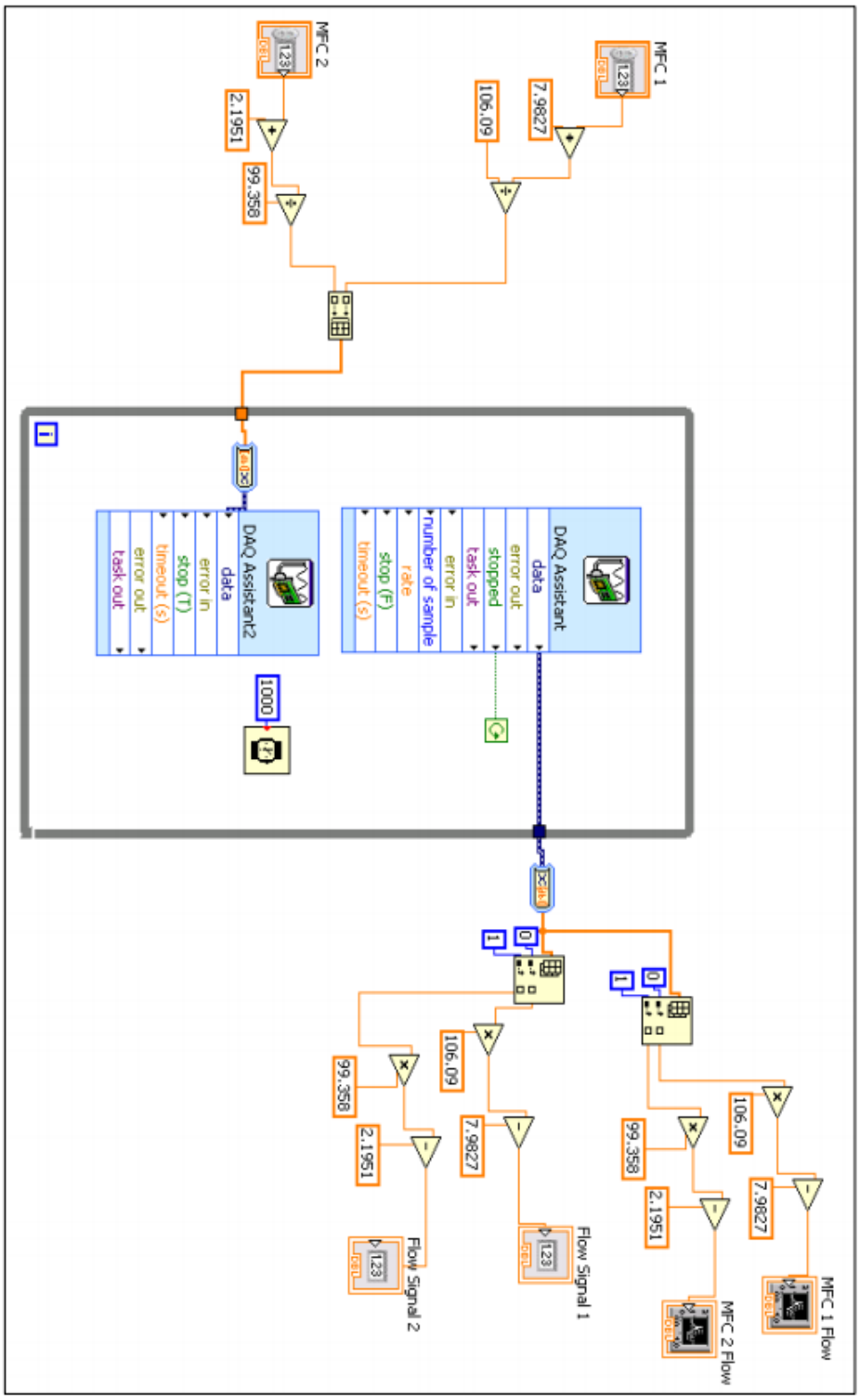


Figure 83: Block diagram for LabView VI used to control mass flow controllers.

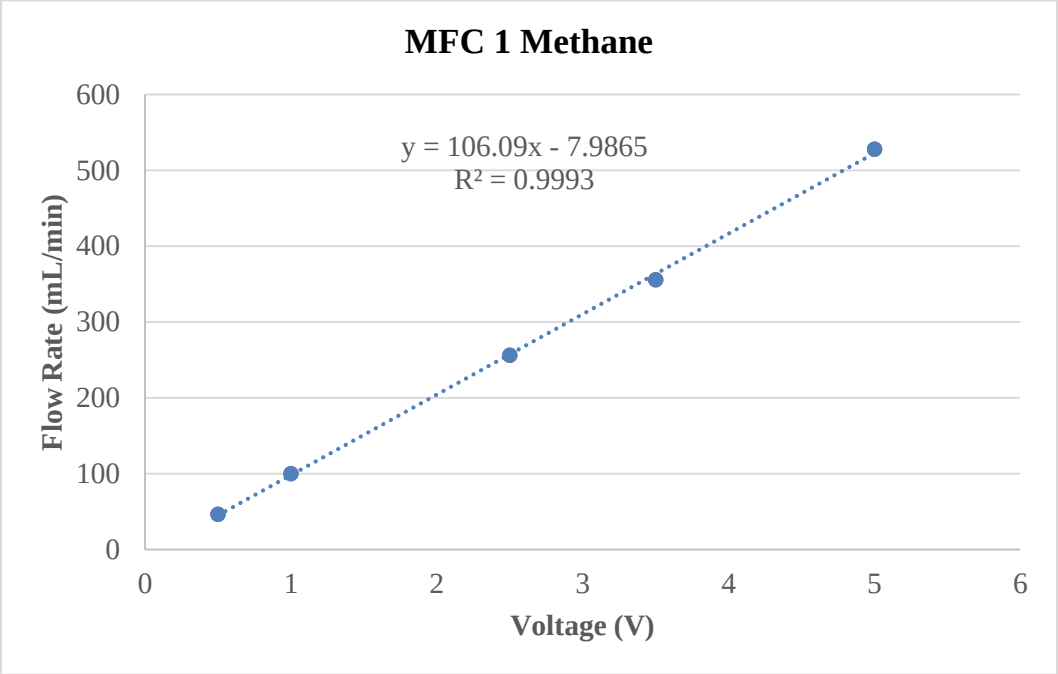


Figure 84: Calibration curve for MFC 1 with methane flows.

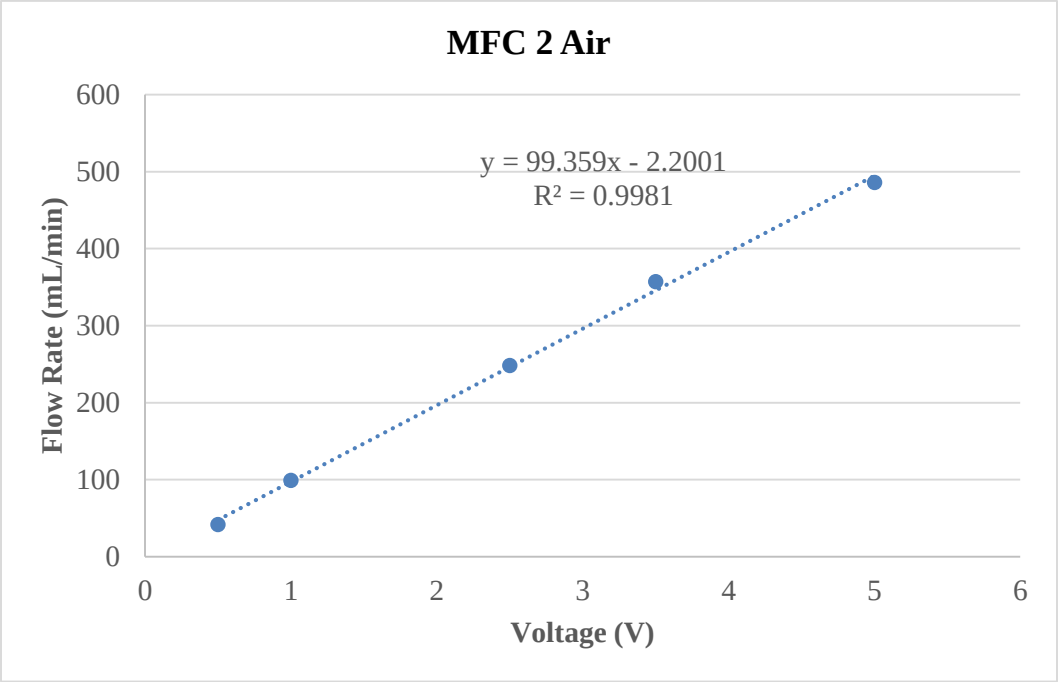


Figure 85: Calibration curve for MFC 2 with air flows.

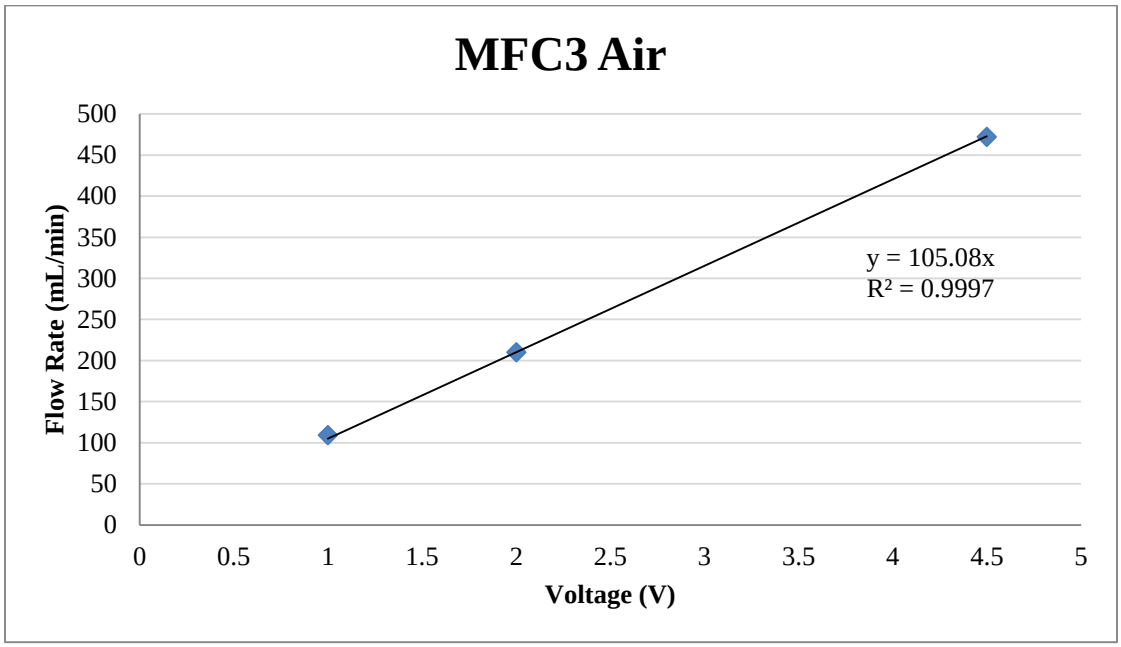


Figure 86: Calibration curve for MFC 3 with air flows.

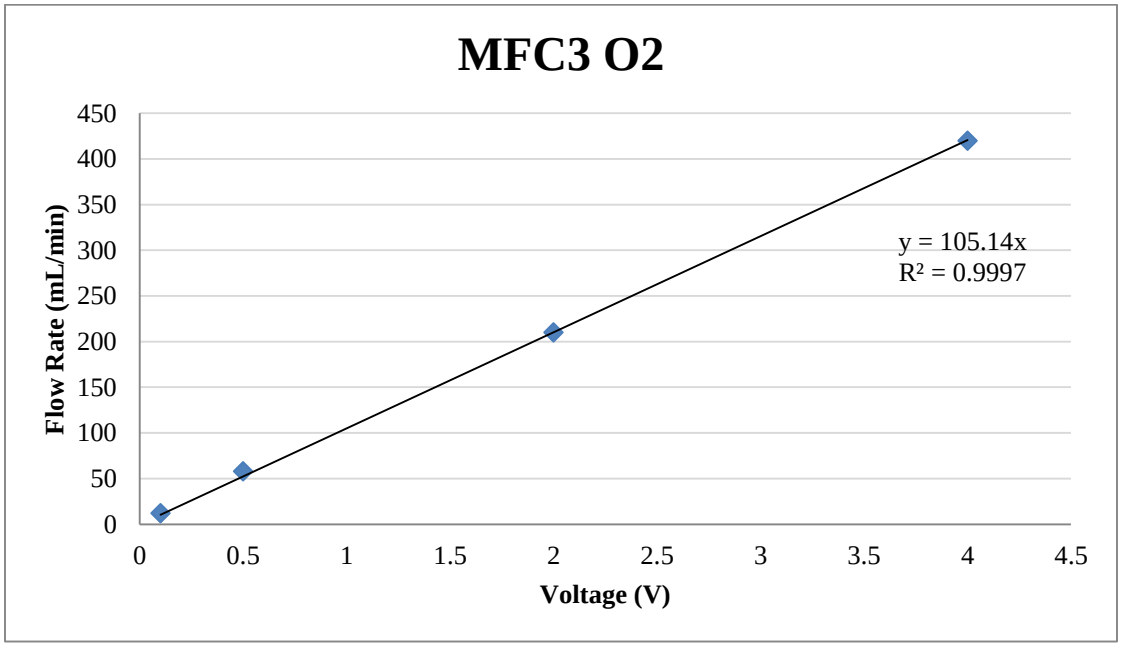


Figure 87: Calibration curve for MFC 3 with oxygen flows.

## Gas Chromatography

All GC data presented in this document was collected on an SRI 8610C gas chromatograph. Most GC traces of note come from a helium ionization detector (HID). A sample chromatogram from the HID detector is shown below. This particular experiment was carried out in the flat plate microreaction system. All post-processing of the collected chromatograms is done inside the PeakSimple program (http://www.srigc.com/pages/software_downloads/). Peak areas are used to create calibration curves for compounds of interest. It should be noted here that HID detectors are suitable for low concentrations of compounds and the calibration curves for certain compounds such as methane, which are regularly fed into the system at higher concentrations, are highly non-linear.

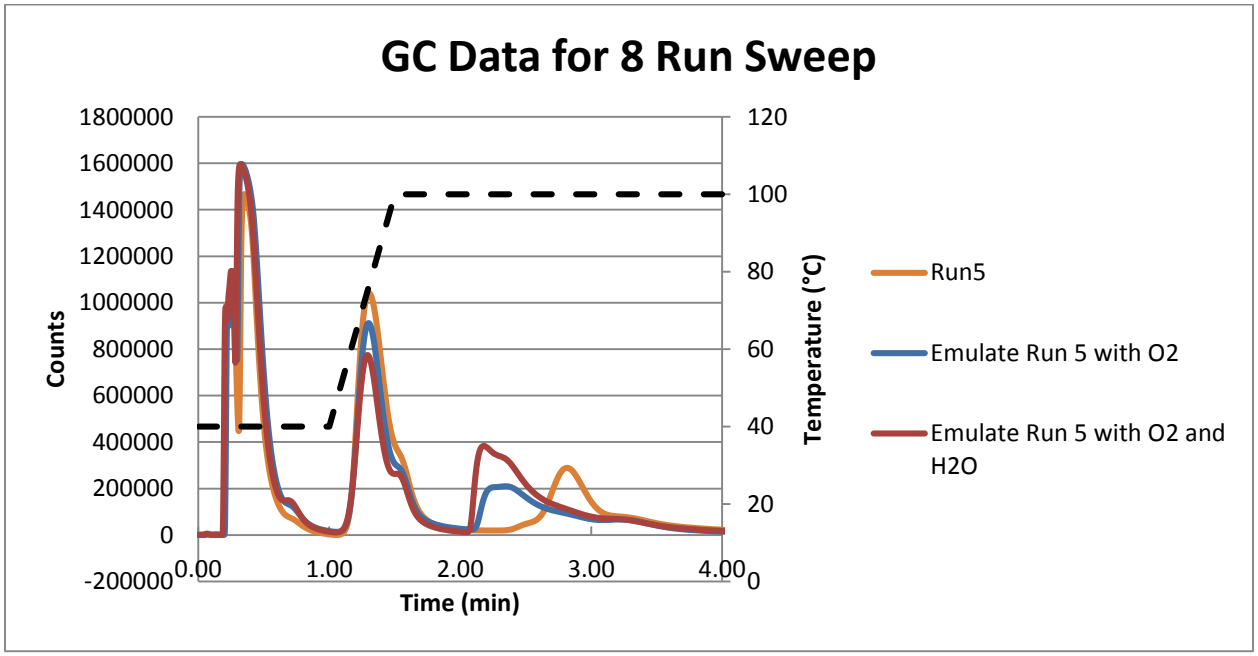


Figure 88: Example chromatogram signals from the HID detector in typical methane/oxygen glow discharge experimental runs in the flat plate microreactor. Temperature profile is shown by the black dotted line.

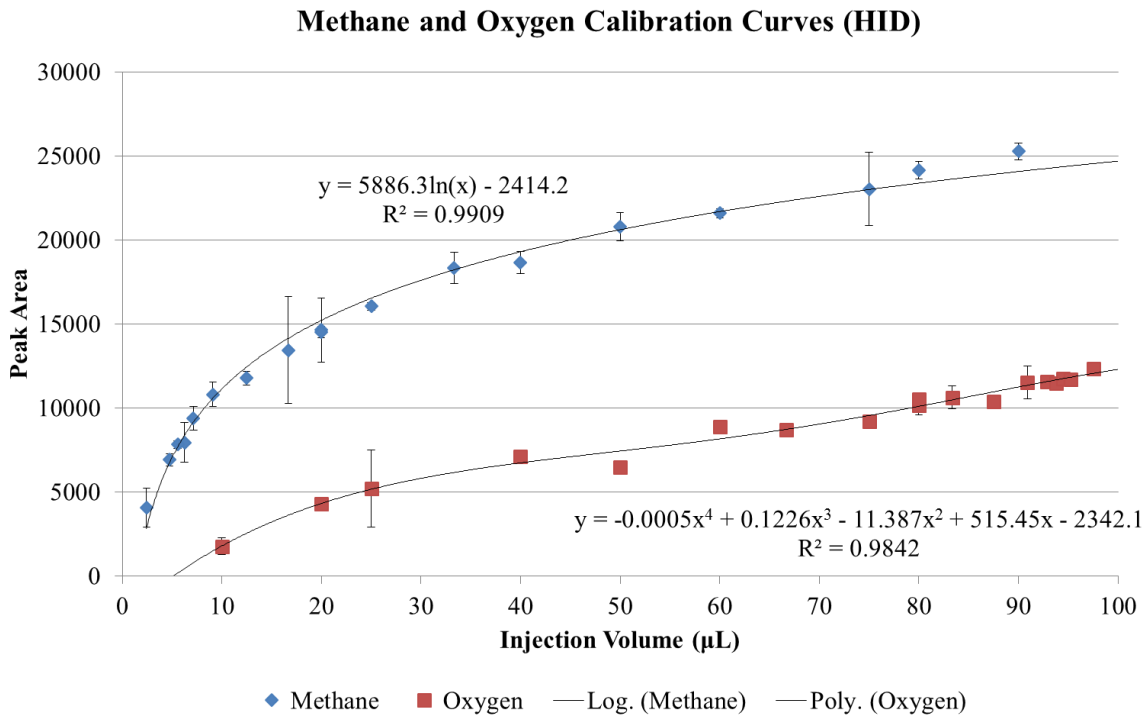


Figure 89: GC HID detector calibration curves for methane and oxygen.

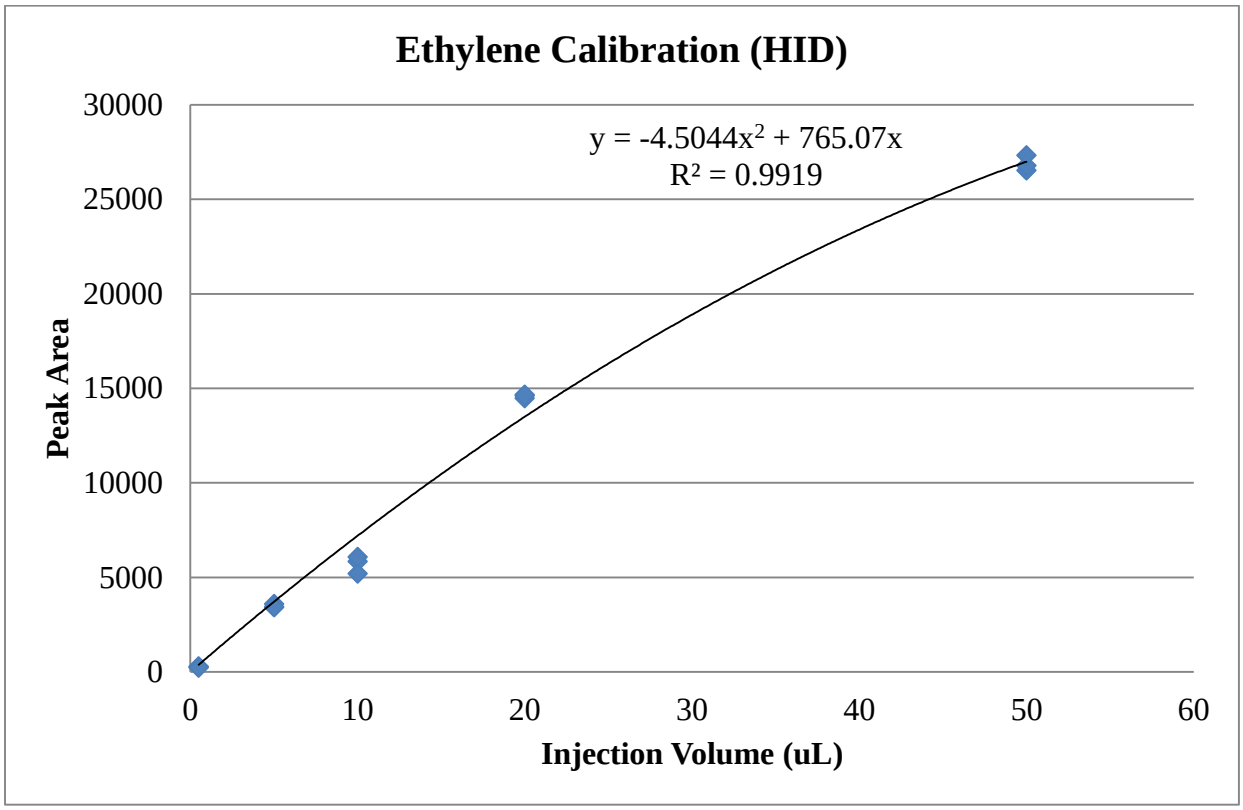


Figure 90: GC HID detector calibration curves for ethylene.

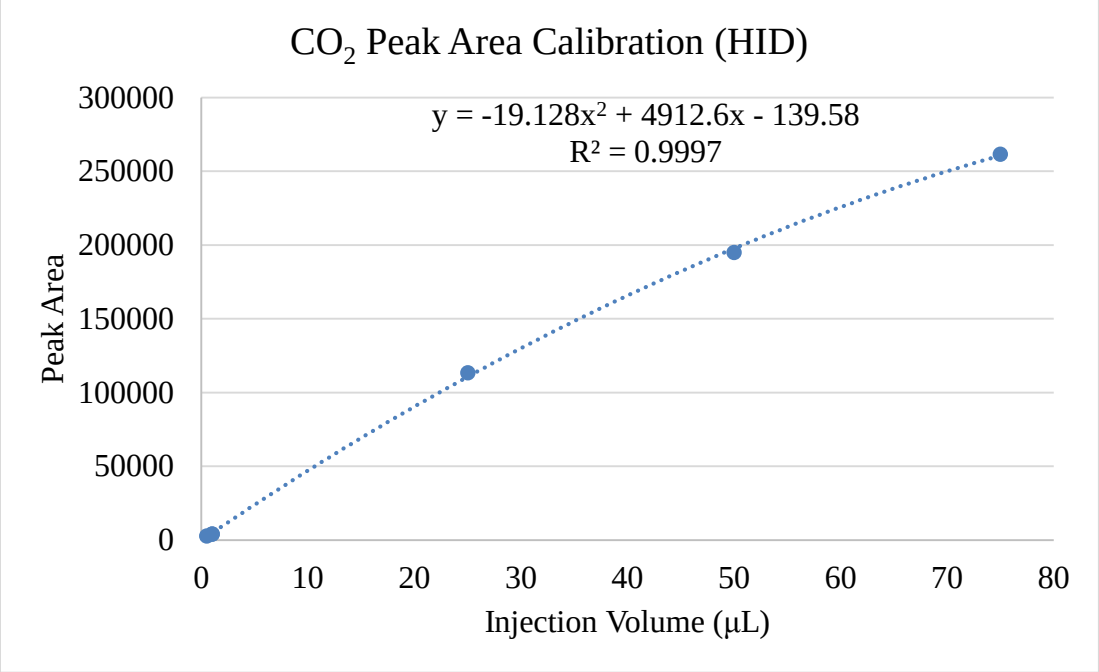


Figure 91: GC HID detector calibration curves for CO2.

## Optical Emission Spectroscopy

Optical emission spectra for various discharges were collected in this work using the Avantes spectroscope. Typical emission spectra were recorded for 1000 ms, and taken as an average of 3 scans.

Emission band heads were compared with standards found in *The identification of molecular spectra* by Pearse and Gaydon.[153] Some of the prominent bands identified are shown and identified in figure 92.

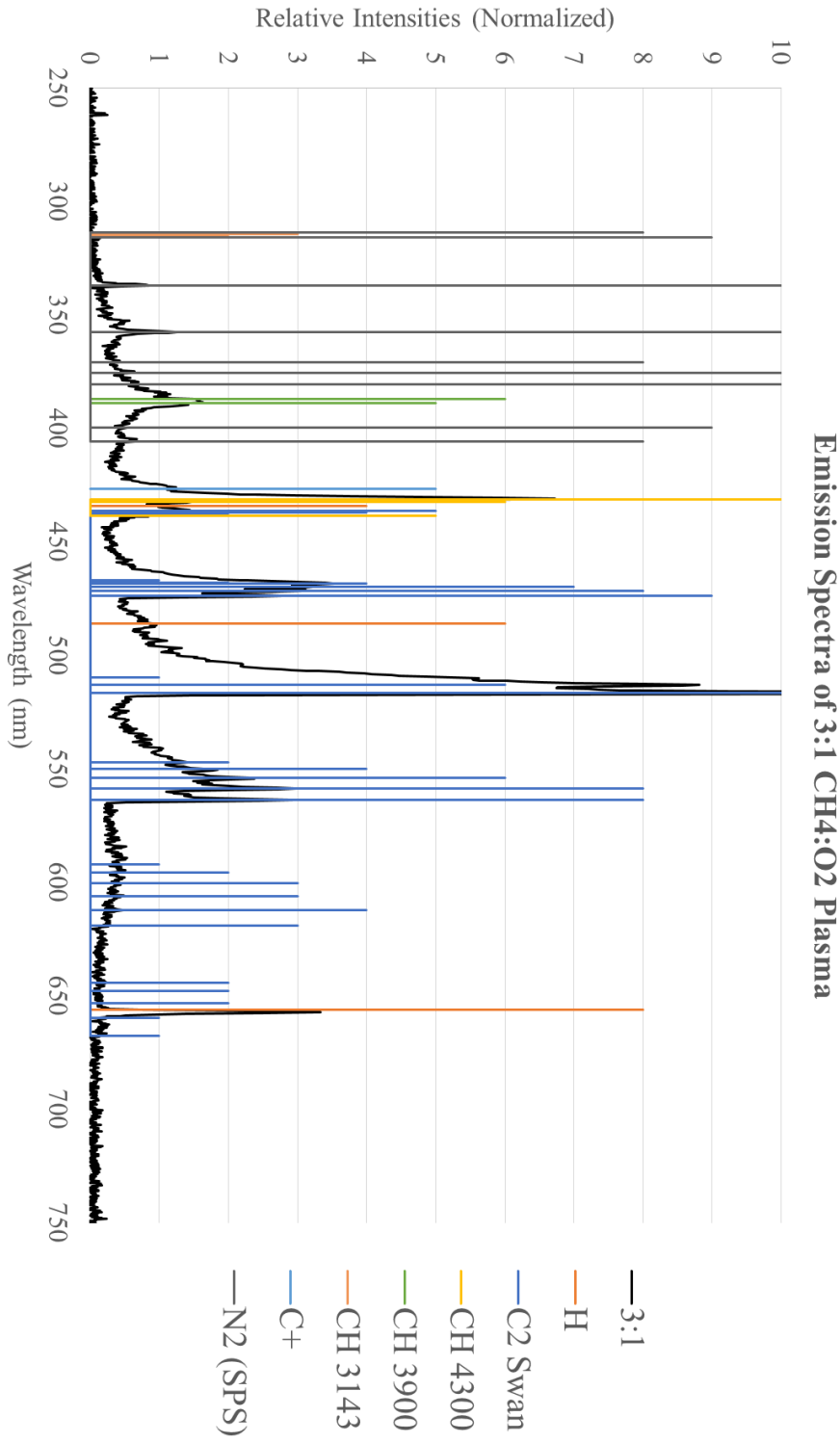


Figure 92: Optical emission spectra and fitted emission band heads for common species.

# IV Curves

IV curves collected for some older reactor designs were not used in the body of this work, but do represent a good deal of time in data collection, and are reported here for completeness. The data contained in these figures may not be of any practical use for future studies, but do provide some insight into how changing certain aspects of the reaction system affect the IV curve. Of particular note is the inclusion of an RC snubber into the circuit (seen in figure 93), which suggests that the pulsing behavior seen in the system is not a result of a lack of stored power in the power supply, but is in fact a fundamental property of the observed discharges.

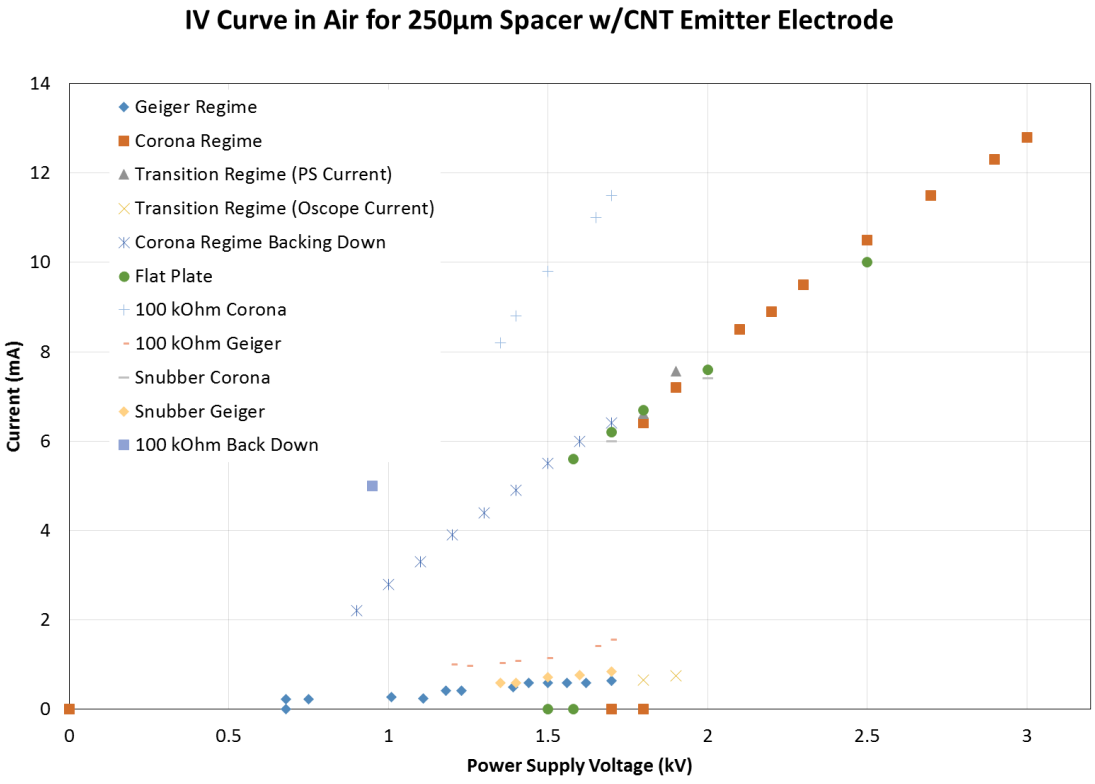


Figure 93: IV curves for the flat plate reactor with CNT enhanced electrodes under different operating conditions.

IV curves for the annular reactor are shown in figure 94.

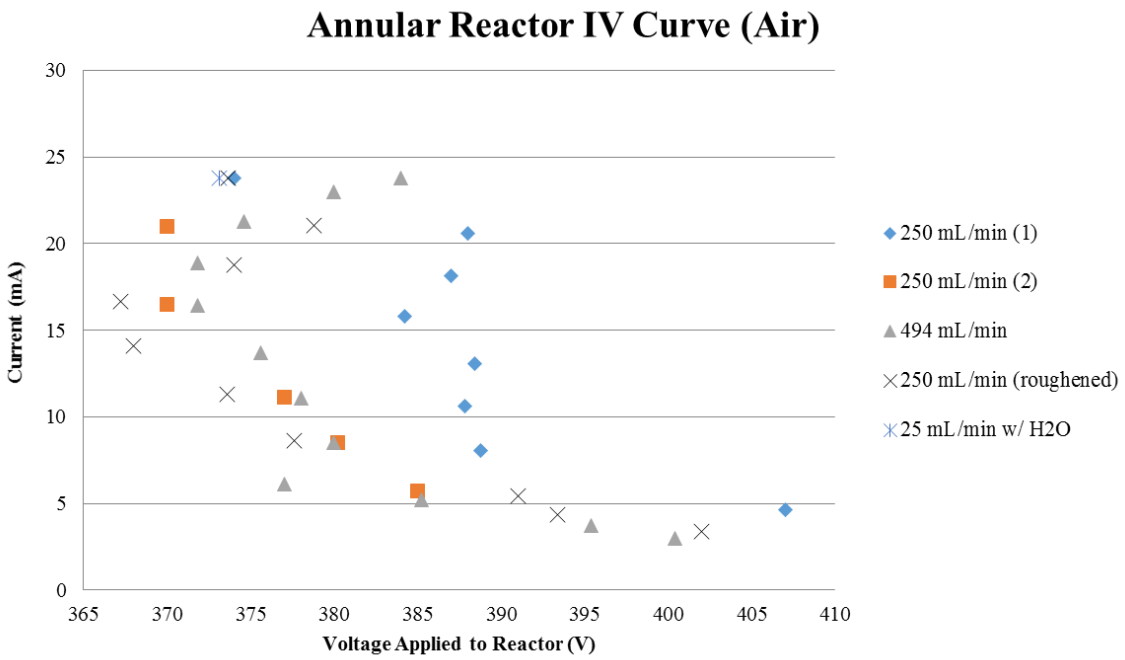


Figure 94: IV curves for the annular reactor operating in air.

## Procedure for Co Nanoparticle Synthesis to favor Nanodisk Formation (Han Song/EECS Collaboration)

A piece of collaborative work undertaken in our lab was the formation of cobalt nanodisks for Han Song in EECS for high frequency magnetic applications. This is the procedure used for the formation of the disks used in that work.

1. Set up a 3 neck flask with a gas inlet and gas outlet, with the center neck equipped with a septum for syringe injection. Wrap the flask in temperature controlled heating tape. The thermocouple can enter the flask and solution in one of the gas connections with a special glass fitting.
2. Added 0.11 g tri-n-octylphospine oxide (TOPO) to 3 neck flask, degas under 125 mL/min N2 flow for 20 min.
3. Premix 1.6 g octadecyl amine (ODA), 0.1 mL Oleic Acid, and 15 mL dichlorobenzene and sonicate for 1 minute to fully dissolve ODA. Add to flask.
4. Separately, dissolve 0.56 g $CO_2(CO)8$ in 3 mL dichlorobenzene, sonicate for 1 minute to dissolve.

5. Heat Flask and contents to 182 C.
6. Using a syringe, inject the cobalt precursor into the hot solution. This process rapidly releases carbon monoxide gas and causes violent boiling of the solution, so this is carried out inside the hood with proper PPE. A larger 3 neck flask volume than is required for synthesis would make this easier.
7. Allow the solution to react for 10 minutes. This time can be adjusted to tune the product size and shape distribution. The heat is turned off after 7 minutes of reaction.
8. Inject about 10 mL of ethanol to quench the reaction.
9. Collect product solution.
10. Apply appropriate nanoparticle cleaning method for desired outcome. I used alternating polar/nonpolar cleaning agents/solvents with centrifugation to concentrate and clean the nanoparticles for TEM imaging, which removes the protective capping agent.
11. Puntes et al., "Synthesis of hcp-Co Nanodisks" was used as a synthetic procedure template. See their work for detailed information on the recipe and protocols.[200]

## Inficon Transpector CPM (MS)

An **Inficon Transpector CPM** residual gas analyzer was purchased on eBay to assist in the on-stream gas analysis of the nonthermal plasmachemical reactions undetaken in this work. Repairs were needed, and the system was sent to Inficon and returned. Upon setup after return, the turbopump would not turn on when the **TWare32** software sent the signal to the pump to turn on. The turbopumps with this model are known to fail and are not covered for maintenance by Inficon. It is possible that the turbopump was not activating because the pressure was too high and an interlock keeps it from spinning if the pressure is too high. If the turbopump can be activated, the CPM is currently configured for atmospheric pressure gas sampling through the sniffer tube. Wayne Odell is the contact that I've been in contact with at Inficon for future technical support (Wayne.Odell@inficon.com).

## HPLC with Universal Chromatography Interface

The corona aerosol detector (CAD) on the HPLC system in Merryfield is currently not functional. We spent a good deal of time troubleshooting the detector, and ultimately could not fix it. The current problem with the system is with gas flow being imbalanced, as the CADs design uses pressure differentials to keep the gas flow rates at the appropriate ratio through the system. Our best guess at the problem with the system lies in the stainless steel filter at the outlet of the corona detector. If this filter is replaced, the system may function as intended.

As a workaround, I installed the universal chromatography interface (Dionex UCI-50) along with an old, analog UV detector to replace the CAD. The Dionex UCI-50 manual describes the setup process fairly well. Currently, any analog detector can be wired into the UCI-50 and used in conjunction with the HPLC system. The CAD signal is replaced with the analog signal from the UCI-50 in the Chromeleon software, and everything else in the HPLC system functions the same way it could with the CAD.

# References

1. Ehrfeld, W.; Hessel, V.; Kiesewalter, S.; Löwe, H.; Richter, T.; Schiewe, J., Implementation of microreaction technology in process engineering. In *Microreaction Technology: Industrial Prospects*, Springer: 2000; pp 14-34.

2. Zhang, Q.; He, D.; Zhu, Q., Recent progress in direct partial oxidation of methane to methanol. *Journal of Natural Gas Chemistry* **2003,** 12, (2), 81-89.

3. Zhou, L.; Xue, B.; Kogelschatz, U.; Eliasson, B., Partial oxidation of methane to methanol with oxygen or air in a nonequilibrium discharge plasma. *Plasma chemistry and plasma processing* **1998,** 18, (3), 375-393.

4. Zhu, Q.; Zhao, X.; Deng, Y., Advances in the partial oxidation of methane to synthesis gas. *Journal of Natural Gas Chemistry* **2004,** 13, (4), 191-203.

5. Yang, Y., Direct non-oxidative methane conversion by non-thermal plasma: experimental study. *Plasma chemistry and plasma processing* **2003,** 23, (2), 283-296.

6. Indarto, A., A review of direct methane conversion to methanol by dielectric barrier discharge. *Dielectrics and Electrical Insulation, IEEE Transactions on* **2008,** 15, (4), 1038-1043.

7. Larkin, D.; Caldwell, T.; Lobban, L.; Mallinson, R. G., Oxygen pathways and carbon dioxide utilization in methane partial oxidation in ambient temperature electric discharges. *Energy & fuels* **1998,** 12, (4), 740-744.

8. Larkin, D. W.; Lobban, L. L.; Mallinson, R. G., The direct partial oxidation of methane to organic oxygenates using a dielectric barrier discharge reactor as a catalytic reactor analog. *Catalysis today* **2001,** 71, (1), 199-210.

9. Liu, C.; Marafee, A.; Hill, B.; Xu, G.; Mallinson, R.; Lobban, L., Oxidative coupling of methane with ac and dc corona discharges. *Industrial & engineering chemistry research* **1996,** 35, (10), 3295-3301.

10. Supat, K.; Chavadej, S.; Lobban, L. L.; Mallinson, R. G., Combined steam reforming and partial oxidation of methane to synthesis gas under electrical discharge. *Industrial & engineering chemistry research* **2003,** 42, (8), 1654-1661.

11. Li, M.-w.; Xu, G.-h.; Tian, Y.-l.; Chen, L.; Fu, H.-f., Carbon dioxide reforming of methane using DC corona discharge plasma reaction. *The Journal of Physical Chemistry A* **2004,** 108, (10), 1687-1693.

12. Supat, K.; Kruapong, A.; Chavadej, S.; Lobban, L. L.; Mallinson, R. G., Synthesis gas production from partial oxidation of methane with air in AC electric gas discharge. *Energy & fuels* **2003,** 17, (2), 474-481.

13. Sobacchi, M.; Saveliev, A.; Fridman, A.; Kennedy, L. A.; Ahmed, S.; Krause, T., Experimental assessment of a combined plasma/catalytic system for hydrogen production via partial oxidation of hydrocarbon fuels. *International journal of hydrogen energy* **2002,** 27, (6), 635-642.

14. Liu, C.; Marafee, A.; Mallinson, R.; Lobban, L., Methane conversion to higher hydrocarbons in a corona discharge over metal oxide catalysts with OH groups. *Applied Catalysis A: General* **1997,** 164, (1), 21-33.

15. Indarto, A.; Lee, H.; Choi, J.-W.; Song, H., Partial oxidation of methane with yttria-stabilized zirconia catalyst in a dielectric barrier discharge. *Energy Sources, Part A* **2008,** 30, (17), 1628-1636.

16. Chen, L.; Zhang, X.; Huang, L.; Lei, L., Post-Plasma Catalysis for Methane Partial Oxidation to Methanol: Role of the Copper-Promoted Iron Oxide Catalyst. *Chemical Engineering & Technology* **2010,** 33, (12), 2073-2081.

17. Huang, J.; Badani, M. V.; Suib, S. L.; Harrison, J. B.; Kablauoi, M., Partial oxidation of methane to methanol through microwave plasmas. Reactor design to control free-radical reactions. *The Journal of Physical Chemistry* **1994,** 98, (1), 206-210.

18. Kalra, C. S.; Gutsol, A. F.; Fridman, A. A., Gliding arc discharges as a source of intermediate plasma for methane partial oxidation. *Plasma Science, IEEE Transactions on* **2005,** 33, (1), 32-41.

19. Blumberg, K. O.; Walsh, M. P.; Pera, C., Low-Sulfur Gasoline & Diesel: The Key to Lower Vehicle Emissions. *Available online [April 24] at:< http://www. theicct. org/documents/Low-Sulfur_Exec_Summ_ICCT_2003. pdf* **2003**.

20. de Souza, W. F.; Guimarães, I. R.; Guerreiro, M. C.; Oliveira, L. C. A., Catalytic oxidation of sulfur and nitrogen compounds from diesel fuel. *Applied Catalysis A: General* **2009,** 360, (2), 205-209.

21. Vasudevan, P.; Fierro, J., A review of deep hydrodesulfurization catalysis. *Catalysis Reviews* **1996,** 38, (2), 161-188.

22. Vrinat, M., The kinetics of the hydrodesulfurization process-a review. *Applied Catalysis* **1983,** 6, (2), 137-158.

23. Dhar, G. M.; Srinivas, B.; Rana, M.; Kumar, M.; Maity, S., Mixed oxide supported hydrodesulfurization catalysts—a review. *Catalysis Today* **2003,** 86, (1), 45-60.

24. Brunet, S.; Mey, D.; Pérot, G.; Bouchy, C.; Diehl, F., On the hydrodesulfurization of FCC gasoline: a review. *Applied Catalysis A: General* **2005,** 278, (2), 143-172.

25. Thanyachotpaiboon, K.; Chavadej, S.; Caldwell, T.; Lobban, L.; Mallinson, R., Conversion of methane to higher hydrocarbons in AC nonequilibrium plasmas. *AIChE journal* **1998,** 44, (10), 2252-2257.

26. Mok, Y. S.; Nam, I.-S., Modeling of pulsed corona discharge process for the removal of nitric oxide and sulfur dioxide. *Chemical Engineering Journal* **2002,** 85, (1), 87-97.

27. Malik, M. A.; Kolb, J. F.; Sun, Y.; Schoenbach, K. H., Comparative study of NO removal in surface-plasma and volume-plasma reactors based on pulsed corona discharges. *Journal of hazardous materials* **2011,** 197, 220-228.

28. Yamamoto, T.; Asada, S.; Iida, T.; Ehara, Y. In *Nobel NOx and Voc Treatment Using Concentration and Plasma Decomposition*, Industry Applications Society Annual Meeting (IAS), 2010 IEEE, 2010; IEEE: 2010; pp 1-6.

29. Dey, G.; Sharma, A.; Pushpa, K.; Das, T. N., Variable products in dielectric-barrier discharge assisted benzene oxidation. *Journal of hazardous materials* **2010,** 178, (1), 693-698.

30. Ye, Z.; Zhang, Y.; Li, P.; Yang, L.; Zhang, R.; Hou, H., Feasibility of destruction of gaseous benzene with dielectric barrier discharge. *Journal of Hazardous materials* **2008,** 156, (1), 356-364.

31. Satoh, K.; Matsuzawa, T.; Itoh, H., Decomposition of benzene in a corona discharge at atmospheric pressure. *Thin Solid Films* **2008,** 516, (13), 4423-4429.

32. Mizuno, A., Generation of non-thermal plasma combined with catalysts and their application in environmental technology. *Catalysis Today* **2013**.

33. Subrahmanyam, C.; Renken, A.; Kiwi-Minsker, L., Novel catalytic dielectric barrier discharge reactor for gas-phase abatement of isopropanol. *Plasma Chemistry and Plasma Processing* **2007,** 27, (1), 13-22.

34. Xia, L.; Huang, L.; Shu, X.; Zhang, R.; Dong, W.; Hou, H., Removal of ammonia from gas streams with dielectric barrier discharge plasmas. *Journal of hazardous materials* **2008,** 152, (1), 113-119.

35. Oda, T.; Yamashita, R.; Haga, I.; Takahashi, T.; Masuda, S., Decomposition of gaseous organic contaminants by surface discharge induced plasma chemical processing-SPCP. *Industry Applications, IEEE Transactions on* **1996,** 32, (1), 118-124.

36. Jarrige, J.; Vervisch, P., Decomposition of three volatile organic compounds by nanosecond pulsed corona discharge: Study of by-product formation and influence of high voltage pulse parameters. *Journal of applied physics* **2006,** 99, (11), 113303-113303-10.

37. Korzekwa, R.; Grothaus, M.; Hutcherson, R.; Roush, R.; Brown, R., Destruction of hazardous air pollutants using a fast rise time pulsed corona reactor. *Review of scientific instruments* **1998,** 69, (4), 1886-1892.

38. Sobacchi, M. G.; Saveliev, A. V.; Fridman, A. A.; Gutsol, A.; Kennedy, L. A., Experimental assessment of pulsed corona discharge for treatment of VOC emissions. *Plasma chemistry and plasma processing* **2003,** 23, (2), 347-370.

39. Chavadej, S.; Saktrakool, K.; Rangsunvigit, P.; Lobban, L. L.; Sreethawong, T., Oxidation of ethylene by a multistage corona discharge system in the absence and presence of Pt/TiO< sub> 2</sub>. *Chemical engineering journal* **2007,** 132, (1), 345-353.

40. Van Brunt, R.; Herron, J., Plasma chemical model for decomposition of SF6 in a negative glow corona discharge. *Physica Scripta* **1994,** 1994, (T53), 9.

41. Herrmann, H. W.; Henins, I.; Park, J.; Selwyn, G., Decontamination of chemical and biological warfare (CBW) agents using an atmospheric pressure plasma jet (APPJ). *Physics of Plasmas* **1999,** 6, 2284.

42. Bai, M.; Zhang, Z.; Bai, X.; Bai, M.; Ning, W., Plasma synthesis of ammonia with a microgap dielectric barrier discharge at ambient pressure. *Plasma Science, IEEE Transactions on* **2003,** 31, (6), 1285-1291.

43. Tanaka, S.; Uyama, H.; Matsumoto, O., Synergistic effects of catalysts and plasmas on the synthesis of ammonia and hydrazine. *Plasma Chemistry and Plasma Processing* **1994,** 14, (4), 491-504.

44. Sugiyama, K.; Akazawa, K.; Oshima, M.; Miura, H.; Matsuda, T.; Nomura, O., Ammonia synthesis by means of plasma over MgO catalyst. *Plasma chemistry and plasma processing* **1986,** 6, (2), 179-193.

45. Amorim, J.; Baravia, G.; Ricard, A., Production of N, H, and NH active species in N2-H2 dc Flowing Discharges. *Plasma Chemistry and Plasma Processing* **1995,** 15, (4), 721-731.

46. Yin, K. S.; Venugopalan, M., Plasma chemical synthesis. I. Effect of electrode material on the synthesis of ammonia. *Plasma chemistry and plasma processing* **1983,** 3, (3), 343-350.

47. Touvelle, M.; Licea, J. M.; Venugopalan, M., Plasma chemical synthesis. II. Effect of wall surface on the synthesis of ammonia. *Plasma chemistry and plasma processing* **1987,** 7, (1), 101-108.

48. Uyama, H.; Matsumoto, O., Synthesis of ammonia in high-frequency discharges. *Plasma chemistry and plasma processing* **1989,** 9, (1), 13-24.

49. Martinez, P.; Brandvold, D. K., Laboratory and field measurements of NO< sub> x</sub> produced from corona discharge. *Atmospheric Environment* **1996,** 30, (24), 4177-4182.

50. Shahin, M., Mass-Spectrometric Studies of Corona Discharges in Air at Atmospheric Pressures. *The Journal of Chemical Physics* **1966,** 45, 2600.

51. Zhao, G. B.; Garikipati, S.; Hu, X.; Argyle, M. D.; Radosz, M., Effect of oxygen on nonthermal plasma reactions of nitrogen oxides in nitrogen. *AIChE journal* **2005,** 51, (6), 1800-1812.

52. Hessel, V.; Anastasopoulou, A.; Wang, Q.; Kolb, G.; Lang, J., Energy, catalyst and reactor considerations for (near)-industrial plasma processing and learning for nitrogen-fixation reactions. *Catalysis Today* **2013**.

53. Moreno-Couranjou, M.; Monthioux, M.; Gonzalez-Aguilar, J.; Fulcheri, L., A non-thermal plasma process for the gas phase synthesis of carbon nanoparticles. *Carbon* **2009,** 47, (10), 2310-2321.

54. Pai, D. Z., Nanomaterials synthesis at atmospheric pressure using nanosecond discharges. *Journal of Physics D: Applied Physics* **2011,** 44, (17), 174024.

55. Bhattacharyya, S.; Staack, D.; Vitol, E. A.; Singhal, R.; Fridman, A.; Friedman, G.; Gogotsi, Y., Localized synthesis of metal nanoparticles using nanoscale corona discharge in aqueous solutions. *Advanced Materials* **2009,** 21, (40), 4039-4044.

56. Mariotti, D.; Sankaran, R. M., Microplasmas for nanomaterials synthesis. *Journal of Physics D: Applied Physics* **2010,** 43, (32), 323001.

57. Liu, C.-j.; Vissokov, G. P.; Jang, B. W.-L., Catalyst preparation using plasma technologies. *Catalysis Today* **2002,** 72, (3), 173-184.

58. Odedairo, T.; Chen, J.; Zhu, Z., Synthesis of Supported Nickel Nanoparticles via a Nonthermal Plasma Approach and Its Application in CO2 Reforming of Methane. *The Journal of Physical Chemistry C* **2013,** 117, (41), 21288-21302.

59. Kortshagen, U., Nonthermal plasma synthesis of semiconductor nanocrystals. *Journal of Physics D: Applied Physics* **2009,** 42, (11), 113001.

60. Gresback, R.; Holman, Z.; Kortshagen, U., Nonthermal plasma synthesis of size-controlled, monodisperse, freestanding germanium nanocrystals. *Applied Physics Letters* **2007,** 91, (9), 093119-093119-3.

61. Radacsi, N.; van der Heijden, A.; Stankiewicz, A.; ter Horst, J., Cold plasma synthesis of high quality organic nanoparticles at atmospheric pressure. *Journal of nanoparticle research* **2013,** 15, (2), 1-13.

62. Bai, M.; Zhang, Z.; Leng, H.; Bai, X.; Yi, C., A study on the treatment of CO2, SO2, NOx, and fly ash by pulse activation. *Journal of the Air & Waste Management Association* **1999,** 49, (7), 854-860.

63. Liu, C.-j.; Xu, G.-h.; Wang, T., Non-thermal plasma approaches in CO< sub> 2</sub> utilization. *Fuel Processing Technology* **1999,** 58, (2), 119-134.

64. Ghorbanzadeh, A.; Lotfalipour, R.; Rezaei, S., Carbon dioxide reforming of methane at near room temperature in low energy pulsed plasma. *international journal of hydrogen energy* **2009,** 34, (1), 293-298.

65. Mikoviny, T.; Kocan, M.; Matejcik, S.; Mason, N.; Skalny, J., Experimental study of negative corona discharge in pure carbon dioxide and its mixtures with oxygen. *Journal of physics D: Applied physics* **2004,** 37, (1), 64.

66. Maezono, I.; Chang, J.-S. In *Reduction of CO 2 from combustion gases by DC corona torches*, Industry Applications Society Annual Meeting, 1988., Conference Record of the 1988 IEEE, 1988; IEEE: 1988; pp 1636-1640.

67. Hwang, B.-B.; Yeo, Y.-K.; Na, B.-K., Conversion of CH4 and CO2 to syngas and higher hydrocarbons using dielectric barrier discharge. *Korean Journal of Chemical Engineering* **2003,** 20, (4), 631-634.

68. Bill, A.; Eliasson, B.; Kogelschatz, U.; Zhou, L.-M., Comparison of CO 2 hydrogenation in a catalytic reactor and in a dielectric-barrier discharge. *Studies in Surface Science and Catalysis* **1998,** 114, 541-544.

69. Eliasson, B.; Kogelschatz, U.; Xue, B.; Zhou, L.-M., Hydrogenation of carbon dioxide to methanol with a discharge-activated catalyst. *Industrial & engineering chemistry research* **1998,** 37, (8), 3350-3357.

70. Kabashima, H.; Einaga, H.; Futamura, S., Hydrogen generation from water, methane, and methanol with nonthermal plasma. *Industry Applications, IEEE Transactions on* **2003,** 39, (2), 340-345.

71. Rehman, F.; Lozano-Parada, J. H.; Zimmerman, W. B., A kinetic model for H< sub> 2</sub> production by plasmolysis of water vapours at atmospheric pressure in a dielectric barrier discharge microchannel reactor. *international journal of hydrogen energy* **2012,** 37, (23), 17678-17690.

72. Jouve, G.; Goldman, A.; Goldman, M.; Haut, C., Surface chemistry induced by air corona discharges in a negative glow regime. *Journal of Physics D: Applied Physics* **2001,** 34, (2), 218.

73. Tendero, C.; Tixier, C.; Tristant, P.; Desmaison, J.; Leprince, P., Atmospheric pressure plasmas: A review. *Spectrochimica Acta Part B: Atomic Spectroscopy* **2006,** 61, (1), 2-30.

74. Kogelschatz, U., Atmospheric-pressure plasma technology. *Plasma Physics and Controlled Fusion* **2004,** 46, (12B), B63.

75. Kogelschatz, U., Applications of microplasmas and microreactor technology. *Contributions to Plasma Physics* **2007,** 47, (1-2), 80-88.

76. Locke, B.; Sato, M.; Sunka, P.; Hoffmann, M.; Chang, J.-S., Electrohydraulic discharge and nonthermal plasma for water treatment. *Industrial & engineering chemistry research* **2006,** 45, (3), 882-905.

77. Bruggeman, P.; Leys, C., Non-thermal plasmas in and in contact with liquids. *Journal of Physics D: Applied Physics* **2009,** 42, (5), 053001.

78. Ravasio, S.; Cavallotti, C., Analysis of reactivity and energy efficiency of methane conversion through non thermal plasmas. *Chemical Engineering Science* **2012,** 84, 580-590.

79. Ağıral, A.; Nozaki, T.; Nakase, M.; Yuzawa, S.; Okazaki, K.; Gardeniers, J., Gas-to-liquids process using multi-phase flow, non-thermal plasma microreactor. *Chemical Engineering Journal* **2011,** 167, (2), 560-566.

80. Okumoto, M.; Kim, H. H.; Takashima, K.; Katsura, S.; Mizuno, A., Reactivity of methane in nonthermal plasma in the presence of oxygen and inert gases at atmospheric pressure. *Industry Applications, IEEE Transactions on* **2001,** 37, (6), 1618-1624.

81. Wang, Q.; Shi, H.; Yan, B.; Jin, Y.; Cheng, Y., Steam enhanced carbon dioxide reforming of methane in DBD plasma reactor. *international journal of hydrogen energy* **2011,** 36, (14), 8301-8306.

82. Li, M.-W.; Liu, C.-P.; Tian, Y.-L.; Xu, G.-H.; Zhang, F.-C.; Wang, Y.-Q., Effects of catalysts in carbon dioxide reforming of methane via corona plasma reactions. *Energy & fuels* **2006,** 20, (3), 1033-1038.

83. Li, M.-W.; Tian, Y.-L.; Xu, G.-H., Characteristics of carbon dioxide reforming of methane via alternating current (AC) corona plasma reactions. *Energy & fuels* **2007,** 21, (4), 2335-2339.

84. Aleknaviciute, I.; Karayiannis, T.; Collins, M.; Xanthos, C., Methane decomposition under a corona discharge to generate CO x-free hydrogen. *Energy* **2013,** 59, 432-439.

85. Nozaki, T.; Okazaki, K., Non-thermal plasma catalysis of methane: Principles, energy efficiency, and applications. *Catalysis Today* **2013,** 211, 29-38.

86. Indarto, A.; Yang, D. R.; Palgunadi, J.; Choi, J.-W.; Lee, H.; Song, H. K., Partial oxidation of methane with Cu–Zn–Al catalyst in a dielectric barrier discharge. *Chemical Engineering and Processing: Process Intensification* **2008,** 47, (5), 780-786.

87. Khirsariya, P.; Mewada, R. K., Single Step Oxidation of Methane to Methanol–Towards Better Understanding. *Procedia Engineering* **2013,** 51, 409-415.

88. Du, C.; Mo, J.; Li, H., Renewable Hydrogen Production by Alcohols Reforming Using Plasma and Plasma-Catalytic Technologies: Challenges and Opportunities. *Chemical reviews* **2014**.

89. Liu, W.-Y.; Lei, Z.-L.; Wang, J.-K., Kinetics and mechanism of plasma oxidative desulfurization in liquid phase. *Energy & fuels* **2001,** 15, (1), 38-43.

90. Ma, C.; Dai, B.; Xu, C.; Liu, P.; Qi, L.; Ban, L., Deep oxidative desulfurization of model fuel via dielectric barrier discharge plasma oxidation using MnO< sub> 2</sub> catalysts and combination of ionic liquid extraction. *Catalysis Today* **2013,** 211, 84-89.

91. Fridman, A., *Plasma chemistry*. Cambridge University Press: 2008.

92. Lindner, P. J.; Besser, R. S., A microplasma reactor for chemical process intensification. *Chemical Engineering & Technology* **2012,** 35, (7), 1249-1256.

93. Kushner, M. J., Modelling of microdischarge devices: plasma and gas dynamics. *Journal of Physics D: Applied Physics* **2005,** 38, (11), 1633.

94. Papadakis, A.; Rossides, S.; Metaxas, A., Microplasmas: A review. *Open Applied Physics Journal* **2011,** 4, (1), 45-63.

95. *NIST Chemistry WebBook, NIST Standard Reference Database Number 69*. 2015.

96. Kim, Y.-K.; Irikura, K. K.; Rudd, M. E.; Ali, M. A.; Stone, P. M.; Chang, J.; Coursey, J. S.; Dragoset, R. A.; Kishore, A. R.; Olsen, K. J.; Sansonetti, A. M.; Wiersma, G. G.; Zucker, D. S.; Zucker, M. A., *Electron-Impact Cross Sections for Ionization and Excitation, NIST Standard Reference Database 107, National Institute of Standards and Technology*. August 2005.

97. Cobine, J. D., *Gaseous conductors: theory and engineering applications*. Dover Publications New York, NY: 1958.

98. Loeb, L. B., Electrical coronas: their basic mechanisms. **1965**.

99. Nasser, E., *Fundamentals of Gaseous Ionization and Plasma Electronics*. Wiley-Interscience New York: 1971; Vol. 197.

100. Starostin, S.; Premkumar, P. A.; Creatore, M.; Van Veldhuizen, E.; De Vries, H.; Paffen, R.; Van de Sanden, M., On the formation mechanisms of the diffuse atmospheric pressure dielectric barrier discharge in CVD processes of thin silica-like films. *Plasma Sources Science and Technology* **2009,** 18, (4), 045021.

101. Foest, R.; Schmidt, M.; Becker, K., Microplasmas, an emerging field of low-temperature plasma science and technology. *International Journal of Mass Spectrometry* **2006,** 248, (3), 87-102.

102. Ito, T.; Izaki, T.; Terashima, K., Application of microscale plasma to material processing. *Thin solid films* **2001,** 386, (2), 300-304.

103. Eden, J.; Park, S.-J.; Cho, J.; Kim, M.; Houlahan, T.; Li, B.; Kim, E.; Kim, T.; Lee, S.; Kim, K., Plasma Science and Technology in the Limit of the Small: Microcavity Plasmas and Emerging Applications. *Plasma Science, IEEE Transactions on* **2013,** 41, (4), 661-675.

104. Staack, D.; Farouk, B.; Gutsol, A.; Fridman, A., Characterization of a dc atmospheric pressure normal glow discharge. *Plasma Sources Science and Technology* **2005,** 14, (4), 700.

105. Becker, K.; Schoenbach, K.; Eden, J., Microplasmas and applications. *Journal of Physics D: Applied Physics* **2006,** 39, (3), R55.

106. Mariotti, D., Nonequilibrium and effect of gas mixtures in an atmospheric microplasma. *Applied Physics Letters* **2008,** 92, (15), 151505.

107. Staack, D.; Farouk, B.; Gutsol, A.; Fridman, A., Stabilization of the ionization overheating thermal instability in atmospheric pressure microplasmas. *Journal of Applied Physics* **2009,** 106, (1), 013303.

108. Farouk, T.; Farouk, B.; Fridman, A., Computational Studies of Atmospheric-Pressure Methane–Hydrogen DC Micro Glow Discharges. *Plasma Science, IEEE Transactions on* **2010,** 38, (2), 73-85.

109. Plasma Module Users Guide. In COMSOL Multiphysics: 2013.

110. Shao, T.; Tarasenko, V. F.; Zhang, C.; Baksht, E. K.; Zhang, D.; Erofeev, M. V.; Ren, C.; Shutko, Y. V.; Yan, P., Diffuse discharge produced by repetitive nanosecond pulses in open air, nitrogen, and helium. *Journal of Applied Physics* **2013,** 113, (9), 093301.

111. Pai, D. Z.; Lacoste, D. A.; Laux, C. O., Transitions between corona, glow, and spark regimes of nanosecond repetitively pulsed discharges in air at atmospheric pressure. *Journal of Applied Physics* **2010,** 107, (9), 093303.

112. Pai, D. Z.; Lacoste, D. A.; Laux, C. O., Nanosecond repetitively pulsed discharges in air at atmospheric pressure—the spark regime. *Plasma Sources Science and Technology* **2010,** 19, (6), 065015.

113. Zhang, C.; Shao, T.; Ma, H.; Zhang, D.; Ren, C.; Yan, P.; Tarasenko, V. F.; Schamiloglu, E., Experimental study on conduction current of positive nanosecond-pulse diffuse discharge at atmospheric pressure. *Dielectrics and Electrical Insulation, IEEE Transactions on* **2013,** 20, (4).

114. Liu, Z.-j.; Wang, W.-c.; Yang, D.-z.; Zhang, S.; Yang, Y.; Tang, K., The effect of dielectric thickness on diffuse nanosecond dielectric barrier discharges using a needle array-plate electrode configuration in air at atmospheric pressure. *Journal of Applied Physics* **2013,** 113, (23), 233305.

115. Shao, T.; Zhang, C.; Yu, Y.; Fang, Z.; Yan, P., Temporal evolution of nanosecond-pulse dielectric barrier discharges in open air. *EPL (Europhysics Letters)* **2012,** 97, (5), 55005.

116. Nozaki, T.; Hattori, A.; Okazaki, K., Partial oxidation of methane using a microscale non-equilibrium plasma reactor. *Catalysis today* **2004,** 98, (4), 607-616.

117. Lu, X.; Xiong, Q.; Xiong, Z.; Xian, Y.; Zhou, F.; Hu, J.; Gong, W.; Zhou, C.; Tang, Z.; Jiang, Z., Effect of nano-to millisecond pulse on dielectric barrier discharges. *Plasma Science, IEEE Transactions on* **2009,** 37, (5), 647-652.

118. Tao, S.; Kaihua, L.; Cheng, Z.; Ping, Y.; Shichang, Z.; Ruzheng, P., Experimental study on repetitive unipolar nanosecond-pulse dielectric barrier discharge in air at atmospheric pressure. *Journal of Physics D: Applied Physics* **2008,** 41, (21), 215203.

119. Schoenbach, K. H.; Zhu, W., High-Pressure Microdischarges: Sources of Ultraviolet Radiation. *Quantum Electronics, IEEE Journal of* **2012,** 48, (6), 768-782.

120. Wu, L.; Lin, A.; Lu, B.; Zheng, B.; Guo, M.; Hui, G. In *Experimental study of corona discharge with multi-walled carbon nanotubes electrode*, Robotics and Biomimetics (ROBIO), 2009 IEEE International Conference on, 2009; IEEE: 2009; pp 2146-2150.

121. Agiral, A.; Groenland, A. W.; Chinthaginjala, J. K.; Seshan, K.; Lefferts, L.; Gardeniers, J. H., On-chip microplasma reactors using carbon nanofibres and tungsten oxide nanowires as electrodes. *Journal of Physics D: Applied Physics* **2008,** 41, (19), 194009.

122. Yun, C.; Jian, Z., Ultra-Low Breakdown Voltage of Field Ionization in Atmospheric Air Based on Silicon Nanowires. *Plasma Science and Technology* **2013,** 15, (11), 1081.

123. Zhou, Z.; Zhang, J.; Ye, T.; Zhao, P.; Xia, W., Hydrogen production by reforming methane in a corona inducing dielectric barrier discharge and catalyst hybrid reactor. *Chinese Science Bulletin* **2011,** 56, (20), 2162-2166.

124. Hou, Z.; Cai, B.; Liu, H., Mechanism of gas breakdown near Paschen's minimum in electrodes with one-dimensional nanostructures. *Applied Physics Letters* **2009,** 94, (16), 163506-163506-3.

125. Wang, Q.; Corrigan, T.; Dai, J.; Chang, R.; Krauss, A., Field emission from nanotube bundle emitters at low fields. *Applied physics letters* **1997,** 70, (24), 3308-3310.

126. Wang, Q.; Setlur, A.; Lauerhaas, J.; Dai, J.; Seelig, E.; Chang, R., A nanotube-based field-emission flat panel display. *Applied Physics Letters* **1998,** 72, (22), 2912-2913.

127. Collins, P. G.; Zettl, A., Unique characteristics of cold cathode carbon-nanotube-matrix field emitters. *Physical Review B* **1997,** 55, (15), 9391.

128. Park, S.-J.; Eden, J.; Park, K.-H., Carbon nanotube-enhanced performance of microplasma devices. *Applied physics letters* **2004,** 84, (22), 4481-4483.

129. Eden, J.; Park, S.; Ostrom, N.; Chen, K., Recent advances in microcavity plasma devices and arrays: a versatile photonic platform. *Journal of Physics D: Applied Physics* **2005,** 38, (11), 1644.

130. Vandsburger, L.; Coulombe, S.; Meunier, J., Degradation of carbon nanotubes in oxygen glow discharges. *Carbon* **2013,** 57, 248-258.

131. Chen, C.-H.; Yeh, J. A.; Wang, P.-J., Electrical breakdown phenomena for devices with micron separations. *Journal of Micromechanics and Microengineering* **2006,** 16, (7), 1366.

132. Radmilović-Radjenović, M.; Radjenović, B.; Matječik, Š.; Klas, M., Field-emission–driven direct current hydrogen discharges in microgaps. *EPL (Europhysics Letters)* **2013,** 103, (4), 45002.

133. Radmilović-Radjenović, M.; Radjenović, B., An analytical relation describing the dramatic reduction of the breakdown voltage for the microgap devices. *EPL (Europhysics Letters)* **2008,** 83, (2), 25001.

134. Strong, F. W.; Skinner, J. L.; Tien, N. C., Electrical discharge across micrometer-scale gaps for planar MEMS structures in air at atmospheric pressure. *Journal of Micromechanics and Microengineering* **2008,** 18, (7), 075025.

135. Radmilović-Radjenović, M.; Radjenović, B., Theoretical study of the electron field emission phenomena in the generation of a micrometer scale discharge. *Plasma Sources Science and Technology* **2008,** 17, (2), 024005.

136. Go, D. B.; Fisher, T.; Garimella, S.; Bahadur, V., Planar microscale ionization devices in atmospheric air with diamond-based electrodes. *Plasma Sources Science and Technology* **2009,** 18, (3), 035004.

137. Hsieh, C.; Jou, S., Titanium nitride electrodes for micro-gap discharge. *Microelectronics journal* **2006,** 37, (9), 867-870.

138. Kim, M.; Cho, J.; Ban, S.; Choi, R.; Kwon, E.; Park, S.; Eden, J., Efficient generation of ozone in arrays of microchannel plasmas. *Journal of Physics D: Applied Physics* **2013,** 46, (30), 305201.

139. Lozano-Parada, J. H.; Zimmerman, W. B., The role of kinetics in the design of plasma microreactors. *Chemical Engineering Science* **2010,** 65, (17), 4925-4930.

140. Okumoto, M.; Rajanikanth, B.; Katsura, S.; Mizuno, A., Nonthermal plasma approach in direct methanol synthesis from CH 4. *Industry Applications, IEEE Transactions on* **1998,** 34, (5), 940-944.

141. Okazaki, K.; Hirai, S.; Nozaki, T.; Ogawa, K.; Hijikata, K., Plasma chemical reactions at atmospheric pressure for high efficiency use of hydrocarbon fuels. *Energy* **1997,** 22, (2), 369-374.

142. Liu, N.; Bai, M.; Wang, M.; Liu, K. In *Hydrogen production by methane reforming based on micro-gap discharge*, Journal of Physics: Conference Series, 2013; IOP Publishing: 2013; p 012146.

143. Nozaki, T.; Moriyama, S.; Okazaki, K.; Abe, S.; Kawai, K. In *Non-thermal plasma enhanced greenhouse gas conversion: Advanced C1-chemistry*, Proceedings of 21st Interantional Symposium on Plasma Chemistry, 2013; 2013.

144. Khoshtinat, M.; Amin, N.; Noshadi, I., A review of methanol production from methane oxidation via non-thermal plasma reactor. *World Academy of Science, Engineering and Technology* **2010,** 62, 354-358.

145. Nozaki, T.; Ağıral, A.; Yuzawa, S.; Han Gardeniers, J.; Okazaki, K., A single step methane conversion into synthetic fuels using microplasma reactor. *Chemical Engineering Journal* **2011,** 166, (1), 288-293.

146. Besser, R.; Lindner, P., Microplasma reforming of hydrocarbons for fuel cell power. *Journal of Power Sources* **2011,** 196, (21), 9008-9012.

147. Hsu, D. D.; Graves, D. B., Microhollow cathode discharge stability with flow and reaction. *Journal of Physics D: Applied Physics* **2003,** 36, (23), 2898.

148. Qiu, H.; Martus, K.; Lee, W.; Becker, K., Hydrogen generation in a microhollow cathode discharge in high-pressure ammonia–argon gas mixtures. *International Journal of Mass Spectrometry* **2004,** 233, (1), 19-24.

149. Lindner, P. J.; Hwang, S. Y.; Besser, R. S., Analysis of a Microplasma Fuel Reformer with a Carbon Dioxide Decomposition Reaction. *Energy & Fuels* **2013,** 27, (8), 4432-4440.

150. Koutsospyros, A. D.; Yin, S.-M.; Christodoulatos, C.; Becker, K., Plasmochemical degradation of volatile organic compounds (VOC) in a capillary discharge plasma reactor. *Plasma Science, IEEE Transactions on* **2005,** 33, (1), 42-49.

151. Mariotti, D.; Sankaran, R. M., Perspectives on atmospheric-pressure plasmas for nanofabrication. *Journal of Physics D: Applied Physics* **2011,** 44, (17), 174023.

152. Bruggeman, P.; Brandenburg, R., Atmospheric pressure discharge filaments and microplasmas: physics, chemistry and diagnostics. *Journal of Physics D: Applied Physics* **2013,** 46, (46), 464001.

153. Pearse, R. W. B.; Gaydon, A. G., *The identification of molecular spectra*. Chapman and Hall London: 1976; Vol. 297.

154. Lunsford, J. H., The catalytic oxidative coupling of methane. *Angewandte Chemie International Edition in English* **1995,** 34, (9), 970-980.

155. Cavallini, M.; Biscarini, F., Electrochemically etched nickel tips for spin polarized scanning tunneling microscopy. *Review of scientific Instruments* **2000,** 71, (12), 4457-4460.

156. Delavari, S.; Amin, N. A. S.; Mazaheri, H., Oxidative coupling of methane in a corona discharge plasma reactor using HY zeolite as a catalyst. *Reaction Kinetics, Mechanisms and Catalysis* **2014,** 113, (2), 557-573.

157. 高鍋和広, Catalytic Conversion of Methane: Carbon Dioxide Reforming and Oxidative Coupling. *Journal of the Japan Petroleum Institute* **2012,** 55, (1), 1-12.

158. Batiot, C.; Hodnett, B., The role of reactant and product bond energies in determining limitations to selective catalytic oxidations. *Applied Catalysis A: General* **1996,** 137, (1), 179-191.

159. Lee, J.; Oyama, S., Oxidative coupling of methane to higher hydrocarbons. *Catalysis Reviews Science and Engineering* **1988,** 30, (2), 249-280.

160. Li, S., Reaction Chemistry of W-Mn/SiO~ 2 Catalyst for the Oxidative Coupling of Methane. *Journal of Natural Gas Chemistry* **2003,** 12, (1), 1-9.

161. Langfeld, K.; Frank, B.; Strempel, V. E.; Berger-Karin, C.; Weinberg, G.; Kondratenko, E. V.; Schomäcker, R., Comparison of oxidizing agents for the oxidative coupling of methane over state-of-the-art catalysts. *Applied Catalysis A: General* **2012,** 417, 145-152.

162. Nozaki, T.; Muto, N.; Kado, S.; Okazaki, K., Dissociation of vibrationally excited methane on Ni catalyst: Part 1. Application to methane steam reforming. *Catalysis Today* **2004,** 89, (1), 57-65.

163. Nozaki, T.; Miyazaki, Y.; Unno, Y.; Okazaki, K., Energy distribution and heat transfer mechanisms in atmospheric pressure non-equilibrium plasmas. *Journal of Physics D: Applied Physics* **2001,** 34, (23), 3383.

164. Suib, S. L.; Brock, S. L.; Marquez, M.; Luo, J.; Matsumoto, H.; Hayashi, Y., Efficient catalytic plasma activation of CO2, NO, and H2O. *The Journal of Physical Chemistry B* **1998,** 102, (48), 9661-9666.

165. Wang, D.; Qian, E. W.; Amano, H.; Okata, K.; Ishihara, A.; Kabe, T., Oxidative desulfurization of fuel oil:: Part I. Oxidation of dibenzothiophenes using tert-butyl hydroperoxide. *Applied Catalysis A: General* **2003,** 253, (1), 91-99.

166. Ogunlaja, A. S.; Walmsley, R. S.; du Sautoy, C.; Torto, N.; Tshentu, Z. R., Development of a continuous flow system for the oxidative desulfurization of refractory organosulfur compounds in hydrotreated diesel. *Energy & Fuels* **2013,** 27, (12), 7714-7723.

167. Zapata, B.; Pedraza, F.; Valenzuela, M. A., Catalyst screening for oxidative desulfurization using hydrogen peroxide. *Catalysis Today* **2005,** 106, (1), 219-221.

168. Sampanthar, J. T.; Xiao, H.; Dou, J.; Nah, T. Y.; Rong, X.; Kwan, W. P., A novel oxidative desulfurization process to remove refractory sulfur compounds from diesel fuel. *Applied Catalysis B: Environmental* **2006,** 63, (1), 85-93.

169. Li, C.; Jiang, Z.; Gao, J.; Yang, Y.; Wang, S.; Tian, F.; Sun, F.; Sun, X.; Ying, P.; Han, C., Ultra-Deep Desulfurization of Diesel: Oxidation with a Recoverable Catalyst Assembled in Emulsion. *Chemistry-A European Journal* **2004,** 10, (9), 2277-2280.

170. Komintarachat, C.; Trakarnpruk, W., Oxidative desulfurization using polyoxometalates. *Industrial & engineering chemistry research* **2006,** 45, (6), 1853-1856.

171. Shiraishi, Y.; Taki, Y.; Hirai, T.; Komasawa, I., Visible light-induced deep desulfurization process for light oils by photochemical electron-transfer oxidation in an organic two-phase extraction system. *Industrial & engineering chemistry research* **1999,** 38, (9), 3310-3318.

172. Shiraishi, Y.; Hirai, T.; Komasawa, I., A deep desulfurization process for light oil by photochemical reaction in an organic two-phase liquid-liquid extraction system. *Industrial & engineering chemistry research* **1998,** 37, (1), 203-211.

173. Torres-Nieto, J.; Arévalo, A.; García, J. J., Catalytic desulfurization of dibenzothiophene and its hindered analogues with nickel and platinum compounds. *Organometallics* **2007,** 26, (9), 2228-2233.

174. Jiang, W.; Zhu, W.; Li, H.; Xue, J.; Xiong, J.; Chang, Y.; Liu, H.; Zhao, Z., Fast Oxidative Removal of Refractory Aromatic Sulfur Compounds by a Magnetic Ionic Liquid. *Chemical Engineering & Technology* **2014,** 37, (1), 36-42.

175. Mei, H.; Mei, B.; Yen, T. F., A new method for obtaining ultra-low sulfur diesel fuel via ultrasound assisted oxidative desulfurization☆. *Fuel* **2003,** 82, (4), 405-414.

176. Lili, B.; Ping, L.; Cunhua, M.; Bin, D., Deep Desulfurization of Diesel Fuels with Plasma/Air as Oxidizing Medium, Diperiodatocuprate (III) as Catalyzer and Ionic Liquid as Extraction Solvent. *Plasma Science and Technology* **2013,** 15, (12), 1226.

177. Ban, L.; Liu, P.; Ma, C.; Dai, B., Deep oxidative/adsorptive desulfurization of model diesel oil by DBD/FeCl 3–SiO 2. *Catalysis Today* **2013,** 211, 78-83.

178. Caple, K. R., Oxidative desulfurization of dibenzothiophene with tert-butyl peroxide in a carbon nanotube supported corona discharge microreactor. **2010**.

179. Andersson, J. T.; Weis, U., Gas chromatographic determination of polycyclic aromatic compounds with fluorinated analogues as internal standards. *Journal of chromatography A* **1994,** 659, (1), 151-161.

180. Jeevanandam, P.; Klabunde, K.; Tetzler, S., Adsorption of thiophenes out of hydrocarbons using metal impregnated nanocrystalline aluminum oxide. *Microporous and Mesoporous Materials* **2005,** 79, (1), 101-110.

181. Yan, X.-M.; Su, G.-S.; Xiong, L., Oxidative desulfurization of diesel oil over Ag-modified mesoporous HPW/SiO 2 catalyst. *Journal of Fuel Chemistry and Technology* **2009,** 37, (3), 318-323.

182. Lin, L.; Hong, L.; Fanfei, M.; Ning, W.; Yiyi, H., Optimization Study on Oxidative Desulfurization of Crude Oil under Electric Field. *China Petroleum Processing and Petrochemical Technology* **2011,** 13, (3), 59-63.

183. Takahashi, A.; Yang, F. H.; Yang, R. T., New sorbents for desulfurization by π-complexation: thiophene/benzene adsorption. *Industrial & Engineering Chemistry Research* **2002,** 41, (10), 2487-2496.

184. Ai, S.; Sui, H.; Li, H., Coordinative Adsorption of Thiophene with Metallic Silver/Adsorbent Cotton Prepared via Aqueous In Situ Reduction for Desulfurization. *Industrial & Engineering Chemistry Research* **2012,** 51, (38), 12337-12343.

185. Meiners, A., Electron Energy Distribution Function. In *COMSOL Blog*, https://www.comsol.com/blogs/electron-energy-distribution-function/, Aug 14, 2014; Vol. 2015.

186. Arutyunov, V. S.; Basevich, V. Y.; Vedeneev, V. I., Kinetic limit of C 2 hydrocarbons yield at gas-phase oxidative coupling of methane. *Studies in Surface Science and Catalysis* **1997,** 107, 351-354.

187. Simon, Y.; Baronnet, F.; Marquaire, P.-M., Kinetic modeling of the oxidative coupling of methane. *Industrial & Engineering Chemistry Research* **2007,** 46, (7), 1914-1922.

188. Farsi, A.; Moradi, A.; Ghader, S.; Shadravan, V.; Manan, Z. A., Kinetics investigation of direct natural gas conversion by oxidative coupling of methane. *Journal of Natural Gas Science and Engineering* **2010,** 2, (5), 270-274.

189. Zhang, J.-q.; Yang, Y.-j.; Zhang, J.-s.; Liu, Q.; Tan, K.-r., Non-oxidative coupling of methane to C2 hydrocarbons under above-atmospheric pressure using pulsed microwave plasma. *Energy & fuels* **2002,** 16, (3), 687-693.

190. Kado, S.; Sekine, Y.; Fujimoto, K., Direct synthesis of acetylene from methane by direct current pulse discharge. *Chem. Commun.* **1999**, (24), 2485-2486.

191. Oumghar, A.; Legrand, J.; Diamy, A.; Turillon, N., Methane conversion by an air microwave plasma. *Plasma Chemistry and Plasma Processing* **1995,** 15, (1), 87-107.

192. J. A. Manion, R. E. H., R. D. Levin, D. R. Burgess Jr., V. L. Orkin, W. Tsang, W. S. McGivern, J. W. Hudgens, V. D. Knyazev, D. B. Atkinson, E. Chai, A. M. Tereza, C.-Y. Lin, T. C. Allison, W. G. Mallard, F. Westley, J. T. Herron, R. F. Hampson, and D. H. Frizzell, NIST Chemical Kinetics Database, NIST Standard Reference Database 17, Version 7.0 (Web Version), Release 1.6.8. In Technology, N. I. o. S. a., Ed. Gaithersburg, Maryland, Data version 2013.03.

193. Kreider, P. B.; Kim, K.-J.; Chang, C.-H., Two-step continuous-flow synthesis of CuInSe 2 nanoparticles in a solar microreactor. *RSC Advances* **2014,** 4, (27), 13827-13830.

194. Kim, K.-J.; Kreider, P. B.; Chang, C.-H.; Park, C.-M.; Ahn, H.-G., Visible-light-sensitive nanoscale Au–ZnO photocatalysts. *Journal of nanoparticle research* **2013,** 15, (5), 1-11.

195. Caple, K.; Kreider, P.; AuYeung, N.; Yokochi, A., Experimental modeling of hydrogen producing steps in a novel sulfur–sulfur thermochemical water splitting cycle. *International Journal of Hydrogen Energy* **2015**.

196. Kim, K.-J.; Kreider, P. B.; Choi, C.; Chang, C.-H.; Ahn, H.-G., Visible-light-sensitive Na-doped p-type flower-like ZnO photocatalysts synthesized via a continuous flow microreactor. *RSC Advances* **2013,** 3, (31), 12702-12710.

197. Kim, K.-J.; Chong, X.; Kreider, P. B.; Ma, G.; Ohodnicki, P. R.; Baltrus, J. P.; Wang, A. X.; Chang, C.-H., Plasmonics-enhanced metal–organic framework nanoporous films for highly sensitive near-infrared absorption. *Journal of Materials Chemistry C* **2015,** 3, (12), 2763-2767.

198. Kim, K.-J.; Li, Y. J.; Kreider, P. B.; Chang, C.-H.; Wannenmacher, N.; Thallapally, P. K.; Ahn, H.-G., High-rate synthesis of Cu–BTC metal–organic frameworks. *Chemical Communications* **2013,** 49, (98), 11518-11520.

199. Kim, K.-J.; Oleksak, R. P.; Pan, C.; Knapp, M. W.; Kreider, P. B.; Herman, G. S.; Chang, C.-H., Continuous synthesis of colloidal chalcopyrite copper indium diselenide nanocrystal inks. *RSC Advances* **2014,** 4, (32), 16418-16424.

200. Puntes, V. F.; Zanchet, D.; Erdonmez, C. K.; Alivisatos, A. P., Synthesis of hcp-Co nanodisks. *Journal of the American Chemical Society* **2002,** 124, (43), 12874-12880.